University of Oviedo

Ph.D. Program in Energy and Process Control

Optimized design of aerodynamic airfoils for vertical axis wind turbines

Andrés Meana Fernández

Optimized design of aerodynamic airfoils for vertical axis wind turbines

A dissertation submitted in accordance
with the requirements of the degree of
Doctor of Philosophy (Energy and Process Control)

by

Andrés Meana Fernández

Fluid Mechanics Area,
Department of Energy,
University of Oviedo.

Gijón, Asturias, Spain.
September 2019

This thesis has been approved by the supervisors:

Prof. Sandra Velarde Suárez
Prof. Jesús Manuel Fernández Oro

Composition of the promotion committee:

Prof. Jorge Luis Parrondo Gayo,
University of Oviedo (chairman)
Prof. MªTeresa Parra Santos,
University of Valladolid (secretary)
Prof. Gabriel Ibarra Berastegui,
University of Basque Country
Prof. Francesco Avallone,
Delft University of Technology
Prof. José González Pérez,
University of Oviedo

Prof. Antonio José Gutiérrez Trashorras,
University of Oviedo (reserve chairman)
Prof. Francisco Castro Ruiz,
University of Valladolid (reserve secretary)
Prof. Gustavo Adolfo Esteban Alcalá,
University of Basque Country (reserve member)
Prof. Daniele Ragni,
Delft University of Technology (reserve member)
Prof. Katia MªArgüelles Díaz,
University of Oviedo (reserve member)

Universidad de Oviedo
Universidá d'Uviéu
University of Oviedo

GOBIERNO DE ESPAÑA
MINISTERIO DE EDUCACIÓN Y FORMACIÓN PROFESIONAL

Keywords: vertical-axis wind turbine; analytical models; CFD simulation; wind tunnel testing

Study and in general the pursuit of truth and beauty is a sphere of activity
in which we are permitted to remain children all our lives.

Albert Einstein (1879-1955)

To my family and friends

Contents

List of Figures

List of Tables

List of Abbreviations

α	Angle of attack
$\bar{u}$	Mean flow velocity
ΔA_i	Area of the cell i
ΔH	Size of the vertical elements of the turbine discretization
Δt_{LES}	Time step size for LES simulations
Δt_{SAS}	Time step size for SAS simulations
Δt_{U-RANS}	Time step size for U-RANS simulations
Δt_{WMLES}	Time step size for WMLES simulations
Δx^+	Normalized wall distance in x-direction
Δy^+	Normalized wall distance in y-direction
Δz^+	Normalized wall distance in z-direction
Δ	Reduction in the maximum bending stress on the blades
δ	Boundary layer thickness
$\Delta \dot{E}_x$	Flow exergy variation
$\Delta \theta$	Size of the azimuthal elements of the turbine discretization
δ^*	Boundary layer displacement thickness
Δ_{cell}	Cell size
$\dot{m}$	Air mass flow
ℓ	Typical flow lengthscale
ℓ_c	Size of the scales corresponding to the cut-off frequency of the LES filter
$\eta_{no\,blades}$	Total efficiency of the turbine system with no blades
η_{struts}	Efficiency of the turbine struts
$\eta_{with\,blades}$	Total efficiency of the turbine system with blades
Γ	Vortex strenght

Γ_d	Bounded circulation downstream from the turbine
γ_d	Vortex sheet strenght at the downstream part of the turbine
Γ_u	Bounded circulation upstream from the turbine
γ_u	Vortex sheet strenght at the upstream part of the turbine
κ_c	frequency of LES filter
λ	Tip-speed ratio
μ	Air dynamic viscosity
ω	Turbine rotational speed, specific dissipation rate
Ω_{ij}	Vorticity tensor
ϕ	Variable used to judge grid convergence
ϕ_{ext}^{ij}	Extrapolated value of the numerical solution
Π	Dimensionless group
ψ_{in}	Flow specific exergy before passing through the turbine
ψ_{out}	Flow specific exergy after passing through the turbine
ρ	Air density
ρ_{Al}	Aluminum density
ρ_{Fe}	Iron density
ρ_{PLA}	PLA density
σ	Turbine solidity
θ	Blade azimuthal position
$\tilde{\nu}$	Modified turbulent viscosity
ε	Exergy efficiency, turbulent dissipation rate
ε_{ijk}	Levi-Civita symbol
ε_{ij}	Absolute error of the variable from the simulation with meshes i and j
$\vec{e}_\omega$	Vortex element direction
$\vec{u}(\vec{x},t)$	Velocity induced by a vortex filament
$\vec{x}$	Position in space
A	Rotor swept area, cross-section area of the support structures

a	velocity induction factor
A_B	Cross-section area of the blades
a_d	Interference factor for the downwind region
a_u	Interference factor for the upwind region
b	Base of the support plates
c	Airfoil chord
C_μ	Constant used for consistency with the definition of turbulent length scales
C_D	Drag coefficient
C_L	Lift coefficient
C_N	Normal force coefficient
C_P	Power coefficient
C_Q	Torque coefficient
C_T	Tangential force coefficient, Thrust coefficient
$C_{D,0^\circ}$	Drag coefficient of the blade airfoil at 0°
$C_{D,struts}$	Drag coefficient of the turbine struts
D	Drag force, turbine diameter, diameter of the support struts
e_a^{ij}	Relative error of the numerical solution
e_{ext}^{ij}	Extrapolated relative error of the numerical solution
f	Frequency of airfoil cycle, solution from numerical simulations, frequency
f	Solution from numerical simulations
F_S	Security factor for the calculation of the GCI
f_{exact}	Continuum value from a numerical simulation with zero grid spacing
f_{up}, f_{dw}	Upwind and downwind actuator disk thrust factors
g_i	Functions defined in the continuum for numerical simulations
GCI^*	Desired grid convergence level
H	Rotor height, angular momentum
h	Grid size parameter, height of the support plates
h_{ST}	Spatial-temporal index for assessing numerical convergence

$k - \varepsilon$	k-epsilon turbulence model
L	Blade support length
L	Largest scales of the flow
L	Lift force, largest scales of the flow, blade support length, characteristic length
L_B	Blade span
L_z	Spanwise extent of the simulation domain
m_B	Mass of the PLA part of the blades
$M_{b,max}$	Maximum bending moment of the blades
m_{blade}	Mass of the blades
$M_{res,blades}$	Torque due to aerodynamic drag on the blades
$M_{res,struts}$	Resistive torque due to drag on the turbine struts
M_{res}	Total resistive torque
m_{SR}	Mass of the iron core rods of the blades
N	Normal force, number of blades
n	Number of actuator disks
N_Ω	Number of cells inside a volumen region
N_θ	Number of azimuthal elements of the turbine discretization
N_S	Number of vertical elements of the turbine discretization
N_s	Number of cells in the simulation domain
N_t	Number of time steps per rotor revolution
P	Turbine aerodynamic power
p	Apparent order of the extrapolation method
P_D	Dynamic pressure
P_e	Turbine electrical power
P_S	Static pressure
P_T	Total pressure
Q	Torque, Quantity for the Q-criterion model
q	Weigth load of the supports

$q(p)$	Function dependent on the drig refinement ratio
R	Turbine radius
r^*	Required grid resolution
r_{ij}	Grid size ratio between meshes i and j
Re	Reynolds number
Re_t	Turbine Reynolds number
S	Airfoil cross section
s	Parameter describing monotonic or oscillatory behavior of the solution
S_{ij}	Rate of strain
St	Strouhal number
T	Tangential force, thrust force
t	Thickness of the support struts
T_B	Torque at a blade, blade passing period
T_S	Torque at a blade element
T_{sh}	Vortex shedding period
TI	Turbulence intensity
U	Velocity of the largest scales of the flow
u'	Longitudinal velocity fluctuations
u_1, u_2	Induction factors for the upwind and downwind parts of the turbine
u_i'	i-component of the turbulent velocity fluctuations
u_k	k-component of the velocity
u_{ℓ_c}	Velocity of the scales corresponding to the cut-off frequency of the LES filter
V	Wind velocity
v'	Transversal velocity fluctuations
V_1	Velocity at the upstream actuator disk
V_2	Velocity at the downstream actuator disk
V_∞	Incoming wind velocity
V_C	Vortex convection velocity

V_d	Velocity jump in the downstream region
V_u	Velocity jump in the upstream region
V_w	Wind wake velocity, velocity jump in the far-wake region
W	Blade relative velocity, power dissipated by the turbine
w	Spanwise extent of the simulation domain
W_z	Bending resistance modulus
W_{AERO}	Aerodynamic power generated by the turbine
W_{struts}	Power dissipated by the turbine struts
$W_{z,B}$	Bending resistance modulus of the blades
x_j	j-direction of space
y^+	Normalized wall distance
AEE	Spanish Wind Energy Association (Asociación Empresarial Eólica)
BAT	Buoyant Airborne Turbine
BEM	Blade Element Method
BPF	Blade passing frequency
BSL $k-\omega$	Baseline k-omega turbulence model
CAD	Computer-Aided Design
CFD	Computational Fluid Dynamics
DDSM	Double-Disc Streamtube Model
DES	Detached Eddy Simulation
DMST	Double-Multiple Streamtube Model
DNS	Direct Numerical Simulations
ELES	Embedded Large Eddy Simulation
FDM	Fused-Deposition Modeling
FVM	Finite Volume Method
GCI	Grid Convergence Index
HAWT	Horizontal Axis Wind Turbine
HWA	Hot-wire anemometry

IPCC	Intergovernmental Panel on Climate Change
IUTA	University Institute of Industrial Technology of Asturias
KH	Kelvin-Helmholtz instabilities
LES	Large Eddy Simulation
LTT	Low Turbulence Tunnel
MSTM	Multiple Streamtubes Model
NASA	National Aeronautics and Space Administration
OMA	Operational Modal Analysis
PIV	Particle Image Velocimetry
PLA	polylactic acid
PSD	Power Spectrum Density
RANS	Reynolds-Averaged Navier-Stokes
RSM	Reynolds Stress turbulence model
S-A	Spalart-Allmaras turbulence model
SAS	Scale-Adaptive Simulation
SC	Stall cell
SIMPLE	Semi-Implicit Method for Pressure Linked Equations
SLS	Selective Laser Sintering
SME	Small and Medium-sized Enterprise
SRS	Scale-Resolving Simulation
SST $k-\omega$	Shear Stress Transport k-omega turbulence model
SSTM	Single Streamtube Model
Std $k-\omega$	Standard k-omega turbulence model
T-GCI	Temporal-Grid Convergence Index
TKE	Turbulent kinetic energy
TSR	Tip-speed ratio
U-RANS	Unsteady Reynolds-Averaged Navier-Stokes
UDF	User-Defined Function

UPS	Uninterruptible power source
VAWT	Vertical Axis Wind Turbine
VGOT	Variable Geometry Oval Trajectory
VP	Vortex packet
WALE	Wall-Adapting Local Eddy-Viscosity Model
WMLES	Wall-Modeled Large Eddy Simulation
WRLES	Wall-Resolved Large Eddy Simulation

Summary

The current world context demands a change towards environmentally friendly energy sources. Luckily, the interest on renewable energy sources has been constantly increasing over the past years. Nowadays, wind energy represents one of the most economical options, employing a totally mature harvesting technology. Due to their higher energy output, horizontal-axis wind turbines have been traditionally the preferred option. Nevertheless, vertical-axis wind turbines are becoming relevant, specially in urban areas. Their advantages evidence the need of further research to overcome the main drawbacks that prevent their implantation.

The main objective of this thesis is the development of scientific-technological knowledge applicable to the design of optimized vertical-axis wind turbines. As an ultimate goal, transfer of this knowledge is foreseen to small and medium-sized enterprises. Firstly, a literature survey about wind power extraction systems has been performed, focusing afterwards in vertical-axis wind turbines, their advantages, disadvantages and research interest. Then, the design and analysis techniques applicable to vertical-axis wind turbines have been reviewed. Afterwards, an analytical model based on streamtube theory has been developed to predict the performance of prospective turbine designs, being able to predict the whole power curve in computational times in the order of minutes. The model has been used to analyze the influencing parameters in the turbine performance, proposing optimal values of these parameters and the optimal characteristics that an airfoil should possess to be suitable for practical applications of these turbines. Subsequently, the focus has been set on Computational Fluid Dynamics models for the study of the aerodynamic performance and the flow field developed by both a vertical-axis wind turbine and an isolate typical turbine airfoil. Guidelines for the numerical simulation of both turbines and airfoils are provided. Additionally, the main flow unsteadiness generation mechanisms, flow field regions and instabilities have been identified. Insight into the loss of performance of these turbines due to fluid dynamics phenomena has been also provided. Finally, all the generated knowledge has been applied to the design of a small-scale turbine model, developing a procedure for the in-house fabrication of turbine blades and an experimental procedure to estimate the aerodynamic performance of the turbine. Hot-wire measurements have been performed in the turbine wake. The experimental results have verified the methodologies developed in this thesis. Finally, the main findings and implications of this study are discussed, and future research possibilities are outlined.

Resumen

El contexto global actual demanda un cambio hacia fuentes de energía más respetuosas con el medio ambiente. Afortunadamente, el interés hacia fuentes de energía renovables ha estado aumentando de forma continua durante los últimos años. Hoy en día, la energía eólica representa una de las opciones más económicas, al utilizar una tecnología de aprovechamiento totalmente madura. Debido a su mayor producción de energía, las turbinas eólicas de eje horizontal han sido tradicionalmente la opción preferida. Sin embargo, las turbinas de eje vertical están ganando importancia, especialmente en entornos urbanos. Sus ventajas evidencian la necesidad de realizar un esfuerzo en investigación para superar las dificultades que impiden su proliferación.

El principal objetivo de esta tesis es el desarrollo de conocimiento científico-tecnológico aplicable al diseño de turbinas eólicas de eje vertical optimizadas. Como fin último, se plantea la transferencia de este conocimiento a pequeñas y medianas empresas. Primero se ha realizado una revisión del estado del arte respecto a los sistemas de extracción de energía eólica, para después centrarse en las turbinas eólicas de eje vertical, sus ventajas, desventajas y el interés de su investigación. Después, se han revisado las técnicas de diseño y análisis aplicables a estas turbinas. Posteriormente, se ha desarrollado un modelo analítico basado en la teoría de tubos de corriente para predecir las prestaciones de distintos diseños de turbinas, siendo capaz de predecir la curva de potencia completa en tiempos computacionales del orden de minutos. El modelo se ha utilizado para analizar los parámetros que influyen en las prestaciones de estas turbinas, proponiendo valores óptimos de dichos parámetros y las características óptimas que un perfil aerodinámico debería poseer para ser utilizado en aplicaciones relacionadas con este tipo de turbinas. Más adelante, se ha centrado la investigación en modelos de Dinámica de Fluidos Computacional para estudiar las prestaciones aerodinámicas y el campo fluido generado por una turbina eólica de eje vertical y un perfil aislado, típico de esta clase de turbinas. Se han proporcionado indicaciones para la simulación numérica tanto de turbinas como de perfiles. Además, se han identificado los principales mecanismos de generación de inestabilidades en el flujo y las regiones e inestabilidades en el campo fluido. También se ha proporcionado una visión acerca de la pérdida de rendimiento de estas turbinas debido a fenómenos fluidodinámicos. Finalmente, todo el conocimiento generado se ha aplicado al diseño de un modelo a escala reducida de una turbina, desarrollando un procedimiento para la fabricación de las palas de la turbina y un procedimiento experimental para estimar el rendimiento aerodinámico de la turbina. Se han realizado medidas de anemometría térmica en la estela de la turbina. Los resultados experimentales han servido para verificar las metodologías desarrolladas en esta tesis. Finalmente, se discuten los principales resultados e implicaciones de este estudio, esbozando posibles líneas de investigación futuras.

Preface

This thesis would not have been possible, or would have turned out completely different, had it not been for the support, guidance and care from the people who have accompanied me throughout this path.

First of all, I would like to thank **Prof. Jorge L. Parrondo Gayo** as the Head of the Department of Energy and **Prof. Eduardo Blanco Marigorta** as the Head of our Research Group in the University of Oviedo, for integrating me and providing help and support when needed.

I would also like to express my gratitude to my thesis promotors. **Prof. Sandra Velarde Suárez**, for introducing me to the Fluid Mechanics Area and providing me with several learning opportunities during the realization of this thesis, as well as the necessary feedback to improve my professional skills. **Prof. Jesús M. Fernández Oro**, for putting all his knowledge and time at my disposal, being always willing to help, and for the personal treatment and encouragement, becoming a role model of good academic practice.

Thanks as well to **Prof. Carlos J. Simão Ferreira** from the Technical University of Delft, for accepting me as a guest researcher for three months in which was one of the best experiences I have ever had during my PhD studies, for letting me learn from him and for caring about my well-being there.

Additionally, I would like to thank the reviewers of this document, **Prof. Sergio Lavagnoli** from the Von Karman Insitute for Fluid Dynamics (Belgium), **Prof. Massimo Masi** from the University of Padova (Italy) and **Prof. Tolga Yasa** from the Eskisehir Technical University (Turkey). Thanks to their altruist revision of this manuscript, it was possible to improve its quality before final submission. I would also like to thank the members of the thesis committee traveling from external universities to attend my dissertation: **Prof. MªTeresa Parra Santos** and **Prof. Francisco Castro Ruiz** from the University of Valladolid (Spain), **Prof. Gabriel Ibarra Berastegui** and **Prof. Gustavo A. Esteban Alcalá** from the University of the Basque Country (Spain); and **Prof. Francesco Avallone** and **Prof. Daniele Ragni** from the Technical University of Delft (Netherlands).

All these years in the research lab would have been completely different without the companionship and support from the people in the Department. Thanks to **Adrián, Alberto, Bruno, Celia, Charo, Fran, Irene, José, Katia, Manuel, Milagros, Mónica, Pedro** and **Raúl**. Thanks to my international friends **Ahmed, Baye, Doddy, Guidong, Hesham** and **Mina** as well. Thanks to **Luis** for all the help and support provided during the construction and improvement of the experimental demonstrator, as well as for the good times spent off-work. Thanks to **Ana**, for the support in the lab and our coffee talks. Thanks to **Helmut**, our Department Secretary, for the long conversations about saving the world; and to **Rosa, Toni, Jesús** and **Modesta**, our building clerks, for talking about everything from my thesis to art, design and football. Thanks to **Gemma**, the Secretary of our PhD program, for helping me going smoothly through all the bureaucracy. Thanks to the people from the **Department of Construction and Manufacturing Engineering**, especially **Agustín**, their technician, for helping us with the construction of the experimental prototype; the **Department of Materials**, for letting us perform experimental fracture tests in our printed parts and the **Department of Electrical, Electronic, Computers and Systems Engineering**, for helping us with the experimental power tests of the turbine model, especially **Manuel Rico** and **Antonio J. Calleja**. Thanks to **Jaime Viña** and **Victoria Mollón** for the corridor chats about the thesis, about running and about the future. Thanks to **Eduardo Álvarez** for his support during the realization of my thesis, for covering my expenses for a conference with his own money and for training me until I could run ten kilometers in below forty minutes and a half marathon in one and a half hour. Thanks to **Antonio J. Gutiérrez** for all the caring and support provided. Thanks to **Aitor** and **Eva** for the nice chats and discussions, as well as to **Antonio Navarro**, who also helped me get an indoor climbing license. Thanks to **Juanjo del Coz**, for providing me with his mentorship and friendship since I can no longer remember. Thanks to **Julio Fernández** for reading my thesis, helping me with the mathematical notation, and providing further support.

Special thanks to two people I have met in this institution: **Alberto Menéndez** and **Bernardo Peris**. Thanks to **Alberto** for being my personal coach during all this path, encouraging me and not letting me lose the vision of my dreams (as well as for reading this whole document and our afterwork sessions). I hope life gives you back at least half of all the good you have done. Thanks to **Bernardo**: when I was showing you Gijón to make the city more comfortable to you, I was not expecting to receive such a good friendship in return, as well as your post-doc perspective that has helped me so much during these last months of my PhD.

Thanks to the people from Arcelor-Mittal in Avilés, who showed me that I could use my skills outside of academia for developing solutions to technical problems applied to day-to-day industry. Special thanks to **Ángel**, which has been the best boss one could dream of and also a real friend, and **Alfonso** and **Chapa**, for showing me the knowledge that is learned outside a classroom with care and patience and making me feel valuable inside the industrial environment.

So far, my life has been a nice trip full of nice people around. I keep record of all of you and I carry you in my heart. From the childhood and adolescence, **thanks to all my friends and teachers in Colegio Corazón de María** in Gijón that have helped me define the core of my personality. Thanks to the friends I made during those summers before coming of age. Thanks to the friends I made in the **University and out of it**, the friends that I made in **Clausthal-Zellerfeld (Germany)**, the ones in **Besançon (France)** and in **Delft (Netherlands)**.

And finally, thanks to **my family**, which has been a constant source of support, care and love since I was born. Thanks to my parents, brother, sister, grandparents, uncles, aunts and cousins. When it all comes down, it is a relief to know that I will always have you.

I will end this section with a list of names which I have not made explicit in this text (it has become long enough at this point and each of you know why you are on this list). Hence, apart from the explicitly mentioned above, thanks to: **Adelina, Adrián, Adriana, Agustín, Ahmed, Aisha, Aitor, Agnes, Alba, Alberto, Alejandra, Alessandro, Alex, Alexandre, Alexy, Ali, Alicia, Almudena, Álvaro, Ana, Anass, André, Andrea, Andreas, Andrés, Ángel, Ángeles, Aniria, Anna, Antonin, Antonio, Arancha, Arda, Aris, Armin, Arun, Astrid, Bárbara, Barnabé, Beatriz, Bernardo, Berta, Bettina, Borja, Brian, Bruce, Bruno, Camila, Can, Canto, Carina, Carlos, Carmen, Carolina, Cecilia, Celia, César, Christian, Christine, Christoph, Ciaran, Claire, Clara, Claudia, Clemens, Cléo, Codruta, Conchita, Consuelo, Corina, Corso, Covadonga, Cristiane, Cristina, Daniel, Daniele, Danielle, David, Delphine, Denis, Dennis, Diego, Doddy, Ebru, Edd, Edgard, Edoardo, Eduardo, Efrén,**

Elena, Eleonora, Eliana, Elisa, Elise, Eloy, Elsa, Emilio, Enol, Enrique, Erik, Esteban, Estela, Ester, Esther, Eva, Fariz, Fe, Federico, Felix, Fernanda, Fernando, Florian, Florine, Francesca, Francesco, Francisco, Frank, Franklyn, Fred, Gabriele, Gemma, Germán, Giacomo, Giannhs, Gilles, Guidong, Guillermo, Hanna, Hannah, Hannes, Hans, Héctor, Hendrik, Hesham, Hugo, Ignacio, Illán, Inés, Íñaki, Íñigo, Irene, Isaac, Isabel, Isam, Israel, Itzíar, Iván, Izabela, Jacob, Jaime, Janine, Javier, Jennifer, Jens, Jesús, Joe, Johan, Johannes, John, Jonathan, Jorge, Jörn, José, José Francisco, José Manuel, Josi, Juan, Juanjo, Julianne, Julien, Jurandi, Kartal, Katarzyna, Katerina, Katharina, Katrin, Kolja, Krista, Lara, Laura, Lea, Leo, Léo, Leonie, Leticia, Lily, Livia, Liz, Liza, Lorena, Lorién, Luca, Lucas, Lucía, Lucie, Ludovic, Luis, Luisa, Luz, Magali,Maila, Manuel, Mar, Marco, Marcos, Mareike, María, MªAdela, MªLuisa, Marina, Mario, Marlene, Marta, Mechines, Melissa, Mercedes, Micaela, Michael, Mikko, Miguel, Miguel Ángel, Milagros, Mina, Mónica, Montse, Murat, Nacho, Nadir, Naghmeh, Natalia, Nathan, Nelly, Nelson, Nerea, Néstor, Nicolás, Niels, Nikos, Nils, Nina, Noelia, Nora, Nuria, Oda, Oihane, Oana, Omayra, Óscar, Pablo, Paco, Paloma, Patrice, Patricia, Patrick, Paul, Paula, Pavan, Pedro, Pelayo, Pepi, Pilar, Piotr, Rafael, Raffaello, Rainer, Raquel, Raúl, Rebeca, Rémy, Renaud, Ricardo, Roberto, Rocío, Roman, Rosa, Rubén, Qingqing, Sabine, Salvador, Sandra, Santiago, Sara, Sarah, Saray, Saúl, Scarlett, Sebastian, Sebastián, Selene, Senda, Sergei, Sergio, Severin, Shen, Silvia, Simón, Simona, Sofia, Sonja, Soraya, Steve, Steyn, Susana, Sven, Sylvain, Tamara, Tamer, Tanuj, Tatiana, Teo, Teresa, Tereza, Thaís, Thorsten, Ulf, Valeria, Verena, Verónica, Víctor, Victoria, Viktor, Vincent, Vinit, Vito, Weronika, Wessel, Wim, Yanka, Yasmin, Yolanda, Youjia, Yuqian and **Zi**.

Finally, thanks to you who are reading this lines. If I have forgotten anyone, it was not my intention, so please excuse me.

Andrés Meana Fernández
Gijón, September 2019

1

Introduction

"How do you know I'm mad?" said Alice.
"You must be," said the Cat, "or you wouldn't have come here."

Lewis Caroll, Alice in Wonderland

The last thing one settles in writing a book
is what one should put in first.

Blaise Pascal, 1623-1662

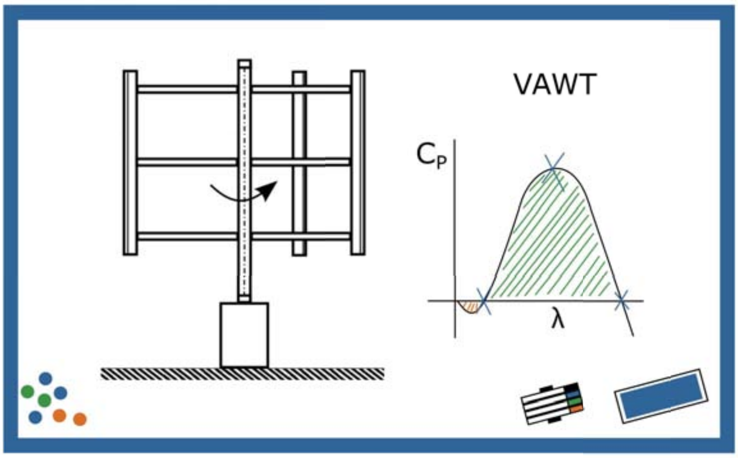

THIS first chapter recalls the importance of wind energy in our world context and outlines the objectives and working methodology of this thesis. The introduction includes a small perspective on the current situation of wind energy and its future prospects. Afterwards, the objectives and scope of the research performed in this thesis and the methodology employed are introduced. Finally, an outline of this document is presented.

1.1. The Energy Challenge

Although wind energy exploitation dates back five thousand years ago, contemporary societies are mainly based on fossil fuels for covering their electrical energy needs [1]. From the first windmill designs of Hero of Alexandria [2], or the Persian windmills in Sistan (with first references appearing in the 9th century A.D. [3]), the first recorded appearance of windmills in northern Europe is found in the 12th century, reaching Spain in the Modern Age. Wind and hydraulic represented a major energy source in Europe until the Industrial Revolution (second half of 18th century), when coal overtook the main role [4]. Then, wind energy suffered a higher recession than hydraulic power, as it could not be transported or stored. Ever since, fossil fuels have risen until becoming the first energy source during the 19th and 20th centuries.

During that period, pumps driven by wind energy were mainly used to transport water. Meanwhile, the first electrical generators were attached to wind turbines to start producing electricity. Additionally, the advances in the aerodynamic design of airplane propellers and wings were also translated into better turbine designs, being wind energy still a minor contributor to the total energy mix.

It was not until the early 1970s that wind energy research came back into scope. On one hand, the oil crisis of 1973 generated unexpected financial support for research and development of wind energy and other alternative energy sources [5]. On the other side, the raising awareness of society on environmental issues and the evidence of the contribution of human activity to global climate changes [6] posed the necessity of shifting towards more sustainable production models (it was in 1975 when Broecker coined the phrase “global warming”). The Declaration of Stockholm (1972), the Montreal and Kyoto Protocols (1987 and 1997), the Paris agreement (2001) and the yearly Climate Change Summits (1995-present) are examples of the gravity and the internationalization of this environmental issue. Figure 1.1 shows the expected global surface temperature rise (relative to the base period of 1986-2005) on the Earth under four different emission scenarios. This is just one of the effects that inadequate actions regarding the environment will have, besides changes in the patterns of precipitation and storms, the melting of ice and thawing of permafrost, the rise of sea levels and the acidification of oceans. Concerning the search for alternative energy sources that are more environmentally friendly, this is one of the major challenges for humanity in the 21st century: the Energy Challenge.

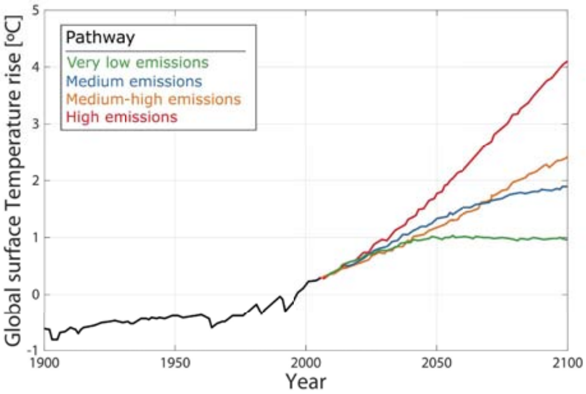

Figure 1.1: Observed and projected changes in global average temperature under four emissions pathways. *Source: Intergovernmental Panel on Climate Change (IPCC), 2013 [7]*

1.2. Alternative energy sources

If no action is taken to reduce greenhouse emissions, the expected scenario is completely worrying. Thus, a change towards environmentally friendly energy sources is required. Luckily, the interest on renewable energy sources has been constantly increasing over the past years. Both companies and institutions all over the world are attracted by ideas such as reducing external energy dependence and opening leadership possibilities in sustainable technologies. The benefits of developing an electrical network based on renewable energy sources are clear: it improves trade balances and leads to the emergence of new industrial and technological sectors (and thus economic growth) [8]. Figure 1.2 shows the available potential of alternative energy sources such as solar energy, wind energy, wave energy, ocean thermal energy conversion, biomass energy, hydropower, geothermal energy and tidal energy. The world power demand is also depicted. It may be appreciated that both solar (23,000 TW) and wind energy (70-120 TW) would be able to cover the world energy demand independently by 2040 (24 TW), so a transition towards a totally renewable energy mix is completely possible.

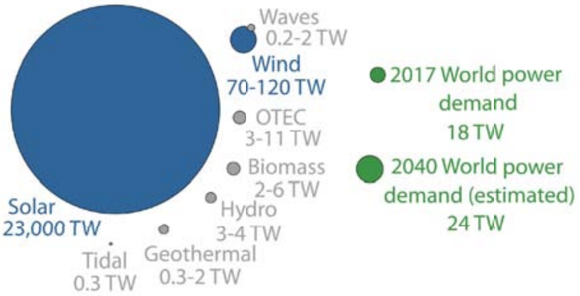

Figure 1.2: Available potential of alternative energy sources and world power demand in TW (adapted from [9])

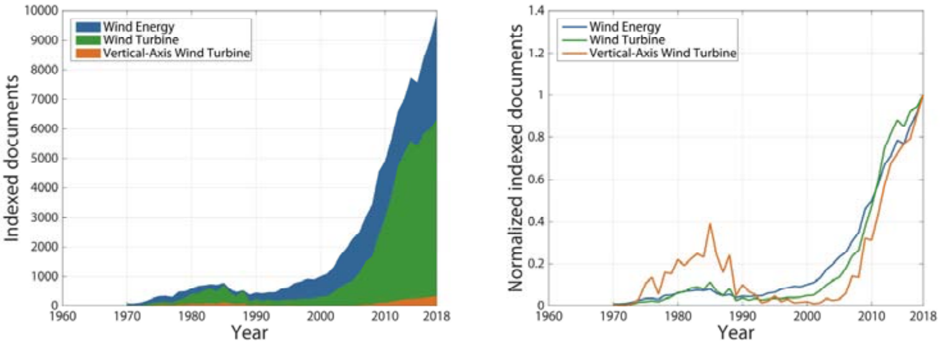

(a) Indexed documents per year

(b) Normalized with respect to the 2018 values

Figure 1.3: Documents indexed in Scopus database, screened from title, abstract and keywords. *Source: Scopus [10]*

1.3. Wind energy: situation and future prospects

After the oil crisis of 1973, the situation led to an increase in the research of alternative energy sources. Figure 1.3a, which shows the indexed documents per year in Scopus in the period 1960-2020, is a proof of the increased interest in wind energy and wind turbines in the period 1970-85. Then, a slight decrease was observed until the mid-1990s. After the first Climate Change Summit (1995), the interest in wind energy has been increasing exponentially, and so have scientific productivity and technological advances. These advances have caused that, nowadays, wind power represents one of the most economical options, employing a totally mature energy harvesting technology. The worldwide installed wind power capacity is constantly increasing, as shown in Figure 1.4. In 2017, this capacity reached almost 0.54 TW. Figure 1.5 collects the annual installed capacity by region. Although the leading role of Europe and North America has been overtaken by Asia in the recent years, some European countries such as Denmark or Spain have managed to cover more than 50% of their electrical energy demand using only wind energy [11]. Spain was actually the first country where wind energy was the first source of electricity for an entire year in 2013, as claimed by the Spanish Wind Energy Association (AEE) Communication Department.

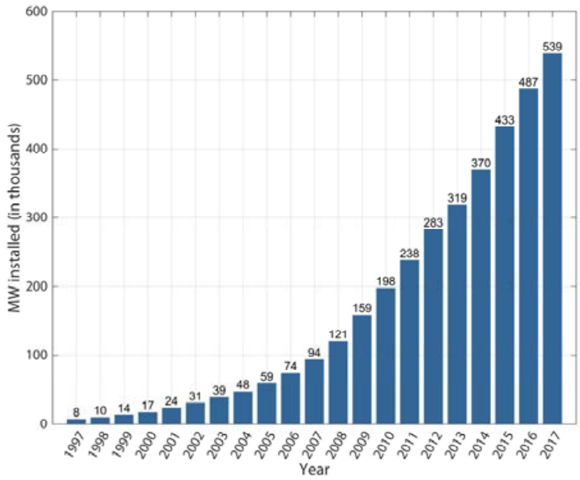

Figure 1.4: Cumulative installed wind power capacity worldwide. *Source: Global Wind Energy Council* [12]

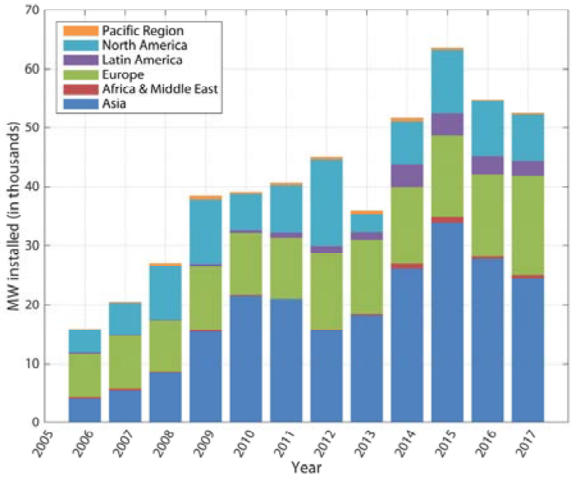

Figure 1.5: Annual installed wind capacity by region. *Source: Global Wind Energy Council* [12]

1.4. Vertical axis wind turbines (VAWTs)

Due to their higher output, horizontal axis wind turbines (HAWTs) have been traditionally the preferred option, detrimental to vertical axis wind turbines (VAWTs). As a consequence, research was mainly focused on these "propeller type" HAWTs. However, VAWTs are becoming relevant, specially in urban areas. They can produce useful energy from lower wind speeds and they do not require constant reorientation with respect to the incident flow. As a result of their lower blade tip speeds, the noise level produced by VAWTs is far below the noise level generated by HAWTs. In addition, VAWT installation and maintenance operations are much simpler because the generator unit is placed at ground level. All these advantages make VAWTs the most suitable option for small scale wind generation in urban places with changeable wind flows and evidence the need of further research to overcome the main drawbacks that prevent their implantation. These disadvantages are basically their difficulty to self-start and the flow complexity through and around the turbine. These two phenomena complicate the prediction of their performance, the main concern of the research community at the present time. Table 1.1 summarizes the main advantages and disadvantages of both VAWT and HAWT technologies.

Table 1.1: Comparison between vertical- and horizontal-axis wind turbines

	Vertical-axis wind turbines (VAWTs)	Horizontal-axis wind turbines (HAWTs)
Power	Lower	Higher
Wind speed	Lower	Higher
Blade tip speed	Lower	Higher
Orientation	Omnidirectional	Monodirectional
Self-starting	Limited	Yes
Montage and maintenance	Easy	Difficult
Noise level	Lower	Higher

1.5. Research gaps

At turbine design stages, there is still a lack of a straightforward procedure, preventing VAWTs from reaching optimal performances. There is still controversy in the optimal design parameters for VAWTs, as well as in the optimal design of airfoils that provide the highest energy capture. A quick tool for the comparison of multiple preliminary designs would be useful at design states.

Additionally, there are several studies based on Computer Fluid Dynamics (CFD) simulations in the literature. Nevertheless, there are still discrepancies in the mesh and temporal requirements for the correct simulation of these machines. Besides, more insight into the flow mechanisms regarding VAWTs would be desirable to identify performance losses and possible improvements. The turbulence model used for the simulation of VAWT and VAWT airfoils is also a topic of interest, as there is still no consensus in the literature.

Finally, among the facts that prevent VAWT proliferation, self-starting is the most determining one. Wind tunnel testing of small-scale prototypes with solidity values close to real applications is seldom found in the literature.

These main research gaps identified are described more extensively and are covered in Chapters 3, 4 and 5.

1.6. Thesis objective

The main objective of this thesis is the development of scientific-technological knowledge applicable to the design of optimized vertical-axis wind turbines. As an ultimate goal, transfer of this knowledge is foreseen to small and medium-sized enterprises (SMEs), which cannot afford complex and high-cost individual studies, but need to offer optimized products adapted to the requirements of every customer.

This main objective may be split into the following three specific objectives:

1. Selection and development of an optimal analysis model for VAWTs, considering the associated costs. A compromise between the precision of the results and the complexity and associated costs is sought, so that the selected model may be applicable for the development of commercial turbines.
2. Elaboration of design guidelines for airfoils aerodynamically optimized for VAWT applications. The developed model will be applied to a series of airfoils, providing insight into the optimal characteristics that an airfoil should possess to be suitable for VAWT applications.
3. Design of an aerodynamically optimized VAWT, using the knowledge generated during the previous research stages.

1.7. Research methodology

In order to fulfill the research objectives, the following research methodology has been applied:

- First of all, a literature survey about the research topic and the numerical and experimental techniques applicable to the research has been conducted.
- Then, the study has been focused on the application of analytical streamtube models based on the actuator disk theory, which have shown a relatively good reliability for the prediction of the global performance of lightly-loaded VAWTs.
- Afterwards, a more complex model based on 2D Computational Fluid Dynamics (CFD) simulations has been developed using Reynolds-Averaged Navier-Stokes (RANS) schemes for the closure of turbulence. The mesh and time step requirements for the simulation of this type of turbines have been determined.
- Subsequently, a 3D CFD model of a typical VAWT airfoil has been developed, comparing different turbulence models for the prediction of its aerodynamic performance.
- Finally, a VAWT prototype has been designed using the generated knowledge and has been tested inside the wind tunnel of the laboratory of the Fluids Mechanic Area. The performance of the turbine prototype and the velocities at the turbine wake have been measured and compared with the predictions from the models.

1.8. Scope and expected results

The Fluid Mechanics Area research group from the University of Oviedo has a wide experience in the design, simulation and experimental testing of turbomachinery. The origin of this research line stems from the Project “Characterization of the aeroacoustic behavior of elliptic airfoils in turbulent flows” (DPI2009-13613 and FC-09-IB09-026). After completing successfully three competitive projects about fluid dynamics and acoustics phenomena in axial turbomachines (“Modeling of the dynamic behavior of subsonic unsteady flow in the interaction between moving and fixed stages of axial turbomachines”, DPI2000-0702-CO2-01; “Modeling of deterministic stresses in axial turbomachines”, DPI2003-09712; and “Characterization of aerodynamic noise generation due to the interaction between rotor and stator vanes in axial fans”, DPI2006-15270), a new research line about elliptic airfoils typically employed in reversible jet axial fans was proposed. Once this project was finished, observing that this type of airfoils is typically used in a type of vertical axis turbines known as Gorlov turbines, it was decided to use the results obtained as a starting point of a new line of research based in wind turbines. With the aim of developing the new research pieces, funding was obtained thanks to the Project "Characterization and prediction of aerodynamic noise generation in wind turbine airfoils" (DPI2011-25419) and a thesis involved in noise prediction of aerodynamic airfoils was read in 2017 [13]. This project ended in 2014, year in which the present thesis was started. In parallel, contacts have been made with companies and other research centers, leading to new funded projects from the University Institute of Industrial Technology of Asturias (IUTA), financed by the city hall of Gijón. Finally, in the last year of the realization of this thesis, a new project from the Spanish Ministry of Economy and Business (Development and Fabrication of Vertical-Axis Wind Turbines for Urban Environments, ENE2017-89965-P) provided the necessary funds to build a turbine prototype and perform wind tunnel measurements in the laboratory of the Fluid Mechanics Area.

This thesis aims to help to consolidate this new research line, focused on wind turbines, and to extend the expertise of the research group in this field. The main result expected from this work is the development of models able to predict the performance of VAWTs and that may be used for the design of optimized turbines.

1.9. Thesis outline

Figure 1.6 outlines the structure of this document, alongside the main points covered in each chapter and the main results obtained. After this introduction, Chapter 2 provides a review of the existing wind power extraction systems, focusing afterwards in VAWTs, their advantages, disadvantages and research interest. Finally, a review of the design and analysis techniques is presented. Chapter 3 focuses on the analytical streamtube model developed in this thesis and the study of the influencing parameters in VAWT performance. Then, Chapter 4 provides the details of the numerical methodology (CFD) employed in this thesis for the analysis of both VAWT and VAWT airfoils, studying both the aerodynamic performance and the developed flow field. Chapter 5 collects all the aspects related to the design, construction and testing of a VAWT experimental demonstrator inside the wind tunnel available in the laboratory of the Fluid Mechanics Area, that led to the development of the in-house fabrication of VAWT blades and an experimental procedure for the estimation of the VAWT power curve. Finally, Chapter 6 assesses the fulfillment of the research objectives, presents the main findings and implications of this work and outlines future research possibilities.

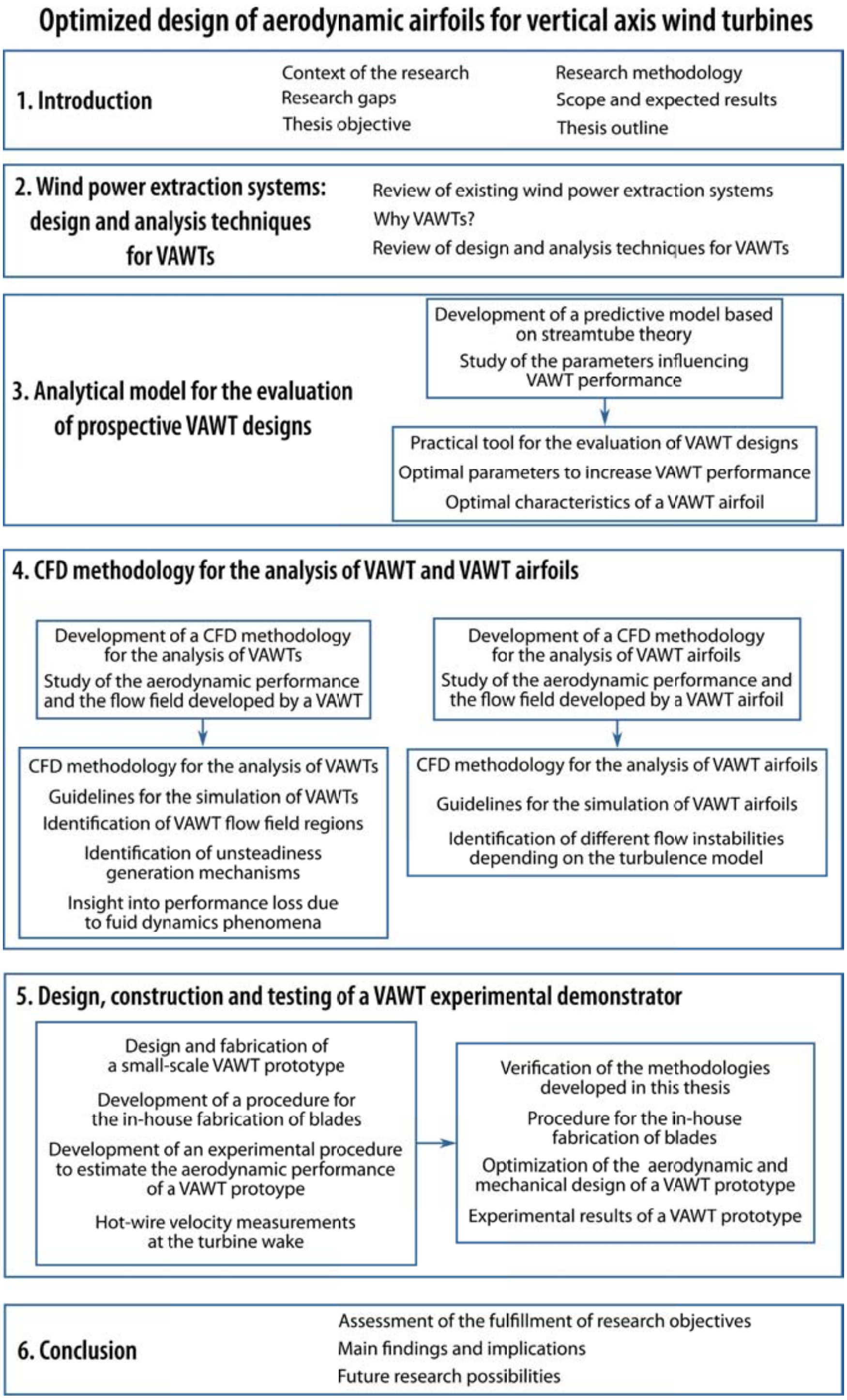

Figure 1.6: Outline of this document

References

[1] J. Kaldellis and D. Zafirakis, *The wind energy (r)evolution: A short review of a long history,* Renewable Energy **36**, 1887 (2011).

[2] B. Woodcroft, *Pneumatics of Hero of Alexandria* (Taylor-Walton and Maberly, London, UK, 1851).

[3] M. Pasqualetti, R. Righter, and P. Gipe, *History of wind energy,* in *Encyclopedia of Energy*, edited by C. Cleveland (Elsevier, Amsterdam, Netherlands, 2004) pp. 419–433.

[4] J. Manwell, J. McGowan, and A. Rogers, *Wind Energy Explained* (John Wiley & Sons Ltd., West Sussex, England, 2002).

[5] T. Ackermann and L. Söder, *An overview of wind energy-status 2002,* Renewable and Sustainable Energy Reviews **6**, 67 (2002).

[6] C. Sagan, O. B. Toon, and J. Pollack, *Anthropogenic albedo changes and the earth's climate,* Science **206**, 1363 (1979).

[7] T. Stocker, D. Qin, G.-K. Plattner, M. Tignor, S. Allen, J. Boschung, A. Nauels, Y. Xia, V. Bex, and P. Midgley, *Climate Change 2013: The Physical Science Basis. Contribution of Working Group I to the Fifth Assessment Report of the Intergovernmental Panel on Climate Change* (Cambridge University Press, Cambridge, United Kingdom and New York, NY, USA, 2013).

[8] A. Lovins, E. Datta, T. Feiler, A. Lehmann, K. Rábago, J. Swisher, and K. Wicker, *Small is Profitable: The Hidden Economic Benefits of Making Electrical Resources the Right Size*, Tech. Rep. (Rocky Mountain Institute, Snowmass, CO, USA, 2002).

[9] R. Perez and M. Perez, *A Fundamental Look at Supply Side Energy Reserves for the Planet*, Tech. Rep. (International Energy Agency, Paris, France, 2015).

[10] *Scopus. Abstract and citation database of peer-reviewed literature,* http://www.scopus.com, accessed: 2019-07-22.

[11] AEE Communication Department, *Spain was in 2013 the first country where wind energy was the first source of electricity for an entire year,* AEE Press Release (2014).

[12] *Global statistics - Global Wind Energy Council,* http://gwec.net/global-figures/graphs/, accessed: 2018-11-02.

[13] I. Solís-Gallego, *Caracterización del comportamiento aeroacústico de perfiles de turbinas eólicas en flujo turbulento (in Spanish)*, Tech. Rep. (Ph.D. Thesis. University of Oviedo, Gijón, Spain, 2017).

2

Wind power extraction systems: design and analysis techniques for VAWTs

We cannot direct the wind,
but we can adjust the sails.

Dolly Parton, 1946-present

Design is not just what it looks like and feels like.
Design is how it works.

Steve Jobs, 1955 - 2011

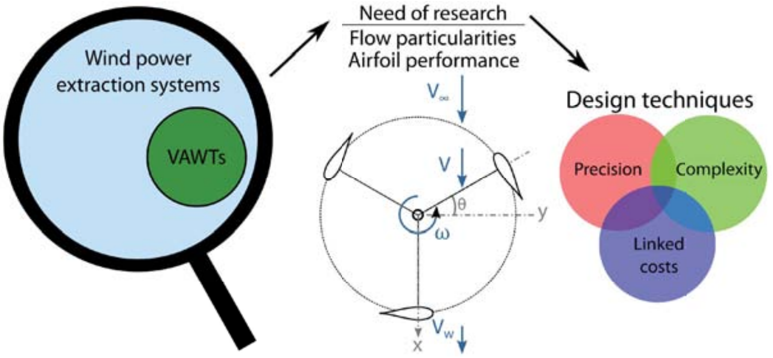

THE purpose of the first section of this chapter is to present the different wind power extraction technologies available nowadays. After discussing horizontal- and vertical-axis wind turbines, turbines based on alternative flow effects are introduced. Then, kite, rail and airborne systems are presented. Finally, other wind power extraction systems (combination of designs or unconventional designs) are commented. Then, focus on vertical-axis wind turbines is placed, highlighting the necessity of research to improve their performance.

The second section of the chapter discusses several VAWT analysis and design methods, with special attention to finding a balance between precision, complexity and their linked costs, as well as their application ranges.

2.1. Wind power extraction systems: focusing on VAWTs

Before proceeding to the review of the available wind power extraction technologies identified in this study, Figure 2.1 has been added for reference. An outlook of the technologies that will be covered in this section is shown.

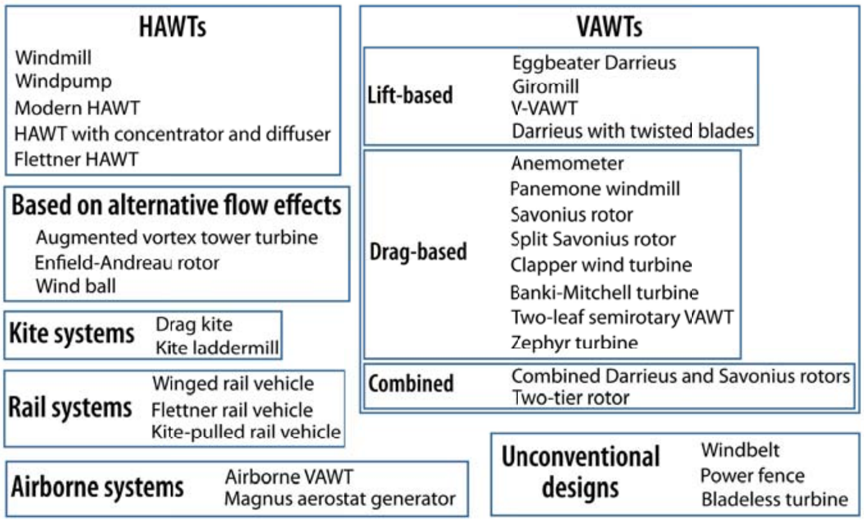

Figure 2.1: Diagram of the reviewed power extraction systems

2.1.1. Horizontal-axis Wind Turbines (HAWTs)

Horizontal-axis wind turbines (HAWTs) are the most popular wind power generation systems. They have, in general, a greater energy production capacity than other systems. Their main drawback is the lack of self-orientation ability, requiring additional mechanisms to place the rotor perpendicularly to the wind direction. The main HAWT types are depicted in Figure 2.2.

The most typical examples of wind energy harvesting are the Dutch windmill and the wind-pump. Both have become part of the typical rural landscapes in Netherlands and the United

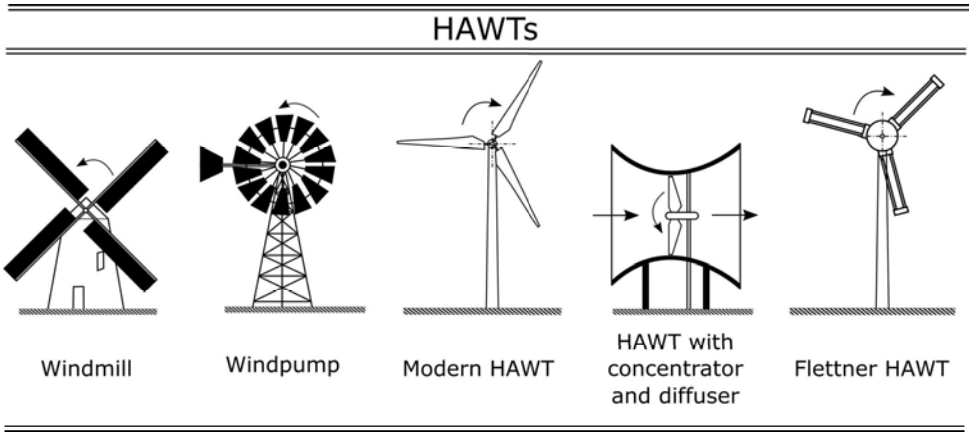

Figure 2.2: Horizontal axis wind turbines

States. Nevertheless, the current paradigm of wind power generation is the modern three-bladed HAWT. This turbine captures energy from wind thanks to the lift generation on its blades. Concentrators and/or difussers may be added to these turbines to improve their performance, as shown in Figure 2.2. Finally, HAWT blades may be replaced by Flettner rotors, working under the Magnus effect. Schefter [1] proposed using this aerodynamic effect as a source of efficient alternative power. However, drag generation on the rotors limits their energy output.

2.1.2. Vertical-axis Wind Turbines (VAWTs)

Although having received much less attention from the research community than HAWTs, VAWTs have increased their popularity with the rise in the demand of renewable energies. The main types of VAWTs, lift-based and drag-based VAWTs, are depicted in Figure 2.3.

Lift-based VAWTs

Lift-based VAWTs are usually the preferred option when dealing with vertical-axis wind turbines, due to their higher power output compared to drag-based VAWTs. Lift enhances torque generation on the rotor, making the blades travel faster than the incoming wind flow. Lift-based VAWTs, however, usually need complementary systems to start rotating and extracting power from the wind.

The original Darrieus turbine, patented by George Jeans Mary Darrieus in 1931 [2], is a lift-driven wind turbine. Although being capable of generating more power than other VAWTs, it generally suffers from self-starting difficulties due to flow complexity and low starting torque. The egg-beater type Darrieus turbine possesses two or more blades arranged as shown in Figure 2.3. Although this type of turbine has a greater power generation capability among other VAWT types, fabrication costs are higher due to geometrical complexity.

Also patented by Darrieus [2], the giromill configuration substitutes the eggbeater blades by straight blades, as depicted in Figure 2.3. Thanks to its simpler geometry, this configuration is more adapted to large-scale fabrication and commercial distribution. The H-rotor name is reserved to the two-bladed giromill configuration. A variation of the giromill is the cycloturbine,

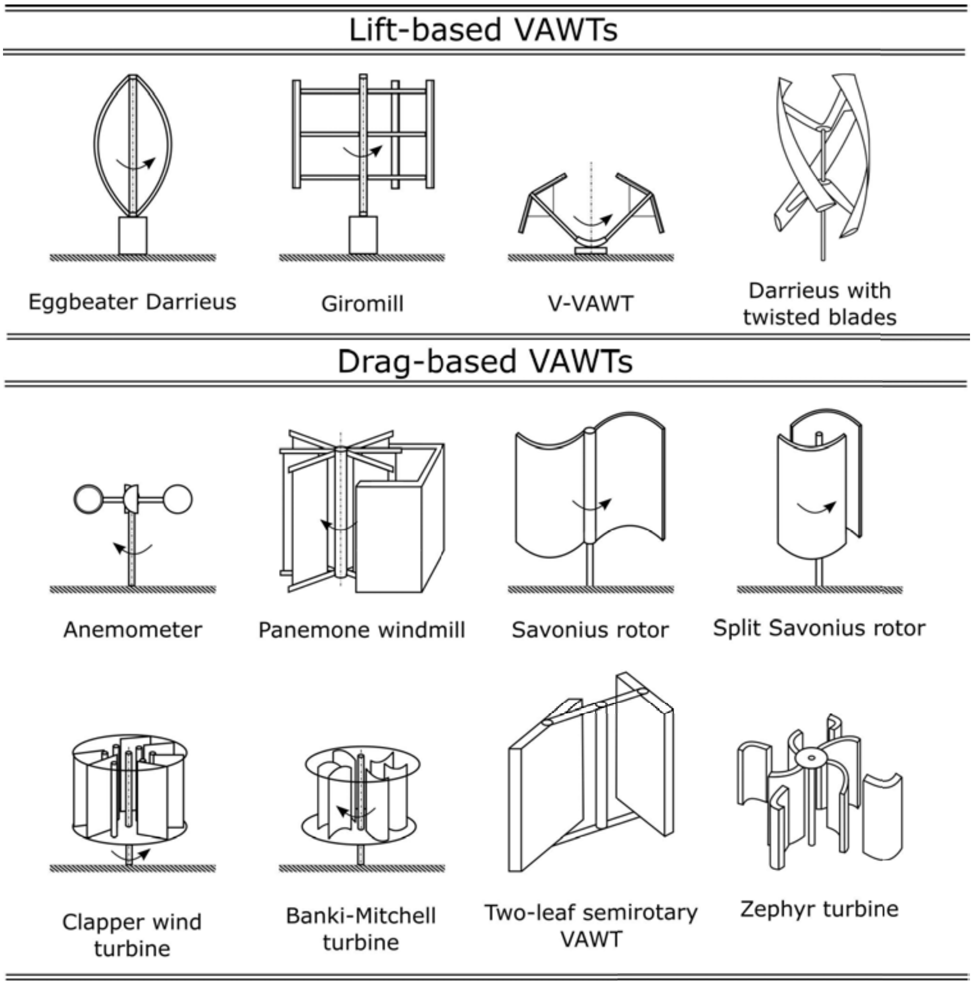

Figure 2.3: Vertical axis wind turbines

in which each blade can rotate around its own vertical axis. Pitching the blades to keep the desired angle of attack mitigates transitory effects in the rotor, so that the power output can be regulated to keep an almost constant value. Self-starting issues are thus completely overcome by this rotor configuration. Nevertheless, pitching mechanisms are usually complex and need additional sensors to correctly move the blades, fact that increases their cost.

Another lift-driven turbine stems from the same concept of blade twisting found in Gorlov hydraulic turbines. The blade twist spreads the torque all over the rotor, helping to flatten oscillations in power output, reduce flow separation and improve self-starting. However, the fabrication process is rather complex in comparison with other types of turbines. Works like the ones from Scheurich et al. [3] or Raciti Castelli et al. [4] have served to obtain insight into the aerodynamics of these turbines.

Finally, V-VAWTs consist of two arms forming a V-shape, in which several blades are positioned along the span and are angled to minimize aerodynamic over-turning moments. A turbine with this configuration (also called Y-shaped) was patented by Wind Power Ltd. [5] in 2007. This VAWT type is suitable for offshore applications, aiming to 10 MW-range power generation [6].

Drag-based VAWTs

The main advantage of drag-based VAWTs is that they can self-start with no complementary mechanisms and, as the rest of VAWTs, they work independently of the wind direction. However, unless some lift is developed on their blades, they will never exceed the incoming flow velocity, so their power output is generally very low compared to other systems.

An anemometer is the most basic example of a wind drag driven device. In fact, the working principle of drag-based wind turbines is very similar: rotating as a result of the drag difference between two halves of the rotor.

The first record of practical windmills has been found in Sistan, Iran. These “panemone” windmills are drag-driven devices, so they do not present self-starting complications. To prevent the blockage of the vanes moving upwind, the panemone is normally shielded as shown in Figure 2.3. However, this shielding may be spared if the vanes are assembled so that they can turn around their own axis to overcome the opposing wind. The turbine enclosure reduces the noise radiated to the surroundings, making this configuration suitable for urban integration. Additionally, the design of the outer enclosure may help to blend the turbine with surrounding architecture, as performed by Chong et al. [7].

The Savonius rotor, patented in 1929 [8], is composed of two hollow half-cylinders fixed to a central axis that rotates due to the incident wind. Despite its lower power output, it is one of the most economical turbines. The Savonius rotor may be split in two overlapped buckets, allegedly increasing the rotor efficiency. A dependence of the optimal overlap ratio on the Reynolds number was found by Morshed et al. [9]. Kamoji et al. [10] found an optimal design with a maximum power coefficient of 0.21, developing a correlation for power and torque coefficients for Reynolds numbers in the range of 80,000-150,000. Increasing the number of blades of the Savonius rotor seems to increase drastically the starting torque, but does not change much the tangential drag coefficient [11]. Another possible modifications to Savonius turbines are the introduction of a diffuser to produce a jet flow through a narrow gap between two tandem blades, increasing drag force and torque [12], spiral twisted blades, which produce better and steadier torque values throughout the rotation [13], or introducing outer-flow controlling devices, such as obstacles shielding the returning blade [14] or curtaining arrangements [15].

The clapper wind turbine, another drag-based VAWT, uses movable blades which collide with different structures when rotating, as shown in Figure 2.3. Collisions orientate the blades, reducing their resistance to the wind and creating a drag difference between the two halves of the rotor.

The Banki-Mitchel or Ossberger turbine, also schematized in Figure 2.3, consists of around 30 blades turning due to the drag force exterted by the wind. Although this turbine is more typically found in water flows, it is also common in ventilation systems and it can obviously be also applied to wind power extraction systems.

A so called two-leaf semi-rotary VAWT, which consists of two blades keeping an angle of 90° between them, as shown in Figure 2.3, was studied by Zhang et al. [16]. The mixture of lift and drag forces on the blades is supposed to enhance a higher energy utilization and the self-starting ability. Following this concept, Bayeul-Lainé et al. [17] have developed a wind turbine which combines the rotation of its main axis and blades.

Finally, the Zephyr VAWT, proposed and analysed by Pope et al. [18], features a rotor enclosed in a series of stator vanes with reversed winglets. The winglets modify the incoming wind flow to enter into the turbine at a particular angle of incidence, reducing turbulence and decreasing aerodynamic loading, thus providing a longer life of the rotor blades. The effect of the rotor blade position on a Zephyr VAWT performance has been studied by Colley et al. [19].

Combination of existing VAWTs

Darrieus and Savonius rotors can be combined on the same hub to overcome the drawbacks they present separately, as shown in Figure 2.4. Experiments were performed on a hybrid H-Savonius rotor by Bhuyan and Biswas [20], obtaining a higher power coefficient than for a simple H-rotor. Besides, the Savonius rotor enables passive self-starting, overcoming the self-start difficulty of the H-rotor. Another way to overcome the self-starting problem of Darrieus turbines is placing two turbines on the same shaft but in different orientations, helping each other out of their shadow zones. Gorelov and Krivospitsky [21] proposed to divide the turbine into two tiers with their blades shifted by 90°, with field tests on a 3 kW prototype showing self-starting at a wind speed of 2 m/s and 39% efficiency.

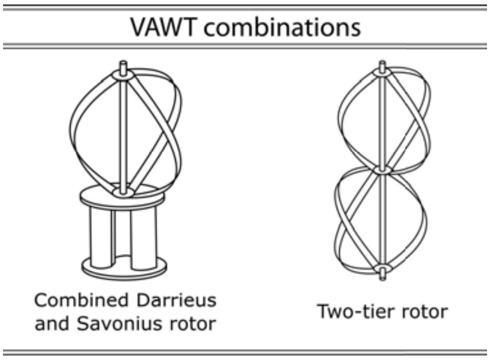

Figure 2.4: Combinations of vertical-axis wind turbines

2.1.3. Alternative power extraction systems

Turbines based on alternative flow effects

Besides lift and drag forces, the generation of vorticity or different pressure zones may be used to move the blades of a turbine and generate energy.

In the augmented vortex turbine, the wind is guided inside an open cylinder with several shutters around it, as shown in Figure 2.5. Inside the cylinder, the guided wind is mixed with the freestream wind from above, creating a strong vortex inside the cylindrical tower. This vortex creates an updraft force which produces the rotation of a turbine placed below the tower.

The Enfield-Andreau wind turbine, also presented in Figure 2.5, consists of hollow blades which expel the air due to centrifugal forces. As a result, a low pressure area is created inside the

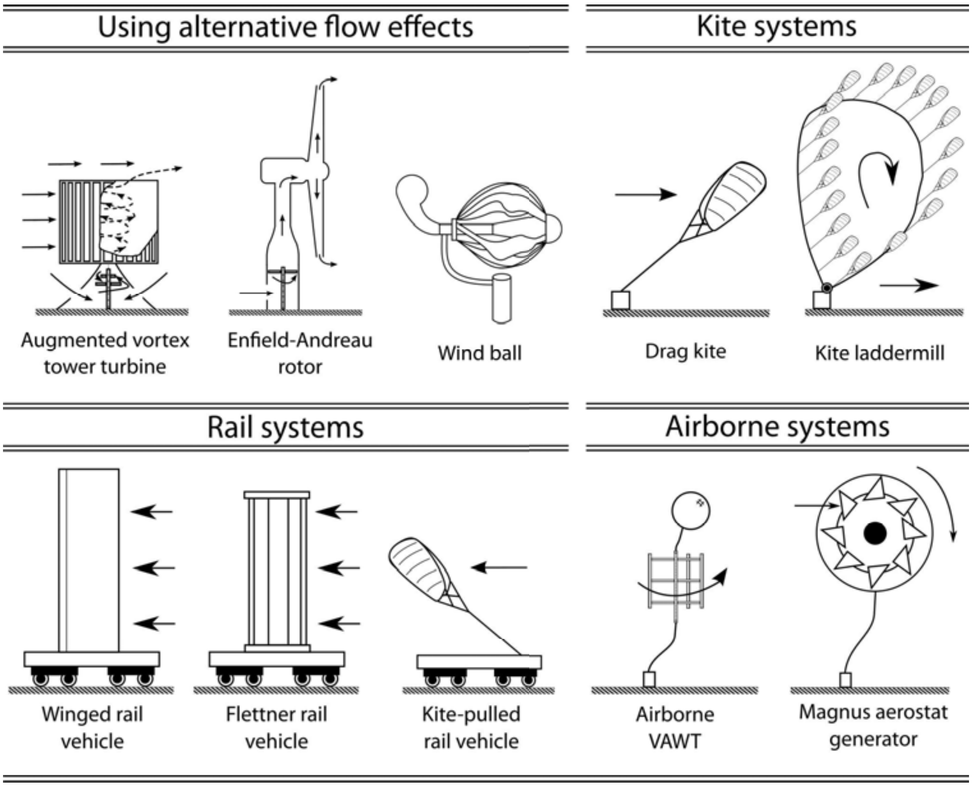

Figure 2.5: Alternative power extraction systems

turbine tower, which generates an airflow that is used to power a turbine placed at the bottom of the tower.

Finally, the windball, a relatively new HAWT design by Paulides et al. [22] based on the Venturi effect, is currently being exploited by Home Energy International B.V. With a 2 m diameter and a permanent magnet brushless generator, this turbine draws air from a bigger area than its projected frontal area with low noise generation.

Kite systems

Kites, as the one depicted in Figure 2.5, can be used to harvest energy from the wind at higher altitudes, where the wind forces are stronger. Jehle and Schmehl [23] have designed a tracking controller for kite power systems and performed field tests, confirming the feasibility of autonomous operation of a traction kite of 25 m^2 in periodic pumping cycles.

A drag kite power generation process comprises two phases. In the power extraction phase, the kite is driven by the wind, generating energy, whereas in the recovery phase energy is consumed to place the kite at its original positon. The net energy outflow is delivered to the electrical network. By steering the kite movement creating eight-like figures (crosswind kite), the effect of lift and drag forces is added up, resulting in higher power generation. Finally, a series of kites can be built up in a looping form as shown in Figure 2.5, creating a so-called kite-laddermill. Thanks to the cyclic movement of the kites, energy may be continuously generated with this arrangement. It must be noted, however, that such a laddermill could be built with airfoil blades as well.

Rail systems

Rail systems consist of rail vehicles which move due to the thrust force generated by different attached devices. The main advantage of these systems is that the vehicles can follow any desired path. The movement may be generated attaching an airfoil blade to the rail vehicle, as depicted in Figure 2.5. Ponta et al. [24] have conceived a configuration for large power generation applications called VGOT (Variable Geometry Oval Trajectory), in which the blades follow an oval trajectory oriented to the most favourable wind direction. Ponta and Lago [25] have developed detailed numerical models for the analysis of this type of turbines. Other possibilities for generating the thrust force are Flettner rotors or kites, as represented in Figure 2.5.

Airborne systems

Wind potential energy increases with altitude. Hence, floating systems represent an interesting alternative to obtain more energy from the wind.

One approach is to design a turbine similar to the ones introduced in this chapter that will be tethered to a balloon, as shown in Figure 2.5. Altaeros Energies, founded in 2010 at the Massachusetts Institute of Technology, has designed a Buoyant Airborne Turbine (BAT) based on this principle [26]. Hwang et al. [27] also proposed an airborne design mounted on a tethered balloon, based on a cycloidal wind turbine with a blade pitching control system.

Another possibility is to integrate the turbine in the balloon, as the Magnus aerostat depicted in Figure 2.5. It represents a helium inflated bladder with a generator on its axle, shaped so that the incident wind makes the balloon rotate, generating electricity.

Although the theoretical available energy is higher, some drawbacks concerning energy transport losses and safety issues have to be considered.

Unconventional designs for wind power extraction

Lastly, three unconventional but innovative designs that do not fit in the other categories are depicted in Figure 2.6.

In 1980, Alvin M. Marks patented a charged aerosol wind generator [28]: the power fence. This device generates electricity from the wind-induced movement of charged aerosol particles between two electrode fences. Wind passes through one fence and drags the charged aerosol particles to the other fence, generating electricity in a similar way to Lord Kelvin's Thunderstorm. With no moving parts, no noise or shadow effects are expected. Nevertheless, the high cost of the components, the constant supply of water required to generate aerosol particles and the fact that the device does not work under rainy conditions has prevented this vaneless ion wind energy generator from actual development until the present days.

The windbelt, invented by Shawn Frayne [29], is a sort of wind harp which uses the string fluttering effect to displace a magnet between one or more coils, inducing a current and generating electrical power. This technology is currently property of Humdinger Wind Energy, LLC and produces enough power to feed small electronic devices. Nowadays, the company claims to have developed 1 m^2 windbelt panels which can deliver up to 7.2 kWh per month, making larger-scale power generation possible.

More recently, in 2014, Vortex Bladeless SL was founded in Spain from the idea of an environmentaly friendly aerogenerator with no blades. They developed a cylinder with an elastic rod that resonates with the incoming wind due to vortex induced vibration. The oscillation of the cylinder generates electricity through an alternator system [30]. This system is omnidirectional, requires no brakes (resonance would disappear at high wind speeds) and it is expected to cause much less impact in wildlife than conventional wind turbines.

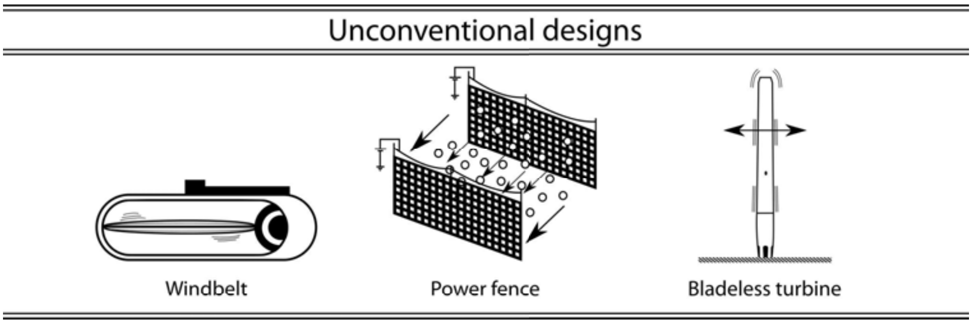

Figure 2.6: Unconventional designs for wind power extraction

2.1.4. A panoramic view: performance of typical rotor types

Figure 2.7 shows the differences between the performance of typical rotor types. The ideal power curve predicted by the actuator disk theory from Glauert [31], as well as the Betz limit that results from the application of this theory, are also shown in Figure 2.7. If a turbine is represented by such an actuator disk, the maximum power that it will be able to capture from the wind is 16/27 of the available power. It may be appreciated how drag-based turbines, such as the windpump or the Savonius rotor, attain lower power coefficients (ratio between the generated power and the power available in the wind), as well as lower tip-speed ratio values (ratio between the blade tip velocity and the incoming wind velocity). Windmills rely on lift effects, thus providing substantially more power than windpumps and rotating at higher speeds. Regarding modern HAWTs, it becomes evident why 3-bladed turbines have become the preferred option in the market, as they are the option with the highest power output. Besides, reducing the number of blades reduces the power output of the turbine, while forcing it to rotate at much higher speeds. Finally, lift-based vertical-axis wind turbines (in blue in Figure 2.7) show a range of tip-speed ratio values considerably lower than modern HAWTs, while maintaining moderate values of the power coefficient. A detailed description of the performance and aerodynamics of these VAWTs is presented in the following section, alongside the reasons that justify their study and application for energy generation purposes.

2.1.5. Why vertical-axis wind turbines?

The development of renewable energy sources is a major concern in many countries. In this context, vertical-axis wind turbines (VAWTs) represent a feasible solution for in situ generation of clean energy in urban areas, being able to produce electricity from lower wind speeds than horizontal-axis wind turbines (HAWTs) [32]. VAWTs are able to produce useful energy from lower wind speeds and they can work independently of the wind direction. As a result of their

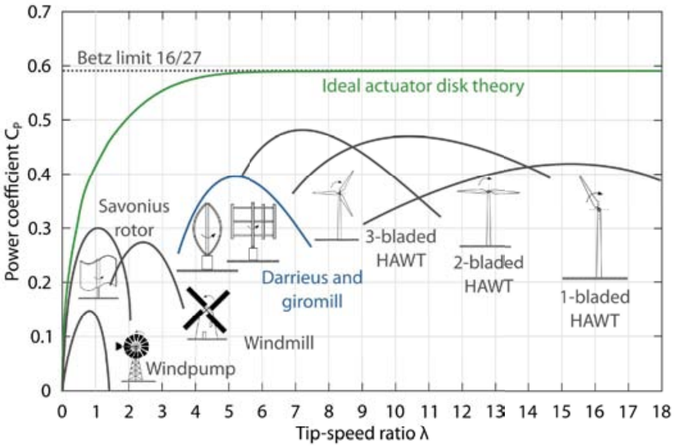

Figure 2.7: Typical performance curves of different wind turbines

lower turbine rotational speeds, their noise levels are lower. In addition, their installation and maintenance operations are much simpler, as the bearings and generator unit may be placed on the ground. Additionally, the blades are much simpler to fabricate because load conditions are practically constant throughout their span. Besides, most of their elements susceptible to inspection and maintenance are at ground level, making these tasks substantially easier.

On the other hand, the main drawback of VAWTs is the complexity of the generated flow. As detailed by Hill et al. [33], this fact is accountable for their difficulty to self-start for low wind velocities, as a result of the continuously changing incidence angle between the wind and the blade. In addition, the integration of wind turbines in urban areas is an ongoing concern that cannot be neglected. Not only structural requirements are to be fulfilled, but also aesthetic factors and noise levels are to be considered.

Airfoil performance

All the advantages of VAWTs show the need of further research to overcome the main obstacles for their implantation, which are basically their difficulty to self-start and the complexity of the flow developed through and around the turbine.

Due to the continuous changing of the relative position of the blades with respect to the incoming wind, the flow behavior is so complex that blades may even work at stall conditions during part of the rotation cycle. Considering this particular characteristic, the importance of employing an optimized airfoil design for the turbine blades is evident.

The magnitude of the lift and drag forces developed on an airfoil depend on the orientation of the airfoil with respect to the incoming wind, as depicted in Figure 2.8a. These two forces are normally expressed in their dimensionless form:

$$C_L = \frac{L}{\frac{1}{2}\rho S V_\infty^2} \qquad C_D = \frac{D}{\frac{1}{2}\rho S V_\infty^2} \tag{2.1}$$

where C_L and C_D are the lift and drag coefficients, L and D are the lift and drag forces, ρ is the air density, S is the cross section of the airfoil and V_∞ is the incoming wind velocity.

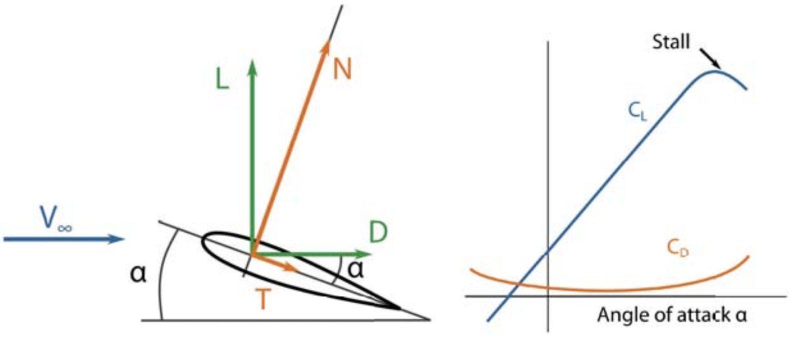

(a) Aerodynamic forces on an airfoil (b) Typical lift and drag curves

Figure 2.8: Discretization and calculation scheme of the analytical models employed in this study

The main factors affecting the value of these coefficients are the geometry of the airfoil, the angle of attack α between the incoming wind direction and the airfoil chord, and the Reynolds number. Figure 2.8b shows the typical evolution of these coefficients with the angle of attack. Lift generally increases with the angle of attack until reaching the stall angle. At this point, there is a sudden drop in lift with a considerable drag increase. For lift-driven VAWTs, the main research focus is the maximization of lift, the reduction of drag and the delay of the stall angle, due to the wide ranges of angles of attack expected.

Particularities of VAWT flow

Flow in VAWTs is particularly complex. Figure 2.9 shows the top view of a straight-bladed rotor. The actual wind velocity that reaches the turbine is V , less than the ambient wind velocity V_∞. Once the wind has passed through the turbine, it has an even lower velocity V_w. Figure 2.9 also shows the velocity triangle and the aerodynamic forces at a particular blade position. The azimuthal blade position is denoted as θ. The rotational velocity of the blade is $R\omega$, being R the turbine radius and ω the rotational speed. The relative velocity of the blade W is obtained from the velocity triangle formed by its rotational ($R\omega$) and absolute velocity (V). The angle of attack α is the angle between the blade chord and the relative velocity, as depicted in Figure 2.9. Finally, regarding the aerodynamic forces, when the wind impinges on a blade airfoil, the force may be decomposed in two components: one in the direction of the wind, drag - D, and other perpendicular to it, lift - L. These forces are combined into two forces normal and tangential to the airfoil N and T, being the tangential force the one that generates torque and power on the turbine shaft.

Before a VAWT starts rotating, the blades are positioned at a full range of angles of attack from -180 to 180°. From Figure 2.9, it is clear that the flow and forces impinging on a blade are constantly changing during the rotor operation. Besides, the blades in the upwind part, as well as the turbine tower, shed vortices that impinge on the downwind blades, affecting their performance.

From dimensional analysis, it is possible to define three quantities that determine the performance of a VAWT: solidity, $\sigma = Nc/R$, being N the number of blades and c the airfoil chord; tip-speed ratio $\lambda = R\omega/V_\infty$ and turbine Reynolds number $Re_t = \rho R\omega c/\mu$. The

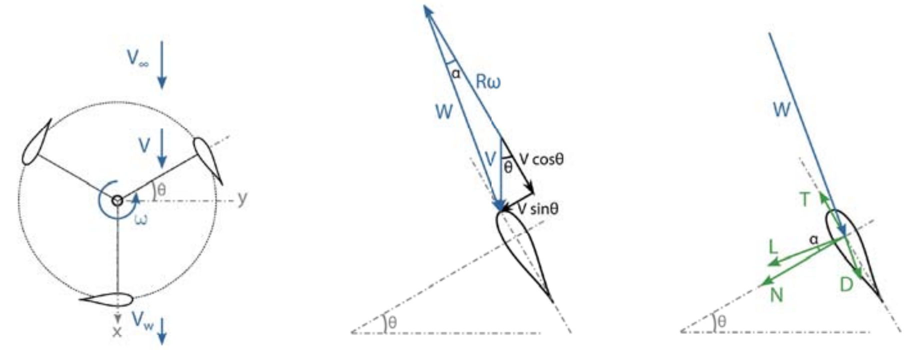

Top view of a straight-bladed VAWT Velocity triangle on a blade Aerodynamic forces on a blade

Figure 2.9: Aerodynamics of a VAWT rotor

power coefficient of the turbine, which is the dimensionless expression of the aerodynamic power,may be expressed as:

$$C_P = f\left(Re_t, \lambda, \sigma, \text{airfoil}\right) \tag{2.2}$$

Therefore, besides the airfoil geometry, the performance of a VAWT depends mainly on the turbine Reynolds number, its tip-speed ratio and its solidity. Typically, the performance curve of a VAWT is given in dimensionless form, with the power coefficient as a function of the tip-speed ratio, as shown in Figure 2.10. When a turbine starts working from rest $(\lambda = 0)$, it moves only due to drag effects. After a while, the turbine accelerates until its tangential velocity reaches the freestream wind velocity $(\lambda = 1)$. If the turbine is successful to exceed freestream velocity, it means that significant lift is being produced on the turbine blades and it may be considered that the starting process of the turbine has finished $(\lambda > 1)$ [33]. Worasinchai [34] divides the self-starting of Darrieus turbines in three periods: in the first one, the rotor is alternatively driven by lift and drag. In the second phase, it is only driven by lift, but in some positions the blades are still ineffective in generating thrust force. In the third period, the rotor accelerates to a steady operating tip speed ratio.

Sadly, for most VAWTs there is a region of negative power coefficients at low tip-speed ratios that prevents the rotor from self-starting. The elimination of this dead band is probably the main challenge for the definitive establishment of VAWT technology.

Regarding the evolution of the performance of a VAWT with the tip-speed ratio, at low λ values, an intense dynamic stall phenomenon appears on the blades, leading to hysteresis loops in lift and drag forces and high amounts of vortex shedding. On the other hand, at high λ, the fast movement of the blades generates too attached boundary layers, responsible for added mass and viscosity effects. As stated by Amet et al. [35], there is an intermediate range of λ values, where none of these effects dominate and the turbine reaches its maximum efficiency.

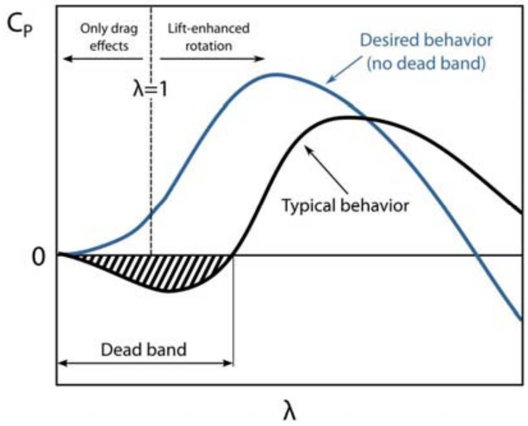

Figure 2.10: Typical power curves with dead band zones

2.2. Design and analysis techniques for VAWTs

In the second section of this chapter, VAWT analysis and design methods are discussed, with special attention to finding a balance between precision, complexity and their linked costs, as well as their application ranges. Three main families of methodologies may be found: analytical and numerical models based on fluid equations developed from the simplification of physical phenomena; Computational Fluid Dynamics (CFD) models, based on the discretized iterative resolution of the Navier-Stokes equations; and experimental tests consisting in the fabrication and testing of turbine prototypes or demonstrators. The following subsections describe the methods found in the literature that may be applied for the study of VAWTs. Figure 2.11 has been added for reference, showing an outlook of all the methods (methods used in this thesis are highlighted in bold)

2.2.1. Dimensional analysis

Every correct physical relationship must allow its statement in dimensionless form [36]. In this sense, dimensional analysis is a powerful analysis tool, widely used for the development of scaling laws, the simplification of problems and the interpretation of experimental data. Regarding wind turbines, dimensional analysis serves to identify the main factors that affect the flow around the turbine and its performance, allowing to reduce the parameters involved at preliminary design stages. The dimensionless groups obtained from this methods may help to develop small-scale models before launching full-sized prototypes and mass production.

Eight variables relevant to the performance of a wind turbine may be identified. Four dependent on the turbine geometry: the rotor radius R, the number of blades N, the chord length c and the rotor swept area A; and four dependent on the flow features: the free-stream wind velocity V_∞ (including turbulence effects), the turbine rotational speed ω, the fluid density ρ and the fluid viscosity μ. Thus, the aerodynamic power of the turbine P, considering the influence of the airfoil employed to build the blades (geometry and surface roughness), may be expressed as:

$$P = f\left(V_\infty, \omega, \rho, \mu, R, N, c, A, \text{airfoil and blade geometry and placement}\right) \tag{2.3}$$

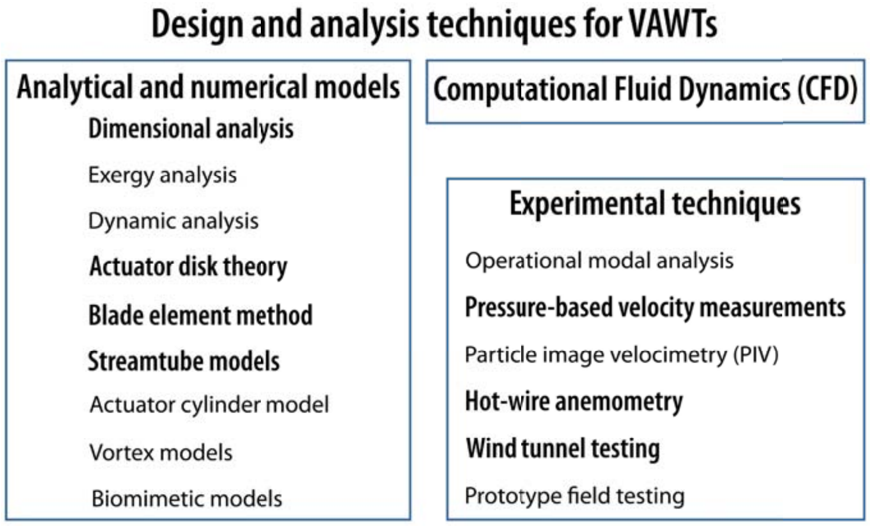

Figure 2.11: Methods for the design and analysis of VAWTs (methods in bold have been used in this work)

Applying the Buckingham Π theorem, the following dimensionless groups may be identified:

$$\Pi_1 = N \qquad \text{Number of blades} \tag{2.4a}$$

$$\Pi_2 = \sigma = \frac{Nc}{R} \qquad \text{Rotor solidity} \tag{2.4b}$$

$$\Pi_3 = Re_t = \frac{\rho R \omega c}{\mu} \qquad \text{Turbine Reynolds number} \tag{2.4c}$$

$$\Pi_4 = \lambda = \frac{R\omega}{V_\infty} \qquad \text{Tip-speed ratio} \tag{2.4d}$$

$$\Pi_5 = C_P = \frac{P}{\frac{1}{2}\rho V_\infty^3 A} \qquad \text{Power coefficient} \tag{2.4e}$$

Recombining these dimensionless groups, a new relationship may be found:

$$C_P = f\left(N, Re_t, \lambda, \sigma, \text{airfoil and blade geometry and placement}\right) \tag{2.5}$$

The same procedure may be followed to both the thrust exerted by the wind on the turbine T and the turbine torque Q:

$$\Pi_6 = C_T = \frac{T}{\frac{1}{2}\rho V_\infty^2 A} \qquad \text{Thrust coefficient} \tag{2.6a}$$

$$\Pi_7 = C_Q = \frac{Q}{\frac{1}{2}\rho V_\infty^2 A R} \qquad \text{Torque coefficient} \tag{2.6b}$$

And so:

$$C_T, C_Q = f\left(Re_t, \lambda, \sigma, \text{airfoil geometry}\right) \tag{2.7}$$

As long as the values of these dimensionless groups for two geometrically similar turbines are maintained, it is possible to correlate their performance. Relationships 2.5 and 2.7 have a great importance, as they ensure that, for a given turbine (σ constant), only the tip-speed ratio λ and the Reynolds number Re_t must be varied in order to characterize the whole performance range of the turbine. This requirement is fulfilled by cross-testing different freestream velocities V_∞ and turbine rotational speeds ω.

The main drawback of dimensional analysis is the inability to predict the behavior of a system per se. Only after obtaining results for a particular turbine, it is possible to extrapolate its behavior to another one working at the same dimensionless numbers. Nevertheless, despite the apparent simplicity of dimensional analysis, powerful correlations for the performance of a turbine may be developed from its application, as performed by Pope at al. [18], [37] and Colley [38] for a Zephyr turbine. This kind of relationships, when adjusted with experimental values, may be extremely useful for turbine manufacturers. Additionally, when preparing experimental tests, this kind of analysis may help to identify the important variables and the relationships between them and thus cover totally and only the necessary range of values of variables for a particular test.

2.2.2. Exergy analysis

Exergy is the fraction of energy in a system that is available to be used. This fraction depends on the system but also on its environment, accounting for the irreversibility of the energetic process. It is always destroyed whenever a temperature change occurs, as a result of the entropy increase of the system and its surroundings. Exergy analysis may be applied to wind turbines by studying the exergy destruction as a result of the conversion of wind energy to electrical power. The exergy efficiency is defined as the relationship between the useful electrical power output P_e and the flow exergy variation across the turbine $\Delta \dot{E}_x$:

$$\varepsilon = \frac{P_e}{\Delta \dot{E}_x} \tag{2.8}$$

The flow exergy variation may be calculated as follows:

$$\Delta \dot{E}_x = \dot{m}(\psi_{in} - \psi_{out}) \tag{2.9}$$

where $\dot{m}$ is the air mass flow and ψ_{in} and ψ_{out} are the wind flow specific exergies [J/kg] before and after passing through the turbine swept area.

Exergy analysis helps to obtain better insight into the origin of the losses produced in wind turbines. Factors to be improved may be identified, leading to the optimization of designs. Pope et al. [39] found that there was a difference of around 50% between the energy and exergy efficiencies of VAWT systems. Roughly, the exergy variation within the flow crossing the VAWT should be equal to the wind power multiplied by Betz's limit. Hence, exergy and energy efficiencies of a well-designed VAWT should differ each other by the value of the Betz's limit (16/27), so there is still room for improvement. Kocer et al. [40] and Ozgener and Ozgener [41] applied this method in their studies as well, proving its meaningfulness to determine better design parameters.

Exergy analysis is useful for optimizing applications with physical restrictions, as the higher the energy efficiency the better the design (and thus the return on investment). However, it has no predictive character in essence, being employed as a post-assessment technique after data from a particular turbine are collected. Nonetheless, there is space for theoretical calculations to analyze the influence of thermodynamic parameters in the exergy efficiency of a VAWT.

2.2.3. Dynamic analysis

The movement of a system may be described as a result of the loads exerted on it, by relating forces and torque to the change in linear and angular momenta. Dynamic analysis focuses on the study of forces and torques and their effect in motion. Regarding VAWTs, simplified models may be developed by studying the dynamics of the tower links and the turbine blades as connected components. Assembling the different equations for every component, the general behavior of the turbine may be computed. By defining a static reference frame XYZ and a reference frame X'Y'Z' rotating with the turbine, the aerodynamic loads acting on a turbine may be related to its movement via the angular momentum conservation equation:

$$\left\{\frac{dH}{dt}\right\}_{XYZ} = \left\{\frac{dH}{dt}\right\}_{X'Y'Z'} + \omega \times H \tag{2.10}$$

where H is the angular momentum and ω the angular velocity of the turbine. Particularizing this equation for every component, the loads and performance of the whole turbine may be calculated. By updating the equations in a time-step basis, it is possible to model the starting process of a turbine from rest. It is also possible to add gyroscopic effects to the models, as well as structural damping and the resonance frequencies of the turbine system. On the other hand, gravity effects are neglected.

Lobitz [42] included a discussion about a lumped spring-mass model that determines the dynamic response of a VAWT rotor, whereas Biswas et al. [43] proposed a new windload estimation technique that showed good agreement with experimental results. Nevertheless, dynamic analysis has a relatively low accuracy compared to more modern prediction methods that do not require substantially more time to obtain results.

2.2.4. Actuator disk theory

The Rankine-Froude disk theory is a mathematical model of an ideal propeller or rotor, based in the momentum equation. The rotor is modeled as an infinitely thin disc and the power, thrust and local wind field are calculated under the following assumptions [44]:

- Homogeneous, incompressible and steady state fluid flow
- No frictional drag
- Infinite number of blades
- uniform thrust over the rotor area
- non-rotating wake
- static pressure far upstream and downstream of the rotor is equal to the undisturbed ambient static pressure.

The actuator disk theory, refined by Glauert [45], applies the momentum equation in a control volume generated by a streamtube enclosing the wind turbine as shown in Figure 2.12. The turbine is represented as a uniform "actuator disk" that causes a pressure discontinuity in the wind flow, slowing it down. The wind velocity is assumed to remain constant through the disk, with its value V depending on the wind thrust. This value is the arithmetic mean of the undisturbed flow velocity V_∞ and the wake velocity V_W

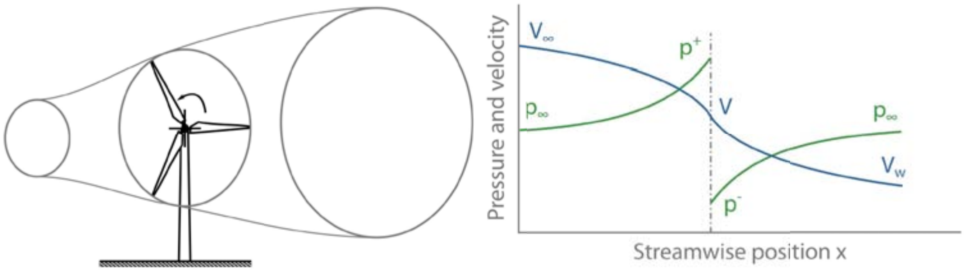

Figure 2.12: Evolution of wind pressure and velocity through a streamtube

An induction factor a is defined as the fractional decrease in wind velocity between V_∞ and V, so that $V = V_\infty(1-a)$ and $V_W = V_\infty(1-2a)$. It must be noted that if $a > 1/2$ the simple theory is no longer valid, as it would mean that $V_W < 0$. The axial thrust on the disc may be calculated as:

$$T = \rho AV(V_\infty - V_W) = \rho A(1-a)V_\infty(V_\infty - V_W) \tag{2.11}$$

being ρ the air density and A the rotor swept area. The power equals the thrust times the velocity at the disk:

$$P = TV = \rho AV^2(V_\infty - V_W) = 2\rho Aa(1-a)^2V_\infty^3 \tag{2.12}$$

Equations 2.11 and 2.12 may be made dimensionless as shown in Equations 2.6a and 2.4e. Maximizing these equations, the maximum poewr coefficient $C_P = 16/27 \approx 0.5926$, the Betz limit, is obtained at $a = 1/3$. This value sets the maximum theoretical rotor power coefficient, corresponding with a thrust coefficient $C_T = 8/9$. Maximum thrust coefficient $C_T = 1$ happens at $a = 1/2$, when $V_W = 0$. This analysis method is really powerful yet simple; nevertheless, breakdown happens at high induction factors. In addition, the induction factor a is normally not known for a particular turbine, so it must be either supposed or obtained by other technique.

2.2.5. Blade element method

The blade element method (BEM) divides the rotor blades in multiple elements and then computes the loads and forces on each element. The whole performance of the rotor is then obtained by an integration over all the elements [44].

In the particular case of wind turbines, the lift and drag coefficients C_L and C_D are calculated for each element depending on the Reynolds number and angle of attack α for all rotor blade positions θ_i. Afterwards, Lift and drag are projected into the directions normal (C_N) and tangential (C_T) to the blade:

$$C_N = C_L\, cos\, \alpha + C_D\, sin\, \alpha \tag{2.13}$$

$$C_T = C_L\, sin\, \alpha - C_D\, cos\, \alpha \tag{2.14}$$

Figure 2.13 depicts the application of the blade element method to a straight-bladed VAWT and the decomposition of the aerodynamic forces in the required directions. Once the forces normal and tangential to the blade are known, it is possible to integrate elemental thrust, torque and power over the blades. Finally, an averaging over every azimuthal blade position yields the total thrust, torque and power of the complete turbine.

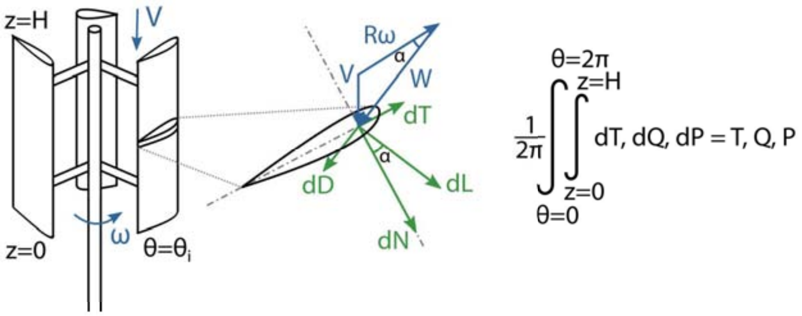

Figure 2.13: Application of the blade element method to a straight-bladed VAWT

This method allows setting specific conditions for every blade element; nevertheless, the same uncertainty in the velocity profiles (induced velocities) commented in the case of the actuator disk theory is still present.

2.2.6. Streamtube models

Both actuator disk and blade element methods make assumptions about the actual wind velocity that reaches the turbine. On their own, they are unable to calculate the value of this velocity. However, it is possible to start with the assumption that the wind velocity arriving to the turbine is the same as the freestream velocity and then iterate between both methods until the actual value is reached. The models that arise from the combination of these methods, extensively described by Paraschivoiu [46], are commonly known as streamtube models. Details about the application of these models, a rapid tool for predicting the performance of wind turbines with reasonable accuracy, will be covered in Chapter 3.

Brahimi et al. [47] developed a streamtube model capable of predicting the aerodynamic loads exerted on the turbine blades by the wind. Bedon et al. [48] applied another streamtube model to optimize a vertical-axis wind turbine, obtaining a substantial improvement on its performance. Brusca et al. [49] studied the effect of the aspect ratio of a turbine on its performance, concluding that as the aspect ratio falls, the Reynolds number rises leading to a higher performance. Merz [50] designed a method including “ghost” blades to provide a continuous record of forces at each position around the rotor, obtaining the load and response spectra of the turbine.

One of the drawbacks of streamtube models is that they are only useful for turbines with relatively low solidity and moderate tip-speed ratio values, as the high induction values present in turbines with high solidity or tip-speed ratio values cause breakdown of the momentum equation from the actuator disk theory. In addition, the simplifications assumed by the actuator disk theory and the blade element method lead to a slight overprediction of the turbine performance. Nevertheless, this small inaccuracy may be resolved using experimental corrections. For instance, if the induction factor becomes too high, there are a series of corrections for the thrust coefficient in the literature. Buhl [51], after revising the results from Glauert [52], Eggleston and Stoddard [53], Spera [54], Burton et al. [55] and Manwell et al. [56], proposed a new empirical correction for the turbine thrust coefficient, later used by Masters et al. [57]. These corrections for high induction values have notably increased the applicability range of streamtube models.

A comparison between analytical streamtube models and CFD models has been performed by Meana-Fernández et al. [58]. Although the implementation of the code for these models took some time, their rapidity in obtaining accurate enough results was found really useful at turbine design stages. So, as far as the solidity values of the prospective turbine allow it, these models represent a great option for the comparison of different airfoils and geometries. As a matter of fact, typical solidity values for modern 3-bladed HAWT ($\sigma = Nc/2\pi R$) are between 0.15 and 0.25, whereas for VAWTs ($\sigma = Nc/R$) this range is between 0.1 and 1.

2.2.7. Actuator cylinder model

In 1982, H.A. Madsen developed a model for predicting the aerodynamic performance of a vertical-axis wind turbine based on an actuator cylinder surface [59] instead of an actuator disk. This model links the blade forces on a vertical-axis wind turbine to a geometry that represents the actual path followed by the blade. The blade aerodynamic forces are then decomposed into the components normal and tangential to the cylinder surface, as shown in Figure 2.14. Finally, the pressure jump caused by the blade forces in the actuator cylinder is used to predict the aerodynamic flow field, including the velocities in the turbine wake.

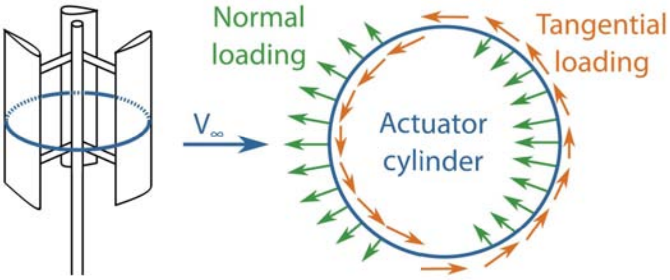

Figure 2.14: Application of the actuator cylinder model to a straight-bladed VAWT

Applying this model, Madsen et al. [60] found strong indications that the maximum power coefficient of a vertical-axis wind turbine could exceed the Betz limit, but there is still need of more insight regarding this issue.

The computational requirements of the actuator cylinder model are not much higher than for typical streamtube models; however, the numerical implementation is much more difficult. Ferreira et al. [61] compared six different prediction models for VAWTs (including streamtube models and the actuator cylinder model). In their study, it was found that although streamtube models can predict turbine power and thrust for certain turbine configurations, models where the wake is explicitly modeled represent an additional advantage over them.

2.2.8. Vortex models

Vortex models are based on the vorticity equations. Pressure does not appear explicitly and the pressure field values are not required to calculate the velocity field [46]. In these models, the blades are modeled as regions of concentrated vorticity. There are two main families of vortex models: free-wake and fixed-wake vortex models.

The free-wake model developed by Strickland et al. [62] replaces each airfoil blade element by a bound vortex filament or lifting line, as shown in Figure 2.15. Following Helmholtz's theorems for vorticity and Kelvin's circulation theory [36], the strength of the bound vortex equals the strength of the trailing tip vortices. In addition, the shed spanwise vortex strength is equal to the change in the bound vortex strength. Thus, the velocity induced by all vortex filaments may be calculated and added to the freestream velocity, obtaining the fluid velocity field. This induced velocity is calculated from the Biot-Savart law:

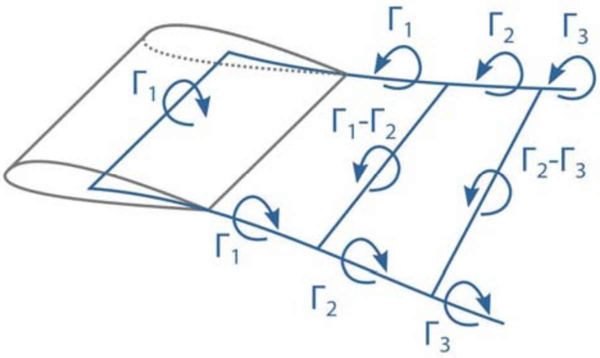

Figure 2.15: Free-wake model: system of vortices for a blade element

$$\vec{u}(\vec{x},t) = \frac{\Gamma}{4\pi}\int_{vortex} \vec{e_\omega} \times \frac{(\vec{x}-\vec{x'})}{\left|\vec{x}-\vec{x'}\right|^3} dl \tag{2.15}$$

where Γ and $\vec{e_\omega}$ are the vortex strength and direction of the vortex element placed at $\vec{x'}$.

Once the velocities are known, they are used to calculate the airfoil lift and drag for the blade element. Then, the bound vortex strength is obtained from the lift coefficient using the Kutta-Joukowski law:

$$\Gamma = \frac{1}{2} W c C_L \tag{2.16}$$

where W is the air relative velocity, c is the airfoil chord and C_L is the lift coefficient. This process is repeated iteratively until convergence is reached.

The original model from Strickland was later modified by Oler and Brownlee [63] to reduce calculation time. Subsequently, novel models appeared such as the ones from Basuno et al. [64] or Dumitrescu and Cardoş [65]. Shi et al. [66] recently predicted the aerodynamic loads and the power output of a 12 kW VAWT, comparing the results with wind tunnel tests on model rotors as well as full scale field measurements and finding a good correspondence between them.

On the other hand, fixed-wake models combine vortex theory and momentum equations. The first model was developed by Wilson and Walker [67]. In this model, the airfoil is supposed to follow a trajectory as depicted in Figure 2.16, moving parallel to the freestream and then suddenly changing direction and moving perpendicularly to the incoming wind. Every time the airfoil changes its direction, lift and circulation are generated. Vortex sheets are thus generated and convected downstream at a constant velocity V_C, leading to the following bounded circulations at the upstream (u) and downstream (d) parts of the cycle:

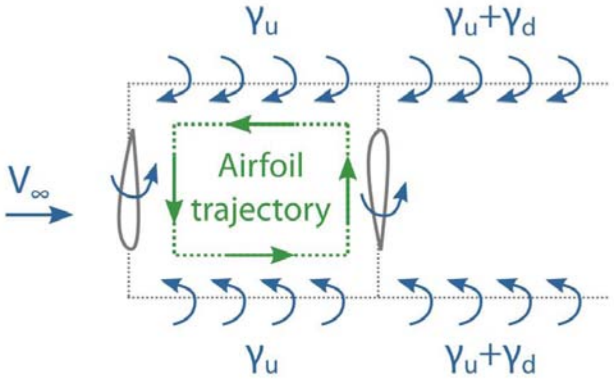

Figure 2.16: Fixed-wake model: system of vortices for a blade element

$$\Gamma_u = V_C \gamma_u / f \tag{2.17a}$$
$$\Gamma_d = - V_C \gamma_d / f \tag{2.17b}$$

where γ_u and γ_d are the vortex sheet strengths and f is the frequency of the airfoil cycles. Combining this equations with momentum theory, the velocity jumps in the upstream (u), downstream (d) and far-wake (w) regions may be calculated as:

$$V_\infty - V_u = \gamma_u / 2 = a_u V_\infty \tag{2.18a}$$
$$V_\infty - V_d = \gamma_u / 2 + (\gamma_u + \gamma_d)/2 = a_d V_\infty \tag{2.18b}$$
$$V_\infty - V_w = \gamma_u + \gamma_d = 2 a V_\infty \tag{2.18c}$$

where a_u, a_d and a are the interference factors for each region. The interference factor a may be obtained from momentum theory, and the other two obtained from their relationship with this one.

Finally, Hirsch and Mandal [68] proposed a model commonly known as "cascade model". Following the typical model used for turbomachinery applications, the blades of a VAWT may be positioned in a cascade arrangement. Then, the combination of vorticity equations and the difference in momentum between the inlet and outlet of the cascade allows to analyze the rotor performance (similarly to the fixed-wake model). This model has shown a better convergence behavior than streamtube models, even for high solidity turbines.

The main strength of vortex models is the possibility of accounting for unsteady flows, velocities that are transversal to the streamwise position and vortex generation in the wake of the turbine. Thanks to considering these effects, they are useful for turbine solidity values or operating conditions for which simpler models would collapse. Additionally, reasonable agreement has been found with experimental data, already with the first versions of free- and fixed-wake models [62], [67]. Nevertheless, these models require substantially more computational time than the previously presented ones. Additionally, experimental corrections may be necessary as well.

2.2.9. Biomimetic models

Biomimicry is the science that studies models, systems and elements of the nature and then applies them for solving human problems. Leonardo da Vinci (1452-1519) is famous for his drawings of the anatomy and flight of birds [69]. He designed several flying machine concepts, although none of them were able to fly. It was not until 1903 that the Wright Brothers flew the first aircraft, inspired by observations of pigeons in flight [70].

Some researchers have tried to find examples in nature with similarities to VAWTs. An analogy between the movement of a flapping wing and the pulsed flow present in VAWTs was presented by Gorelov [71]. The experimental tests in this study were performed with an ideal rotor, with no support brackets between the blades and the shaft. Gorelov claimed to have obtained a power coefficient of 0.72, much higher than the Betz limit. However, the tests were conducted under unsteady conditions, whereas the Betz limit is derived from the actuator disk theory under the assumption of steady motion.

A review on the development of propulsive systems and objects with flapping wings was performed by Rozhdestvensky and Ryzhov [72]. Analytical models describing the pitching motion of airfoils, as well as numerical simulations, may be found in the literature. Additionally, some VAWTs have benefited from flapping mechanisms for the active control of the flow. Bouzaher and Hadid [73] placed two small flapping wings after the trailing edge of the turbine blades, resulting in an important mitigation of the generated wakes and the reducing the disturbances in the downwind part of the turbine. A flapping wing turbine driven at low wind speed and with low noise levels was developed by Alam and Hirahara [74], suitable for applications near residential areas. Finally, Liu and Xiao [75] have simulated flexible blades for a straight bladed VAWT, finding an increase in the performance with slightly flexible blades, but also high blade stresses and an abrupt decrease in the performance when the blade stiffness was too high.

Nature is a source of ideas and concepts that may be mimicked for the design of novel turbines. Nevertheless, there is still need of research for the development of accurate fluid-structure interaction models that describe the behavior of these design concepts. Additionally, analytical biomimetic models are still underdeveloped in relationship with the analytical models introduced in the previous sections.

2.2.10. Computational Fluid Dynamics (CFD)

Numerical techniques have experienced a great development in the last decades. Particularly, in the field of fluid mechanics, Computational Fluid Dynamics (CFD) techniques based on the Finite Volume Method (FVM) have become a useful tool for the prediction of flow behavior with the aid of computers. CFD models part from the discretization of the Navier-Stokes equations in a mesh representing the fluid portion of the simulated domain, solving them iteratively until convergence (and thus a solution) is found.

These methods have been also applied to vertical axis wind turbines, saving time and economic efforts at wind turbine design steps while maintaining a good accuracy in their predictions. Just to introduce some examples (these techniques will be extensively covered in Chapter 4), Gupta et al. [76] applied a CFD model to determine the performance of a twisted airfoil shaped H-Darrieus rotor of fiberglass reinforced plastic, with deviations of only $\pm 2.68\%$ and $\pm 3.66\%$ in the power and torque coefficients between experimental and numerical results. Amet et al. [35] performed 2D numerical simulations of the blade-vortex interaction in a Darrieus turbine, visualizing the dynamic stall and the shed vortices, as well as the hysteresis loops in lift and drag coefficients. Shamsoddin and Porté-Agel [77] used a Large Eddy Simulation(LES) model to investigate the wake behind a vertical-axis wind turbine in three-dimensional turbulent flow. CFD models can also provide a prediction of the noise radiated by a wind turbine. Iida et al. [78] obtained an overall estimation of the noise level radiated by a VAWT using numerical techniques. Finally, it is interesting to remark that CFD techniques tend to obtain more accurate predictions than the previously introduced methods. Beri and Yao [79] applied both a double multiple streamtube model and a CFD model to analyse the performance of a vertical axis wind turbine, finding discrepancies between both models for low tip speed ratios . For low TSRs, the streamtube model predicted a negative torque, whereas the CFD model showed that an actual positive torque was generated. However, although the accuracy of CFD techniques is supposed to be greater than other predictive methods, they are more time-consuming and a model must be developed for each turbine design by a high specialized person. Currently, there is no possibility of coding a simple program to test every desired turbine configuration with the precision that these techniques require.

2.2.11. Operational modal analysis

Operational Modal Analysis (OMA) is a technique that uses experimental vibration data from a structure to identify its modal properties: natural frequencies, damping ratios and mode shapes. Nowadays, the vibration data is collected with the structure under operating conditions, with no initial or added excitations.

The knowledge of the frequency response of a turbine is important in order to prevent certain rotational speeds that could damage the rotor structure. Carne et al. [80] performed in 1982 a finite element analysis and modal tests on a vertical axis wind turbine. In the beginning, field tests were more difficult, as the protoype excitation source had to be reloaded for every test. However, natural wind soon started to be used as the source of excitation for the tests [81], reducing drastically the testing times. The inception of this analysis method has been extensively described by Carne and James [82]. Finally, a computing package was developed by El-Sayed et al. [83] to evaluate the resonant frequencies and modes of a turbine using finite element methods and aerodynamic calculations. A reasonable agreement between the calculated and field test results was observed.

2.2.12. Pressure-based velocity measurements

In steady flows with high enough velocities, pressure probes may be used to obtain the flow velocity by means of the Bernoulli equation [84] from the flow dynamic pressure.

The total pressure of the flow may be measured with the so-called Pitot probes. Measuring the static pressure by means of a wall tapping or a static tube, the dynamic pressure of the flow may be obtained and the flow velocity may be calculated. Another option is to integrate the static tube in the Pitot probe, measuring the flow dynamic pressure directly as shown in Figure 2.17.

These techniques allow the measurement of just one flow component, the one corresponding with the direction of the probe. However, in some applications, the flow incoming angle is unknown or changes depending on the position. In these cases, multihole probes allow obtaining the static and dynamic pressure, as well as the flow direction. These probes consist of a central hole combined with a number of hole pairs symmetrically displaced and with equal and opposite angles between their faces and the flow, as shown in Figure 2.18. Multihole probes are widely used in turbomachinery applications, particularly in the measurement of the performance of fans [85]. Moscardi and Johnson [86] employed a 5-hole probe for measuring local inflow effects on a HAWT.

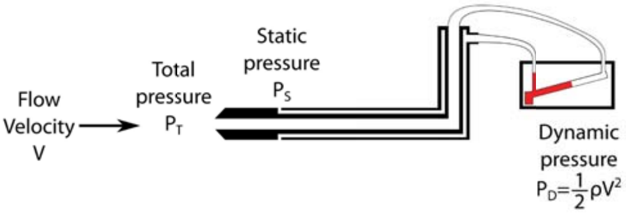

Figure 2.17: Measurement of flow velocity with a Pitot probe

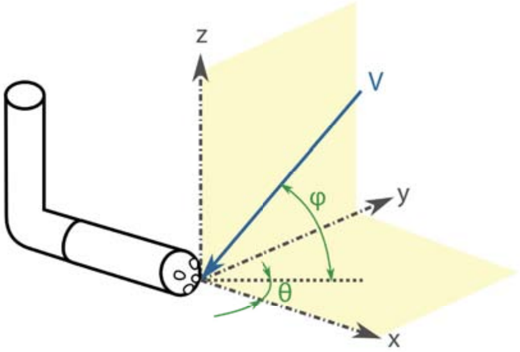

Figure 2.18: Measurement of flow velocity with a multihole probe

2.2.13. Particle image velocimetry (PIV)

Particle image velocimetry (PIV) is a powerful tool for flow visualization. This technique is based on the measurement of the displacement of small tracer particles injected into the fluid

[84]. A thin pulsed laser sheet is used to illuminate the particles at two instants as shown in Figure 2.19, and the light scattered by the particles is captured with a digital camera synchronized with the laser pulses. PIV is a non-invasive method, but optical access to the experiment is necessary for the laser emission and the capture of the images. Additionally, the particles must be homogeneously distributed throughout all the observed flow region. After capturing the images, a computer post-processing is required. The captured frames are divided in several so-called interrogation regions, and a cross-correlation analysis of the particle-frame patterns between the two frames is performed. The local fluid velocity is finally obtained from the displacement of these patterns divided by the image magnification and the time delay between the laser pulses. Dyes and smoke may be also employed for fluid visualization, rendering a

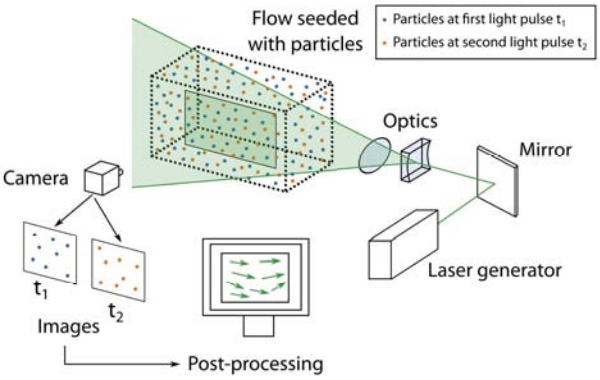

Figure 2.19: Scheme showing the Particle Image Velocimetry (PIV) technique

qualitative description of the flow field. The main advantage of PIV over these methods is the qualitative description of the instantaneous flow field. Nevertheless, this technique requires a higher expertise level.

Direct observation of the flow around wind turbines may provide information about flow effects disregarded by analytical and numerical models, as well as a deeper understanding of the turbulence produced during the operation of a turbine. Fujisawa and Shibuya [87] designed an experiment applying PIV techniques to a small-scale Darrieus in a water tunnel, with the aim of visualizing dynamic stall. Two pairs of stall vortices were successively shed from the blade moving upstream. Consequently, they could attribute the mechanism of dynamic stall to the successive generation of separation on the inner surface of the blade, followed by the formation of roll-up vortices from the outer surface. Later, Ferreira et al. [88] performed a similar experiment using wind instead of water. Ferreira et al. [89] studied the effects of skewed flow in a VAWT using PIV, finding that the extra power obtained with skewed flow comes from the area increase in the downwind blade passage outside the upwind generated wake. More recently, Eboibi et al. [90] have developed a flow field measurement method based on PIV for VAWTs, detailing parameters such as the blade treatment, the seeding concentration and the laser power. Parker and Leftwich [91] also used PIV to study the blockage effect produced by a VAWT.

PIV requires a high degree of expertise to be performed. On the other side, its applications are wide for both research and educational purposes, providing detailed descriptions of the flow around turbines which can identify previously unnoticed phenomena. This may lead to corrections in other analysis models, such as the refinement of certain CFD mesh zones or the introduction of turbulent effects in analytical models.

2.2.14. Hot-wire anemometry

Hot-wire anemometers use a fine wire, with a diameter in the range of several micrometers, which is heated up. The air that flows past the wire has a cooling effect, causing a decrease in the temperature of the wire. This temperature decrease is used to determine the fluid velocity by means of a calibrated correlation. The hot-wire anemometry technique (HWA) can be also applied to VAWTs. Ferreira [92] performed hot-wire measurements which allowed him to characterize the air velocity profiles around a VAWT, obtaining a detailed description of the flow past the turbine and the wake. This flow field description was very useful to identify the wake behavior and it may be used to correct predictive models, such as the vortex method, to obtain more accurate predictions for other VAWT configurations. Bergeles, Michos and Athanassiadis [93] also used hot-wire measurements to characterize the velocity field in the symmetry plane of a VAWT, whereas Fortunato et al. [94] performed measurements in two horizontal planes in the wake of a VAWT. Hot-wire anemometry is a very delicate technique. Despite its powerfulness, the wire is very sensitive and is bound to be broken at the smallest impact. This technique, nevertheless, possesses a really fine spatial resolution compared to other measurement methods, which explains why it is universally applied for the study of turbulent phenomena. In contrast to PIV, which offers a more qualitative point of view, HWAT allows to perform precise measurements of wind velocities at very specific points, being able to correct predictive models once the velocity profiles around a family of wind turbines are known.

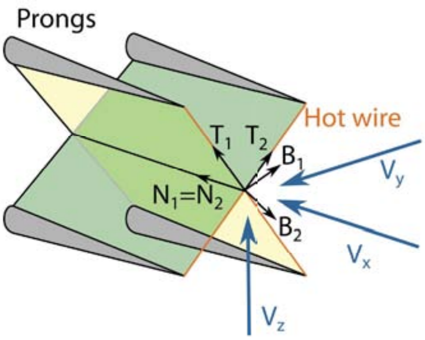

Figure 2.20: Hot-wire anemometry probe with two wires and their reference frames

2.2.15. Wind tunnel testing

Wind tunnel testing is a highly employed experimental technique in all fields of aerodynamics. An object is placed inside a tunnel capable of generating a wind current and experimental tests are performed on it. If the size of the object allows it, its response to wind flows can be directly analyzed without a predictive model. However, this is not always possible and small-scale models must be developed, extrapolating afterwards the results to the actual object using nondimensional parameters. Wind tunnel testing of small-scale VAWT prototypes is the last available step before actual field tests. Every possible flow effect is considered and the accuracy of the results depends only on the precision of the measurements, so this technique is the preferable when time and budget are not a fundamental obstacle. Nevertheless, the required time, financial and human resources cannot be neglected. In the case of high-solidity turbines, analytical models often collapse and the practical options for research are CFD methods or experimental tests, as the ones performed by Fiedler and Tullis [95], who investigated the blade offset and pitch effects on a high solidity VAWT using an open-air wind tunnel facility. On the other hand, Selig and McGranahan [96] performed wind tunnel aerodynamic tests of six airfoils for their possible use on small wind turbines. As wind tunnel testing does not neglect almost any effect, it is a suitable method for analyzing the self-starting of wind turbines when discrepancies are found between other analysis methods. Singh et al. [97] designed a wind tunnel test bench to investigate the self-starting of a three-bladed S1210 H-rotor with high solidity, obtaining the maximum Cp of 0.32 for a rotor solidity of 1.0. Benchmark experiments were also performed by Rolland et al. [98], who combined the performance tests with smoke plume tests to visualize the development of vortices. However, there are some limits concerning the conservation of the dimensionless numbers related to the flow when varying the scale of the testing models. The conservation of the Reynolds number may suppose problems due to the imposition of very high testing velocities. In addition, there are difficulties to keep the tip speed ratio of the turbine constant, which is analogous to the Strouhal number for VAWTs. These difficulties have been experienced by Meana-Fernández et al. [58], who compared analytical and CFD models validating them through experimentation. This experimental method, with a high degree of accuracy, may be also used for experimental validation of other simpler methods, as done by Kirke and Lazauskas [99] to verify a mathematical model for predicting the performance of a variable pitch VAWT. Li et al. [100] also used wind tunnel tests to validate a vortex model for determining the power and torque performance of a 2 kW straight-bladed VAWT.

2.2.16. Prototype field testing

Before mass production of any novel product begins, it is advisable to test if the product will meet the design requirements. Thus, the fabrication and testing of a prototype is always the final step before starting mass production. Once an almost final design for a VAWT is achieved, field tests must be performed to assess the actual performance of the designed wind turbine. Ashwill [101] prepared a report for Sandia National Laboratories which included aerodynamic and structural performances of a 34-meter VAWT, as well as its stress amplitude spectra, start-up torque, normal operation and braking data. Huskey et al. [102] tested a 1 kW wind turbine in Colorado in a normal production mode configuration and in a power-optimized configuration, which increased the power output in 0.3 kW. Prototype field testing represents the final step to assure that a turbine fulfills the purposes it was designed for. The results obtained from the measurements can be assumed to be the same results that will be obtained from the future turbines that follow the same design. Besides, every flow effect is considered as it is going to arise in real turbines once they are fabricated. On the other hand, the very high consumption of financial, time and human resources required to accomplish this tests prevents their application until there is almost no uncertainty in the selected design alternative. The rest of the design techniques are the ones suitable to compare different designs, while this technique should be applied afterwards for the assessment of the selected alternative.

2.2.17. Conclusion

The main wind power extraction technologies available nowadays have been reviewed in this chapter, from the oldest windmills to the most modern turbines, including unconventional designs. A panoramic view of the performance of typical rotor types has been presented, focusing afterwards on vertical-axis wind turbines. The main advantages and disadvantages of lift-driven VAWTs have been discussed, highlighting their particularly suitability for urban areas. A brief theoretical background on airfoil performance and particularities of the flow developed by a VAWT has been then presented. Finally, the main design and analysis techniques that may be applied for the study of VAWTs have been reviewed, commenting on their precision, complexity, application ranges and associated costs. The methods that have been used to perform the research presented in this thesis have been highlighted and are the following: dimensional analysis (throughout the whole thesis); actuator disk theory, blade element method and streamtube models (to develop the methodology presented in Chapter 3, but also during the rest of the thesis); Computational Fluid Dynamics (CFD) models (to develop the methodology presented in Chapter 4, but also to validate the methodology of Chapter 3 and predict the performance of the experimental prototype described in Chapter 5); and pressure-based velocity measurements, hot-wire anemometry and wind tunnel testing (for the prototype presented in Chapter 5).

References

[1] J. Schefter, *Barrel-blade windmill - efficient power from the Magnus effect?* Popular Science **223**, 60 (1983).

[2] G. J. M. Darrieus, *Turbine having its rotating shaft transverse to the flow of the current,* (1931).

[3] F. Scheurich and R. Brown, *Modelling the aerodynamics of vertical-axis wind turbines in unsteady wind conditions,* Wind Energy **16**, 91 (2013).

[4] M.Raciti Castelli, S. D. Betta, and E. Benini, *Three-dimensional modeling of a twisted-blade Darrieus vertical-axis wind turbine,* World Academy of Science, Engineering and Technology **7**, 372 (2013).

[5] Wind Power Ltd., *Vertical axis turbine apparatus,* (2007).

[6] A. Shires, *Development and evaluation of an aerodynamic model for a novel vertical axis wind turbine concept,* Energies **6**, 2501 (2013).

[7] W. Chong, K. Pan, S. Poh, A. Fazlizan, C. Oon, A. Badarudin, and N. Nik-Ghazali, *Performance investigation of a power augmented vertical axis wind turbine for urban high-rise application,* Renewable Energy **51**, 388 (2013).

[8] S. Savonius, *Rotor adapted to be driven by wind or flowing water,* (1929).

[9] K. Morshed, M. Rahman, G. Molina, and M. Ahmed, *Wind tunnel testing and numerical simulation on aerodynamic performance of a three-bladed Savonius wind turbine,* International Journal of Energy and Environmental Engineering , 4 (2013).

[10] M. Kamoji, S. Kedare, and S. Prabhu, *Experimental investigations on single stage modified Savonius rotor,* Applied Energy 86 , 1064–73 (2009).

[11] R. Hossain and S. Ahmed, *"a study of aerodynamic characteristics of S-shaped Savonius rotor with different number of blades,* International Journal of Engineering Research & Technology (IJERT) **2**, 1406 (2013).

[12] B. Wahyudi, S. Soeparman, and H. M. Hoeijmakersc, *Optimization design of Savonius diffuser blade with moving deflector for hydrokinetic cross flow turbine rotor,* Energy Procedia **68**, 244 (2015).

[13] K. Can, Z. Feng, and M. Xuejun, *Comparison study of a vertical-axis spiral rotor and a conventional Savonius rotor,* in *Power and Energy Engineering Conference (APPEEC), 2010 Asia-Pacific* (Chengdu, China, 2010).

[14] M. Mohamed, G. Janiga, E. Pap, and D. Thévenin, *Optimal blade shape of a modified Savonius turbine using an obstacle shielding the returning blade,* Energy Conversion and Management **52**, 236 (2011).

[15] B. Altan, M. Atilgan, and A. Özdamar, *An experimental study on improvement of a Savonius rotor performance with curtaining,* Experimental Thermal and Fluid Science **32**, 1673–8 (2008).

[16] Q. Zhang, H. Chen, and B. Wang, *Modeling and simulation of two-leaf semi-rotary VAWT,* International Conference on Intelligent Computing for Sustainable Energy and Environment, ICSEE 2010 , 389 (2010).

[17] A. Bayeul-Lainé, S. Simonet, and G. Bois, *Unsteady flow field in a mini VAWT with relative rotation blades: analysis of temporal results,* IOP Conf. Series: Materials Science and Engineering **52** (2013).

[18] K. Pope, V. Rodrigues, R. Doyle, A. Tsopelas, R. Gravelsins, G. Naterer, and E. Tsang, *Effects of stator vanes on power coefficients of a zephyr vertical axis wind turbine,* Renewable Energy **35**, 1043–51 (2010).

[19] G. Colley, R. Mishra, H. Rao, and R. Woolhead, *Effect of rotor blade position on vertical axis wind turbine performance,* in *International Conference on Renewable Energies and Power Quality* (Granada, Spain, 2010).

[20] S. Bhuyan and A. Biswas, *Investigations on self-starting and performance characteristics of simple H and hybrid H-Savonius vertical axis wind rotors,* Energy Conversion and Management **87**, 859 (2014).

[21] D. Gorelov and V. Krivospitsky, *Prospects for development of wind turbines with orthogonal rotor,* Thermophysics and Aeromechanics **1**, 153 (2008).

[22] J. H. Paulides, L. Encica, J. Jansen, E. Lomonova, and D. van Wijck, *Small-scale urban Venturi wind turbine: Direct-drive generator,* in *Electric Machines and Drives Conference, 2009. IEMDC '09. IEEE International* (Miami, FL, USA, 2009).

[23] C. Jehle and R. Schmehl, *Applied tracking control for kite power systems,* Journal of Guidance, Control and Dynamics **37**, 1211 (2014).

[24] F. Ponta, J. Seminara, and A. Otero, *On the aerodynamics of variable-geometry oval-trajectory Darrieus wind turbines,* Renewable Energy **32**, 35–56 (2007).

[25] F. Ponta and L. Lago, *Analysing the suspension system of VGOT-Darrieus wind turbines,* Energy for Sustainable Development **12**, 5 (2008).

[26] J. Samson, R. Katebi, and C. Vermillion, *A critical assessment of airborne wind energy systems,* in *Renewable Power Generation Conference (RPG 2013), 2nd IET* (Beijing, China, 2013).

[27] I. Hwang, W. Kang, and S. Kim, *An airborne cycloidal wind turbine mounted using a tethered balloon,* International Journal of Aeronautical & Space Sciences **12**, 354–9 (2011).

[28] A. M. Marks, *Charged aerosol generator with uni-electrode source,* (1980).

[29] S. Frayne, *Generator utilizing fluid-induced oscillations,* (2009).

[30] D. Yáñez Villareal, *VIV resonant wind generators*, Tech. Rep. (Vortex Bladeless S.L., Madrid, Spain, 2018).

[31] H. Glauert, *The Elements of Aerofoil and Airscrew Theory*, 2nd ed. (Cambridge University Press, Canada, 1947).

[32] A. Tummala, R. Velamati, D. Sinha, V. Indraja, and V. H. Krishna, *A review on small scale wind turbines,* Renewable and Sustainable Energy Reviews **56**, 1351 (2016).

[33] N. Hill, R. Dominy, G. Ingram, and J. Dominy, *Darrieus turbines: the physics of self-starting,* Proceedings of the Institution of Mechanical Engineers, Part A: Journal of Power and Energy **223**, 21 (2009).

[34] S. Worasinchai, *Small Wind Turbine Starting Behaviour*, Tech. Rep. (Durham theses, Durham University, 2012).

[35] E. Amet, T. Maître, C. Pellone, and J.-L. Achard, *2D Numerical Simulations of Blade-Vortex Interaction in a Darrieus Turbine,* Journal of Fluids Engineering **131**, 1 (2009).

[36] P. Kundu, I. Cohen, and D. Downling, *Fluid Mechanics, 6th Edition* (Academic Press, 2015).

[37] K. Pope, G. Naterer, I. Dincer, and E. Tsang, *Power correlation for vertical axis wind turbines,* International Journal of Energy Research **35**, 423 (2011).

[38] G. Colley, *Design, Operation and Diagnostics of a Vertical Axis Wind Turbine*, Tech. Rep. (University of Huddersfield, Huddersfield, UK, 2012).

[39] K. Pope, I. Dincer, and G. Naterer, *Energy and exergy efficiency comparison of horizontal and vertical axis wind turbines,* Renewable Energy **35**, 2102 (2010).

[40] A. Kocer, Y. Yuksel, and M. Ozturk, *Thermodynamic and environmental assessment of a wind turbine system,* The 5th International Symposium on Sustainable Development , 219 (2014).

[41] O. Ozgener and L. Ozgener, *Exergy and reliability analysis of wind turbine systems: A case study,* Renewable and Sustainable Energy Reviews **11**, 1811–26 (2007).

[42] D. Lobitz, *Dynamic analysis of Darrieus vertical axis wind turbine rotors*, Tech. Rep. (Sandia National Laboratories. Applied Mechanics Division, Albuquerque, New Mexico, USA, 1981).

[43] S. Biswas, B. Sreedhard, and Y. Singh, *Dynamic analysis of a vertical axis wind turbine using a new windload estimation technique,* Computers & Structures **65**, 903 (1997).

[44] J. Manwell, J. McGowan, and A. Rogers, *Wind Energy Explained: Theory, Design and Application* (John Wiley and Sons, Ltd, Chichester, UK, 2009).

[45] H. Glauert, *The Elements of Aerofoil and Airscrew Theory* (Cambridge University Press, 1926).

[46] I. Paraschivoiu, *Wind Turbine Design: With Emphasis on Darrieus Concept* (Presses internationales Polytechnique, Canada, 2002).

[47] M. Brahimi, A. Allet, and I. Paraschivoiu, *Aerodynamic analysis models for vertical-axis wind turbines,* International Journal of Rotating Machinery **2**, 15 (1995).

[48] G. Bedon, M. Raciti Castelli, and E. Benini, *Optimization of a Darrieus vertical-axis wind turbine using blade element - momentum theory and evolutionary algorithm,* Renewable Energy **59**, 184 (2013).

[49] S. Brusca, R. Lanzafame, and M. Messina, *Design of a vertical-axis wind turbine: how the aspect ratio affects the turbine's performance,* International Journal of Energy and Environmental Engineering **5**, 333 (2014).

[50] K. Merz, *A method for analysis of VAWT aerodynamic loads under turbulent wind and platform motion,* Energy Procedia **24**, 44 (2012).

[51] M. J. Buhl, *A New Empirical Relationship between Thrust Coefficient and Induction Factor for the Turbulent Windmill State*, Tech. Rep. (National Renewable Energy Laboratory, Golden, Colorado, USA, 2005).

[52] H. Glauert, *The Analysis of Experimental Results in the Windmill Brake and Vortex Ring States of an Airscrew*, Tech. Rep. (Aeronautical Research Committee Reports and Memoranda, London: Her Majesty's Stationery Office, 1926).

[53] D. Eggleston and F. Stoddard, *Wind turbine Engineering Design* (Van Nostrand Reinhold, New York, NY, USA, 1987) pp. 30–35.

[54] D. Spera, *Wind Turbine Technology* (ASME Press, New York, USA, 1994).

[55] T. Burton, D. Sharpe, N. Jenkins, and E. Bossanyi, *Wind Energy Handbook* (John Wiley & Sons Ltd., West Sussex, England, 2011).

[56] J. Manwell, J. McGowan, and A. Rogers, *Wind Energy Explained* (John Wiley & Sons Ltd., West Sussex, England, 2002).

[57] I. Masters, J. Chapman, J. C. Orme, and M. Willis, *Modelling high axial induction flows in tidal stream turbines with a corrected blade element model,* in *3rd International Conference on Ocean Energy* (Bilbao, Spain, 2010).

[58] A. Meana-Fernández, I. Solís-Gallego, J.M. Fernández Oro, K.M. Argüelles Díaz, and S. Velarde-Suárez, *Prediction of the performance of straight-bladed vertical axis wind turbines using analytical models,* in *Spain Minergy 2015* (Gijón, Asturias, Spain, 2015).

[59] H. Madsen, *The actuator cylinder - A Flow Model for Vertical Axis Wind Turbines*, Tech. Rep. (Ph.D. Thesis. Aalborg University Centre, Aalborg, Denmark, 1982).

[60] H. Madsen, U. Paulsen, and L. Vitae, *Analysis of VAWT aerodynamics and design using the actuator cylinder flow model,* Journal of Physics: Conference Series **555**, 012065 (2014).

[61] C. Ferreira, H. Madsen, M. Barone, B. Roscher, P. Deglaire, and I. Arduin, *Comparison of aerodynamic models for vertical axis wind turbines,* Journal of Physics: Conference Series **524**, 012125 (2014).

[62] J. Strickland, B. Webster, and T. Nguyen, *A Vortex Model of the Darrieus Turbine: an Analytical and Experimental Study*, Tech. Rep. (Technical Report SAND81-7017, Albuquerque, NM, USA, 1981).

[63] J. Oler and G. Brownlee, *A high-speed lifting line model for darrieus turbines,* Proceedings of the 5th ASME Wind Energy Symposium , 59 (1986).

[64] B. Basuno, F. Coton, and R. Galbraith, *A prescribed wake aerodynamic model for vertical axis wind turbines,* Proceedings of the Institution of Mechanical Engineers, Part A: Journal of Power and Energy **206**, 159 (1992).

[65] H. Dumitrescu and V. Cardoş, *A free wake method for vertical-axis wind turbine performance prediction,* Rev. Roum. Sci. Techn. – Méc. Appl. **54**, 87 (2009).

[66] L. Shi, V. Riziotis, S. Voutsinas, and J. Wang, *A consistent vortex model for the aerodynamic analysis of vertical axis wind turbines,* Journal of Wind Engineering and Industrial Aerodynamics **135**, 57 (2014).

[67] R. Wilson and S. Walker, *Fixed-Wake Analysis of the Darrieus Rotor*, Tech. Rep. (Sandia National Laboratories, Allbuquerque, New Mexico, USA, 1981).

[68] H. Hirsch and A. Mandal, *A cascade theory for the aerodynamic performance of darrieus wind turbines,* Wind Engineering **11**, 164 (1987).

[69] M. Kemp, *Leonardo da Vinci: The Marvellous Works of Nature and Man* (Oxford University Press, Oxford, UK, 2006).

[70] J.D. Anderson Jr., *Inventing Flight: The Wright Brothers and Their Predecessors* (Johns Hopkins University Press, Baltimore, Maryland, USA, 2004).

[71] D. Gorelov, *Analogy between a flapping wing and a wind turbine with a vertical axis of revolution,* Journal of Applied Mechanics and Technical Physics **50**, 297 (2009).

[72] K. Rozhdestvensky and V. Ryzhov, *Aerohydrodynamics of flapping-wing propulsors,* Progress in Aerospace Sciences **39**, 585 (2003).

[73] M. Bouzaher and M. Hadid, *Active control of the vertical axis wind turbine by the association of flapping wings to their blades,* Procedia Computer Science **52**, 714 (2005).

[74] M. Alam and H. Hirahara, *Numerical performance assessment of a flapping-type vertical axis wind turbine with chebyshev-dyad linkage,* Smart Grid and Renewable Energy **8**, 53 (2017).

[75] W. Liu and Q. Xiao, *Investigation on Darrieus type straight blade vertical axis wind turbine with flexible blade,* Ocean Engineering **110**, 339 (2015).

[76] R. Gupta, S. Roy, and A. Biswas, *Computational fluid dynamics analysis of a twisted airfoil shaped two-bladed H-Darrieus rotor made from fibreglass reinforced plastic (FRP),* International Journal of Energy and Environment **1**, 953 (2010).

[77] S. Shamsoddin and F. Porté-Agel, *Large eddy simulation of vertical axis wind turbine wakes,* Energies **7**, 890 (2014).

[78] A. Iida, A. Mizuno, and K. Fukudome, *Numerical simulation of aerodynamic noise radiated from vertical axis wind turbines,* Proceedings of the 18th International Congress on Acoustics ICA 2004 **2**, 1311 (2004).

[79] H. Beri and Y. Yao, *Double multiple stream tube model and numerical analysis of vertical axis wind turbine,* Energy and Power Engineering **3**, 262 (2011).

[80] T. Carne, D. Lobitz, A. Nord, and R. Watson, *Finite Element Analysis and Modal Testing of a Rotating Wind Turbine*, Tech. Rep. (Sandia National Laboratories, Albuquerque, New Mexico, USA, 1982).

[81] T. Carne, J. Lauffer, A. Gomez, and H. Benjannet, *Modal testing an immense flexible structure using natural and artificial excitation,* The International Journal of Analytical and Experimental Modal Analysis **3**, 117 (1988).

[82] T. Carne and G. I. James, *The inception of OMA in the development of modal testing technology for wind turbines,* Mechanical Systems and Signal Processing **24**, 1213 (2010).

[83] A. El-Sayed, C. Hirsch, and R. Derdelinckx, *Dynamics of vertical axis wind turbines (Darrieus type),* International Journal of Rotating Machinery **2**, 33 (1995).

[84] C. Tropea, A. Yarin, and J. Foss, *Handbook of Experimental Fluid Mechanics* (Springer, 2007).

[85] S. Castegnaro, M. Masi, and A. Lazzaretto, *Preliminary Experimental Assessment of the Performance of Rotor-only Axial Fans Designed with Different Vortex Criteria,* in *Proceedings of the 12th European Conference on Turbomachinery Fluid dynamics & Thermodynamics* (European Turbomachinery Society, Stockholm, Sweden, 2017) pp. ETC2017–055.

[86] A. Moscardi and D. Johnson, *A compact in-blade five hole pressure probe for local inflow study on a horizontal axis wind turbine,* Wind Engineering **40**, 360 (2016).

[87] N. Fujisawa and S. Shibuya, *Observations of dynamic stall on Darrieus wind turbine blades,* Journal of Wind Engineering and Industrial Aerodynamics **89**, 201 (2001).

[88] C. Ferreira, G. van Kuik, G. van Bussel, and F. Scarano, *Visualization by PIV of dynamic stall on a vertical axis wind turbine,* Experiments in Fluids **46**, 97 (2009).

[89] C. S. Ferreira, A. van Zuijlen, H. Bijl, G. van Bussel, and G. van Kuik, *Simulating dynamic stall in a two-dimensional vertical-axis wind turbine: verification and validation with particle image velocimetry data,* Wind Energy **13**, 1 (2010).

[90] O. Eboibi, J. Edwards, R. Howell, and L. Danao, *Development of velocity flow field measurement method around a vertical axis wind turbine blade using particle image velocimetry,* Proceedings of the World Congress on Engineering 2014, WCE 2014 **2**, 1184 (2014).

[91] C. Parker and M. Leftwich, *The effect of tip speed ratio on a vertical axis wind turbine at high Reynolds numbers,* Experiments in Fluids **57**, 74:1 (2016).

[92] C. Ferreira, *The near wake of the VAWT - 2D and 3D views of the VAWT aerodynamics*, Tech. Rep. (Ph.D. Thesis. Delft Technical University, Delft, The Netherlands, 2009).

[93] G. Bergeles, A. Michos, and N. Athanassiadis, *Velocity vector and turbulence in the symmetry plane of a Darrieus wind generator,* Journal of Wind Engineering and Industrial Aerodynamics **37**, 87 (1991).

[94] B. Fortunato, S. Camporeale, M. Torresi, D. De Fazio, and M. Giordani, *Experimental results of a Vertical Axis Wind Turbine,* in *Proceedings of the ASME-ATI-UIT 2010 Conference on Thermal and Environmental Issues in Energy Systems* (ASME, Sorrento, Italy, 2010).

[95] A. Fiedler and S. Tullis, *Blade offset and pitch effects on a high solidity vertical axis wind turbine,* Wind Engineering **3**, 237 (2009).

[96] M. Selig and B. McGranahan, *Wind Tunnel Aerodynamic Tests of Six Airfoils for Use on Small Wind Turbines*, Tech. Rep. (National Renewable Energy Laboratory, Golden, Colorado, USA, 2004).

[97] M. Singh, A. Biswas, and R. Mishra, *Investigation of self-starting and high rotor solidity on the performance of a three S1210 blade H-type Darrieus rotor,* Renewable Energy **76**, 381 (2015).

[98] S. Rolland, M. Thatcher, W. Newton, A. Williams, T. Croft, D. Gethin, and M. Cross, *Benchmark experiments for simulations of a vertical axis wind turbine,* Applied Energy **111**, 1183 (2013).

[99] B. Kirke and L. Lazauskas, *Experimental verification of a mathematical model for predicting the performance of a self-acting variable pitch vertical axis wind turbine,* Wind Engineering **17**, 58 (1993).

[100] Y. Li, F. Feng, W. Tian, and Q. He, *Simulation and wind tunnel test on a straight-bladed vertical axis wind turbine,* Research Journal of Applied Sciences, Engineering and Technology **5**, 2892 (2013).

[101] T. Ashwill, *Measured Data for the Sandia 34-Meter Vertical Axis Wind Turbine*, Tech. Rep. (Sandia National Laboratories, Albuquerque, New Mexico, USA, 1992).

[102] A. Huskey, A. Bowen, and D. Jager, *Wind Turbine Generator System Power Performance Test Report for the Mariah Windspire 1-kW Wind Turbine*, Tech. Rep. (National Renewable Energy Laboratory, Golden, Colorado, USA, 2009).

3

Analytical model for the evaluation of prospective VAWT designs

From the viewpoint of positivist philosophy, however,
one cannot determine what is real.
All one can do is find which mathematical models
describe the universe we live in.

Stephen Hawking, The Universe in a Nutshell (2001)

Perhaps it is good to have a beautiful mind,
but an even greater gift is to discover a beautiful heart.

John Forbes Nash Jr., A Beautiful Mind (2002)

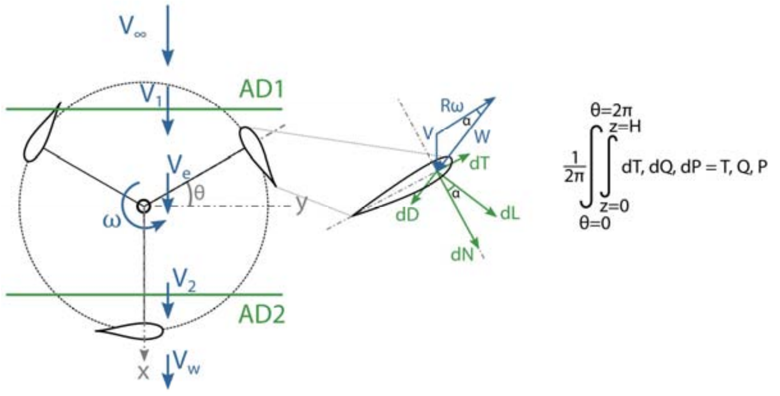

Parts of this chapter have been published in Energy **147**, (2018) [1].

AFTER the review of the design and analysis techniques for vertical-axis wind turbines performed in the previous chapter, it was observed that streamtube models combine a relatively good accuracy with a low computational cost. Hence, it was decided to develop a predictive computational tool based on these models, so that it can be applied to the development of commercial turbines at early design stages. In this chapter, the development process of this tool is explained, focusing on allowing a significant reduction in the number of numerical simulations or experimental tests at initial design stages. This tool, after being validated with experimental results and CFD simulations, has been used to study the influence of solidity, blade Reynolds number and airfoil geometry on the performance of the turbine. An increase in solidity up to 0.5 was found to give higher power coefficients, but at the expense of a narrower high-efficiency band. The results from the analysis of the blade Reynolds number provided insight into the self-starting behavior and performance of the VAWT, depending on the incoming velocity and the rotor size. The best candidate airfoils tend to be thin, with low or almost no camber, allowing for VAWT self-starting and the development of a wide high-efficiency band. Particularly, the DU-06-W-200, the S1012, the NACA0012H and the NACA 23016 airfoils behaved quite efficiently. Finally, based on the results obtained, two optimized VAWT designs for medium and low wind speeds are proposed.

3.1. Introduction and research gaps addressed

At early turbine design stages, it would be desirable to test several different configurations before selecting a final design. However, there is still lack of a straightforward procedure, fact that prevents typical VAWT designs from achieving a higher performance [2].

Streamtube models represent a very convenient method for VAWT design and optimization exercises [3], as they are faster than numerical computational fluid dynamics (CFD) simulations with regards to computational effort and time. Different authors have also highlighted the importance of these models for the industrial environment, due to their extremely small computational requirements [4]. Despite their robustness, these methods require abundant experimental data for the airfoil lift and drag characteristics over a wide range of angles of attack and Reynolds numbers [5], [6].

The performance of a VAWT depends on several parameters related to the whole turbine and flow conditions. As introduced in Chapter 2, there are three parameters that have a major influence on the turbine performance: the turbine solidity, the flow Reynolds number and the airfoil used to fabricate the blades [7], [8]. Many authors have tried to provide optimum values of these parameters, but the results found seem to be contradictory. Paraschivoiu [9] and Goselin et al. [10] proposed an optimal value of 0.2 for the solidity, whereas other authors propose value ranges between 0.2 and 0.6 [2], 0.3 and 0.5 [11], or 0.4 and 0.8 [12], while others have found such dissimilar values as 1 [13], 0.93 [14] or 0.34 [15]. This disparity highlights that there is still no consensus on the optimal solidity for a VAWT, with authors like Jain and Abhishek [16] finding an increase in the power coefficient with the increase of solidity and others like Li et al. [17], [18] finding exactly the opposite behavior. Subramanian et al. [19] verified that high solidity turbines performed better at low tip-speed ratios. As remarked by Ghasemian [20], some researchers recommend either high solidity values that increase the performance at lower tip-speed ratios, or low solidity values that increase the performance at higher tip-speed ratios with a wider operating range [21], [14], [12]. All these findings reveal that more insight into the optimum values of solidity is needed.

Regarding the airfoil chosen to build the turbine blades, there is even more controversy between symmetrical and unsymmetrical airfoils. Beri and Yao [22] state that symmetrical airfoils have minimum or negative torque generation at lower tip-speed ratios, but unsymmetrical blades show a reduced peak efficiency compared to conventional symmetrical airfoils. Bianchini et al. [23] also pose some doubts in the effective application of cambered blades due to their different behavior depending on the sign of the angle of attack. Chen and Kuo [24] state that the larger the camber of the blade, the better is the self-starting capability of the VAWT, and Sengupta et al. [8] have shown improved performance of cambered blades with respect to symmetrical blades. On the other hand, El-Samanoudy et al. [25] and Jafaryar et al. [26] claim that symmetrical or almost symmetrical airfoils perform better. Besides, as highlighted by Qamar and Janajreh [27], the literature does not show a comprehensive understanding of how solidity affects the performance of cambered VAWTs, especially with regard to the optimal configuration. These authors [28] found an improvement in the performance of VAWT at lower speeds using cambered blades. All the different results present in the literature suggest the need to obtain more insight into the influence of airfoil camber on the performance of VAWTs. Finally, most of the studies focus on the investigation of a particular airfoil or airfoil family and sometimes the proposal of variations on them. The reasons seem clear: the cost of the experimental design in the case of experimental studies, the time and computational costs required to perform CFD simulations of different airfoil geometries and, in the case of momentum models, the lack of airfoil data available to introduce in the models [2], [4].

In this chapter, the research gaps previously mentioned are intended to be assessed. Firstly, an analytical methodology based on streamtube models is developed, resulting in a practical and cost-effective tool for the prediction of the performance of prospective VAWT designs. Then, an exhaustive analysis of the influence of different variables (solidity, blade Reynolds number and airfoil geometry) on the performance of a VAWT is performed using this tool, and optimum values for these influencing variables are proposed. Finally, in order to illustrate the usefulness of this tool, two VAWT designs for low and medium wind speeds are proposed.

3.2. Methodology

3.2.1. Streamtube models

Streamtube models combine the actuator disk theory proposed by Glauert [29] iteratively with the blade element method in order to obtain the performance of a VAWT. There are several streamtube models, depending on the discretization of the turbine assumed. The Single Streamtube Model (SSTM), firstly proposed by Templin [30], considers a unique streamtube enclosing the whole turbine. However, due to the aerodynamic changes on the airfoils during the rotation of the blades, it seems interesting to divide the turbine into multiple streamtubes and calculate the wind profile along the turbine. This lead to the Multiple Streamtubes Model (MSTM) from Strickland [31]. As the behavior of the turbine is completely different in the upwind and downwind zones, the turbine could be modeled as well as two actuator disks in tandem enclosed by a single streamtube (Double-Disc Streamtube Model, DDSM). Finally, the most complex model employs two actuator disks and multiple streamtubes (Double-Multiple Streamtube Model, DMST) and was developed by Paraschivoiu [9]. Figure 3.1 shows the discretization and the calculation scheme of these four analytical models implemented in this study.

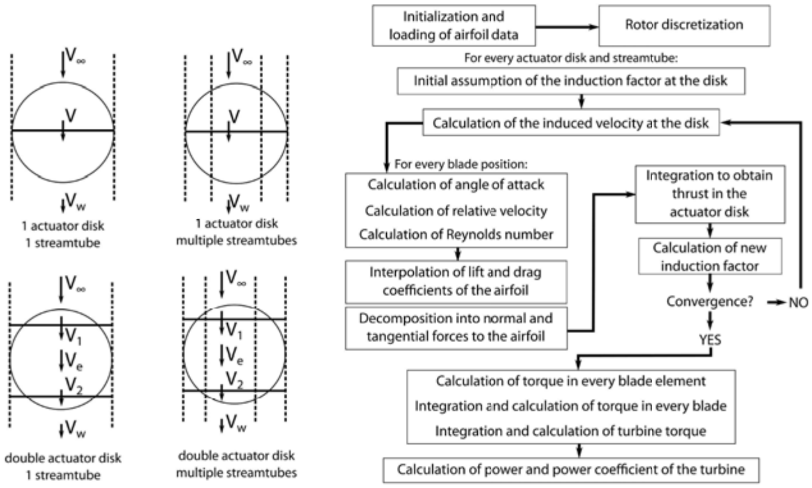

Figure 3.1: Discretization and calculation scheme of the analytical models employed in this study

These four models have been implemented using a home-made code programmed in MATLAB®, obtaining a tool capable of comparing relatively fast different turbine designs and avoiding the greater time lapse required by CFD simulations. The DMST model calculation scheme, the most complex one, is detailed in Figure 3.2. As the rest of the models follow similar calculation schemes, they are not shown for the sake of brevity. The convergence criterion for the calculation of the induction factor has been set to 10^{-6} and the maximum number of iterations has been set to 1000. With these criteria, the time required for the models to yield the complete C_P-λ curve of the VAWT is around five minutes in a typical desktop computer. Nevertheless, the equations used under the actuator disk approach are not applicable beyond high induction factors (0.5) [32]. In addition, some models present convergence problems for low wind incoming speeds (due to the occurrence of high induction factors or high λ), especially the ones with the double disk approach [9]. The breakdown problem of the momentum equation has been addressed via empirical correlations, enlarging the application range of these models (Glauert [29], Eggleston and Stoddard [33], Spera [34], Burton et al. [35], Manwell et al. [7], Buhl [32]). In this work, the Spera correction [34] has been applied for high induction factors.

Finally, before passing to the next section, a comment about the actuator disk theory and the Betz limit (16/27) must be made. This limit, well-known as the theoretical maximum power coefficient of a wind turbine, has been derived from the actuator disk theory with just one actuator disk. This is a commonly known limitation in case of HAWT [7]. However, the actuator disk theory, as studied by Newman [36], may be extended to multiple actuator disks in tandem, showing that the maximum power coefficient for a turbine modeled with n actuator disks is $8n(n+1)/[3(2n+1)^2]$. Hence, the maximum theoretical power coefficient is 16/25 for the models that consider two actuator disks (DDSM and DMST). Altough this seems surprising, there are some authors claiming that the surpass of the Betz limit by vertical-axis wind turbines is possible ([37], [38]).

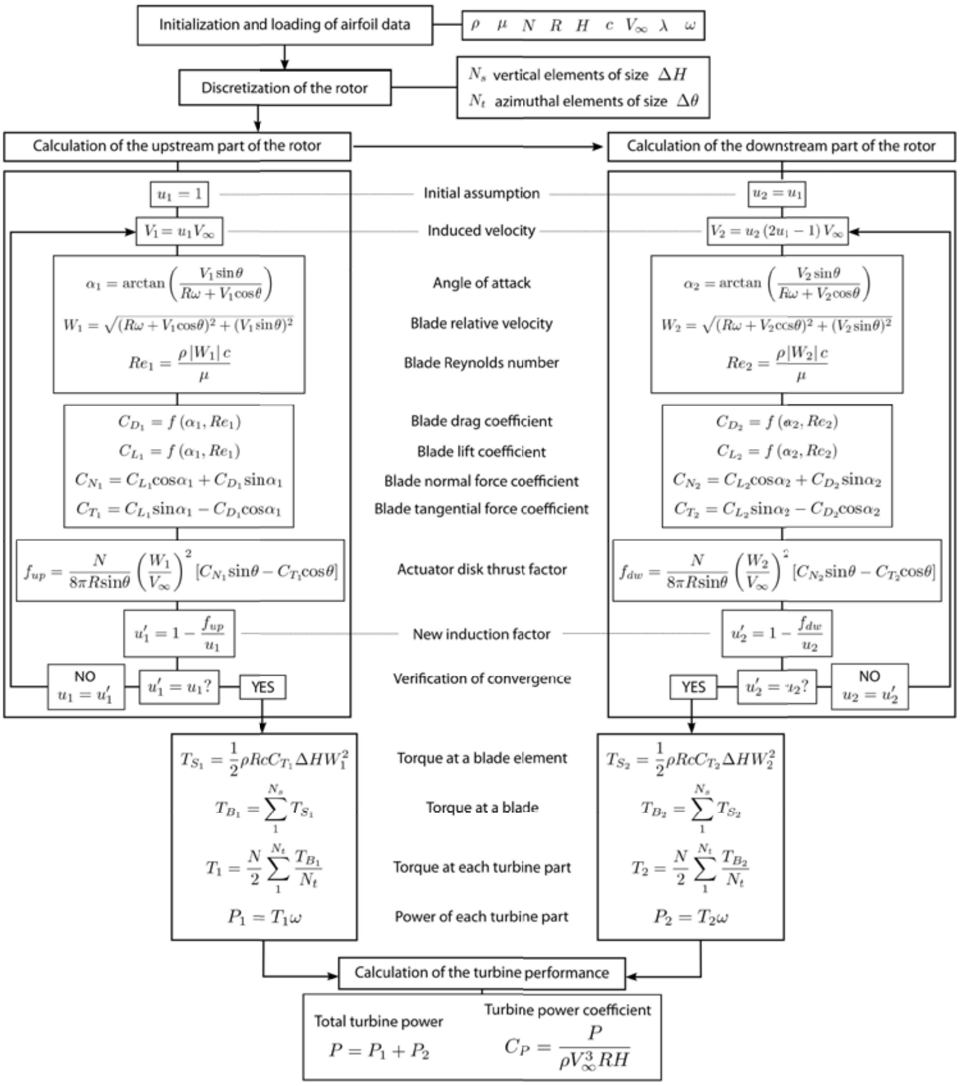

Figure 3.2: Calculation scheme of DMST model

3.2.2. Generation of airfoil data

Aerodynamic forces on an airfoil depend on the angle of attack and the Reynolds number of the flow. In order to compute the lift and drag coefficients at the different blade positions, streamtube models require values of these coefficients for a wide range of angles of attack and Reynolds numbers. Although experimental values would be desirable, a literature survey highlights the difficulty of finding enough data, specially for high angles of attack and low Reynolds numbers. Sheldal and Klimas, in 1981 [39], performed wind tunnel test series for 4 NACA airfoils at Reynolds numbers of 0.35×10^6, 0.50×10^6 and 0.70×10^6. With the aim of extending the airfoil data to other airfoil sections as well as lower Reynolds numbers, they used a synthesizer computer code, PROFILE [40]. However, some authors like Lazauskas [41] considered the data obtained by Sheldal and Klimas for low Reynolds numbers as unusual and atypical, so they employed a minimum Reynolds number of 80,000 for their calculations. The effect of Reynolds number is determinant in the aerodynamic performance of VAWTs, as found by Bogateanu et al. [42]. Additionally to this uncertainty in lift and drag values for different airfoils, the angle of attack and Reynolds number are constantly changing during VAWT operation, so hysteresis effects arise in lift and drag forces. Nevertheless, the consideration of hysteresis effects and other effects neglected by the model formulation (streamtube expansion, rotor tower and wake effects...) would increase substantially the computational time. So, with the aim of developing a simple and practical model, XFOIL [43] has been used for generating the airfoil data. The viscous formulation of this software has proven to be very useful for subcritical airfoil design, being particularly applicable to low Reynolds airfoils [43]. However, XFOIL predictions begin to fail past the airfoil stall angle. Nevertheless, it has been shown that almost all airfoils behave as a flat plate for values of the angle of attack higher than 30°, as the airfoil geometry becomes unimportant [44]. Hence, the models have a reduced region of uncertainty between the stall angle and 30°, which will affect the solution for particular blade positions. Anyway, this will only happen for a minimum part of the whole range of angles of attack found by the blade as it travels along the rotor, so this approach is still valid for the aim of this work.

The range of airfoil data needed for a particular application may be found from the mathematical definitions of the angle of attack and blade Reynolds number. Before reaching $\lambda = 1$, the maximum angle of attack is always found at the position $\theta = \pi$ (see Figure 2.9 for reference) and decreases linearly from π at $\lambda = 0$ to $\pi/2$ at $\lambda = 1$. Once the turbine has passed $\lambda = 1$, the maximum angle of attack is found at the angular position:

$$\theta = \arccos\left(\frac{-u}{\lambda}\right) \tag{3.1}$$

The value of this maximum angle of attack is, therefore:

$$\alpha = \arctan\left(\frac{\lambda u \sin\left[\arccos\left(\frac{-u}{\lambda}\right)\right]}{\lambda^2 - u^2}\right) \tag{3.2}$$

On the other hand, the maximum and minimum Reynolds numbers are always found at $\theta = 0$ and $\theta = \pi$, where the blade moving velocity is completely aligned with or opposed to the incoming wind velocity, and their values are:

$$Re_{\theta=0} = \frac{\rho c V_\infty}{\mu}(\lambda + u) \tag{3.3}$$

$$Re_{\theta=\pi} = \frac{\rho c V_\infty}{\mu}(\lambda - u) \tag{3.4}$$

Setting $u = 1$ into the equations, the limits for the angles of attack and Reynolds numbers required for the analysis are obtained:

$$\alpha = \arctan\left(\frac{\lambda \sin\left[\arccos\left(\frac{-1}{\lambda}\right)\right]}{\lambda^2 - 1}\right) \tag{3.5}$$

$$Re_{\theta=0,\pi} = \frac{\rho c V_{\infty}}{\mu} (\lambda \pm 1) \tag{3.6}$$

In this work, airfoil data have been generated for all angles of attack (-180 to $180°$) and the following Reynolds numbers: 10000, 20000, 40000, 80000, 160000, 360000, 700000, 1000000, 2000000 and 5000000. Linear interpolation is employed for Reynolds numbers between the generated ones. First of all, some typical 4-digit NACA airfoil families have been selected to obtain insight into the influence of thickness and camber in the performance of a VAWT. Then, other airfoils specially designed for low-Reynolds applications have been selected from the literature to study their suitability for VAWT applications: DU-06-W-200, an airfoil designed in Delft University [45] and that is allegedly supposed to present a good self-starting behavior; NACA 0012H, a modification of the NACA 0012 employed for some Sandia VAWT tests [39]; the Wortmann FX-63-137 airfoil [46], inspired on the liver puffin wing; three Selig airfoils S1020, S1012 and S8037; and two Natural-Laminar-Flow airfoils NLF(1)-0115 and NLF-1015 [47]. The geometry of all these airfoils is depicted in Figure 3.3.

Table 3.1: Families of 4-digit NACA airfoils considered for the study

Thickness	Camber				
	0% c	2% c	4% c	6% c	8% c
12% c	NACA 0012	NACA 2412	NACA 4412	NACA 6412	NACA 8412
15% c	NACA 0015	NACA 2415	NACA 4415	NACA 6415	NACA 8415
18% c	NACA 0018	NACA 2418	NACA 4418	NACA 6418	NACA 8418
21% c	NACA 0021	NACA 2421	NACA 4421	NACA 6421	NACA 8421
25% c	NACA 0025	NACA 2425	NACA 4425	NACA 6425	NACA 8425

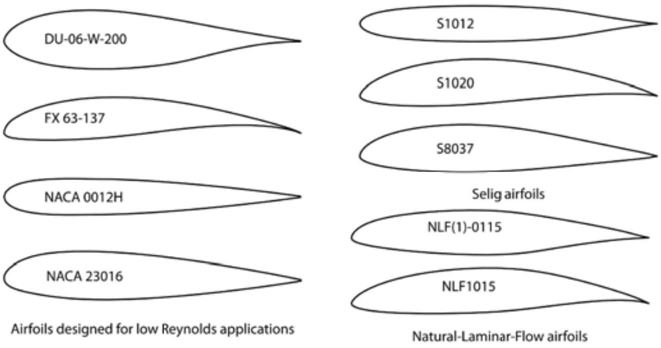

Figure 3.3: Typical airfoils for low-Re applications included in the study

3.2.3. Validation and selection of the final formulation

Before proceeding to the evaluation of the different turbine configurations, results from the four developed models were compared with CFD and experimental results from Raciti Castelli et al. [48], as shown in Figure 3.4. Table 3.2 collects the geometrical characteristics of the VAWT. It may be appreciated that, for low tip-speed ratios, corresponding to lightly-loaded

Table 3.2: Geometrical characteristics of the VAWT from Raciti Castelli et al.[48]

Number of blades N	3
Rotor radius R	0.515 m
Rotor height H	1.45 m
Blade chord c	85.8 mm
Rotor solidity σ	0.5
Airfoil	NACA 0021
Tip-speed ratio λ	0 to 4

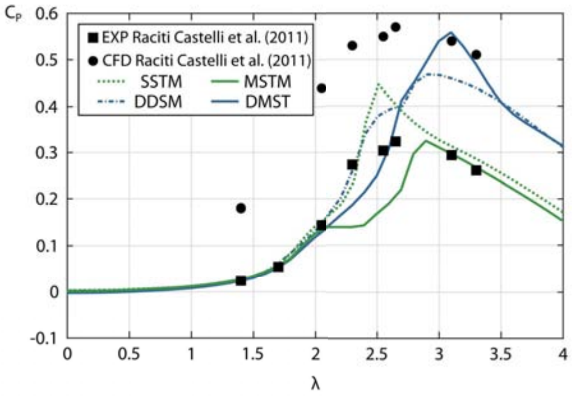

Figure 3.4: Comparison of streamtube models with CFD and experimental results from Raciti Castelli et al. [48]

blades, there is a very good correspondence between all the models and the experimental results. However, at higher tip-speed ratios, there is a certain discrepancy between the models that employ just a streamtube (SSTM and DDSM) and the models that consider multiple streamtubes (MSTM and DMST). This may be attributed to more non-uniform velocity distributions associated to the higher induction produced by the turbine on the flow, which are better estimated by the models that employ multiple streamtubes. It must be noticed that this turbine has a relatively high solidity (around 0.5), so breakdown of the momentum equation could happen at high tip-speed ratios. In these cases, the introduction or not of the empirical correlations might change the results predicted by the models. Anyway, all the developed models are able to follow the evolution of the C_P curve up to the maximum value and predict reasonably well the tip-speed ratio at which the maximum power coefficient is attained (from the experimental results, it may be observed that this tip-speed ratio lays between 2.5 and 3). The predictions made by streamtube models match even better the experimental values than the CFD results, being the DMST model the most accurate.

In order to validate further the proposed design methodology, a CFD simulation of a straight-bladed VAWT with a lower solidity was performed. CFD tools may be used as a source of data for improving the predictions of lower order models, which are key to industrial design due to their extremely small computational requirements [49]. The geometrical characteristics of this turbine, with a solidity value of 0.24, as well as the mesh generation and numerical solver setup will be detailed in the next Chapter.

As it may be observed in Figure 3.5, the results from the streamtube models and the CFD simulations are much more similar than in the previous validation case, in part due to the reduction of the turbine solidity. In this case, the results from the four models follow almost perfectly the tendency of the simulated curve. Nevertheless, the double disk approach is capable of predicting with greater accuracy the tip-speed ratio at which the peak power coefficient is obtained.

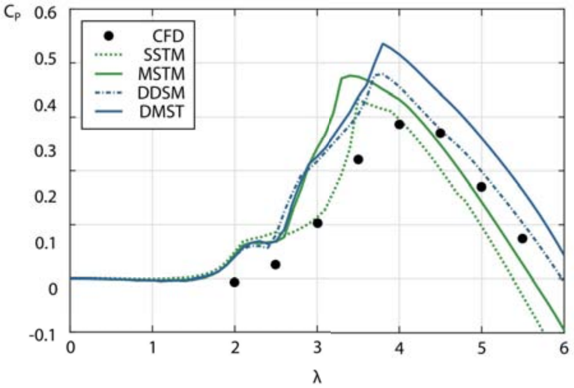

Figure 3.5: Comparison of streamtube models with CFD results

Before deciding which of the four models was the most suitable for the subsequent analyses, the evolution of the flow velocity with the streamwise position along the rotor was compared with the velocities predicted by each model at the actuator disks. In Figure 3.6, which shows the results of this comparison, it may be appreciated that the DMST model is the most accurate one, as the DDSM model underpredicts the velocities at the downstream part of the rotor. Although the SSTM and MSTM models show good agreement with the simulation results, they provide no information about the evolution of the flow velocity as it passes across the rotor. The exact values of the velocity ratio (V/V_∞) for the CFD and streamtube models (crosswise average values) at $\lambda = 4$ may be found in Table 3.3.

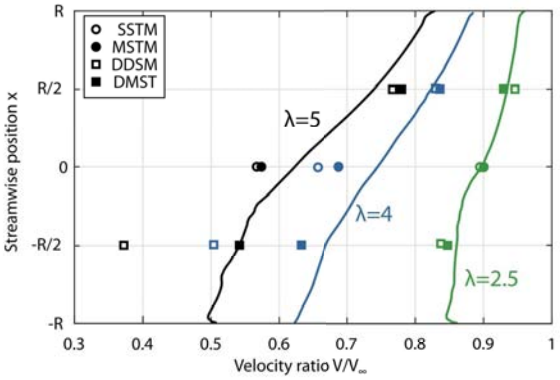

Figure 3.6: Evolution of the flow velocity along the turbine rotor

To analyze the differences between the four models in a deeper level, a preview of the contours

Table 3.3: Non-dimensional throughflow velocity along the streamwise coordinate of the rotor for $\lambda = 4$

Position	$y = R$	$y = R/2$	$y = 0$	$y = -R/2$	$y = -R$
CFD	0.8896	0.8232	0.7438	0.6675	0.6219
SSTM			0.6568		
MSTM			0.6863		
DDSM		0.8307		0.5048	
DMST		0.8354		0.6330	

of vorticity from the CFD simulations is shown in Figure 3.7. These results will be described in detail Chapter 4, still, it may be advanced that the vortices shed by the blades are carried in the streamwise direction, interacting with the blades and other vortices. From the analysis of the figure, the blade path may be divided into four different regions: upwind, downwind, windward and leeward, following the convention introduced in [50]. The flow behavior is noticeably different between the upwind and downwind parts of the rotor, but there are also significant differences between the windward and leeward regions as a consequence of the relative movement of the blade with respect to the streamwise flow direction. This fact may explain why the DMST model is the one that provides the most accurate results, as it considers not just the difference in the velocity deficit between the upwind and downwind parts of the rotor but also between the different azimuthal positions.

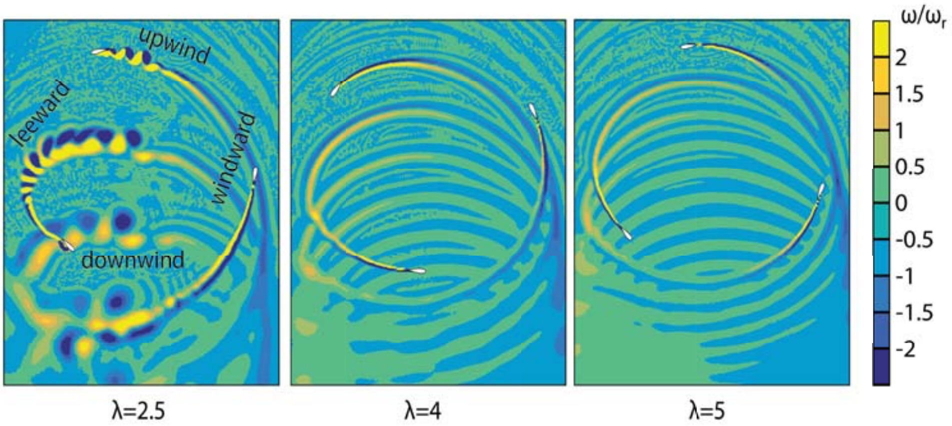

Figure 3.7: Contours of normalized vorticity in the fluid domain close to the VAWT rotor for three tip-speed ratio values

For further insight into the DMST model, Figure 3.8 shows the flow velocity ratio (V/V_∞) along the azimuthal positions of the rotor, comparing the results from the CFD simulations (dashed lines) and the DMST model (solid lines). Apart from the peaks observed in the CFD results as a consequence of the passage of a blade at a particular time, it may be appreciated that the DMST model is capable of predicting the velocity distribution with relatively high accuracy. A last comparison between the CFD results and the DMST model has been performed in Figure 3.9, which shows the evolution of the stream and cross-streamwise forces on the blades as a function of the blade azimuthal position for different tip-speed ratios. The DMST model reproduces the behavior from the CFD simulations with good accuracy. The greatest discrepancies are found for the lowest tip-speed ratio ($\lambda = 2.5$), probably as a consequence of the wakes shed by the blades at this operating condition. Nevertheless, even at this tip-speed ratio, the DMST model follows the tendency of the CFD results, peaking at the same positions.

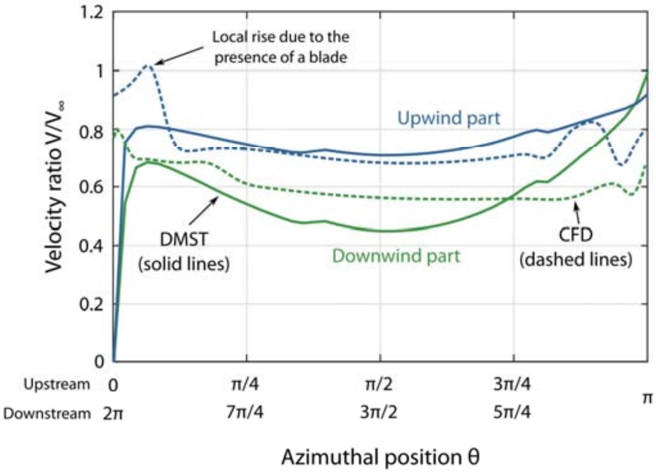

Figure 3.8: Velocity ratio along the rotor azimuthal positions (DMST model - solid lines, CFD - dashed lines)

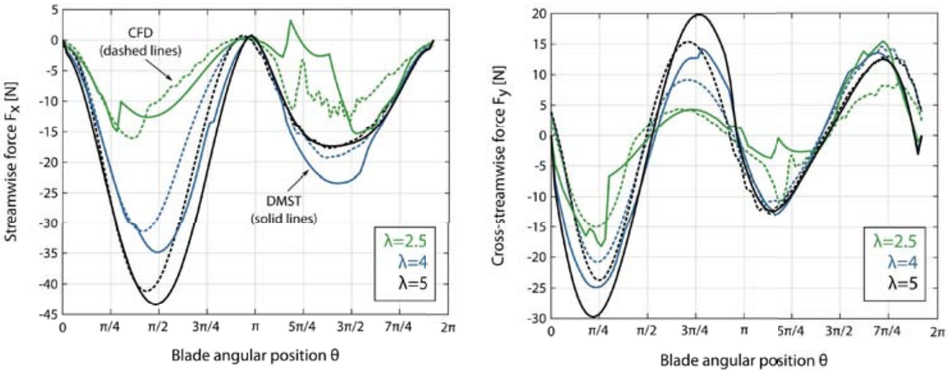

Figure 3.9: Stream and cross-streamwise forces on the blades for different tip-speed ratio values (DMST model - solid lines, CFD - dashed lines)

To conclude, the DMST model has shown to predict accurately the aerodynamic variables of interest for the design of a VAWT: power coefficient as a function of the tip-speed ratio, evolution of the wind velocity throughout the rotor and forces exerted by the wind on the turbine blades. However, care must be taken if the design solidity or tip-speed ratio value is relatively high, as problems could arise when trying to reach convergence.

3.2.4. Comparison with other benchmarks

After validating the model and before proceeding to evaluate the effect of the influencing parameters in the turbine performance, a benchmark with results from other authors has been developed with the aim of increasing the reliability of the model. Momentum models (Paraschivoiu et al. [51], Ahmadi et al.[2], Jain et al. [16]), CFD simulations (Bedon et al. [6], Gosselin et al. [10]) and experiments (Kjellin et al. [52], Eboibi et al. [15]) have been included. Figure 3.10 shows the comparison of the developed model with the developed benchmark. There is a good agreement of the C_P values predicted, being possible to attribute the deviations in the results to the simplicity of the developed model (no dynamic stall effects, strut losses, streamtube expansion, rotor tower and wake effects considered). Nevertheless, it must be noticed that this model provides the whole $C_P - \lambda$ curve in a time of around five minutes. Therefore, and considering the good ratio between model accuracy and the computation time, it may be concluded that the developed model is suitable for the quick evaluation of different prospective VAWT designs, as well as the analysis of the influencing variables on the performance of a VAWT in order to get insight into the optimum solidity and best airfoil characteristics.

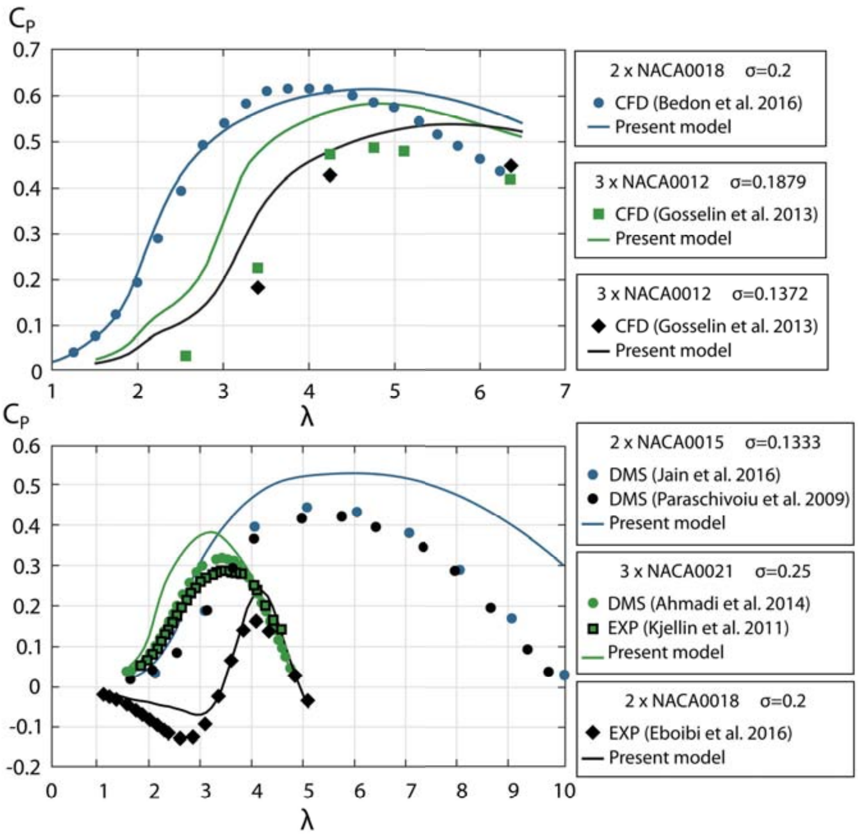

Figure 3.10: Comparison of the developed model with CFD benchmarks

3.3. Analysis of the influencing variables in VAWT performance

After validating the model, 70 different VAWT configurations have been tested in order to study the influence of the main parameters that affect the performance of a VAWT: the rotor solidity, the Reynolds number and the airfoil geometry. To ensure consistency with the previous section, the airfoil chosen to evaluate the influence of solidity and Reynolds number is the DU-06-W-200. Then, the different airfoil geometries selected for the study have been evaluated with a constant value of solidity. Finally, two optimized designs for medium and low wind speeds are proposed.

3.3.1. Influence of solidity

The effect of changing the turbine solidity on its performance is shown in Figure 3.11. As explained before, although it may seem shocking to have surpassed the Betz limit (16/27), in the case of the DMST model the maximum theoretical power coefficient is 16/25 (0.64) [36]. Regarding the values obtained, the power coefficient peaks at around a solidity of 0.5 and a tip-speed ratio of 2.7. Nevertheless, the band at which the power coefficient increases becomes narrower with the increase of solidity. An optimal solidity range may be established from 0.2 to 0.5, in agreement with the results from [11] and [15]. Hence, the range of optimal solidity values proposed by [12] and [2] should be reduced, discarding values higher than 0.5 as they only lead to an increase in turbine loading without increasing the power extracted from the air. Finally, as the difference in the maximum power coefficients for solidity values of 1/2 and 1/3 is relatively small, the value of 1/3 has been chosen as the optimum solidity for the subsequent analyses. This lower solidity value, besides presenting a wider high-efficiency operating band, will lead to lower induction values, so it is less likely to cause breakdown of the momentum equation and lead to inaccurate results.

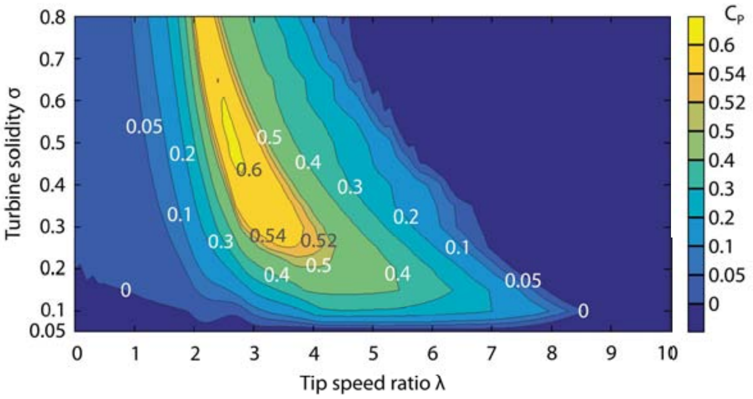

Figure 3.11: Influence of solidity in the performance of a VAWT

3.3.2. Influence of the blade Reynolds number

The blade Reynolds number changes with the azimuthal blade position and, for a given λ, there are two main parameters that affect the turbine blade Reynolds number: the freestream velocity and the turbine size (rotor radius).

In Figure 3.12, top, the influence of the incoming freestream velocity in the performance of a VAWT with solidity $1/3$ and radius R =1 m is shown. There is an identifiable region below a threshold velocity (cut-in wind speed) where the VAWT is unable to generate power. This result, in agreement with the observed behavior in VAWTs [9], [53], highlights the need of performing this kind of parametric study before proposing a VAWT design. With the increase in the freestream velocity, so do the blade Reynolds number and the power coefficient increase. Nevertheless, from a certain velocity (Reynolds number), the turbine performance does not exhibit a significant further increase. Furthermore, the forces on the blades become greater, up to a point that the structural integrity of the blades becomes endangered. This is the reason behind defining a cut-out wind speed that prevents damage of the turbine structure. Finally, the behavior of some VAWTs that self-start after a wind gust may be explained with help of Figure 3.12. If a certain turbine is unable to start working at steady wind conditions at a particular $\lambda_1 < 1$ and there is a sudden increase in the wind velocity, the turbine will rotate faster ($\lambda_1' < 1$). Then, once the incoming wind speed returns to its steady value while the turbine keeps rotating at the same speed, the working point of the turbine will shift towards a $\lambda_3 > 1$ and start producing power. An analog reasoning may be followed for the case of a sudden drop in the incoming wind speed. In this case, the turbine will keep rotating at the same speed for a while, shifting towards a $\lambda_2 > 1$, that will be kept once the original incoming wind speed is recovered.

On the other hand, if the wind incoming velocity is fixed, the other parameter that determines the blade Reynolds number is the turbine size (i.e. the turbine radius). In Figure 3.12, bottom, the effect of the rotor size in the performance of a turbine with solidity $1/3$ and a fixed incoming wind velocity V_∞ =9 m/s is shown. A greater radius corresponds directly to greater Reynolds numbers for the same tip-speed ratio and wind incoming velocity, thus increasing the performance of the turbine. Hence, a larger rotor is more likely to self-start than a smaller one. In the particular case depicted in Figure 3.12, a rotor radius lower than 0.25 m results in no power generation at all. This effect might help to discard certain turbine sizes before fabricating a prototype. In addition, it may explain the difficulty suffered by certain small-scale models to self-start and generate power as a consequence of a wide dead band. Finally, another idea that may be drawn from these results is that, even though a small-scale model could fail to generate useful power, a full-scale model with the same geometrical proportions could be able to work efficiently.

3.3.3. Influence of the airfoil geometry

As previously introduced, the airfoil geometry is one of the most important contributors to the performance of a VAWT. The main characteristics of an airfoil geometry are the airfoil thickness and camber, so a first analysis of a series of typical 4-digit NACA airfoils will be presented to obtain insight into the influence of these two characteristics.

Influence of thickness

The influence of airfoil thickness in the performance of a VAWT with symmetrical NACA00xx blades is shown in Figure 3.13. Thicker airfoils help starting the turbine and attaining higher power coefficients; nevertheless, increasing airfoil thickness past a certain value becomes detrimental to the turbine performance, possibly due to the increase in drag forces on the blade. Drag forces may help the turbine to start rotating, but at nominal speeds they reduce the amount

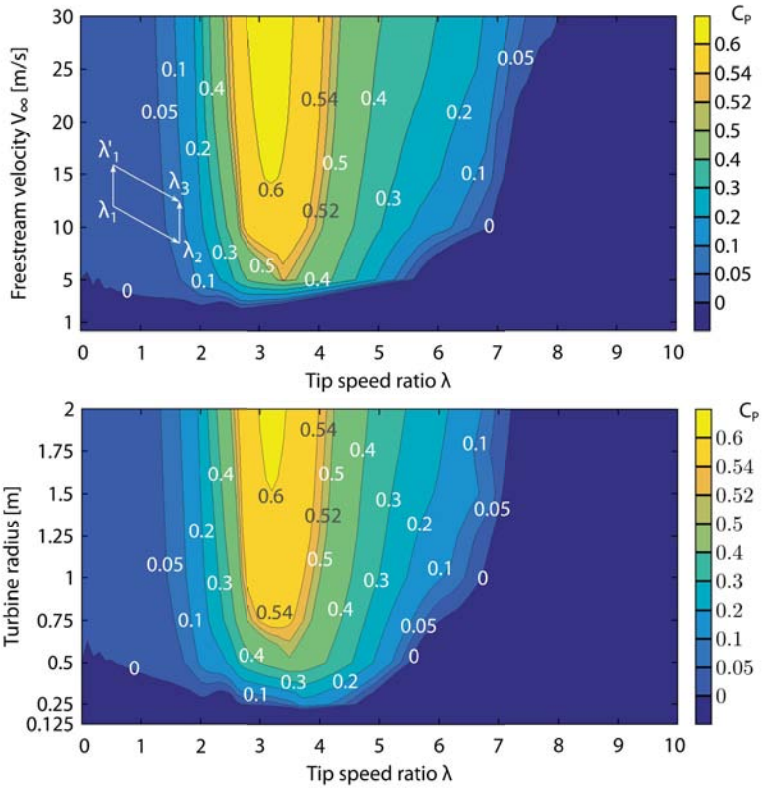

Figure 3.12: Influence of the freestream velocity and turbine radius in the performance of a VAWT

of power captured from the wind. To summarize, the most suitable airfoil would be as thin as possible, but allowing for self-starting and the development of a wide high-efficiency band. Thickness values between 15% and 21% seem convincing, in agreement with the results from Goselin et al. [10], who found NACA 0015 to be optimal compared to thinner and thicker airfoils of the same family.

Influence of camber

Figure 3.14 shows the results of adding camber to a NACA 0018 airfoil in the performance of a VAWT. When camber is added to the airfoil, the upwind part of the turbine benefits from higher lift at smaller angles of attack, at the cost of a worse performance at the downwind part. As the energy available in the wind is higher in the upwind part, adding a small amount of camber to the blade enhances the turbine performance, as stated by Jain and Abhishek [26] and as shown in Figure 3.14. However, too much camber results in a worse performance, as a result of the abrupt decrease in the energy extraction in the downwind part of the turbine. In Figure 3.14, for 6% camber, the maximum power coefficient reached is below 0.5, confirming that too unsymmetrical blades reach reduced peak efficiencies compared to conventional symmetrical airfoils [22]. Hence, the selection of the airfoil for a VAWT should lean towards symmetrical or

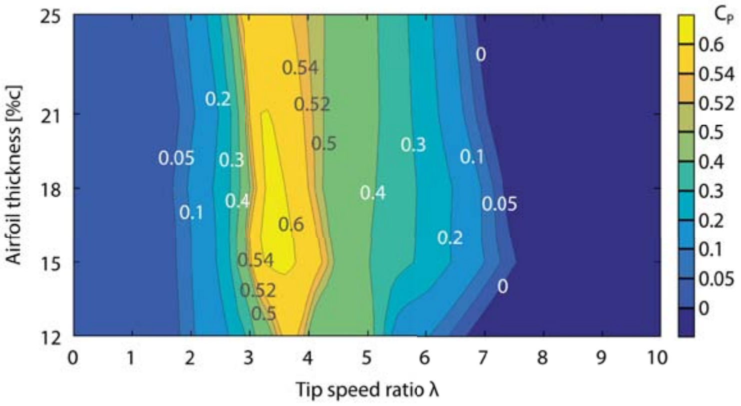

Figure 3.13: Influence of airfoil thickness in the performance of a VAWT with NACA blades

low-cambered airfoils with less than 3% camber, as those will produce the highest power output (as found by [28]). Airfoils with higher camber values would be justified for small VAWTs, in order to help them self-start due to the increase in the lift forces in the upwind part of the turbine.

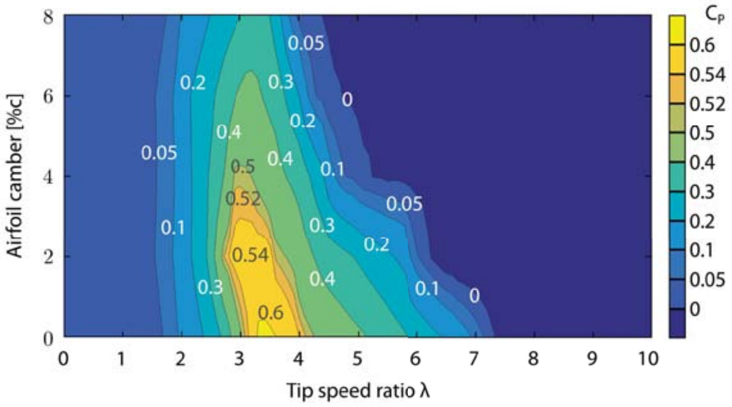

Figure 3.14: Influence of airfoil camber in the performance of a VAWT with NACA blades

Performance of typical airfoils for low Reynolds applications

The results from the analysis of the selected airfoils specially designed for low Reynolds applications are shown in Figure 3.15.

The Natural-Laminar-Flow airfoils studied present a worse behavior than the other airfoils. The NLF(1)-0115 shows a wide high performance band that could help the electronic regulation of the turbine, but the peak power coefficient is around 0.4. On the other hand, the high camber of the NLF1015 airfoil prevents it from reaching a good performance.

Regarding the Selig airfoils studied, quite different behaviors were found. In Figure 3.15, it may be appreciated that the S1012 shows an excellent performance when compared to the other two. The S1020 presents a steeper $C_P - \lambda$ curve as a consequence of the higher camber, but at the cost of peaking at a lower power coefficient value. Finally, the addition of a slight amount of camber in the S8037 airfoil results in a a steeper $C_P - \lambda$ curve, related to a better self-starting behavior. Additionally, as the peak performance is not much lower than for the S1012 airfoil, this airfoil could represent a good choice for small-scale VAWTs.

Finally, from the last set of airfoils, the FX 63-137 airfoil is unable to reach power coefficients higher than 0.37 due to its high camber. Nevertheless, this airfoil was designed for flight applications, so it was not expected to work at such high angles of attack as the ones that may be found in VAWT applications [46]. NACA 0012H and NACA 23016 seem excellent candidates for VAWT applications, as it may be appreciated in Figure 3.15 from the predicted power curves. However, the DU-06-W-200 airfoil outperforms the rest of the studied airfoils. This airfoil, based on an optimization that stems from a NACA 0018 airfoil by adding a small amount of camber, has an enhanced self-starting capability, while the peak efficiency is not heavily affected. Comparing all the results from this study, the DU-06-W-200 airfoil seems the best choice among the rest of the airfoils in terms of performance.

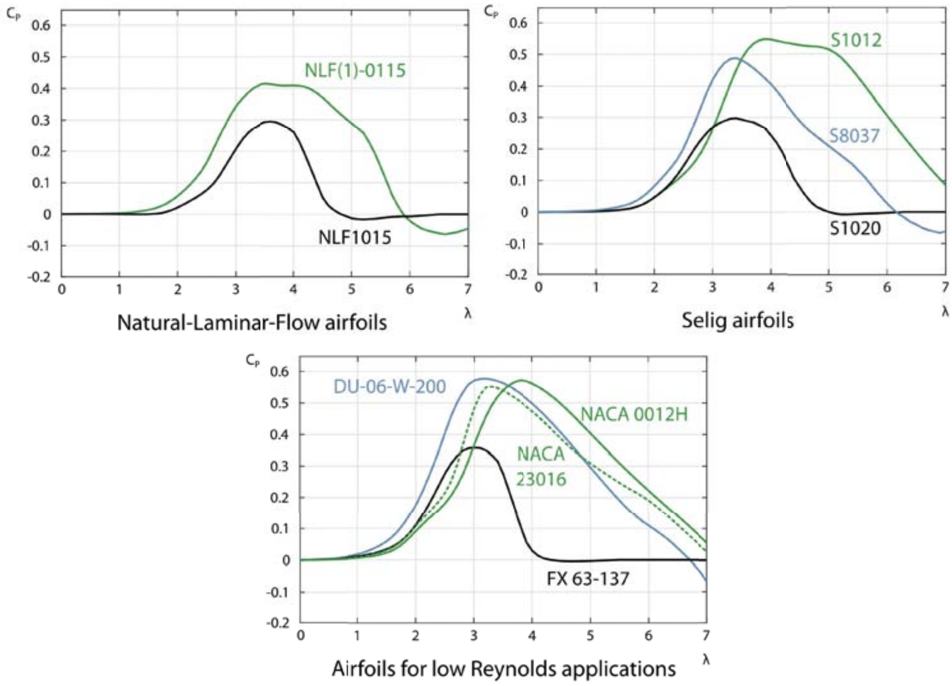

Figure 3.15: Performance curves of a VAWT with different airfoil geometries

3.3.4. Application of the model to a case study: VAWTs for low and medium wind speeds

The model developed in this chapter allows the proposal of VAWT optimized designs. Following the previous results, two turbine designs for low and medium wind speeds may be proposed, both following the $Cp - \lambda$ curve of the DU-06-W-200 airfoil. Both designs are collected in Table 3.4: the design for a medium wind speed (9 m/s) provides a prospective power output of 1.5 kW, whereas the design for a low wind speed (4.5 m/s) has a prospective power of 1 kW.

Table 3.4: Characteristics of the proposed VAWT designs

Wind speed	Medium	Low
Number of blades N	3	3
Rotor radius R	1 m	3 m
Rotor height H	3 m	5 m
Blade chord c	111 mm	333 mm
Rotor solidity σ	1/3	1/3
Airfoil	DU-06-W-200	DU-06-W-200
Nominal wind speed	9 m/s	4.5 m/s
Rated power	1.5 kW	1 kW
Maximum power coefficient	0.5798	0.5996

3.4. Conclusions

In this chapter, the convenience of employing low order models such as streamtube models at early design stages of VAWTs has been confirmed, as they present a high ratio between accuracy and computational cost. Four streamtube models have been implemented in MATLAB ® with self-made codes. The lack of available airfoil data for streamtube models has been covered by generating a database of lift and drag coefficients for 34 airfoils using the software XFOIL. The combination of the codes and the database has resulted in a practical and cost-effective tool for the quick comparison of VAWT designs, with just a few minutes of calculation time to obtain the whole power curve of the turbine.

After validating the model with numerical and experimental results, the main parameters influencing the performance of a VAWT have been analyzed: turbine solidity, blade Reynolds number and airfoil geometry. As there is still no consensus neither on the optimal solidity for a VAWT nor on the turbine size or the airfoil geometry chosen for the blades, it has been intended to assess these research gaps. Based on the results obtained, a more reduced range of optimal solidity values (0.2-0.5) has been proposed. The study of the influence of the blade Reynolds number has given insight into VAWT self-starting and power generation. Concerning the airfoil for the turbine blades, it was found that optimal airfoils were as thin as possible and nearly symmetrical or low-cambered (below 3% camber), allowing for self-starting and the development of a wide high-efficiency band. To conclude, some airfoils specially designed for low-Reynolds applications were analyzed using the developed model, finding DU-06-W-200, S1012, NACA0012H and NACA 23016 as the most suitable airfoils. Finally, two VAWT designs for low (4.5 m/s) and medium (9 m/s) wind speeds are proposed, illustrating the potential of the developed tool.

However, care must be taken when modeling turbines with high solidities due to the breakdown of the momentum equation. In addition, the formulation of the model does not account for streamtube expansion and rotor tower and blade wake effects, so a complete characterization of the flow field is not possible. Nevertheless, this tool is able to predict the performance of a VAWT in calculation times in the order of a few minutes, helping designers to propose different designs and predict their performance almost instantaneously. This fact made possible analyzing 70 different configurations within the work presented in this chapter.

References

[1] A. Meana-Fernández, I. Solís-Gallego, J.M. Fernández Oro, K.M. Argüelles Díaz, and S. Velarde-Suárez, *Parametrical evaluation of the aerodynamic performance of vertical axis wind turbines for the proposal of optimized designs,* Energy **147**, 504 (2018).

[2] M. Ahmadi-Baloutaki, R. Carriveau, and D.-K. Ting, *Straight-bladed vertical axis wind turbine rotor design guide based on aerodynamic performance and loading analysis,* Proceedings of the Institution of Mechanical Engineers, Part A: Journal of Power and Energy **228**, 742 (2014).

[3] M. A. Akbar and V.Mustafa, *A new approach for optimization of Vertical Axis Wind Turbines,* Journal of Wind Engineering and Industrial Aerodynamics **153**, 34 (2016).

[4] J. Thé and H. Yu, *A critical review on the simulations of wind turbine aerodynamics focusing on hybrid RANS-LES methods,* Energy **138**, 257 (2017).

[5] J. Chen, L. Chen, H. Xu, H. Yang, C. Ye, and D. Liu, *Performance improvement of a vertical axis wind turbine by comprehensive assessment of an airfoil family,* Energy **114**, 318 (2016).

[6] G. Bedon, S. D. Betta, and E. Benini, *Performance-optimized airfoil for Darrieus wind turbines,* Renewable Energy **94**, 328 (2016).

[7] J. Manwell, J. McGowan, and A. Rogers, *Wind Energy Explained* (John Wiley & Sons Ltd., West Sussex, England, 2002).

[8] A. Sengupta, A. Biswas, and R. Gupta, *Studies of some high solidity symmetrical and unsymmetrical blade H-Darrieus rotors with respect to starting characteristics, dynamic performances and flow physics in low wind streams,* Renewable Energy **93**, 536 (2016).

[9] I. Paraschivoiu, *Wind Turbine Design: With Emphasis on Darrieus Concept* (Presses internationales Polytechnique, Canada, 2002).

[10] R. Gosselin, G. Dumas, and M. Boudreau, *Parametric study of H-Darrieus vertical-axis turbines using uRANS simulations,* in *21st Annual Conference of the CFD Society of Canada* (Sherbrooke, Canada, 2013) pp. 1–16.

[11] P. Sabaeifard, H. Razzaghi, and A. Forouzandeh, *Determination of Vertical Axis Wind Turbines Optimal Configuration through CFD Simulations,* in *IPCBEE vol.28* (IACSIT Press, Singapore, 2012) pp. 109–113.

[12] M. Mohamed, *Performance investigation of H-rotor Darrieus turbine with new airfoil shapes,* Energy **47**, 522 (2012).

[13] M. Singh, A. Biswas, and R. Mishra, *Investigation of self-starting and high rotor solidity on the performance of a three S1210 blade H-type Darrieus rotor,* Renewable Energy **76**, 381 (2015).

[14] D. Gang and W. Kau, *Unsteady Flow Numerical Simulation of Vertical Axis Wind Turbine,* Procedia Engineering **99**, 734 (2015).

[15] O. Eboibi, L. Danao, and R. Howell, *Experimental investigation of the influence of solidity on the performance and flow field aerodynamics of vertical axis wind turbines at low Reynolds numbers,* Renewable Energy **92**, 474 (2016).

[16] P. Jain and A. Abhishek, *Performance prediction and fundamental understanding of small scale vertical axis wind turbine with variable amplitude blade pitching,* Renewable Energy **97**, 97 (2016).

[17] Q. Li, T. Maeda, Y. Kamada, J. Murata, K. Shimizu, T. Ogasawara, A. Nakai, and T. Kasuya, *Effect of solidity on aerodynamic forces around straight-bladed vertical axis wind turbine by wind tunnel experiments (depending on number of blades),* Renewable Energy **96**, 928 (2016).

[18] Q. Li, T. Maeda, Y. Kamada, K. Shimizu, T. Ogasawara, A. Nakai, and T. Kasuya, *Effect of rotor aspect ratio and solidity on a straight-bladed vertical axis wind turbine in three-dimensional analysis by the panel method,* Energy **121**, 1 (2017).

[19] A. Subramanian, S. Yogesh, H. Sivanandan, A. Giri, M. Vasudevan, V. Mugundhan, and R. Velamati, *Effect of airfoil and solidity on performance of small scale vertical axis wind turbine using three dimensional CFD model,* Energy **133**, 179 (2017).

[20] M. Ghasemian and Z. A. A. Sedaghat, *A review on computational fluid dynamic simulation techniques for Darrieus vertical axis wind turbines,* Energy Conversion and Management **149**, 87 (2017).

[21] Y.-T. Lee and H.-C. Lim, *Numerical study of the aerodynamic performance of a 500 W Darrieus-type vertical-axis wind turbine,* Renewable Energy **83**, 407 (2015).

[22] H. Beri and Y. Yao, *Effect of camber airfoil on self starting of a vertical axis wind turbine,* Journal of Environmental Science and Technology **4**, 302 (2011).

[23] A. Bianchini, G. Ferrara, and L. Ferrari, *Design guidelines for H-Darrieus wind turbines: Optimization of the annual energy yield,* Energy Conversion and Management **89**, 690 (2015).

[24] C.-C. Chen and C.-H. Kuo, *Effects of pitch angle and blade camber on flow characteristics and performance of small-size Darrieus VAWT,* Journal of Visualization **16**, 65 (2013).

[25] M. El-Samanoudy, A. Ghorab, and S. Youssef, *Effect of some design parameters on the performance of a Giromill vertical axis wind turbine,* Ain Shams Engineering Journal **1**, 85 (2010).

[26] M. Jafaryar, R. Kamrani, M. Gorji-Bandpy, M. Hatami, and D. Ganji, *Numerical optimization of the asymmetric blades mounted on a vertical axis cross-flow wind turbine,* International Communications in Heat and Mass Transfer **70**, 93 (2016).

[27] S. Qamar and I. Janajreh, *A comprehensive analysis of solidity for cambered darrieus VAWTs,* International Journal of Hydrogen Energy **42**, 19420 (2017).

[28] S. Qamar and I. Janajreh, *Investigation of Effect of Cambered Blades on Darrieus VAWTs,* Energy Procedia **105**, 537 (2017).

[29] H. Glauert, *The Elements of Aerofoil and Airscrew Theory*, 2nd ed. (Cambridge University Press, Canada, 1947).

[30] R. Templin, *Aerodynamic Performance Theory for the NRC Vertical-Axis Wind Turbine*, Tech. Rep. (N.A.E. Report LTR-LA-160, 1974).

[31] J. Strickland, *The Darrieus Turbine: A Performance Prediction Model Using Multiple Streamtube*, Tech. Rep. (Sandia Laboratories Report SAND75-0431, 1974).

[32] M. J. Buhl, *A New Empirical Relationship between Thrust Coefficient and Induction Factor for the Turbulent Windmill State*, Tech. Rep. (National Renewable Energy Laboratory, Golden, Colorado, USA, 2005).

[33] D. Eggleston and F. Stoddard, *Wind turbine Engineering Design* (Van Nostrand Reinhold, New York, NY, USA, 1987) pp. 30–35.

[34] D. Spera, *Wind Turbine Technology* (ASME Press, New York, USA, 1994).

[35] T. Burton, D. Sharpe, N. Jenkins, and E. Bossanyi, *Wind Energy Handbook* (John Wiley & Sons Ltd., West Sussex, England, 2011).

[36] B. Newman, *Multiple actuator-disk theory for wind turbines,* Journal of Wind Engineering and Industrial Aerodynamics **24**, 215 (1986).

[37] D. Gorelov, *Analogy between a flapping wing and a wind turbine with a vertical axis of revolution,* Journal of Applied Mechanics and Technical Physics **50**, 297 (2009).

[38] R. Vennell, *Exceeding the Betz limit with tidal turbines,* Renewable Energy **55**, 277 (2013).

[39] R. Sheldal and P. Klimas, *Aerodynamic Characteristics of Seven Symmetrical Airfoil Sections Through 180-Degree Angle of Attack for Use in Aerodynamic Analysis of Vertical Axis Wind Turbines, Tech. Rep. SAND80-2114*, Tech. Rep. (Sandia National Laboratories, Albuquerque, NM, USA, 1981).

[40] R. Eppler, *Turbulent airfoils for general aviation,* Journal of Aircraft **15**, 93 (1978).

[41] L. Lazauskas, *Three pitch control systems for vertical axis wind turbines compared,* Wind Engineering **16**, 269 (1992).

[42] R. Bogateanu, A. Dumitrache, H. Dumitrescu, and C. Stoica, *Reynolds Number Effects on the Aerodynamic Performance of Small VAWTs,* U.P.B. Sci. Bull., Series D **76**, 25 (2014).

[43] M. Drela, *Xfoil: An analysis and design system for low reynolds number airfoils,* in *Proceedings of the Conference Notre Dame* (Springer-Verlag Berlin Heidelberg, Indiana, USA, 1989) pp. 1–12.

[44] J. Manwell, J. McGowan, and A. Rogers, *Wind Energy Explained: Theory, Design and Application* (John Wiley and Sons, Ltd, Chichester, UK, 2009).

[45] M. Claessens, *The Design and Testing of Airfoils for Application in Small Vertical Axis Wind Turbines*, Master's thesis (2006).

[46] D. Althaus and F. Wortmann, *Stuttgarter Profilkatalog 1: Messergergebnisse aus dem Laminarwindkanal des Instituts fur Aerodynamik und Gasdynamik der Universitat Stuttgart* (Vieweg Verlag, Braunschweig, Wiesbaden, Germany, 1981).

[47] *UIUC Airfoil Data Site* ((accessed March 27, 2017)), http://m-selig.ae.illinois.edu/ads/coord_database.html.

[48] M.Raciti Castelli, A. Englaro, and E. Benini, *The Darrieus wind turbine: Proposal for a new performance prediction model based on CFD,* Energy **36**, 4919 (2011).

[49] F. Balduzzi, J. Drofelnik, A. Bianchini, G. Ferrara, L. Ferrari, and M. S. Campobasso, *Darrieus wind turbine blade unsteady aerodynamics: a threedimensional Navier-Stokes CFD assessment,* Energy **128**, 550 (2017).

[50] G. Tescione, D. Ragni, C. He, C. Ferreira, and G. van Bussel, *Near wake flow analysis of a vertical axis wind turbine by stereoscopic particle image velocimetry,* Renewable Energy **70**, 47 (2014).

[51] I. Paraschivoiu, O. Trifu, and F. Saeed, *H-Darrieus wind turbine with blade pitch control,* International Journal of Rotating Machinery **2009**, 1 (2009).

[52] J. Kjellin, F. Bulow, S. Eriksson, P. Deglaire, M. Leijon, and H. Bernhoff, *Power coefficient measurement on a 12 KW straight bladed vertical axis wind turbine,* Renewable Energy **36**, 3050 (2011).

[53] M. Bausas and L. Danao, *The aerodynamics of a camber-bladed vertical axis wind turbine in unsteady wind,* Energy **93**, 1155 (2015).

4

CFD methodology for the analysis of VAWTs and VAWT airfoils

What is real? How do you define real?
If you're talking about what you can feel,
what you can smell, what you can taste and see,
then real is simply electrical signals interpreted by your brain.

Morpheus, The Matrix (1999)

A machine is different from a person. Hence, they think differently.
The interesting question is, just because something, uh...
thinks differently from you, does that mean it's not thinking?

Alan Turing, The Imitation Game (2014)

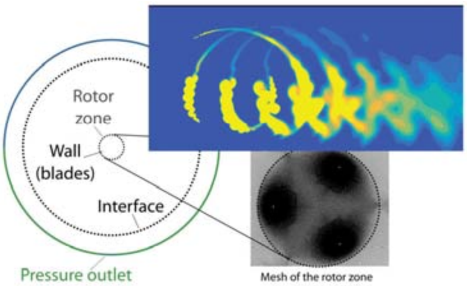

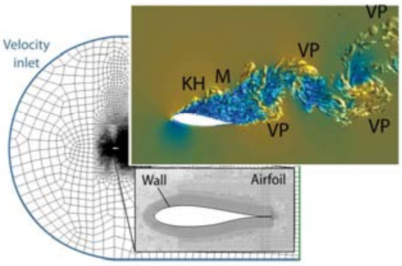

Parts of this chapter have been published in Engineering Applications of Computational Fluid Mechanics **13**, (2019) [1] and Energies **12**, (2019) [2].

IN this chapter, the focus is set on Computational Fluid Dynamics (CFD) models, as they present better accuracy levels than analytical methodologies and are able to provide more details into the developed flow field. Although experimental tests would be always desirable, the complete description of the flow field requires exhaustive measurement campaigns. Therefore, at turbine design stages, the potential of CFD simulations to obtain a complete picture of the flow field represents a great advantage. The first section of this chapter presents a CFD methodology for the 2D analysis of VAWTs, focusing on obtaining clear guidelines for the correct simulation of this type of turbines.

On the other hand, the airfoil used to build the blades of a turbine determines the aerodynamic forces developed on its surface and hence the amount of energy that may be extracted from the wind. Therefore, it was decided to investigate at a deeper level the numerical simulation of a typical VAWT airfoil (DU-06-W-200), comparing different turbulence models. The second section of this chapter focuses on a methodology for the numerical simulation of the flow around typical VAWT airfoils.

4.1. CFD methodology for the analysis of VAWTs

In this section, a methodology for the CFD simulation of VAWTs is presented. The applicability of the Richardson extrapolation method to assess numerical convergence has been studied for several working points in the useful range of the power curve of a VAWT. A 2D domain of the rotor has been simulated, monitoring the turbine power coefficient as the convergence parameter. This methodology has proven to a be straightforward procedure to assess convergence of VAWT simulations. Additionally, guidelines regarding the required mesh and temporal discretization levels are provided. Once the simulations have been validated, the flow field is analyzed, revealing two main vortex shedding mechanisms in the rotor and providing insight into the loss of performance of a VAWT when working at off-design conditions.

4.1.1. Introduction and research gaps addressed

When performing CFD analyses, sometimes there is a lack of verification and validation of the employed numerical codes. However, without a proper assessment of mesh and temporal numerical convergence, it is difficult to trust the validity of the solutions obtained.

In the literature, different procedures to verify the validity of CFD simulations may be found. The typically preferred solution is the validation by comparison of the numerical results with experimental ones. Sui et al. [3] studied the transitional effect on a turbulence model for a wind turbine blade and Lee et al. [4] and Li et al. [5] studied the performance of a VAWT, all of them validating their simulations with experimental results.Yang et al. [6] validated their study of tip vortex shedding from a VAWT with experiments as well. Lam and Peng [7] validated their 2D and 3D simulations to study the wake of a VAWT with PIV measurements, whereas Abdalrahman et al. [8] compared their results with existing CFD and experimental benchmarks to validate their model for the study of the effect of the blade pitch angle on the performance of a VAWT.

Another procedure to assess the validity of the simulations is the study of numerical convergence. This procedure is typically performed by refining the mesh until the solution no longer changes. Although this refinement is performed by several authors in the literature, there are discrepancies that sometimes result in an unnecessary waste of numerical resources.

Bhargar et al. [9] used two different meshes and two time step sizes to study the influence of fluctuating wind conditions on a VAWT. Li et al [10] studied the convergence of their simulations for the point of maximum power coefficient of the turbine with two different meshes as well. Bianchini et al. [11] also used two meshes, but refining the grid only in the rotating part of the domain. Chen et al. [12] analyzed a VAWT at its design point using three meshes and comparing their results with simulations from other authors. Chen and Lian [13] used three meshes as well to investigate the vortex dynamics in a VAWT. Meng et al. [14] also employed three meshes for the simulation of an offshore VAWT. Make and Vaz [15] analyzed the scaling effects on offshore wind turbines with five different meshes. Balduzzi et al. [16] also used five different meshes, with ten different time step sizes, to propose dimensionless numbers for the assessment of mesh and temporal requirements for the CFD simulation of VAWTs. Jin et al. [17] used seven different meshes to verify grid independence. Lin et al. [18] also used seven different levels of refinement near the wall region of the blades to study the effect of modifications in the blade trailing edge on the performance of a VAWT. Finally, Wang et al. [19] recently studied the capacity of wind concentration over a roof using eight different meshes.

Finally, some authors combine the verification of grid independence and the validation with experimental results. Subramanian et al. [20] used two different meshes and time step sizes and validated their results experimentally. Wekesa et al. [21] studied the effect of turbulence on the aerodynamic performance of a VAWT, using two meshes for testing grid independence and validating the simulations with their own experiments. Lei et al. [22] refined the grid close to the blades, generating three meshes and using the grid with the medium refinement because its results resembled more the experimental results. Qamar and Janajreh [23] used three 2D VAWT meshes for the grid independence study and validated their simulations with experimental results. Tian et al. [24] used three meshes and validated experimentally the performance of a VAWT in the wake of moving vehicles. Réthoré et al. [25] verified and validated an actuator disk model for wind turbines using four different grid levels and validating the results experimentally. Marinić-Kragić et al. [26] performed 40 mesh modifications based on the combinations of different element sizing values along the blade and near the trailing edge. Then, after employing six different time step sizes, they validated their results experimentally. Finally, Rezaeiha et al. [27], [28] studied the effect of the shaft on the performance of a VAWT with three grids, validating their results experimentally.

As remarked by Lockard [29] and shown by Vassberg and Jameson [30], it is not unusual to find inconsistent and somewhat disappointing convergence properties on CFD codes. In this context, grid convergence analyses based on the Richardson extrapolation method have been continuously used in different kinds of fluid dynamics related problems [31], [32], [33], [34]. Even some studies applying this methodology to the nominal working point of vertical axis wind turbines may be found in the literature [27], [35], [36], [37]. Nevertheless, the wide operational ranges of a VAWT require the simulation of different tip-speed ratio (λ) values, so it becomes difficult to accept that verifying and validating the numerical code for just the nominal λ is enough.

As it may be appreciated in the previous paragraphs, there is still a clear research gap with respect to the mesh and temporal requirements for the proper simulation of a VAWT, regardless of the availability (or not) of experimental data. Additionally, a straightforward procedure to assess numerical convergence in VAWT simulations would be useful for future research.

4.1.2. Numerical Methodology

VAWT geometry, computational domain and mesh

A 3-bladed low-solidity VAWT with DU 06-W-200 airfoils with a radius of $0.5\ m$ was simulated in a 2D domain. The details of the turbine, in line with optimum parameters reported in the literature [38], are presented in Figure 4.1. Due to the great number of cells required to model a full 3D turbine, most of the analysis in the literature are performed using 2D simulations. The main tridimensional aerodynamic effects are the blade tip effects, detrimental to the turbine performance, but with a high enough turbine aspect ratio (height/radius), a 2D simulation of the turbine mid-plane seems a reasonable choice for the scope of this work.

A range of tip-speed ratio value from 2 to 5.5 has been selected to compare the results at the nominal working point ($\lambda = 4$) with two offset points, one in the dynamic stall region ($\lambda = 2.5$) and other with the turbine producing a high flow blockage ($\lambda = 5$) [39]. The rotor tower has not been included in the design, as not all VAWT design concepts include it. In case it were necessary, the grid requirements for the boundary layers of the blade airfoils may be easily extrapolated to the tower.

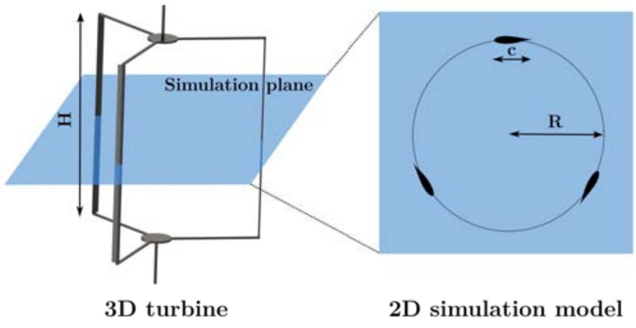

Number of blades N	3
Rotor radius R	0.5 m
Rotor height H	1 (2D)
Rotor swept area S	1 m^2
Blade chord c	40 mm
Rotor solidity σ	0.24
Airfoil	DU 06-W-200
Tip-speed ratio λ	2 to 5.5
Freestream velocity	9 m/s

Figure 4.1: Geometrical characteristics of the simulated VAWT

In Figure 4.2, the different regions of the computational domain are shown. An interface between the turbine rotating zone and the fixed one has been placed at a distance of $5.5D$ (rotor diameters) from the rotor, in order to avoid distortion effects in the transfer of information between adjacent fluid regions. The total size of the circular computational domain is $12D$, in agreement with the values reported in the literature, ensures that the boundary conditions will not interfere in the flow developed inside the rotor [35], [37], [40], [41], [42].

In order to apply the Richardson extrapolation method to assess the mesh convergence, three meshes with different discretization levels have been generated using the software GAMBIT®. The grids have been generated with triangular elements; however, quadrilateral elements have been employed in the near-wall regions (distance to the wall < 2 mm) for a better control of the mesh growth from the wall. The nearest nodes from the wall have been placed ensuring a normalized wall distance y^+ value less than 1. Detailed views of the mesh around the airfoils are depicted at the bottom of Figure 4.2, and specific details about the number of nodes in the region near the airfoils are collected in Table 4.1. In summary, Mesh #1 (fine mesh) has 989770 elements, Mesh #2 (medium mesh) has 554,694 and Mesh #3 (coarse mesh) has 328724.

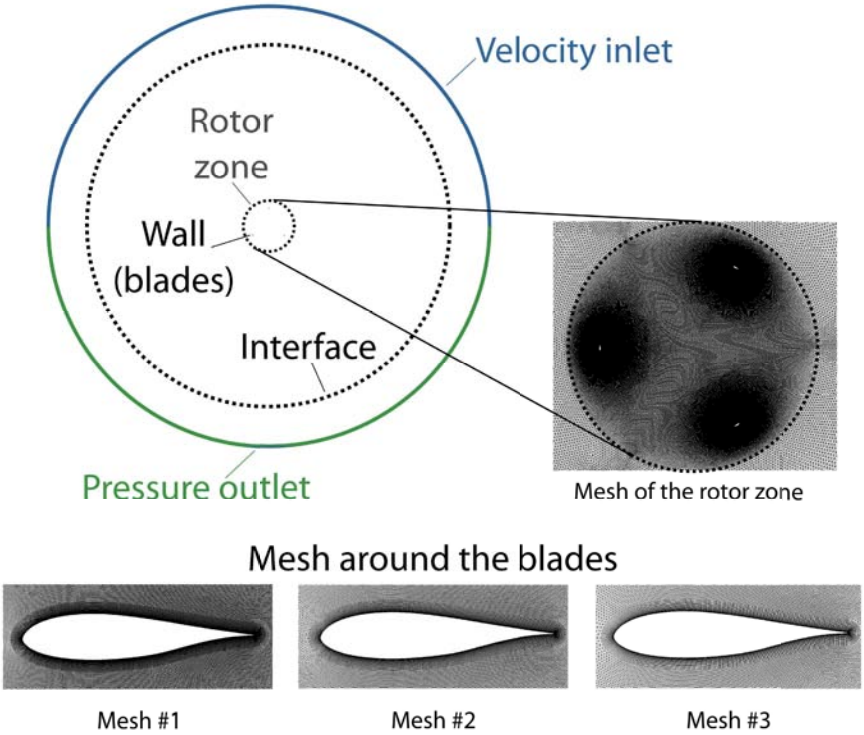

Figure 4.2: Computational domain and boundary conditions applied. Details of the grid for the three meshes generated

Table 4.1: Grid characteristics near the airfoil walls

Mesh	**#1**	**#2**	**#3**
Cells in streamwise direction	520	392	300
Cells in cross-streamwise direction	40	30	24
Grid increasing ratio (cross-streamwise)	1.054	1.110	1.178

Numerical solver

The incompressible unsteady Reynolds-Averaged Navier-Stokes equations have been solved with the commercial package ANSYS FLUENT®, using the k-ω-SST model [43] for the turbulence closure. This model combines the advantages of k-ε and k-ω models in predicting aerodynamic flows, particularly with boundary layers under strong adverse pressure gradients [44]. The boundary conditions applied may be identified in Figure 4.2. A constant inlet velocity condition of 9 m/s, a typical design value for VAWTs, and an outlet pressure equal to atmospheric pressure have been set. The sliding mesh technique has been applied thanks to the previously defined interface between the rotor and outer domain zones. Finally, a wall boundary condition has been applied to the rotor blades. The pressure-velocity coupling is made via the Semi-Implicit Method for Pressure Linked Equations(SIMPLE) algorithm. The spatial discretization schemes are: Least Squares Cell Based for gradients, Second Order for the pressure, and Second Order Upwind for the momentum, turbulent kinetic energy and specific dissipation rate. The temporal discretization scheme is Second Order Implicit. The time step used to perform the simulations is discussed in the following subsection.

Grid and temporal convergence analysis

The applicability of the Richardson extrapolation method [45] to the CFD simulations of VAWT is studied in this subsection. This method, also known as "h^2 extrapolation", "the deferred approach to the limit" or "iterated extrapolation", provides a higher-order estimate of the continuum value (value at zero grid spacing) from a series of lower-order discrete values. As introduced by Roache [46], a numerical simulation yields a quantity f that may be expressed as:

$$f = f_{exact} + g_1 h + g_2 h^2 + g_3 h^3 + ... \tag{4.1}$$

where h is the grid spacing of the simulation. f_{exact} is the continuum value at zero grid spacing. Functions g_i are defined in the continuum, so they are independent of the grid spacing.

As stated in [46], for a second-order method ($g_1 = 0$), by combining the results f_1 and f_2 from two different grids of spacing h_2 (coarse) and h_1 (fine) and neglecting third- and higher-order terms, an estimate for f_{exact} may be obtained, resulting into the original statement of Richardson [45] for the h^2 extrapolation:

$$f_{exact} \simeq f_1 + \frac{h_2^2 f_1 - h_1^2 f_2}{h_2^2 - h_1^2} \tag{4.2}$$

Defining the grid refinement ratio as:

$$r = \frac{h_{coarse}}{h_{fine}} = \frac{h_2}{h_1} \tag{4.3}$$

, Equation 4.2 may be rewritten as:

$$f_{exact} \simeq f_1 + \frac{f_1 - f_2}{r^2 - 1} \tag{4.4}$$

and then be generalized to p-th order methods [31] as:

$$f_{exact} \simeq f_1 + \frac{f_1 - f_2}{r^p - 1} \tag{4.5}$$

For the practical application of the method, the guidelines proposed in [47] have been followed:

- First of all, a representative grid size parameter, relating the cell size and the number of cells, has been defined as:

  $$h = \left[\frac{1}{N_s} \sum_{i=1}^{N_s} (\Delta A_i) \right]^{\frac{1}{2}} \tag{4.6}$$

  being N_s the total number of cells in the simulation domain and ΔA_i the area of a cell i.

- Then, as already introduced in subsubsection 4.1.2, three meshes with different h_1, h_2 and h_3 values have been generated. Being the number of cells in the mesh $N_1 = 989770$, $N_2 = 554694$ and $N_3 = 328724$, the corresponding h values are $h_1 = 0.01069$, $h_2 = 0.01428$ and $h_3 = 0.01855$, resulting in the grid size ratios of $r_{21} = h_2/h_1 = 1.3358$ and $r_{32} = h_3/h_2 = 1.2990$, well near the value of 1.3 recommended by Roache [31]. In this work, the variable ϕ used to judge grid convergence is the mean-time power coefficient of the turbine monitored from the simulations.

- Afterwards, the apparent order of the method has been calculated as:

$$p = \frac{1}{\log(r_{21})} \left| \log \left| \frac{\varepsilon_{32}}{\varepsilon_{21}} \right| + q(p) \right| \tag{4.7}$$

where $\varepsilon_{32} = \phi_3 - \phi_2$, $\varepsilon_{21} = \phi_2 - \phi_1$ are the absolute errors of the variable of interest ϕ obtained with the three different meshes. $q(p)$ is a function that depends on the grid refinement ratios and the behavior of the solutions obtained as the grid is refined, defined as:

$$q(p) = \log \left(\frac{r_{21}^p - s}{r_{32}^p - s} \right) \tag{4.8}$$

where s is the parameter related to a monotonic or oscillatory behavior of the solution as the grid is refined:

$$s = \frac{\varepsilon_{32}/\varepsilon_{21}}{|\varepsilon_{32}/\varepsilon_{21}|} \tag{4.9}$$

Negative values of s are an indication of oscillatory convergence. As it may be observed, Equations 4.7 and 4.8 must be solved iteratively. Additionally, if either ε_{32} or ε_{21} is very close to zero, the above procedure does not necessarily work. This breakdown may be ascribed to oscillatory convergence or, in some cases, it could mean that the exact solution has been already attained [46].

- Once the exact values of p, $q(p)$ and s were obtained, the extrapolated value of the solution (the estimator of the exact solution) has been calculated in a similar way to Equation 4.5:

$$\phi_{ext}^{21} = \frac{\phi_1 - \phi_2}{r_{21}^p - 1} + \phi_1 \tag{4.10}$$

- Then, the error estimates for the relative error and extrapolated relative error have been obtained as:

$$e_a^{21} = \left| \frac{\phi_1 - \phi_2}{\phi_1} \right| \tag{4.11}$$

and

$$e_{ext}^{21} = \left| \frac{\phi_{ext}^{21} - \phi_1}{\phi_{ext}^{21}} \right| \tag{4.12}$$

- Finally, the Grid Convergence Index (GCI) has been used as an indicator of the mesh convergence level:

$$GCI^{21} = \frac{F_S \quad e_a^{21}}{r_{21}^p - 1} \tag{4.13}$$

being F_S a security factor for the calculation of this index, which may be set to 1.25 when having three different meshes [31].

As an additional step, if a certain grid convergence level GCI^* were desired, the required grid resolution r^* with respect to the finer mesh might be obtained as:

$$r^* = \left(\frac{GCI^*}{GCI^{23}} \right)^{\frac{1}{p}} \tag{4.14}$$

An example of the values obtained with this method for the three working points with maximum performance, $\lambda = 3.5$, 4 and 4.5, is displayed in Table 4.2.

Table 4.2: Sample calculation of the discretization error

ϕ	C_P ($\lambda = 3.5$)	C_P ($\lambda = 4$)	C_P ($\lambda = 4.5$)
ϕ_1	0.22403	0.2825	0.26766
ϕ_2	0.22141	0.2817	0.28155
ϕ_3	0.21358	0.2761	0.27850
p	4.3815	7.6152	4.8656
e_a^{21}	1.17%	0.28%	5.18%
e_{ext}^{21}	0.46%	0.034%	1.71%
GCI^{21}	0.57%	0.043%	2.10%

For every case, it was observed that the mean value of the power coefficient of the turbine attained convergence after 6 rotor revolutions, as shown in Figure 4.3 for $\lambda = 4$. Computational times were in the order of 1 week in a 4-nodes Intel Core i7-52820K at 3.3 GHz and 64 Gb RAM. Although values over 20 revolutions have been reported in the literature for convergence [27], the extrapolation towards $t \to \infty$ of the mean C_P value using an exponential function gave almost the same value as the one monitored in the last time step. Regarding industrial purposes, it would be possible to simulate just a few rotor revolutions and then extrapolating the results towards infinity, if only the C_P value is sought

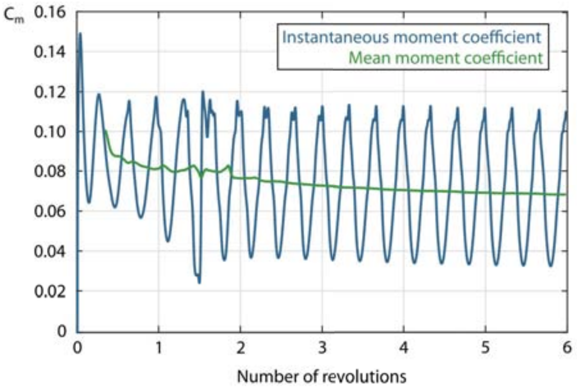

Figure 4.3: Convergence of mean moment coefficient for $\lambda = 4$ and the finest mesh

Figure 4.4 collects the results from the Richardson extrapolation, showing the different values of the power coefficient obtained with the three meshes at different tip-speed ratio values. The figure also shows the extrapolation of the values towards $h \to 0$, which would correspond to a mesh composed of an infinite number of elements (continuous solution).

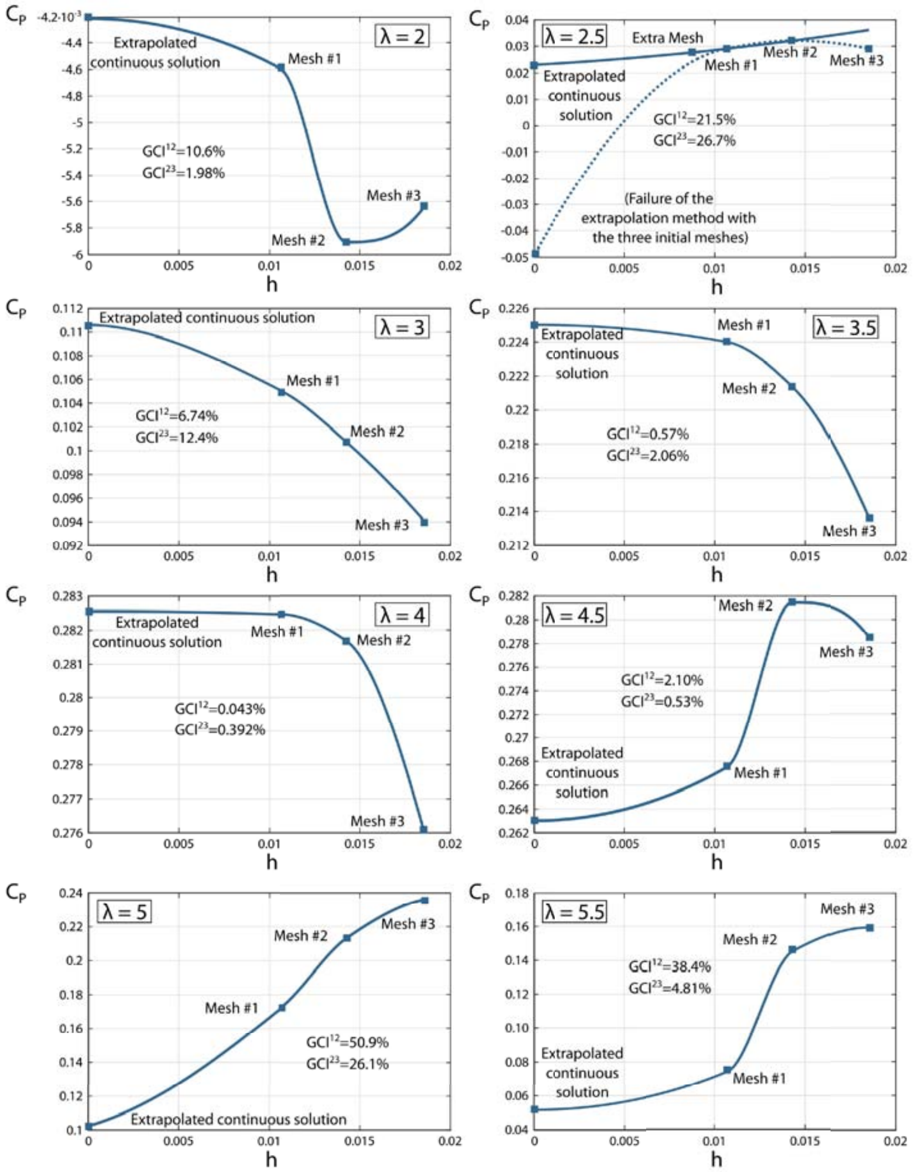

Figure 4.4: Extrapolation of the power coefficient with the Richardson method

Mesh convergence levels are really good near the nominal working point of the turbine $\lambda = 3.5$ to $\lambda = 4.5$ (below 2% and even 0.043% at the nominal working point). Outside these region, the levels are not so accurate. Breakdown of the method is clearly happening at a particular value ($\lambda = 2.5$), where the oscillatory convergence is apparent in Figure 4.4. This result is consistent with the issues found by Celik and Li [32] when extrapolating their cases with non-monotonic convergence. In order to determine the origin of this behavior, a new simulation with a mesh one level finer than Mesh #1 was performed and the Richardson extrapolation method was applied again with this new mesh and meshes #1 and #2. Looking at the new continuum value in Figure 4.4 for $\lambda = 2.5$, it may be observed that the method now converges, providing a more reasonable value for the power coefficient. As previously introduced, if the differences between the values of the magnitudes used to study mesh convergence are very small (and so is the case), the procedure might not reach a trustworthy solution. The analysis with an extra mesh shows that the values for the three initial meshes were near the exact solution, causing $\varepsilon_{21}, \varepsilon_{32} \to 0$ and extrapolating the values towards an unreliable point. Regarding the highest tip-speed ratios ($\lambda = 5$ and $\lambda = 5.5$), the increase in the grid convergence level may be attributed to thin boundary layers attached to the blades, revealing the importance of the mesh refinement in the boundary layer regions in order to model correctly the flow behavior. Nevertheless, it has been shown that the Richardson extrapolation method is applicable to the study of numerical convergence of VAWT simulations, providing a cuantitative value of the grid convergence level and reducing the amount of meshes required for verification of the numerical code to three (four in the case breakdown of the method occurs for certain working points).

For further validation of the accuracy of the procedure and the finest mesh results, the evolution of the streamwise and cross-streamwise forces on an airfoil during a turbine revolution is shown in Figure 4.5 for the three meshes employed. The evolution of the aerodynamic torque of the turbine is also shown. Values for three different tip-speed ratios are shown ($\lambda = 2.5$ [low], $\lambda = 4$ [nominal] and $\lambda = 5$ [high]).

Convergence is very good for the low and nominal tip-speed ratio values, to the point it becomes difficult to distinguish between the results from the three meshes. For the highest tip-speed ratio, even when it is possible to differentiate the evolution of the curves from the three different meshes (especially for the aerodynamic torque), the agreement between the results obtained is also relatively good. Hence, the discretization of the finest mesh may be considered fine enough to model accurately the flow behavior. Regarding the results for $\lambda = 2.5$, it may be concluded that, at low tip-speed ratios, the force oscillations in the downwind part of the turbine must be considered when defining the structural and electronic design of the turbine.

Finally, in order to select an adequate time step for the simulations, the finest mesh has been used to perform a convergence study of the temporal resolution. Three discretization levels have been tested, corresponding to a rotor advancement of 1°, 0.5° and 0.25° per time step. Following the guidelines for the Richardson extrapolation method, a so-called spatial-temporal h_{ST} index has been defined as:

$$h_{ST} = \left[\frac{1}{N_t N_s} \sum_{i=1}^{N_s} (\Delta A_i) \frac{2\pi}{\omega} \right]^{\frac{1}{3}} \tag{4.15}$$

being N_s the number of cells, N_t the number of time steps per rotor revolution, ΔA_i the area of the cell i and ω the turbine rotational speed.

The results from the extrapolation method are shown in Figure 4.6, resulting in a T-GCI

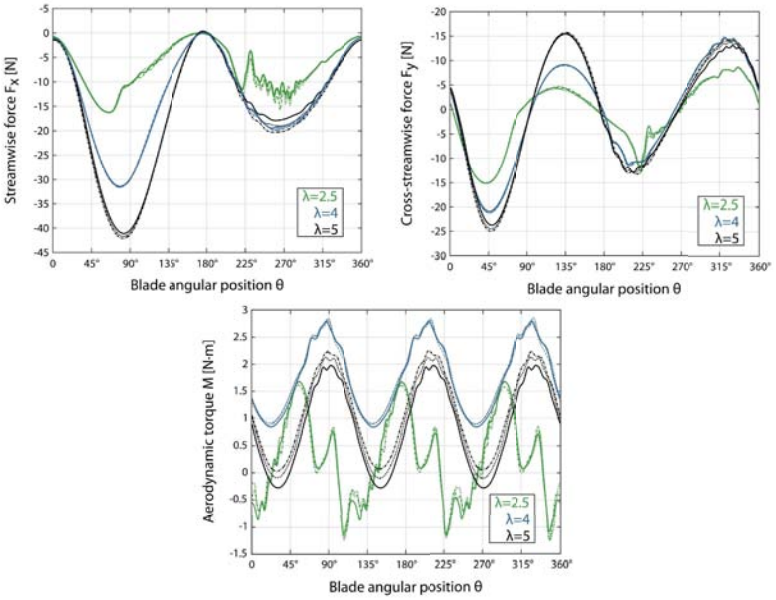

Figure 4.5: Evolution of streamwise and cross-streamwise forces on a blade during turbine rotation for the three different meshes (top). Evolution of the aerodynamic torque of the turbine (bottom). Mesh #1 - solid line, Mesh #2 - dashed line, Mesh #3 - dash-dotted line

(Temporal-Grid Convergence Index) of 0.05% for the medium-to-smallest time step at $\lambda = 4$. Therefore, all the simulations presented in this chapter have been performed with a time step corresponding to a rotor advancement of 0.25° per time step, i.e, 1440 time steps per rotor revolution.

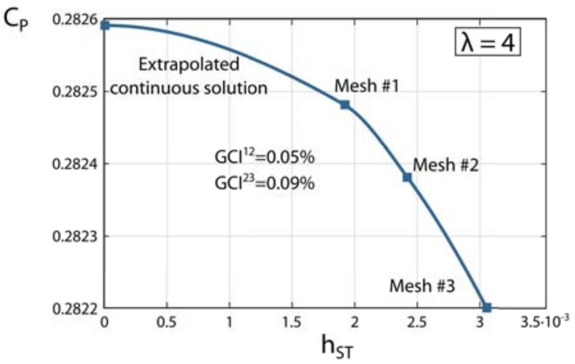

Figure 4.6: Analysis of temporal convergence with the Richardson extrapolation method

Comparison with existing benchmarks

The results of the CFD simulations have been compared with the double multiple streamtube model (DMST) presented in Chapter 3. The power curves predicted by CFD simulations with the three different meshes and the one predicted by the DMST model are shown in Figure 4.7. Both methods predict the peak power coefficient at the same tip-speed ratio and, despite the flow assumptions performed by the DMST model (wake not modeled, downwind zone of the rotor assumed to be in the fully expanded wake of the upwind zone, influence of the downwind zone on the upwind zone neglected), the slopes of the DMST curve and the finest mesh match. By looking further at Figure 4.7 and relating it to the Richardson extrapolation analysis, it may be observed that the difference in the power coefficient predicted by the three meshes at the lower tip-speed ratios is almost negligible. Therefore, it may be assured that an accurate solution had been already found with the coarsest mesh, explaining the decrease in the relative errors that led to breakdown of the extrapolation method for $\lambda = 2.5$. Whereas the coarser meshes could be used for simulating the lower tip-speed ratio values (and even the nominal one), the only mesh that should be used for simulating the higher tip-speed ratios is the finest mesh, as it may be deduced from the right part of the power curves.

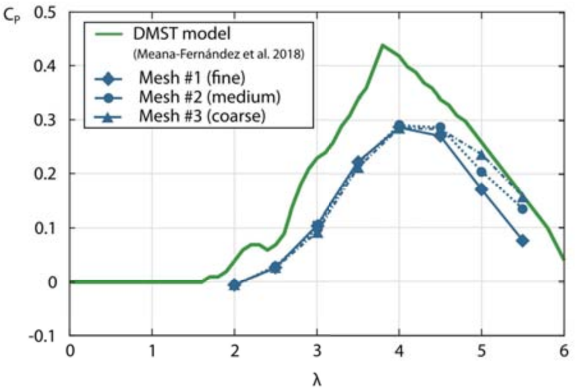

Figure 4.7: Power coefficient curves obtained with the three different meshes. Comparison with results from double-multiple streamtubes model

Additionally, in order to place the results of the CFD model within the existing literature, a small benchmark has been developed with results from other authors, trying to find VAWTs with similar solidities and blade airfoils [48], [49], [50]. The characteristics of the selected turbines are collected in Table 4.3.

Table 4.3: Benchmark for the comparison with existing results

Study	**Methodology**	**Freestream Reynolds number**	**Solidity**	**Airfoil**	Max. C_P
Current study	CFD simulations	25344	0.24	DU-06-W-200	0.2880
Bedon et al. [48]	CFD simulations	1232040	0.2	NACA 0018	0.2884
Sabeifard et al. [49]	Experimental tests & CFD	35000	0.1 - 0.75	DU-06-W-200	0.3002
Delafin et al. [50]	Vortex model	369802	0.22	NACA 0015	0.4359

Figure 4.8 shows the comparison between the optimal tip-speed ratio of the turbines depending on their solidity. In the case of the turbines with a similar solidity to the turbine presented in this chapter (Bedon et al. [48], Delafin et al. [50]), the maximum power coefficient is attained at similar tip-speed ratio values. Regarding the results from Sabaeifard et al. [49], with the same airfoil and a similar freestream Reynolds number to the turbine from this work, the optimal tip-speed ratio of the simulated turbine fits perfectly into the trend of the values obtained by these authors. The turbine from Delafin et al. [50] presents a higher power coefficient than the rest. Firstly, it has been modeled with a vortex model, which might overpredict results when compared to CFD simulations. Secondly, it employs a NACA 0015 airfoil, which has a higher efficiency than thinner or thicker airfoils from its family [38], [51]. Additionally, it has been observed that an increase in the Reynolds number shifts the power curve up- and leftwards [38], [52], [53], so the slight differences between the other turbines may be either ascribed to the differences in the Reynolds numbers or the small diferences between the NACA 0018 and the DU 06-W-200 airfoil. Therefore, it may be considered that the results of this study are consistent with the results found in the literature.

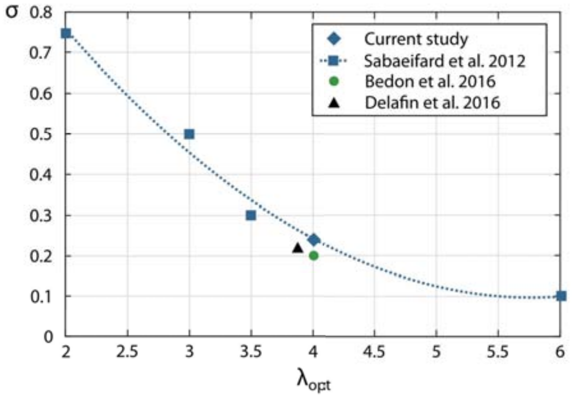

Figure 4.8: Comparison of the optimal tip-speed ratio of the studied turbine with existing results for similar turbines

As an additional validation source, the power curves obtained by Sabaeifard et al. [49] with CFD simulations have been plotted in Figure 4.9. It may be appreciated that the shape of the turbine simulated in this work fits consistently into the graph, being the smaller value of the peak power coefficient ascribable to the lower turbine Reynolds number.

4.1.3. Numerical description of the flow field

After having verified the validity of the CFD simulations and confirmed the applicability of the Richardson extrapolation method to the simulation methodology, the CFD results have been analyzed to provide insight into the flow behavior around the turbine. Three different working points have been studied: $\lambda = 2.5$, corresponding with a working point in the vortex shedding predominant region; $\lambda = 4$, corresponding with the nominal working point; and $\lambda = 5$, corresponding with a working point past the nominal working point, with highly attached boundary layers and predominant viscous effects.

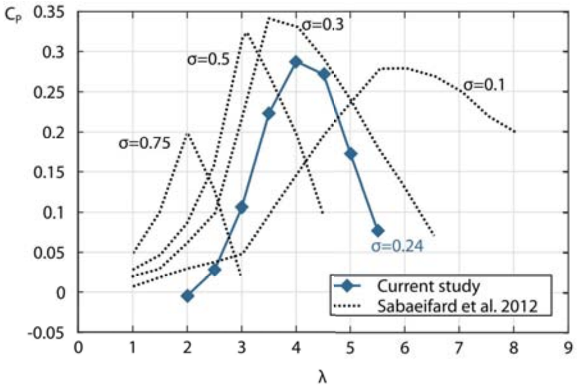

Figure 4.9: Position of the power curve of the studied turbine with respect to its solidity

Pressure on the turbine blades

The chordwise distribution of the pressure coefficient on a blade during the turbine rotation is shown in Figures 4.10, 4.11 and 4.12 for $\lambda = 2.5$, $\lambda = 4$ and $\lambda = 5$ respectively

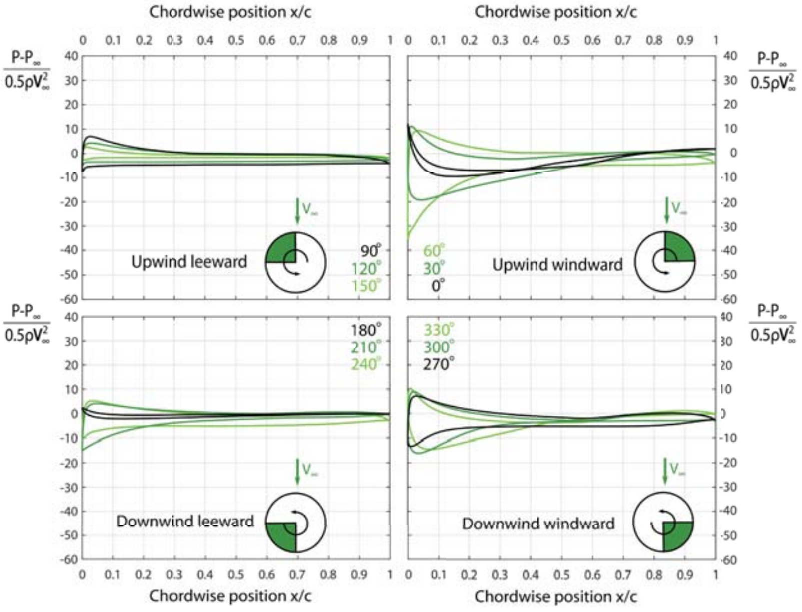

Figure 4.10: Pressure coefficient distribution on a blade along the rotor cycle ($\lambda = 2.5$)

The strong pressure gradients appreciated justify the selection of the k-ω-SST model for the closure of turbulence [41]. The maximum pressure differences arise in the upwind part of the turbine, where the first energy extraction stage occurs. Additionally, differences between windward and leeward zones of the turbines may be observed, as the blades in the windward

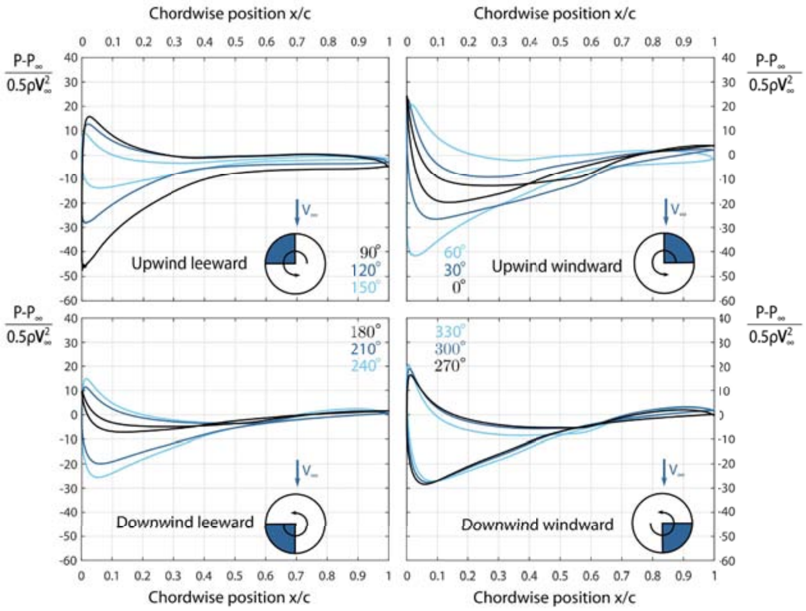

Figure 4.11: Pressure coefficient distribution on a blade along the rotor cycle ($\lambda = 4$)

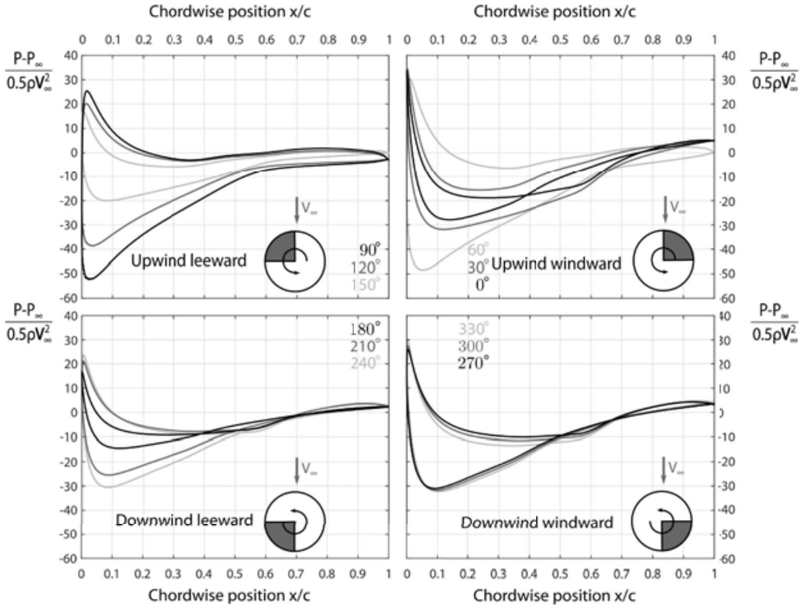

Figure 4.12: Pressure coefficient distribution on a blade along the rotor cycle ($\lambda = 5$)

regions suffer greater pressures from the incoming wind. There is a region from 30° to 150°, one third of the rotating path, in which the highest pressures are concentrated. This might explain the predominance of 3-bladed turbines, as in this way only one blade remains in the high-loading zone at every time. The position with the highest pressure seems to happen at 60°.

Comparing the three figures for the different tip-speed ratio values, it is easy to identify the effects of increasing the rotational speed of the turbine with respect to the incoming wind. At $\lambda = 2.5$, the difference between the pressure coefficient in the pressure and suction sides of the blades (and thus the lift force) is only slightly higher in the windward region. The rest of the blade moving path does not exhibit great shifts in the pressure distribution along the blades, fact that explains the low power extraction capability of the turbine at this working point. At $\lambda = 4$, there are changes in the pressure coefficient distribution according to the blade position, so it is evident that significant power is being extracted from the wind. Lastly, at $\lambda = 5$, there is an increase in the values of the pressure coefficient with respect to $\lambda = 4$. However, the lower power coefficient at this working point allows to conclude that this pressure rise does not translate into effective power generation. Of course, the relative velocity increases as λ does, but, the higher the tip-speed ratio, the higher the alignment of the relative velocity vector with the blade chord. In turn, this results in an aerodynamic force (mainly lift) more aligned with the rotor radius and, accordingly, less effective for torque (and power) generation.

Velocity field

Figure 4.13 shows the contours of normalized velocity V/V_∞ for one blade passing period T_B for $\lambda = 2.5, 4$ and 5. At a first glance, a wake of a width in the order of the turbine diameter D is clearly identifiable. The vortices shed by the blades at $\lambda = 2.5$ are clearly visible. At this λ, the blockage produced by the rotor in the wind current is very low, so it is not surprising that the turbine is not able of extracting enough power. At higher tip-speed ratios ($\lambda = 4$ and 5), the higher velocity deficit in the wake may be confirmed. Nevertheless, the higher blockage at $\lambda = 5$ does not translate into higher power extraction, being the blockage level at $\lambda = 4$ the optimal one to maximize energy harvesting.

Turbulent kinetic energy

The contours of normalized turbulent kinetic energy (TKE) for $\lambda = 2.5, 4$ and 5 are depicted in Figure 4.14. Turbulent kinetic energy is defined as:

$$TKE = \frac{1}{2}\overline{u_i' u_i'} \tag{4.16}$$

where u_i' are the turbulent velocity fluctuations in the flow.

Representing this variable results very useful for the identification of the main regions of turbulence production and its further convection downstream. At $\lambda = 2.5$, vortex shedding phenomena are easy to locate. These vortices start to roll up behind the airfoil before being convected downstream. Besides the obvious differences between the upwind and downwind parts of the rotor (before reaching the upwind part, the wind comes “unperturbed” from the energy extraction process, while in the downwind part, blade performance is clearly affected by the wakes from the upwind part), there is a totally different behavior between the windward and leeward rotor zones. In the windward zone, with blades moving towards the wind at higher

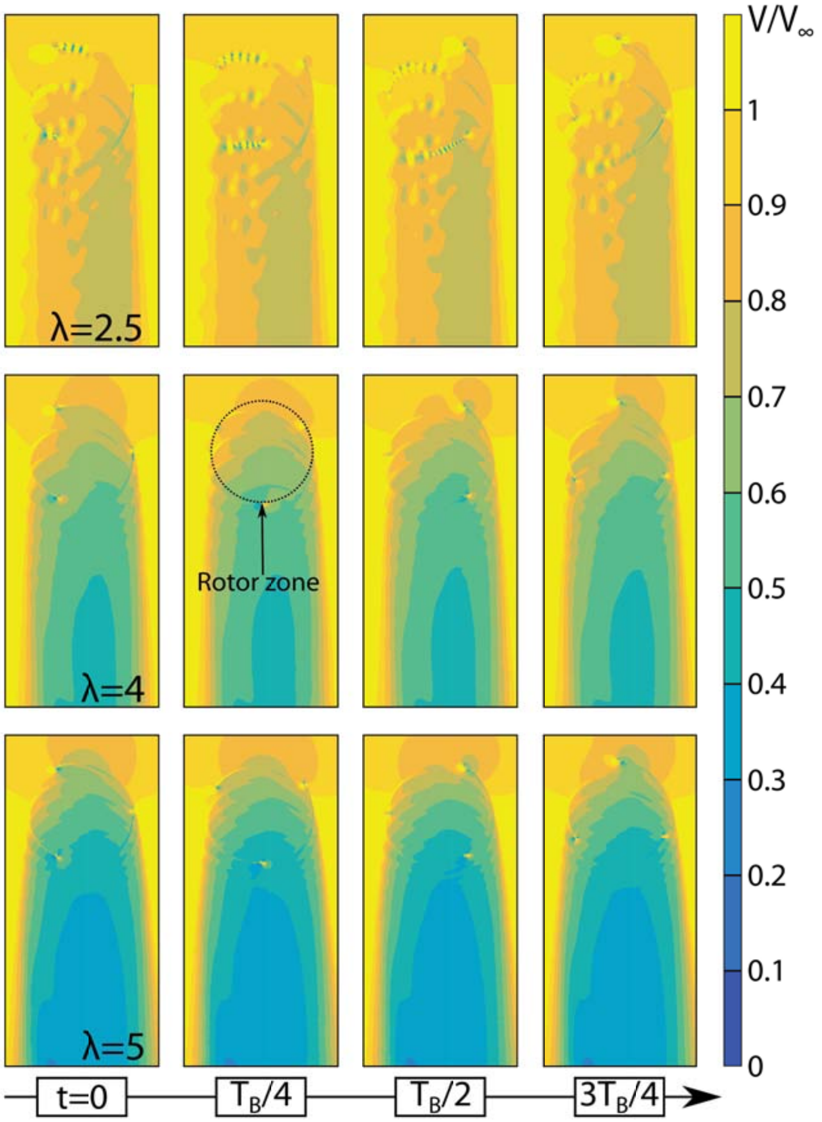

Figure 4.13: Normalized velocity contours for a whole rotor cycle and $\lambda = 2.5$, 4 and 5

relative velocities, the wakes generated are much narrower. Additionally, the air that flows through the turbine convects the vortices before they can start to roll up, resulting in a much cleaner flow pattern that makes easy to identify the path followed by the blades during turbine rotation. On the leeward side, oppositely, vortices shed from the blades roll up before being convected, resulting in more intrincate flow patterns, with new vortices shed from the incoming blades being convected across the sea of vortices shed by the previous blades. Although the flow

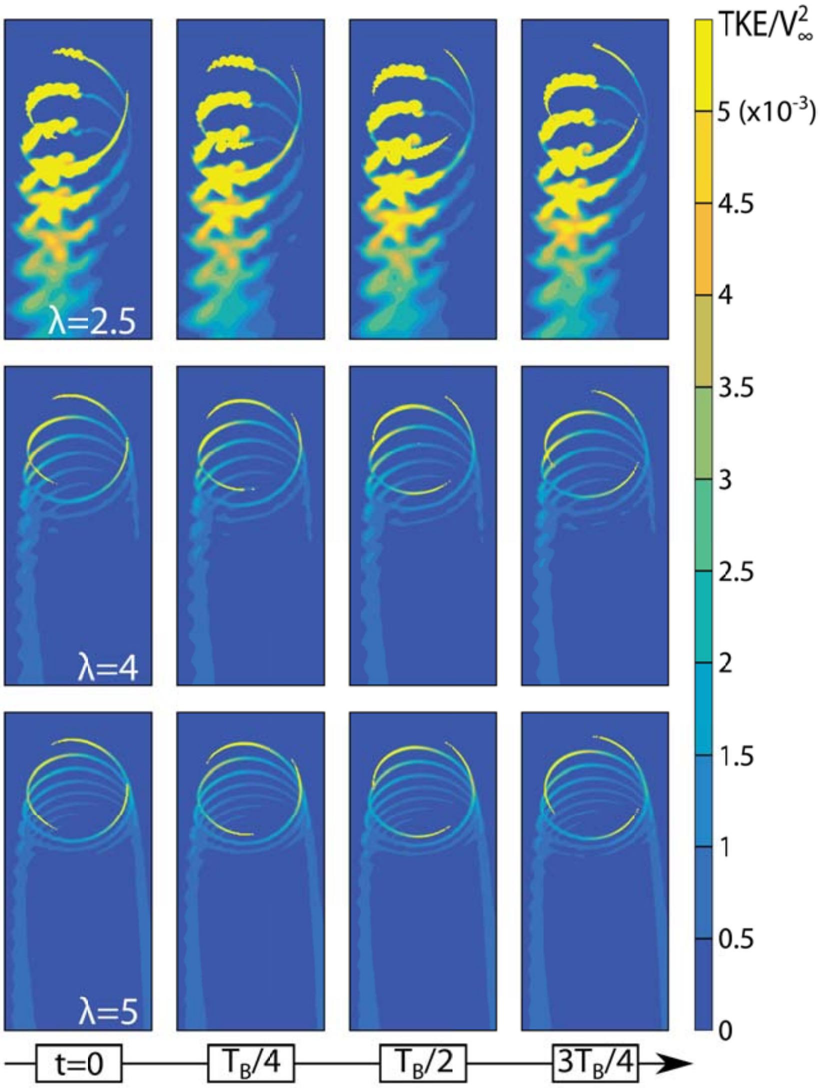

Figure 4.14: Normalized turbulent kinetic energy contours for a whole rotor cycle and $\lambda = 2.5$, 4 and 5

becomes blurry, it is possible to associate each wake to its corresponding blade. This difference between leeward and windward regions could have been already noticed in Figure 4.5, as it is the reason behind the oscillatory behavior of the forces on the blade (see Figure 4.5, angles corresponding to the downwind-leeward zone). Finally, comparing the contours at $\lambda = 4$ and 5, some insight into the reasons behind the higher performance of the turbine at $\lambda = 4$ may be sought. When a blade enters the downwind-leeward region, it must cross the turbulent kinetic energy traces left from the previous ones. In the case of $\lambda = 4$, four traces may be identified, whereas for $\lambda = 5$ there are six traces. This must be translated into a loss of efficiency in the performance of the airfoil in this region, which adds to the increasing viscous forces due to the higher rotational speed of the turbine and the decrease in rotor loading, explaining why further increases in the tip-speed ratio are detrimental to the turbine performance. Additionally, the "turbulent kinetic energy" wake on the windward side of the rotor is much longer at $\lambda = 5$, fact that may be attributed to a poorer airfoil performance in that region. The higher rotational speed of the turbine, besides preventing the airfoil from reaching angles of attack high enough to ensure significant lift generation, leaves less available time for the shed wakes to be swept away from the rotor by the incoming wind.

Vorticity

Vorticity is typically used as a measure of the tendency of the fluid to rotate and is defined by:

$$\omega_i = \varepsilon_{ijk} \frac{\partial u_k}{\partial x_j} \tag{4.17}$$

where ε_{ijk} is the Levi-Civita symbol, u_k are the velocity components and x_j are the directions of space.

Figure 4.15 shows the contours of in-plane vorticity for $\lambda = 2.5$, 4 and 5, normalized with the rotational speed of the turbine ω.

Two main different mechanisms of vortex shedding and wake development may be identified. The first one, of greater magnitude, is blade vortex shedding. After each blade trailing edge, two opposite-sign high-vorticity regions may be identified. The second mechanism arises from the combination of turbine rotation and the incoming wind. The vortices shed from the blades are convected downstream, generating different patterns depending on the tip-speed ratio but resulting in a wider wake of a size in the order of the turbine diameter D. The magnitude of vorticity in this wake is lower, as the vortex mixing process starts as soon as the vortices leave the blades, so that vorticity drops with the streamwise convection. Inside this wake, two different regions with opposite vorticity signs, corresponding with leeward and windward rotor zones may be identified. Comparing the different tip-speed ratio values, for $\lambda = 2.5$, there is a high amount of unsteadiness due to the delay in the dissipation of the big vortices shed from the blades, so the two opposite-sign zones in the turbine wake are more blurred. Looking at the contours for $\lambda = 4$ and 5, the distinction between the leeward and windward regions of the turbine wake becomes more evident, with the wake divided in two halves of opposite vorticity. The flow pattern in the wake resembles the wake shed by a cylinder of the same diameter of the turbine. Following this line of thinking, it seems feasible to save computational costs by considering the actuator cylinder models available in the literature in their analytical formulation or as part of a CFD simulation (for instance, for the simulation of VAWT farms). Lastly, comparing the contours for $\lambda = 4$ and 5, the greater number of shifts in the vorticity sign for $\lambda = 5$ in the area enclosed by the rotor may be associated with the greater generation of blade wakes, previously identified in the vorticity contours. And, although the width of the wakes is smaller, the interaction between successive blade passings generates greater levels of undsteadines that finally transform into a loss of performance.

4.1.4. Conclusions

A 3-bladed low-solidity VAWT with DU 06-W-200 airfoils has been simulated in a 2D domain using a computational fluid dynamics (CFD) model. The applicability of the Richardson

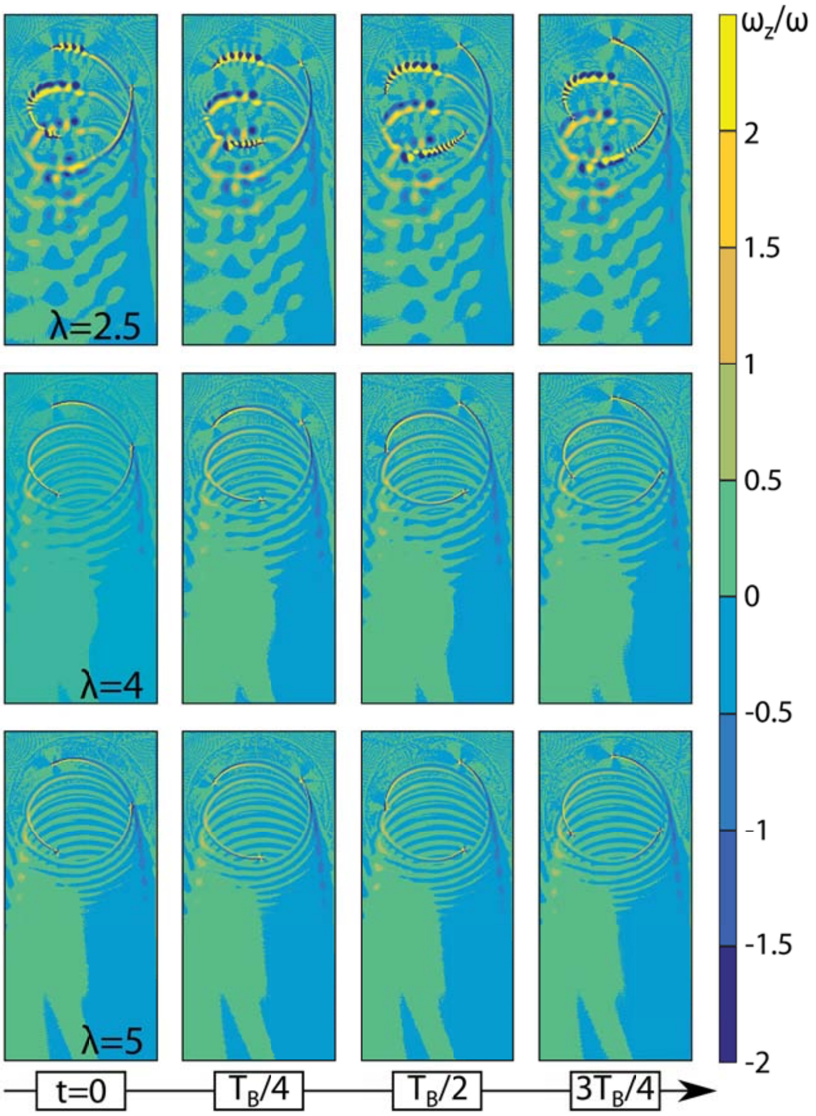

Figure 4.15: Normalized vorticity contours for a whole rotor cycle and $\lambda = 2.5$, 4 and 5

extrapolation method for the study of the numerical convergence of VAWT simulations has been confirmed, resulting in a straightforward procedure to ensure grid size convergence. This method has been used to determine the mesh and temporal requirements for the simulation of this type of turbines: it has been found that, in order to capture the relevant aerodynamic phenomena, a spatial discretization of 40 cells in the first 2 mm in the cross-streamwise direction from the airfoil wall and 12 cells/mm in the streamwise direction for the airfoil chord was enough to capture all the relevant fluid phenomena. A rotor advancement of 0.25° per time step has been found adequate for performing the simulations. The results of the numerical simulations have been compared with existing benchmarks, finding a reasonable agreement. After verifying the simulations, the flow field around the turbine has been studied at three characteristic tip-speed ratio values, corresponding with: working point in the vortex shedding predominant region ($\lambda = 2.5$), nominal working point ($\lambda = 4$) and working point beyond the nominal operational conditions ($\lambda = 5$). Vortex convection develops in a different way depending on the rotor zone (upwind, downwind, windward or leeward). The loss of performance outside the nominal working point of the turbine has been analyzed and related to the fluid dynamics phenomena generated by the interaction of the turbine with the incoming wind. Two main unsteadiness generation mechanisms have been identified: the blade vortex shedding and the interaction of the turbine rotation with the incoming wind, which generates a wake similar to the one developed by a cylinder of the same size as the turbine diameter.

Tridimensional effects have not been considered in this work, so future efforts should include 2.5D or full 3D simulations using the discretization proposed in this chapter. Additionally, experimental tests on a turbine prototype to determine the power curve of the turbine would be helpful to provide a more precise validation of the simulations and develop a more comprehensive understanding of the fluid phenomena generated. The similarities between a vertical-axis wind turbine and a cylinder is another topic that should be studied in depth.

4.2. CFD methodology for the analysis of typical VAWT airfoils

In this section, different turbulence models have been applied to predict the performance of a DU-06-W-200 airfoil [54] via 3D CFD simulations. A compromise between the simulation time and the results is sought, not focusing just in the prediction of the aerodynamic forces but also being able to provide some insight into the flow field developed around and downstream the airfoil. The results have allowed to propose the most suitable models depending on the outcome desired from the simulations (aerodynamic forces, airfoil flow field or VAWT simulation).

4.2.1. Introduction and research gaps addressed

The airfoil used to build the blades of a turbine determines the aerodynamic forces developed on its surface and hence the amount of energy that may be extracted from the wind. Wind tunnel experiments using a force balance are the most typical way of obtaining airfoil aerodynamic forces (lift, drag and moment coefficients) as a function of the incoming wind speed and angle of attack [55]. However, the design of the experiments, the construction of airfoil prototypes and the costs related to reservation and use of experimental facilities require an amount of time and effort that some small and medium-sized enterprises (SMEs) and institutions cannot afford at the first design stages. At these stages, Computational Fluid Dynamics (CFD) simulations become convenient to predict the behavior of a prospective airfoil shape before proceeding to more expensive experimental tests.

The main aim of this study is to find a compromise between the simulation time and the results, not focusing just in the prediction of the airfoil aerodynamic forces but also being able to provide insight into the flow field developed around and downstream the airfoil. Concerning VAWTs, an accurate description of the vortex shedding from the blades at the upwind part of the turbine would allow to rely on realistic flow incoming conditions for the downwind part of the turbine. Reynolds Averaged Navier-Stokes equations (U-RANS) models, which apply a phase-averaging to the Navier-Stokes equations to model the turbulent part of the flow, offer the most economic approach for the computation of complex turbulent flows [56]. These models are suitable for many engineering applications and typically provide the level of accuracy required. An alternative to these models are Scale-Resolving-Simulation (SRS) models, which resolve at least a portion of the turbulence for at least a portion of the fluid domain (typically, the larger and more problematic scales), leaving the turbulence model to account only for the effects of the more universal and isotropic smaller scales [57]. This family includes Direct Numerical Simulations (DNS), which solve all the flow scales belonging to the continuum; Large Eddy Simulations (LES), which solve the largest scales of the flow; and hybrid LES-RANS models, like Scale-Adaptive Simulation (SAS) models, Detached Eddy Simulation (DES) models and Embedded LES (ELES) models, which combine elements of LES and RANS approaches to allow the simulation of high Reynolds flows avoiding the high resolution requirements of LES. Regarding the scope of this work, it has been intended to go further from the application of Reynolds Averaged Navier-Stokes equations (U-RANS) models and include Scale-Resolving Simulations (SRS) in the study. Finally, from the results from this work, some indications regarding the selection of the turbulence model depending on the desired outcome (airfoil aerodynamic forces, airfoil flow field or VAWT simulation) are provided. The ultimate goal is to select an optimum turbulence model for the numerical simulation of both VAWT and VAWT airfoils.

4.2.2. Numerical methodology

Experimental reference case

An experimental reference case was used to validate the numerical simulations. The experimental data were obtained at the Low Turbulence Tunnel (LTT) from the Technical University of Delft [54]. This tunnel has a test section of 1.8 m times 1.25 m (width x length) and a turbulence level of 0.02%. The airfoil tested had a DU-06-W-200 section with a chord of 0.25 m. This airfoil was specifically designed for vertical-axis wind turbine applications, and it has been claimed that it has the ability to self-start the turbine. The Reynolds number used for the tests was 300000, corresponding to an incoming flow velocity of approximately 17 m/s.

Geometry of the domain and study of the proper mesh size

In order to select a proper domain size, a literature survey was performed. Table 4.4 shows the typical domain sizes found in the literature in airfoil chord units c for the simulation of airfoils. For the case to be simulated in this work, a distance to the inlet of $12.5c$ and a distance to the outlet of $20c$ were considered enough to avoid the effect of the boundaries on the development of the flow inside the domain region. Figure 4.16 shows the final domain employed for the simulation, alongside the mesh and the boundary conditions applied.

Table 4.4: Typical domain sizes found in the literature (in airfoil chord units c)

Authors	Distance to the inlet/sides	Distance to the outlet
Athadkar and Desai (2014) [58]	$10c$	$15c$
Cao (2011) [59]	$12.5c$	$20c$
Hawley (2013) [60]	$5c$	$6c$
Kasibhotla and Tafti (2014) [61]	$15c$	$60c$
Liang and Li (2018) [62]	$25c$	$25c$
Millán Sanz (2011) [63]	$60c$	$60c$
Shah et al. (2015) [64]	$15c$	$25c$

The initial aim of this work was to compare wall-resolved and wall-modeled turbulent schemes, so two different grids with different requirements were generated using the software GAMBIT®. For the calculation of the grid size, the displacement thickness (δ^*) of the airfoil boundary layer at a medium angle of attack (15°) was estimated using the software XFOIL [65]. At a Reynolds number of 300000, this size was estimated to be around 25 mm (sum of the pressure and suction side values). As the boundary layer thickness δ is larger than δ^* and the largest scales in a boundary layer are of a typical size $L \sim \delta/2$ to $\delta/8$, it may be assumed that L is approximately of the same size as the displacement thickness calculated with XFOIL. Following the recommendations of Davidson and Dahlström, the largest scales in a boundary layer are in the order of δ and these scales are probably also apparent in the spanwise direction [66], [67]; thus the ratio δ/L_z should at least be less than one, being L_z the spanwise extent of the domain. Hence, L_z was chosen to be 25 mm, twice the estimated displacement thickness, resulting in a ratio between the spanwise extent of the domain ($L_z/c = 0.1$), higher than the one reported in [66].

Regarding the number of nodes in the spanwise direction, the guidelines proposed in [68] and [57] were followed. As there are different mesh requirements depending on whether the flow near the walls is to be resolved (wall-resolved LES resolution, WRLES) or modeled (wall-modeled LES resolution, WMLES), two different meshes were generated. In order to obtain a wall-resolved LES resolution, a dimensionless wall distance $\Delta z^+ \sim 10$ to 40 is recommended. Taking 20 as a reasonable value, the cell size would be 0.75 mm, which results in 33 cells inside the boundary layer. For a wall-modeled LES resolution, it is enough with Δz^+ values between 100 and 300 (a cell size around 3.75 mm, resulting in 7 cells inside the boundary layer). On the other hand, following the recommendation from [68], 20 cells are recommended inside the boundary layer, resulting in a typical cell size of 1.25 mm, which was the value finally adopted.

Concerning the in-plane mesh requirements [67], the recommendations are $\Delta x^+ = 50$ to 150 and $\Delta y^+ = 20$ to 150 for wall-modeled LES resolution. For wall-resolved LES resolution, the values are $\Delta x^+ = 50$ to 150 and $\Delta y^+ = 1$ These requirements result in typical cell sizes of 11 mm and 1.5 mm in the x-direction for wall-modeled and wall-resolved LES respectively, and 0.75 mm and 0.04 mm in the y-direction. These values are aligned with the value proposed by [68], $\Delta x \sim \delta/10 = 2.5$ mm.

Additionally, the total number of cells recommended in the volume region inside the boundary layer is scaled with the Reynolds number of the flow [57] with the following formulas:

- For the outer layer region ($y^+ \simeq 100$ to $\delta^+ \simeq 1360$):

$$N_\Omega = 3000 \cdot (w/c) \cdot Re^{0.4} \tag{4.18}$$

- For the inner layer region ($y^+ \simeq 0$ to $y^+ \simeq 100$):

$$N_\Omega = 5 \cdot 10^{-4} \cdot (w/c) \cdot Re^{1.8} \tag{4.19}$$

being Re the flow Reynolds number, w the spanwise extent of the domain and c the airfoil chord. Additionally, it is advisable to have between 3 and 5 cells in the region below $y^+ \sim 10$. Following all of these recommendations, values of $\Delta y \sim 2.5$ mm and $\Delta y \sim 0.027$ mm were adopted for the outer and inner layer respectively.

Finally, the total number of cells in the outer region of the boundary layer ($y^+ \simeq 100$ to $\delta^+ \simeq 1360$) was set according to the typical cell size calculated for the wall-modeled LES requirements (1.5 mm in the streamwise direction and 2.5 mm in the spanwise direction). These values are consistent with the values proposed by Chapman [69], [70], who proposes a value of $\Delta_{cell} \sim \delta/N^{1/3} \sim 1.9$ mm, and Pope [68], who proposes $\Delta_{cell} = \pi/\kappa_c \sim 2$ mm , being $\kappa_c \simeq 38/L$ the frequency of the LES filter that accounts for 80% of the turbulent kinetic energy.

Following all these guidelines, the wall-modeled and wall-resolved LES meshes resulted in 1640394 and 4328775 cells respectively. Figure 4.16 shows the final mesh for the wall-modeled simulations, with details of the mesh near the leading and the trailing edge of the airfoil.

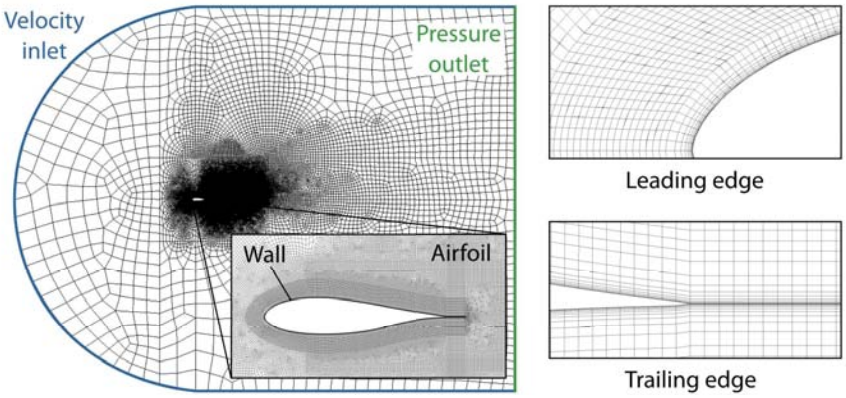

Figure 4.16: Mesh and 2D boundary conditions

Numerical solver, boundary conditions and turbulence models

The Navier-Stokes equations have been solved in an incompressible fashion using the commercial software ANSYS-FLUENT®. The boundary conditions of the simulation domain are shown in Figure 4.16 alongside the mesh. A velocity-inlet condition has been set at the domain inlet with the value 17 m/s that corresponds to a Reynolds number of 300000. At the domain outlet, a pressure-outlet condition equal to atmospheric pressure has been set. The airfoil has been defined with the wall boundary condition (no-slip) and the spanwise limits of the domain have been set as a symmetry boundary condition.

To calculate the turbulence values at the inlet, knowing the wind tunnel turbulence intensity ($TI = 0.02\%$), the typical lengthscale of the tunnel was estimated as [56]:

$$\ell = \frac{0.07L}{C_\mu^{3/4}} = 0.767\,\mathrm{m} \tag{4.20}$$

where $L = 1.8\ m$ is the characteristic length of the wind tunnel and $C_\mu = 0.09$ is a constant used to ensure consistency with the definition of turbulent length scales. With these two values, the turbulent kinetic energy at the inlet is calculated as:

$$TKE = \frac{3}{2}(\bar{u}TI)^2 = 1.743 \cdot 10^{-5}\,\mathrm{m}^2/\mathrm{s}^2 \tag{4.21}$$

where $\bar{u}$ is the mean flow velocity. Then, depending on the turbulence model, the corresponding turbulent variables may be calculated as:

- Modified turbulent viscosity

$$\tilde{\nu} = C_\mu \sqrt{\frac{3}{2}} \bar{u} T I \ell = 2.874 \cdot 10^{-4}\,\mathrm{m}^2/\mathrm{s} \tag{4.22}$$

- Turbulent dissipation rate

$$\varepsilon = \frac{TKE^{3/2}}{\ell} = 9.492 \cdot 10^{-8}\,\mathrm{m}^2/\mathrm{s}^3 \tag{4.23}$$

- Specific dissipation rate

$$\omega = \frac{TKE^{1/2}}{C_\mu \ell} = 0.0605\,\mathrm{s}^{-1} \tag{4.24}$$

The U-RANS turbulence models tested in this study are the following:

1. Strain-based Spalart-Allmaras
2. Realizable $k - \varepsilon$ with Enhanced Wall Treatment
3. $k - \omega$ (Standard, Baseline and Shear Stress Transport)
4. Linear Pressure-Strain Reynolds Stress model with Enhanced Wall Treatment

And the SRS models studied are:

1. Scale Adaptive Simulation (SAS) with $k-\omega$ Standard and Shear Stress Transport models
2. Wall-Modeled Large Eddy Simulation (WMLES Standard and WMLES $S - \Omega$)
3. Large Eddy Simulation (LES) with the Wall-Adapting Local Eddy-Viscosity (WALE) model
4. Detached Eddy Simulation with the $k - \omega$ Shear Stress Transport model

Additionally, XFOIL [65] has been employed to calculate the airfoil aerodynamic forces with a complementary method.

Due to the variety of turbulence models, several discretization schemes were employed. The SIMPLE algorithm was used for the pressure-velocity coupling for all the cases studied. The spatial discretization regarding the gradient terms was selected to be the Least Squares Cell Based discretization. The rest of the spatial discretization schemes (pressure, momentum, turbulent quantities) were chosen to be at least of second order for all the cases. Finally, regarding the transient formulation, the Second Order Implicit formulation was chosen for the U-RANS (Reynolds Averaged Navier Stokes) models, whereas the Bounded Second Order Implicit were used for the SRS (Scale-Resolving Simulation) models.

Selection of the time step and calculation time

The selection of the time step for the simulations depends on the chosen turbulence model. For U-RANS models, it was assumed that only the fluctuations associated to vortex shedding are captured, related to a value of 0.2 for the Strouhal number [71] based on the blade chord (c) and the bulk velocity $\bar{u}$, thus corresponding to a vortex shedding period of:

$$T_{sh} = \frac{c}{0.2 \cdot \bar{u}} = 0.073\,\mathrm{s} \tag{4.25}$$

Assuming that at least 25 time steps per cycle are required to capture those fluctuations, the time step for the U-RANS simulations was chosen as $\Delta t_{U-RANS} = 2.5 \times 10^{-3}$ s. For SAS models, as higher fluctuation levels are expected, this time step was set to be one order of magnitude less than for U-RANS simulations, $\Delta t_{SAS} = 2.5 \times 10^{-4}$ s. This value lies between the value set for the U-RANS and for the LES simulations (not as much fluctuations as for the LES models is expected).

For wall-modeled Large Eddy Simulations, aiming at resolving around 80% of the turbulent kinetic energy of the flow [68], $\kappa_c L \simeq 38$ with $\kappa_c \sim 2\pi/\ell_c$, so that $\ell_c/L \simeq 0.16$. Applying the concept of the energy cascade ($u_{\ell_c}^3/\ell_c \simeq U^3/L$), that relates the scales and velocities of the greater vortices (L, U) and the vortices corresponding to the cut-off frequency of the LES filter (ℓ_c, u_{ℓ_c}), it is possible to determine the time step for the WMLES simulation: $\Delta t_{WMLES} \simeq \frac{1}{25}\frac{\ell_c}{u_{\ell_c}} \simeq \frac{1}{25}\frac{\ell_c}{U(\ell_c/L)^{1/3}} \simeq \frac{1}{25}\frac{0.16L}{U(0.16)^{1/3}} = \frac{0.16^{2/3}}{25}\frac{L}{U}$. Assuming that $L \sim \delta \sim 25$ mm and $U \sim 1.7$ m/s, one order of magnitude less than the mean flow velocity, the time step required for the wall-modeled Large Eddy Simulations simulations is $\Delta t_{WMLES} \simeq 1.75 \times 10^{-4}$ s.

Finally, for wall-resolved Large Eddy Simulations, the time step may be calculated as the ratio between the smallest cell size and the fluctuating velocity U. Assuming a $y^+ \sim 1$, the required time step is: $\Delta t_{LES} \simeq \frac{\Delta y}{U} \simeq \frac{3.5\times10^{-5}}{1.7} \simeq 2 \times 10^{-5}$ s. Table 4.5 collects the time step sizes selected for each family of turbulence models.

Table 4.5: Time step sizes selected for each family of turbulence models

Turbulence model family	Time step [s]	Average simulation time per case [h]
U-RANS	2.5×10^{-3}	6
SAS	2.5×10^{-4}	200
WMLES	1.75×10^{-4}	250
WRLES/DES	2×10^{-5}	500

The flow has been simulated at the following angles of attack: 0°, 5°, 10°, 15°, 20°, 25° and 30°. The simulations were performed using a 4-nodes Intel Core i7-52820K at 3.3 GHz and 64 Gb RAM, with the simulation time depending on the chosen turbulence model as stated in Table 4.5.

4.2.3. Prediction of the aerodynamic forces on the airfoil

Results from the U-RANS simulations

Figure 4.17 shows the experimental results from the wind tunnel (black line) alongside the predictions of XFOIL (blue line) and the different U-RANS models tested in this study. It may be observed that the predictions of XFOIL are quite accurate before the stall angle, as already known in the literature [65]. The experimental results present a characteristic hysteresis

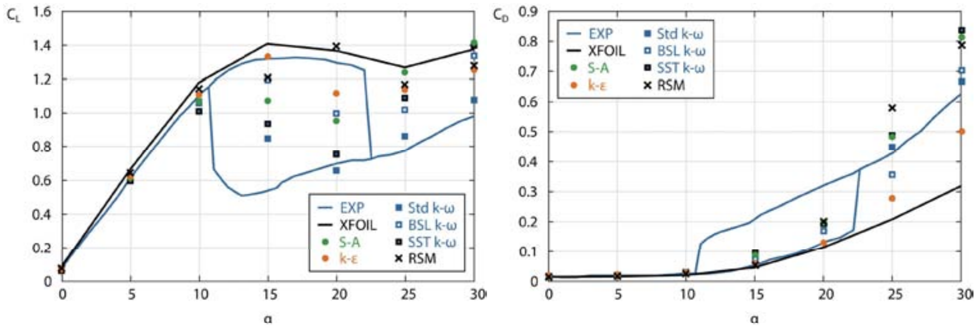

(a) Lift coefficient

(b) Drag coefficient

Figure 4.17: Comparison of experimental and U-RANS results

loop, typically found for airfoils at high angles of attack at low Reynolds numbers and related to the stall behavior of the airfoil and the possible formation of a laminar separation bubble [72]. Regarding the CFD models, both the Spalart-Allmaras (S-A) and k-epsilon ($k-\varepsilon$) models fail to accurately predict the airfoil aerodynamic forces after stall. The S-A model overpredicts both lift and drag, whereas the $k-\varepsilon$ model overpredicts lift but underpredicts drag, artificially increasing the performance of the airfoil. The Reynolds stress model (RSM) employed, besides requiring more computational effort (5 additional equations), did not yield better results. The best results were obtained with the $k-\omega$ models, which have been found to be well adapted to low-Reynolds flows with adverse pressure gradients [44]. More specifically, the Standard (Std) and Shear Stress Transport (SST) models seem to provide the best results. For these reasons, those two models were selected to perform Scale Resolving Simulations (Scale Adaptive Simulations and Detached Eddy Simulations) and provide more insight into the details of the flow around the airfoil. It must be noticed that the simulations were performed independently for every angle of attack, as the characterization of the hysteresis behavior of the airfoil is not within the scope of this work.

Results from the SRS simulations

Figure 4.18 shows the aerodynamic force predictions of the selected U-RANS models ($k-\omega$ Standard and SST) alongside the SRS models based on those U-RANS models (SAS and DES). Regarding the prediction of the airfoil aerodynamic forces, the $k-\omega$ Standard (U-RANS) is the most accurate model. The formulations based on the SST model are not so accurate in the U-RANS and SAS cases, especially at higher angles of attack. On the other hand, the DES formulation seems to predict reasonably well the forces at high angles of attack after the stall angle. Thus, the models that seem more suitable for the prediction of airfoil aerodynamic forces are the U-RANS $k-\omega$ Standard, the SAS (with $k-\omega$ Standard formulation) and the DES (with $k-\omega$ SST formulation), being the U-RANS $k-\omega$ Standard model the best recommendation if the only objective of the study is the prediction of the aerodynamic forces for an airfoil (insight into the flow field will be later discussed).

With the aim of investigating the causes underneath the differences in the predicted values between the three selected models, Figures 4.19, 4.20 and 4.22 have been added, showing the temporal evolution of the lift and drag coefficients for three angles of attack: 5° (low) , 15°

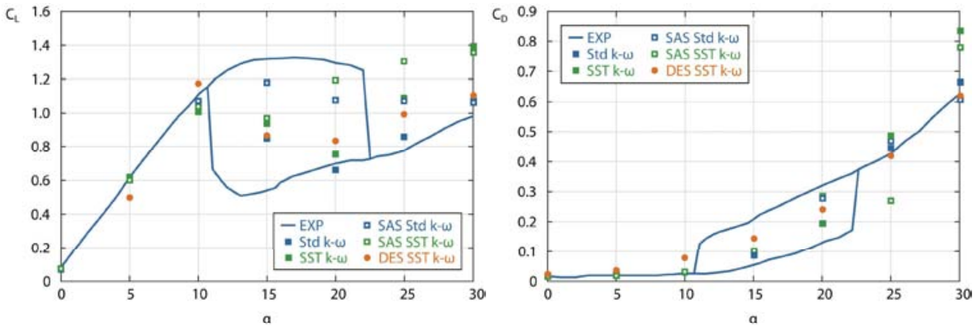

(a) Lift coefficient

(b) Drag coefficient

Figure 4.18: Comparison of the results from the selected U-RANS models with experimental and SRS results

(medium) and 25° (high). The experimental values are time-averaged, so they have been represented with dashed lines in the figures.

Regarding the predicted values at 5° (low angle of attack, Figure 4.19), both the U-RANS and SAS models predict values very close to the experimental values, whereas the DES model tends to underpredict lift and overpredict drag slightly. This could be explained by the small size of the boundary layer, still too attached to the airfoil, that could activate the LES filter of the DES modeling, affecting the U-RANS solution. In other words, it is not recommended to employ SRS models for the description of non-detached flows in case of relatively coarse grids with respect to the boundary layer size.

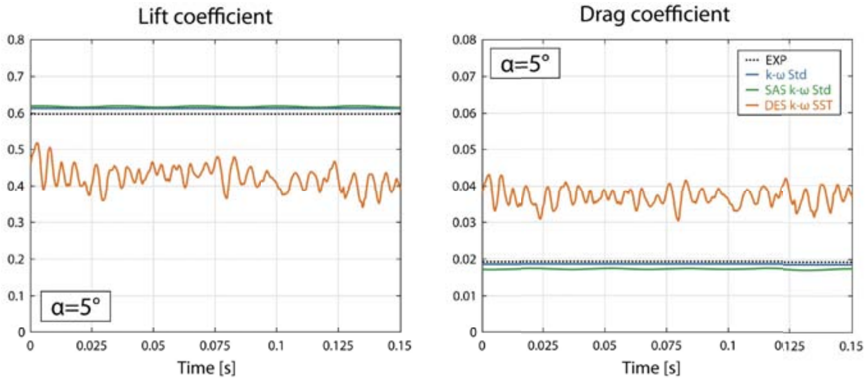

Figure 4.19: Evolution of lift and drag coefficients for $\alpha = 5°$

At a medium angle of attack (15°, Figure 4.20), the experimental values oscillate between a maximum and a minimum value (the result of the hysteresis loop related to stall, previously commented). All the turbulence models predict values between these experimental values (grey zone in Figure 4.20), so it is not easy to determine which of the models is the most suitable one. The U-RANS and DES models predict similar values for the lift, with the SAS formulation predicting higher values; whereas, for the drag prediction, the DES formulation is the one predicting higher values, with the U-RANS and SAS models predicting almost the same value. Figure 4.21, which shows the pressure coefficient on the airfoil at this angle of attack (15°), has been added to highlight the mechanisms behind the discrepancies between the values predicted by the three different models. The area enclosed by the pressure coefficient curve of the SAS model is substantially bigger than for the other two models, according to the higher lift values predicted by this model. On the other hand, the parts of the curves on the suction side are very similar for the three models. No specific recommendations can be provided regarding intermediate angles of attack.

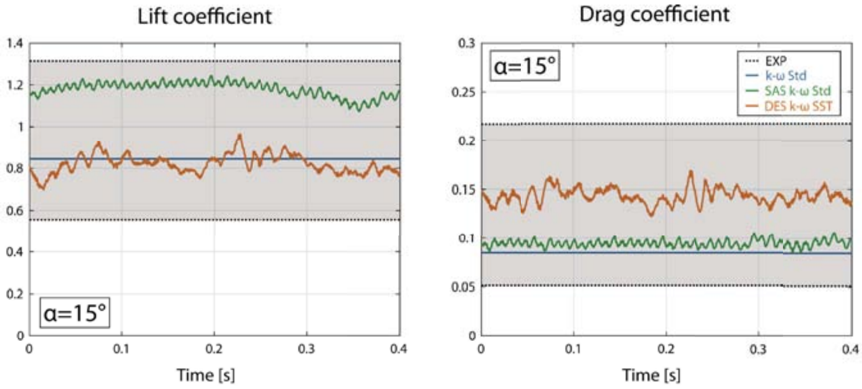

Figure 4.20: Evolution of lift and drag coefficients for $\alpha = 15^{\circ}$

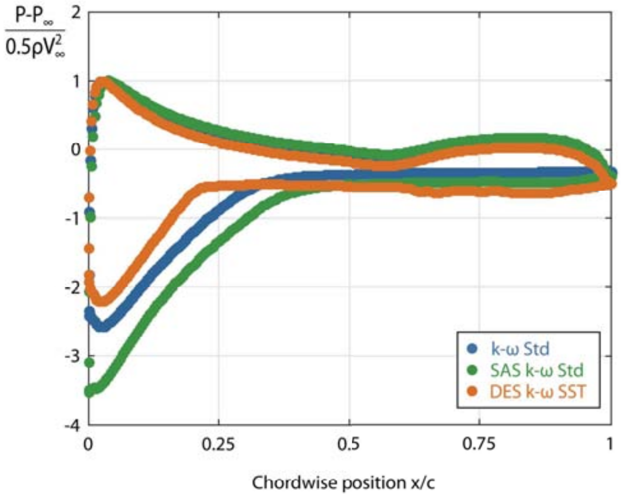

Figure 4.21: Pressure coefficient on the airfoil at $\alpha = 15^{\circ}$

Finally, at a high angle of attack (25°, Figure 4.22), there is a high instability in the values of lift and drag for the the SRS models. The fluctuations in the values of the forces are also patent in the U-RANS model. The three models oscillate around a mean value, being again the U-RANS model the one which yields values more similar to the experimental ones. In this case, the DES model performs better than the SAS model, which overpredicts slightly the values of both aerodynamic forces. This post-stall situation of the airfoil, with a fully detached wake, might benefit from the turbulent description of the DES model.

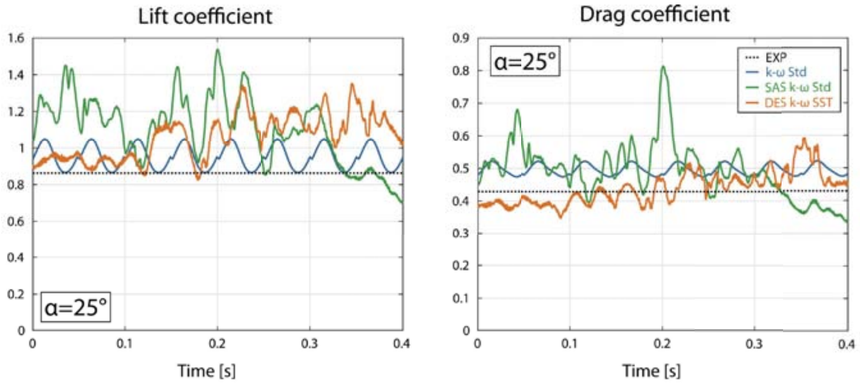

Figure 4.22: Evolution of lift and drag coefficients for $\alpha = 25^\circ$

Additional remarks

The mesh requirements for performing WMLES and LES simulations ([66], [67], [57]) were carefully followed. Despite the mesh, the results obtained were not substantially better than the results from the other turbulence models. Presumably, the mixing length model employed near the wall for the WMLES model is too simple compared to the other turbulence models employed, being unable to model correctly the adverse pressure gradient that develops around the airfoil surface. In the pure LES case, however, the reason behind the model performance is likely to be due to the need of a mesh refinement near the airfoil wall. Anyway, since both WMLES and LES simulations were already much more time-consuming than the other ones, a further mesh refinement would lead to extremely high computational times, far beyond the required balance between simulation time and accuracy for the present research.

4.2.4. Analysis of the flow field

After discussing the results of the prediction of the aerodynamic forces on the airfoil, the results for the flow field prediction around the airfoil are discussed in this section.

Figure 4.23 shows the contours of the instantaneous normalized velocity field around the airfoil for the three models selected in the previous section of this study: U-RANS $k - \omega$ Standard, SAS $k - \omega$ Standard and DES $k - \omega$ SST, and the three angles of attack detailed before: 5°, 15° and 25°. On top of the contours, isosurfaces of Q-criterion$= 50\ \mathrm{s}^{-2}$ have been added to make the identification of vortical structures easier. The Q-criterion method, the most widely used in LES-based simulations [73], defines a vortex as a spatial region where the Euclidean norm of the vorticity tensor (Ω_{ij}) dominates that of the rate of strain (S_{ij}) tensor: $Q = \frac{1}{2}\left(|\Omega_{ij}\Omega_{ij}|^2 - |S_{ij}S_{ij}|^2\right) > 0$.

The differences in the prediction of the flow field between the different models are quite apparent. The $k-\omega$ Standard model shows a clean flow pattern at all the angles of attack studied, with big blobs of isovalues of Q being convected by the incoming wind flow. The SAS $k-\omega$ Standard approach allows the break-up of these large structures into smaller scales. This approach leaves the U-RANS part of the model unaffected by the grid spacing [56], so it does not allow the deterioration of the model accuracy in regions of refined grid but insufficient flow instability (this behavior has been observed in DES models and could explain the results commented before for $\alpha = 5°$). However, in these cases where the flow instability is not strong enough, the SAS will remain in U-RANS mode and will not produce unsteady structures (as seen precisely for $\alpha = 5°$ in Figure 4.23) [56]. The DES $k-\omega$ SST formulation produces unsteady structures for all the angles of attack, yielding a more realistic flow pattern behind the airfoil, accordingly to the typical patterns observed in the literature for airfoils at low Reynolds numbers ([74]). Some roll-up vortices caused by Kelvin-Helmholtz instabilities in the shear layer may be identified (marked as KH in Figure 4.23), and a small wake with not very organized structures becomes apparent as in the work of Yarusevych et al. [75].

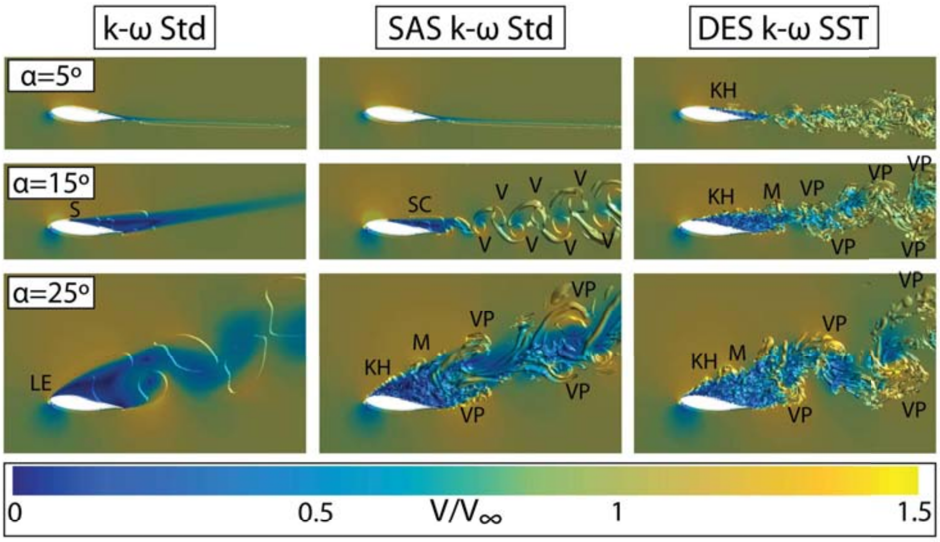

Figure 4.23: Normalized velocity field around the airfoil with iso-surfaces at $Q = 50\ s^{-2}$

With the increase of the angle of attack, the widening of the wake and vortex shedding phenomena become apparent. The separation of the shear layer (S) and the development of a stall cell (SC), also found in the work of Sarlak et al. [72], are detectable with the three turbulence models employed. Additionally, at $\alpha = 15°$, the flow instability is strong enough for the SAS formulation to produce unsteady structures. A coherent vortex shedding pattern, similar to a von Karman vortex street, appears downstream from the airfoil in a clearly organized pattern (the identified vortices are marked as V in Figure 4.23). Nevertheless, the DES formulation shows a more intricate pattern, in which the periodicity of the shedding phenomena is not so clearly visible, but is clearly more realistic according to the bibliography ([75],[74], [76]). Kelvin-

Helmholtz instabilities arise in the shear layer, generating roll-up vortices (KH) that eventually merge (M), then break down into smaller scales and accumulate into larger structures forming packets. These vortex packets (VP), such as the ones found by Rodríguez et al. [76], are present, but their pattern is not so clear, suggesting a broadband frequency centered activity similar to the one found by Yarusevych et al. [75]. This is related to weaker and less coherent structures, which could be generated by a the separation of a bubble from the airfoil surface [72] that could explain the static stall hysteresis behavior found in this airfoil. Finally, for the highest angle of attack, $\alpha = 25^{\circ}$, the wake is so wide and unsteady that even the U-RANS $k-\omega$ Standard is able to capture the vortex shedding blobs in the flow as they are convected downstream. Separation occurs already at the airfoil leading edge (LE) for the three turbulence models. Roll-up vortices in the shear layer related to Kelvin-Helmholtz instabilities (KH) and their merging (M) are captured by both SAS and DES models, and vortex packets (VP) are easily identifiable. In this case, shifting towards more scale-resolving models, such as SAS or DES, increases substantially the richness of the flow description (and as previously confirmed, with no harsh effect in the prediction of the aerodynamic forces on the airfoil).

Lastly, the Power Spectrum Density (PSD) of the instantaneous velocity signal has been computed at a point placed in the middle of the airfoil wake at $\alpha = 15^{\circ}$, $0.24c$ downstream the airfoil. Figure 4.24 shows the results for the two scale-resolving models (SAS k-ω Std and DES k-ω SST) as a function of the Strouhal number, providing more insight into the pictures in the middle row of Figure 4.23. The results from the RANS model are not shown, as the magnitude of the fluctuations captured was not significant, in agreement with the flow field depicted in Figure 4.23. The Strouhal numbers have been calculated with the projection of the airfoil chord in the cross-streamwise direction and the incoming flow velocity as $St = fc\,\sin(\alpha)/\bar{u}$, where f is each corresponding frequency and c is the chord. With the scale-resolving models, higher frequencies may be captured and the energy is no longer concentrated in the large-scales, as now they are able to break up. In the SAS modeling, the peak in the spectrum is produced at a $St = 0.438$. The clear peaks of the spectrum are related to the clean vortex street that was apparent in Figure 4.23. On the other hand, regarding the DES simulations, the spectrum is smoother, with a small peak at $St = 0.486$, the same Strouhal number as for the SAS simulations. Another peak at around half of that value, $St = 0.233$, is also apparent in the spectrum, and may be related to the subharmonic frequency due to the merging of the roll-up vortices from the shear layer. This subharmonic peak has been also observed in previous research ([75], [76]). Finally, a broadband frequency centered activity is visible in the spectrum, related to the low-frequency oscillation mechanism reported at near-stall angles by Rodríguez et al. [76]. The DES modeling allows a more realistic break up of the large eddies and the capture of this broadband frequency activity, which may explain the sea of vortices found in Figure 4.23, although some periodicity may be deduced from a deeper analysis of the figure.

From the previous analyses of this study, it is clear that the turbulence model should be adjusted depending on the desired outcome from the simulations. The U-RANS model used in this study is able, at a very low computational cost (3% of the simulation time of a SAS), to predict accurately the aerodynamic forces on an airfoil. So, if the only aim were to predict the forces on an airfoil, it would make sense to perform only a U-RANS simulation using the $k - \omega$ model for the closure of turbulence. However, if it were desired to characterize the flow field behind the airfoil, at least a SAS formulation should be employed and a DES formulation would be advisable to get information about the smallest scales of the flow (always

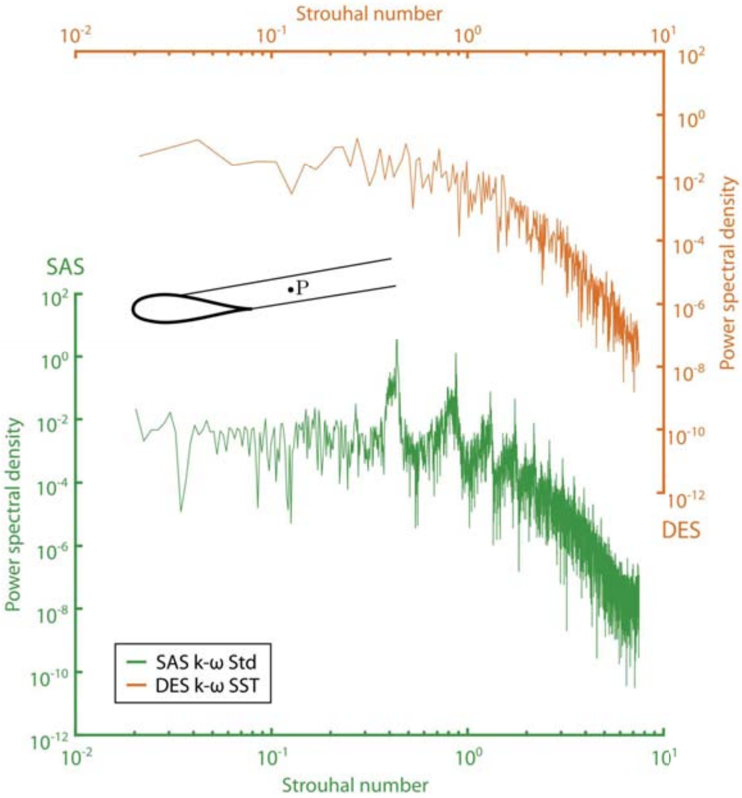

Figure 4.24: Power spectral density (PSD) of the instantaneous velocity signal in the middle of the wake, 0.24c downstream of the airfoil, at $\alpha = 15°$

being careful with the grid in cases with not enough flow instability). Additionally, in the case of airfoils suffering from hysteresis loops in the aerodynamic forces, special attention should be paid to the turbulence model in order to capture accurately the separation of the boundary layer from the airfoil.

Nevertheless, these conclusions should not be straightforwardly extrapolated to airfoils working as part of a vertical-axis wind turbine. Even if it were desired to predict only the forces on the turbine blades (and thus a U-RANS model would be the best option in terms of accuracy/cost), when the blades pass by the downstream half of the turbine, it is unlikely that they will find the flow conditions shown in Figure 4.23, left. Indeed, a correct description of the flow downstream from the airfoils passing by the upwind half of the turbine such as the provided by a DES model could prove itself useful to a better prediction of the incoming flow conditions in the downstream part of the turbine. In addition, the flow field developed by the turbine will depend strongly on the ratio between its rotational speed and the incoming wind speed, leading to different flow patterns with more or less detached flow from the airfoils. Thus, it could be wise to apply the SRS models with high resolution capabilities when the rotational velocity of the turbine is slow compared with the incoming wind speed to correctly resolve the detached flow field that will arise. On the other hand, turbines with higher rotational speeds will present more attached boundary layers and smaller eddy sizes. In these cases, maybe a U-RANS model is able to describe the flow field with relatively enough accuracy whilst reducing the computational resources required substantially.

4.2.5. Conclusions

Different turbulence models have been applied to predict the performance of a particular VAWT airfoil. The best results among the U-RANS models were obtained with the $k-\omega$ turbulence models. $k-\omega$-based SAS and DES models predict the aerodynamic forces with relatively good accuracy, resolving also the flow scales that arise with detached flow conditions. U-RANS models are able (with only 3% of the computational cost of a SAS), to predict accurately the aerodynamic forces on the airfoil. On the other hand, SAS or DES formulations are advisable to obtain information about the smallest scales of the flow. In addition, in the case of hysteresis loops in the aerodynamic forces, special attention should be paid to the turbulence model to capture accurately the separation of the boundary layer from the airfoil. Future studies could focus on the characterization of the hysteresis loop of this airfoil.

In the case of airfoils working as part of a vertical-axis wind turbine, these conclusions do not extrapolate directly. The flow field at the downstream half of the turbine is affected by the flow detached from the airfoils at the upwind half, so a correct description of the flow downstream the airfoils such as that provided by SRS models seems more meaningful than a U-RANS model. In addition, as the flow field developed by the turbine depends strongly on the ratio between its rotational speed and the incoming wind velocity, employing U-RANS or SRS formulations depending on the expected flow conditions would provide the best ratio between the quality of the results and the computational cost.

References

[1] A. Meana-Fernández, J.M. Fernández Oro, K.M. Argüelles Díaz, M. Galdo-Vega, and S. Velarde-Suárez, *Application of richardson extrapolation method to the CFD simulation of vertical-axis wind turbines and analysis of the flow field,* Engineering Applications of Computational Fluid Mechanics **13**, 359 (2019).

[2] A. Meana-Fernández, J.M. Fernández Oro, K.M. Argüelles Díaz, and S. Velarde-Suárez, *Turbulence-model comparison for aerodynamic-performance prediction of a typical vertical-axis wind-turbine airfoil,* Energies **12**, 488 (2019).

[3] C. Sui, K. Lee, Z. Huque, and R. Kommalapati, *Transitional effect on turbulence model for wind turbine blade,* in *Proceedings of the ASME 2015 Power Conference POWER 2015* (ASME, San Diego, California, 2015) pp. 1–8.

[4] C. Lee, S. Min, C. Park, and S. Kim, *Optimal design and verification tests of cycloidal vertical axis wind turbine,* Journal of Renewable and Sustainable Energy **7**, 063116 (2015).

[5] Q. Li, T. Maeda, Y. Kamada, J. Murata, T. Kawabata, K. Shimizu, T. Ogasawara, A. Nakai, and T. Kasuya, *Wind tunnel and numerical study of a straight-bladed vertical axis wind turbine in three-dimensional analysis (Part I: For predicting aerodynamic loads and performance),* Energy **106**, 443 (2016).

[6] Y. Yang, Z. Guo, Y. Zhang, H. Jinyama, and Q. Li, *Numerical Investigation of the Tip Vortex of a Straight-Bladed Vertical Axis Wind Turbine with Double-Blades,* Energies **10**, 1721 (2017).

[7] H. Lam and H. Peng, *Study of wake characteristics of a vertical axis wind turbine by two and three-dimensional computational fluid dynamics simulations,* Renewable Energy **90**, 386 (2016).

[8] G. Abdalrahman, W. Melek, and F.-S. Lien, *Pitch Angle Control for Small-Scale Darrieus Vertical Axis Wind Turbine with Straight Blades (H-type VAWT),* Renewable Energy **114**, 1353 (2017).

[9] M. Bhargav, V. Kishore, and V. Laxman, *Influence of fluctuating wind conditions on vertical axis wind turbine using a three dimensional CFD model,* Journal of Wind Engineering and Industrial Aerodynamics **158**, 98 (2016).

[10] C. Li, Y. Xiao, Y.-L. Xu, Y.-X. Peng, G. Hu, and S. Zhu, *Optimization of blade pitch in H-rotor vertical axis wind turbines through computational fluid dynamics simulations,* Applied Energy **212**, 1107 (2018).

[11] A. Bianchini, F. Balduzzi, P. Bachant, G.Ferrara, and L.Ferrari, *Effectiveness of two-dimensional CFD simulations for Darrieus VAWTs: a combined numerical and experimental assessment,* Energy Conversion and Management **136**, 318 (2017).

[12] W.-H. Chen, C.-Y. Chen, C.-Y. Huang, and C.-J. Hwang, *Power output analysis and optimization of two straight-bladed vertical-axis wind turbines,* Applied Energy **185**, 223 (2017).

[13] Y. Chen and Y. Lian, *Numerical investigation of vortex dynamics in an H-rotor vertical axis wind turbine,* Engineering Applications of Computational Fluid Mechanics **9**, 21 (2015).

[14] L. Meng, Y.-P. He, J. Wu, Y.-S. Zhao, and Z.-W. Guo, *Simulation of Tower Shadow Effect for Offshore Wind Turbine by CFD Method,* in *Proceedings of the Twenty-sixth (2016) International Ocean and Polar Engineering Conference* (International Society of Offshore and Polar Engineers (ISOPE), Rhodes, Greece, 2016) pp. 385–390.

[15] M. Make and G. Vaz, *Analyzing scaling effects on offshore wind turbines using CFD,* Renewable Energy **83**, 1326 (2015).

[16] F. Balduzzi, A. Bianchini, G. Ferrara, and L. Ferrari, *Dimensionless numbers for the assessment of mesh and timestep requirements in CFD simulations of Darrieus wind turbines,* Energy **97**, 246 (2016).

[17] X. Jin, Y. Wang, W. Ju, J. He, and S. Xie, *Investigation into parameter influence of upstream deflector on vertical axis wind turbines output power via three-dimensional CFD simulation,* Renewable Energy **115**, 41 (2018).

[18] S.-Y. Lin, Y.-Y. Lin, C.-J. Bai, and W.-C. Wang, *Performance analysis of vertical-axis-wind-turbine blade with modified trailing edge through computational fluid dynamics,* Renewable Energy **99**, 654 (2016).

[19] B. Wang, L. Cot, L. Adolphe, and S. Geoffroy, *Estimation of wind energy of a building with canopy roof,* Sustainable Cities and Society **35**, 402 (2017).

[20] A. Subramanian, S. Yogesh, H. Sivanandan, A. Giri, M. Vasudevan, V. Mugundhan, and R. Velamati, *Effect of airfoil and solidity on performance of small scale vertical axis wind turbine using three dimensional CFD model,* Energy **133**, 179 (2017).

[21] D. Wekesa, C. Wang, Y. Wei, and W. Zhu, *Experimental and numerical study of turbulence effect on aerodynamic performance of a small-scale vertical axis wind turbine,* Journal of Wind Engineering and Industrial Aerodynamics **157**, 1 (2016).

[22] H. Lei, D. Zhou, J. Lu, C. Chen, Z. Han, and Y. Bao, *The impact of pitch motion of a platform on the aerodynamic performance of a floating vertical axis wind turbine,* Energy **119**, 369 (2017).

[23] S. Qamar and I. Janajreh, *A comprehensive analysis of solidity for cambered Darrieus VAWTs,* International Journal of Hydrogen Energy **42**, 19420 (2017).

[24] W. Tian, Z. Mao, X. An, B. Zhang, and H. Wen, *Numerical study of energy recovery from the wakes of moving vehicles on highways by using a vertical axis wind turbine,* Energy **141**, 715 (2017).

[25] P.-E. Réthoré, P. van der Laan, N. Troldborg, F. Zahle, and N. Sørensen, *Verification and validation of an actuator disc model,* Wind Energy **17**, 919 (2014).

[26] I. Marinić-Kragić, D. Vucina, and Z. Milas, *Numerical workflow for 3D shape optimization and synthesis of vertical-axis wind turbines for specified operating regimes,* Renewable Energy **115**, 113 (2018).

[27] A. Rezaeiha, I. Kalkman, and B. Blocken, *CFD simulation of a vertical axis wind turbine operating at a moderate tip speed ratio: Guidelines for minimum domain size and azimuthal increment,* Renewable Energy **107**, 373 (2017).

[28] A. Rezaeiha, I. Kalkman, H. Montazeri, and B. Blocken, *Effect of the shaft on the aerodynamic performance of urban vertical axis wind turbines,* Energy Conversion and Management **149**, 616 (2017).

[29] D. Lockard, *In search of grid converged solutions,* Procedia Engineering **6**, 224 (2010).

[30] J. Vassberg and A. Jameson, *In pursuit of grid convergence for two-dimensional Euler solutions,* Journal of Aircraft **47**, 1152 (2010).

[31] P. Roache, *Verification and Validation in Computational Science and Engineering* (Hermosa Publishers, Albuquerque, USA, 1998).

[32] I. Celik and J. Li, *Assessment of numerical uncertainty for the calculations of turbulent flow over a backward-facing step,* International Journal For Numerical Methods in Fluids **49**, 1015 (2005).

[33] C. Marchi, M. Martins, L. Novak, L. Araki, M. Pinto, S. Gonçalves, D. Moro, and I. Freitas, *Polynomial interpolation with repeated Richardson extrapolation to reduce discretization error in CFD,* Applied Mathematical Modelling **40**, 8872 (2016).

[34] E. Tengs, P.-T. Storli, and M. Holst, *Optimization procedure for variable speed turbine design,* Engineering Applications of Computational Fluid Mechanics **12**, 652 (2018).

[35] K. Almohammadi, D. Ingham, L. Maa, and M. Pourkashan, *Computational fluid dynamics (CFD) mesh independency techniques for a straight blade vertical axis wind turbine,* Energy **58**, 483 (2013).

[36] E. Tingey and A. Ning, *Parameterized vertical-axis wind turbine wake model using CFD vorticity data,* in *Proceedings of the ASME Wind Energy Symposium* (American Institute of Aeronautics and Astronautics, San Diego, California, USA, 2016) pp. 1–12.

[37] S. Zadeh, M. Komeili, and M. Paraschivoiu, *Mesh convergence study for 2-D straight-blade vertical axis wind turbine simulations and estimation for 3-D simulations,* Transactions of the Canadian Society for Mechanical Engineering **38**, 487 (2014).

[38] A. Meana-Fernández, I. Solís-Gallego, J.M. Fernández Oro, K.M. Argüelles Díaz, and S. Velarde-Suárez, *Parametrical evaluation of the aerodynamic performance of vertical axis wind turbines for the proposal of optimized designs,* Energy **147**, 504 (2018).

[39] E. Amet, T. Maitre, C. Pellone, and J. Achard, *2D numerical simulations of blade-vortex interaction in a Darrieus turbine,* Journal of Fluids Engineering-Transactions of the ASME **131**, 111103 (2009).

[40] A. Rezaeiha, I. Kalkman, and B. Blocken, *Effect of pitch angle on power performance and aerodynamics of a vertical axis wind turbine,* Applied Energy **197**, 132 (2017).

[41] A. Alaimo, A. Esposito, A. Messineo, C. Orlando, and D. Tumino, *3D CFD analysis of a vertical axis wind turbine,* Energies **8**, 3013 (2015).

[42] M. Mohamed, A. Ali, and A. Hafiz, *CFD analysis for H-rotor Darrieus turbine as a low speed wind energy converter,* Engineering Science and Technology, an International Journal **18**, 1 (2015).

[43] F. Menter, *Two-equation eddy-viscosity turbulence models for engineering applications,* AIAA Journal **32**, 1598 (1994).

[44] C. Argyropoulos and N. Markatos, *Recent advances on the numerical modelling of turbulent flows,* Applied Mathematical Modelling **39**, 693 (2015).

[45] L. Richardson and J. Gaunt, *The deferred approach to the limit,* Philosophical Transactions of the Royal Society of London **Ser.A 226**, 299 (1927).

[46] P. Roache, *Quantification of uncertainty in computational fluid dynamics,* Annual Review of Fluid Mechanics **29**, 123 (1997).

[47] *Procedure for estimation and reporting of uncertainty due to discretization in CFD applications,* Journal of Fluids Engineering **130**, 078001 (2008).

[48] G. Bedon, S. D. Betta, and E. Benini, *Performance-optimized airfoil for Darrieus wind turbines,* Renewable Energy **94**, 328 (2016).

[49] P. Sabaeifard, H. Razzaghi, and A. Forouzandeh, *Determination of Vertical Axis Wind Turbines Optimal Configuration through CFD Simulations,* in *IPCBEE vol.28* (IACSIT Press, Singapore, 2012) pp. 109–113.

[50] P. Delafin, T. Nishino, L. Wang, and A. Kolios, *Effect of the number of blades and solidity on the performance of a vertical axis wind turbine,* Journal of Physics: Conference Series **753** (2016).

[51] R. Gosselin, G. Dumas, and M. Boudreau, *Parametric study of H-Darrieus vertical-axis turbines using uRANS simulations,* in *21st Annual Conference of the CFD Society of Canada* (Sherbrooke, Canada, 2013) pp. 1–16.

[52] I. Paraschivoiu, *Wind Turbine Design: With Emphasis on Darrieus Concept* (Presses internationales Polytechnique, Canada, 2002).

[53] M. Bausas and L. Danao, *The aerodynamics of a camber-bladed vertical axis wind turbine in unsteady wind,* Energy **93**, 1155 (2015).

[54] M. Claessens, *The Design and Testing of Airfoils for Application in Small Vertical Axis Wind Turbines*, Master's thesis (2006).

[55] C. Tropea, A. Yarin, and J. Foss, *Handbook of Experimental Fluid Mechanics* (Springer, 2007).

[56] ANSYS, Inc., *ANSYS-FLUENT User's Guide. Release 16.2,* (2016).

[57] P. Tucker, *Unsteady Computational Fluid Dynamics in Aeronautics* (Springer, 2014).

[58] M. Athadkar and S. Desai, *Importance of the extent of far-field boundaries and of the grid topology in the CFD simulation of external flows,* International Journal of Mechanical and Production Engineering **2**, 69 (2014).

[59] H. Cao, *Aerodynamics Analysis of Small Horizontal Axis Wind Turbine Blades by Using 2D and 3D CFD Modelling*, Master's thesis, University of Central Lancashire (2011).

[60] J. Hawley, *An OpenFoam analysis - The Joukowski airfoil at different viscosities*, Tech. Rep. (2013).

[61] V. Kasibhotla and D. Tafti, *Large eddy simulation of the flow past pitching NACA0012 airfoil at 1e5 Reynolds number,* in *Proceedings of the ASME 2014 4th Joint US-European Fluids Engineering Division Summer Meeting*, Vol. FEDSM2014 (ASME, Chicago, Illinois, USA, 2014) pp. FEDSM2014–21588.

[62] C. Liang and H. Li, *Aerofoil optimization for improving the power performance of a vertical axis wind turbine using multiple streamtube model and genetic algorithm,* Royal Society Open Science **5**, 180540 (2018).

[63] J. M. Sanz, *CFD study of thick flatback airfoils using OpenFOAM*, Master's thesis, Technical University of Denmark (2011).

[64] H. Shah, S. Mathew, and C. Lim, *Numerical simulation of flow over an airfoil for small wind turbines using the* $\gamma - re_\theta$ *model,* International Journal of Energy and Environmental Engineering **6**, 419 (2015).

[65] M. Drela, *Xfoil: An analysis and design system for low reynolds number airfoils,* in *Proceedings of the Conference Notre Dame* (Springer-Verlag Berlin Heidelberg, Indiana, USA, 1989) pp. 1–12.

[66] S. Dahlström and L. Davidson, *Large eddy simulation of the flow around an aerospatiale a-aerofoil,* in *European Congress on Computational Methods in Applied Sciences and Engineering ECCOMAS 2000* (ECCOMAS, Barcelona, Spain, 2000) pp. 1–20.

[67] L. Davidson and S. Dahlström, *Hybrid LES-RANS: An approach to make LES applicable at high Reynolds number,* International Journal of Computational Fluid Dynamics **19**, 415 (2005).

[68] S. Pope, *Turbulent Flows* (Cambridge University Press, Cambridge, UK, 2000).

[69] P. Tucker, *Computation of unsteady turbomachinery flows: Part 2 - LES and hybrids,* Progress in Aerospace Sciences **47**, 546 (2011).

[70] D. Chapman, *Computational aerodynamics development and outlook,* AIAA Journal **17**, 1293 (1979).

[71] F. White, *Fluid Mechanics, 7th Ed.* (McGraw-Hill, 2011).

[72] H. Sarlak, A. Frère, R. Mikkelsen, and J. Sørensen, *Experimental investigation of static stall hysteresis and 3-dimensional flow structures for an NREL S826 wing section of finite span,* Energies **11**, 1418 (2018).

[73] G. Haller, *An objective definition of a vortex,* Journal of Fluid Mechanics **525**, 1 (2005).

[74] M. Alam, Y. Zhou, H. Yang, H. Guo, and J. Mi, *The ultra-low Reynolds number airfoil wake,* Experiments in Fluids **48**, 81 (2010).

[75] S. Yarusevych, P. Sullivan, and J. Kawall, *On vortex shedding from an airfoil in low-Reynolds-number flows,* Journal of Fluid Mechanics **632**, 245 (2009).

[76] I. Rodríguez, O. Lehmkuhl, R. Borrel, and A. Oliva, *Direct numerical simulation of a NACA0012 in full stall,* International Journal of Heat and Fluid Flow **43**, 194 (2013).

5

Design, construction and testing of a VAWT experimental demonstrator

Insanity is doing the same thing over and over again,
but expecting different results.

Rita Mae Brown (1944 - currently)

Murphy's Law doesn't mean that something bad will happen.
It means that whatever can happen, will happen.

Cooper, Interstellar (2014)

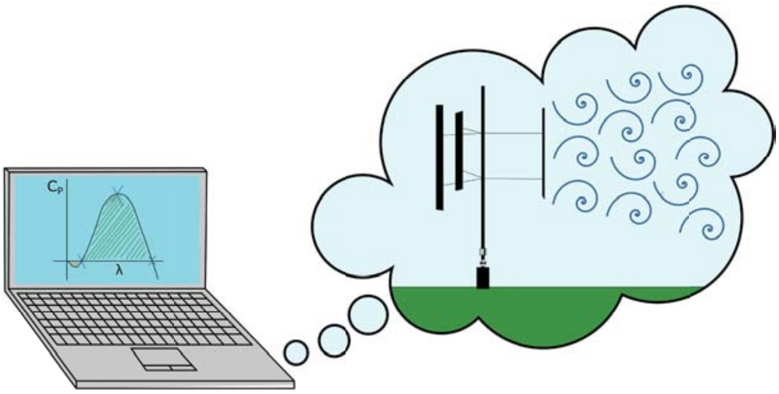

THIS chapter collects all the procedures followed to design, build and test a VAWT experimental demonstrator in the wind tunnel of the laboratory of the Fluid Mechanics Area. The methodology developed in the previous chapters has proven to be useful for the proposal and performance prediction of VAWT optimized designs. However, before fabricating a real-scale turbine, wind tunnel experiments on small-scale models may help to provide more insight into the actual performance of the design. After revising some designs found in the literature, a design is proposed using the methodologies presented in this thesis, considering the constraints of the experimental equipment available in the laboratory. After experiencing unfortunate issues with the first prototype, research into blade fabrication technologies and different design techniques was performed. This allowed the fabrication of a second prototype, which was suitable for the wind tunnel tests. The experimental results obtained were compared with those from the predictive models, finding good correspondence.

5.1. Introduction and research gaps addressed

Although it requires more investment than analytical models or numerical simulations, wind tunnel testing of experimental models is one of the most useful techniques to predict the performance of real-scale applications. As explained in Chapter 2, they do not neglect any flow feature. Therefore, many researchers try to develop experimental models to validate their simulations. Nevertheless, the wind tunnel test section size constraints the maximum size of the model that may be tested, so most of the tests are usually performed with small-scale models.

Although some researchers have tested actual turbines with large diameters ([1], [2], [3], [4] [5]) in field applications, previous wind tunnel testing helps to reduce development costs, until the design is almost complete. In these cases, an actual alternator may be used to obtain the electrical power generated by the turbine [5]. Nevertheless, some authors, after calculating the inertia of the turbine, were able to obtain the torque by measuring the angular acceleration of the turbine when a particular known value of torque was applied to it [2].

When testing a small-scale mode in a wind tunnel, attention must be paid to keep the dimensionless numbers introduced in Section 2.2 as close as possible to the ones corresponding to the real-scale machine. The number of blades and rotor solidity are easy to be maintained when scaling the geometry, and the tip-speed ratio is typically varied during the tests, obtaining the power coefficient as the result. However, difficulties may arise when trying to keep the Reynolds number equal to the real-scale application, so it is typically assumed that the small-scale model is working similarly to the real-scale machine if both Reynolds number are of the same order of magnitude.

Some authors, such as Bergeles, Michos and Anathassiadis [6], Bravo, Tullis and Ziada [7], Fiedler and Tullis [8], Raciti Castelli et al. [9] or Li et al. [10], have been able to measure the performance of VAWT prototypes with diameters larger than 1 m. With this size, there was almost no scaling done to the design before wind tunnel testing, so these turbines were suited for actual wind energy production after the wind tunnel tests were successful. This has been possible thanks to the use of large wind tunnels, which allowed low blockage levels at their test sections. Typically, torque is measured via torque transducers [10]. Another option is to combine a brake and a load cell coupled to the motor connected to the turbine [7], [8]. Note that most of these turbines are already considered “small VAWTs”, despite being the largest ones successfully tested in wind tunnels (data from Raciti Castelli et al. [9] were used for the experimental validation of the model presented in Chapter 3).

As typical sizes of the wind tunnels found in laboratories all over the world do not allow testing such large machines, most experimental tests are performed for VAWTs with diameters smaller than 1 m. Figure 5.1 shows the benchmark presented in this introduction, where it may be appreciated that most of the turbines fall in the range of diameters below 1 m. With this size, self-starting issues and the high rotational speeds required to reach the same tip-speed ratio values than larger turbines compel turbine designers to choose higher solidity values (it was presented in Chapter 3 that an increase in solidity lead to lower rotational speeds and helped the turbine self-start process). Nevertheless, as it may be observed in Figure 5.1, these solidity values are clearly far from the optimal power generation region for VAWTs. Additionally, the maximum power coefficient of these designs lay near the values obtained with optimized Savonius designs, which, in addition, do not present self-starting issues. Hence, developing an optimized VAWT with less than 1 m diameter that works efficiently becomes a really challenging task. Figure 5.1 also shows the values of the first prototype attempt performed in this research and the final prototype design, in the context of the presented benchmark.

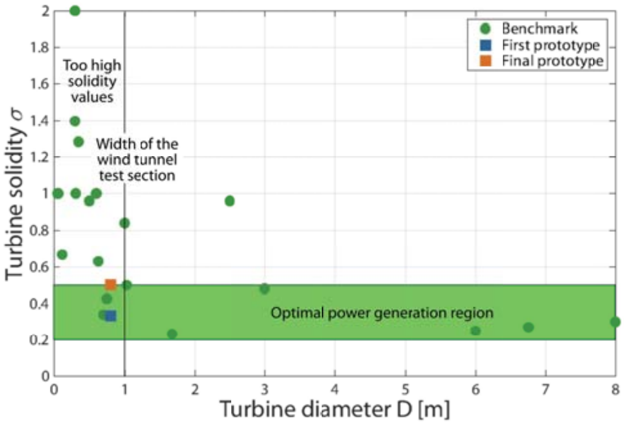

Figure 5.1: Benchmark of different VAWT experimental designs

An option to increase the Reynolds number of the experimental tests is using water channels as an alternative to wind tunnels, thanks to the higher density of water. These channels also enable using dyes for flow visualization, as performed by Brochier et al. [11], who used a water channel to study dynamic stall on the blades of a VAWT model. They also used Laser Doppler Velocimetry (LDV) to measure velocities quantitatively. Fujisawa and Takeuchi [12] and Fujisawa and Shibuya [13] used dye injection and performed Particle Image Velocimetry (PIV) measurements around the blade to obtain the flow velocity field. In these cases, the turbine worked thanks to a motor that set the desired rotational speed, as these turbines had diameters of 12 [11] and 6 cm [12], [13]. More recently, Bachant and Wosnik [14] have been able to perform experiments on a high-solidity turbine with a diameter of 1 m, measuring the torque with a transducer and the wake velocities with LDV, studying the effects of the Reynolds number.

Regarding wind tunnel experiments for the characterization of the performance of VAWT prototypes, usually torque and rotational speed are measured to obtain the power captured by the turbine [15]. The most direct method for torque measurement are torque transducers [16], [17]. However, these transducers are more expensive than other methods and the expected torque values must be known before acquiring them. Therefore, other methodologies such as measuring torque by braking the turbine and using spring balances or load cells are commonly used [18], [19], [20]. Edwards, Danao and Howell [21] developed a novel procedure for the determination of the experimental power curve of a VAWT. They would accelerate the turbine from rest without blades, until it reached the desired tip-speed ratio. Afterwards, they would brake the turbine with a known braking torque. By measuring the angular deceleration and knowing the inertia of the turbine, it was possible to determine the resistive torque of the structure. By repeating the same procedure with the blades mounted, they would obtain a different value of torque. The aerodynamic torque of the turbine would be then calculated from the difference between these two values. This procedure, named as "spindown-test", was also employed by Eboibi, Danao and Howell [22] to study the influence of solidity on the performance and flow field of a VAWT. Wind tunnel experiments on VAWT have been also performed by Ferreira et al. [23] to investigate the effect of skewed flow on a VAWT. Jeong, Lee and Kwon [24] have studied the effect of blockage on the performance of a high-solidity VAWT. Finally, Parker and Leftwich [25] performed PIV experiments for flow visualization, identifying blockage at high tip-speed ratio values, with negative velocities appearing in the wake region.

Figure 5.1 shows a line representing the width of the wind tunnel test section available in the laboratory of the Fluid Mechanics Area. It may be appreciated that there is a research gap regarding lift-driven VAWTs below 1 m diameter, optimized so that they yield the maximum possible amount of energy, with just the turbines designed by Edwards et al. [21] and Ferreira et al. [23] inside this region. Therefore, it was decided to build an experimental prototype inside this optimum region. Additionally, a low solidity value of the turbine would allow employing the analytical model developed in Chapter 3 alongside CFD simulations.

5.2. Experimental methodology

5.2.1. Experimental facility

The wind tunnel to be employed for the characterization of the model is a closed-loop, open jet wind tunnel, comprising a test chamber 420 cm long with a cross-sectional area of 445 x 280 cm^2 (width x height). The wind tunnel is suited to perform acoustic measurements. The nozzle discharge section is 115 x 100 cm^2. The scheme of the wind tunnel is shown in Figure 5.2. Following the recommendations for wind tunnel blockage values from NASA [26], the maximum dimensions of the prototype to reduce blockage were calculated to be 80 cm x 60 cm (width x height). Thus, the diameter of the small-scale rotor was chosen to be D=80 cm and the blade span was chosen as H=60 cm, the maximum possible size to capture as much energy from the wind as possible.

Previous measurements of the turbulence level at the wind tunnel test sections obtained a value of approximately 5%. So firstly, to try to reduce this turbulence level, a home-made wood honeycomb was built and set in the settling chamber alongside a sewed screen. Figure 5.3 shows the construction and assembly procedure of the honeycomb, as well as the complete honeycomb assembly.

After assembling the honeycomb and screen, hot-wire measurements were performed at

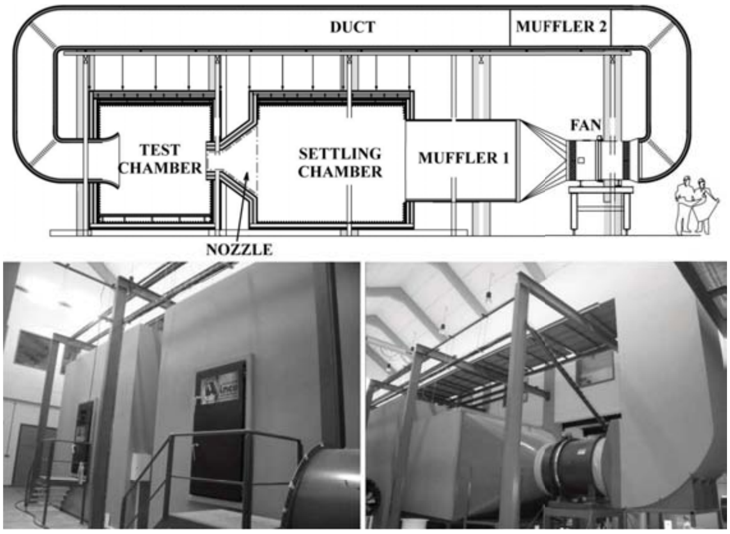

Figure 5.2: Wind tunnel used for the experimental measurements

the wind tunnel test section at different z positions alongside the test section width w. As it may be observed in Figure 5.4, the overall turbulence level $TI = (u'^2 + 2v'^2)^{1/2}$ has been reduced from 5 to roughly 3%, achieving a reduction in longitudinal velocity fluctuations u' from 0.77% to 0.56%. and a reduction in transversal velocity fluctuations v' from 3.02% to 1.73%.

5.2.2. Design of the first prototype

In order to select an appropriate airfoil for the blades, the methodology explained in Chapter 3 was applied. Using a double-multiple streamtube model (DMST), different solidity values for the turbine and different airfoil geometries were compared to select the final design. This model combines momentum and blade element theories to evaluate the performance of the turbine in a very short lapse of time compared to Computational Fluid Dynamics (CFD) simulations. The details of the discretization and calculation scheme of the model, as well as its validation, may be found in Chapter 4 [27]. An optimal solidity of $\sigma = 1/3$, based on the criteria of maximum energy yield and relatively low rotational speeds at operation, and the DU-06-W-200 airfoil were selected for the turbine model. This airfoil, developed in the TU Delft [28], is supposed to possess self-starting capabilities. With these values, an airfoil chord of $c = 44.4$ mm resulted for a three-bladed rotor. The final geometric characteristics of the VAWT model are collected in Table 5.1.

Table 5.1: Geometrical characteristics of the VAWT model

Airfoil	Radius	Height	Number of blades	Airfoil chord	Turbine solidity
DU-06-W-200	400 mm	600 mm	3	44.44 mm	1/3

Once an optimal design was selected, a numerical simulation using Computational Fluid

(a) Construction of a half of the honeycomb (b) Assembly of a half of the honeycomb (c) Complete honeycomb assembly

Figure 5.3: Construction and assembly of a turbulence reduction honeycomb for the wind tunnel

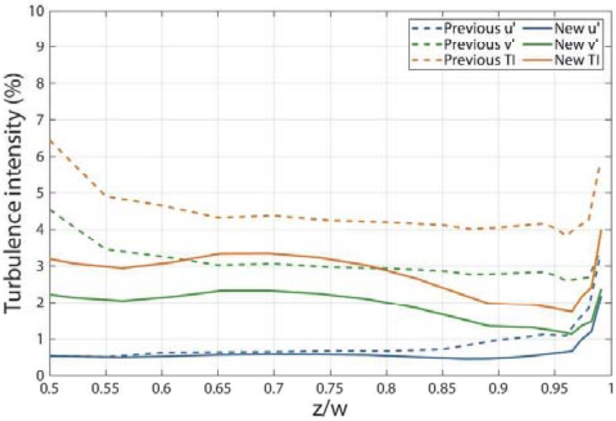

Figure 5.4: Reduction of the wind tunnel test section turbulence levels after honeycomb and screening

Dynamics (CFD) was performed using the methodology introduced in Chapter 4, in order to obtain a more precise description of the flow field as well as the performance of the model. Figure 5.5 shows the simulation domain, mesh and boundary conditions applied. As it may be appreciated, the domain shape is now rectangular for the sake of cell economy. The mesh was generated using the software GAMBIT®. Special effort was made during the meshing process to have as many hexahedral cells as possible, in order to reduce computational times.

The Navier-Stokes equations that describe the fluid dynamics were solved with ANSYS FLUENT®, using the k-ω-SST model for the turbulence closure. A velocity-inlet condition of 10 m/s was imposed at the domain inlet, and a pressure-outlet condition equal to atmospheric pressure was applied at the domain exit. Symmetry conditions were applied to the lateral limits of the domain, and a no-slip wall boundary condition was applied to the blades. Finally, an interface zone separates the rotor moving zone from the rest of the domain.

Figure 5.6 shows the power curve of the proposed design, predicted by both the streamtube

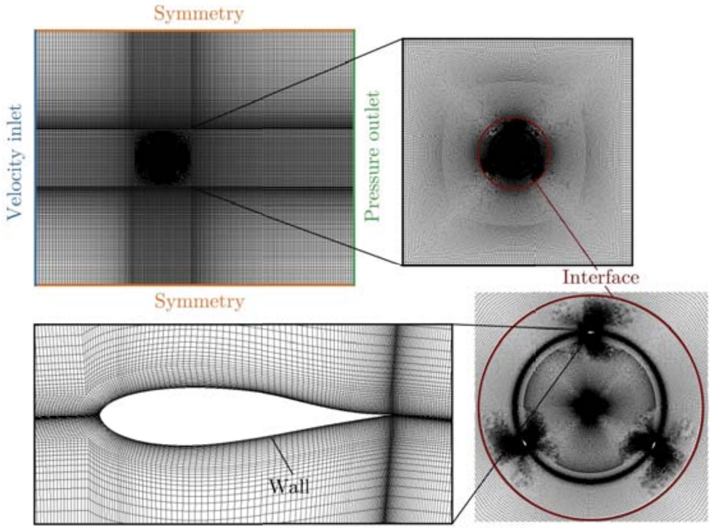

Figure 5.5: Simulation domain, mesh and boundary conditions for the first prototype

model and the CFD simulations. Although there are some differences between the values of the expected power coefficients, both predict the maximum performance of the turbine at the same tip speed ratio value of 3.5. The differences may be attributed to the effect of the wakes shed on the upwind part of the turbine on the downwind blades, as well as to the assumptions performed by the streamtube model about the flow behavior. Anyway, these aspects are to be confirmed after the experimental characterization of the model.

The blades were fabricated with polyamide via Selective Laser Sintering (SLS) and are depicted in Figure 5.7, as this technique provides a nice surface finish. An aluminum shaft of 15 mm diameter was employed, and support plates were specifically designed to join the blades to the turbine shaft at their ends. Finally, a support structure was built with aluminum profiles to hold the turbine at the correct position. Figure 5.8 shows a CAD view of the rotor alongside the support structure and the final mounting in the wind tunnel test chamber.

Despite the best efforts at the design stage, the blades of the prototype failed due to centrifugal forces, as shown in Figure 5.9. This highlighted the necessity of further research into the blade fabrication technology itself, as well as into different design strategies, which go beyond aerodynamics, to ensure prototype integrity.

5.2.3. Research into blade fabrication technology and different design strategies

The first step in ensuring structural integrity of the prototype was to develop more resistant blades. A series of DIY Fused-Deposition Modeling (FDM) machines (HTA3D$^{®}$ P3Steel) were acquired by the Department of Energy and one of them was assembled and adjusted in the context of this project. The material used by these machines is polylactic acid (PLA). A procedure for the in-house fabrication of the blades was developed, with the following steps:

- Computer-Aided Design of the blades

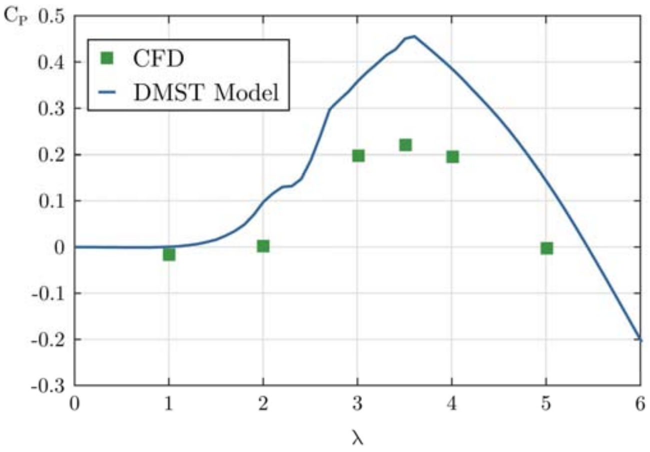

Figure 5.6: Predicted power curve with the DMST model and CFD simulations

Figure 5.7: Polyamide blades fabricated using Selective Laser Sintering (SLS)

- "Slicing" of the geometry: the manufacturing parameters (layer height, temperatures, etc.) must be introduced in a code for the FDM machine.
- FDM manufacturing of blade parts
- Visual inspection
- Insertion of the core iron rods into the blade parts and assembly
- Joint and crack filling with paste
- Manual milling and sanding
- Epoxy coating

Figure 5.10 shows a manufactured blade after paste filling, manual milling and sanding, before applying the final epoxy coating.

Typically, FDM manufactured parts with a constant section are fabricated so that every layer contains the cross section of the part. This layer orientation usually results in better surface

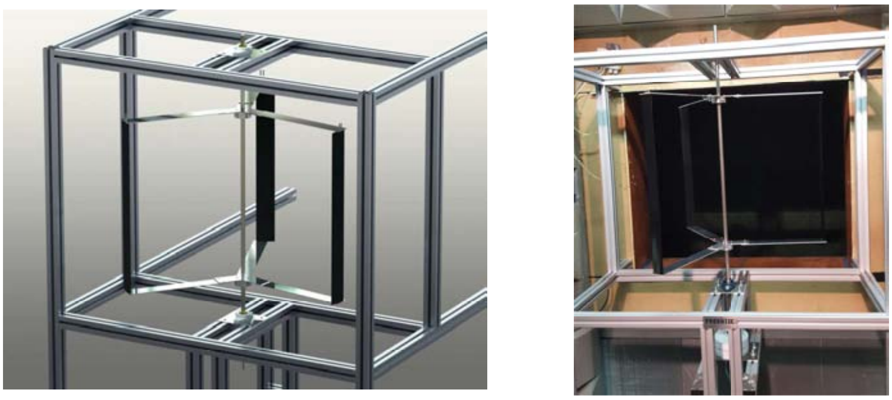

(a) CAD view

(b) Assembly and placing into the wind tunnel

Figure 5.8: First turbine protoype

Figure 5.9: Blade failure after testing the first prototype

Figure 5.10: Manufactured blade after paste filling, manual milling and sanding, before final coating

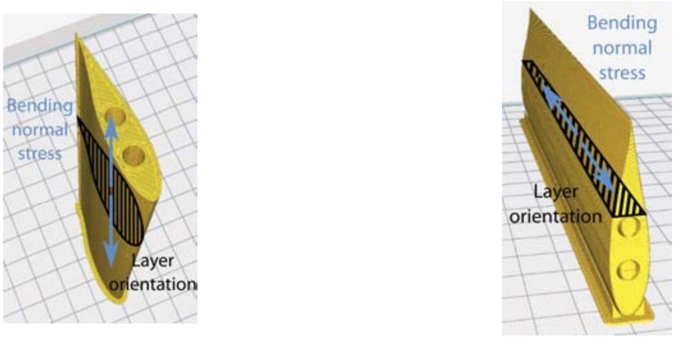

(a) Conventional orientation

(b) Drop orientation

Figure 5.11: Different layer orientations tested for the fabrication of the new blades

finish, geometry fidelity and smaller manufacturing times. Nevertheless, in this case, the highest stress that the blades are bound to endure is due to centrifugal forces, acting perpendicularly to the layer plane. This orientation would make the blade resistance strongly dependent on the adhesion forces between the layers. Therefore, an alternative “drop orientation” was proposed to make the blade resistance mainly dependent on the material strength. The two orientations tested are shown in Figure 5.11.

After the fabrication of two test specimens, they were visually inspected and tested in the laboratory of the Department of Materials Science and Metallurgical Engineering in Gijón. The results showed that the bending resistance of the drop orientation was around 1.7 times higher than the resistance of the conventional orientation. In addition, whereas the conventional orientation exhibited a fragile fracture, the drop orientation showed a ductile fracture with around 2.6 times more elongation. The results of the test are shown in Figure 5.12. The specimen fabricated with the conventional orientation clearly showed that the blade layers had been separated, withstanding a maximum load of 777.03 N and almost with no strain. On the other hand, the “drop orientation” specimen was able to bear a maximum load of 1371.4 N. Finally, the epoxy coating added to the specimen with drop orientation increased the maximum load to 1447.76 N, at the expense of a smaller strain value.

From the results observed, the drop orientation was selected as the most suitable one due to its resistance. As surface finish and geometrical fidelity could be improved to similar levels as the conventional orientation ones by appropriate selection of the manufacturing parameters and post-processors, this orientation presents more advantages for the purpose of this project.

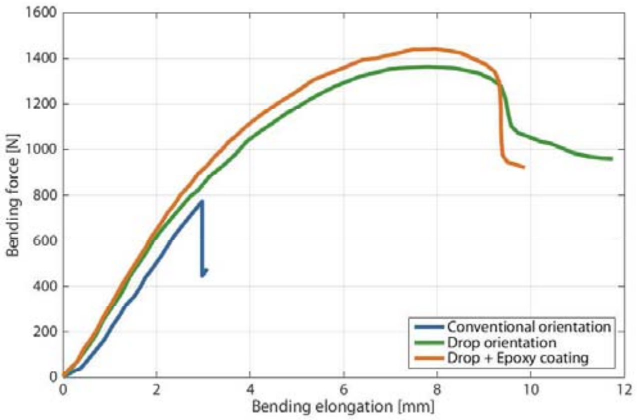

Figure 5.12: Bending test results for the blade specimens tested

Additionally, to reduce blade deformation in the centrifugal direction, auxiliary steel strings were attached to the blades, as shown in Figure 5.13.

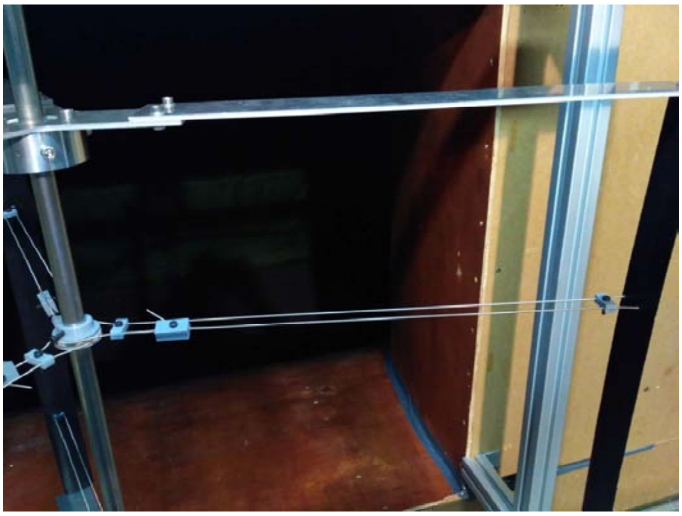

Figure 5.13: Auxiliary steel strings to reduce blade deformation

When this modified prototype was placed into the wind tunnel, it withstood the centrifugal load satisfactorily up to the rotational speeds tested. Nevertheless, it was unable to reach rotational speeds higher than around 300 rpm, due to the relatively great mechanical losses with respect to the aerodynamic power available.

5.2.4. Design of the second prototype: optimization

From the previous experiences, it was clear that some changes in the design of the prototype were required, mainly to reduce mechanical losses in the experimental setup. The main problems affecting the experimental model were identified as the following:

- Mass of the rotor: it increases bearing friction and hinders turbine starting.
- Bending due to gravity on the support plates that join the blades to the shaft: it reduces rotor efficiency.
- Great bending stress on the blades: it limits operational speed and could break the blades.

With these problems in sight, a series of changes in the prototype were proposed. These changes are specified in the following subsections.

Increase of the rotor solidity and reduction of the incoming wind speed

The solidity of the rotor was increased to 0.5 in an attempt to increase the bending resistance of the blades and reduce the required rotational speeds for the prototype. This meant increasing the blade chord to 66.67 mm. The geometrical characteristics of this new design are collected in Table 5.2.

Table 5.2: Geometrical characteristics of the second VAWT model

Airfoil	Radius	Height	Number of blades	Airfoil chord	Turbine solidity
DU-06-W-200	400 mm	600 mm	3	66.67 mm	0.5

Additionally, the incoming wind speed for the tests was reduced from 10 m/s to 7.5 m/s (the minimum reachable velocity in the wind tunnel) with the aim of decreasing even more the required model rotational speeds. With this new design and using the DMST model developed in Chapter 3, the maximum rotational speed expected by the model is around 825 rpm instead of 970 rpm. Additionally, the nominal rotational speed has been reduced from 645 to 540 rpm. Furthermore, the increase on the size of the blades, at the cost of an increase on blade weight, increases blade bending resistance and allows a better surface finish and geometrical fidelity.

Changes on the support structure for the blades

The blade supports were changed from the original end plates to tubular struts of 10 mm diameter and 1 mm thickness. The struts were placed at 1/4 and 3/4 of the blade span instead of fixing the blades at the end. This reduced the mass of the rotor, the bending stress on the blades and the bending due to gravity on the struts.

Figure 5.14 shows the Computer-Aided Design (CAD) of the new prototype design. Additionally, the aluminum parts that had been used to fix the former support plates to the blade shaft were substituted by FDM manufactured parts to reduce even more the rotor weight. The FDM technology eased geometrical modifications of these fixing parts, as well as the blades, to allow proper insertion and fixation of the struts with bolts. The CAD view and the assembly and placing of the prototype into the wind tunnel are depicted in Figure 5.15.

Figure 5.14: New design of the prototype: blades and struts

Quantification of the design improvement

By considering the turbine former support plates (1) and the new struts (2) as beams with one fixed end, the bending resistance moduli and the own weight loads may be calculated and compared.

The cross section areas are:

$$A_1 = bh = 100 \text{ mm}^2 \tag{5.1}$$

for the former support plates, where $b = 50$ mm and $h = 2$ mm are the base and height of the plates, and

$$A_2 = \pi \frac{D^2 - (D - 2t)^2}{4} = 28.27 \text{ mm}^2 \tag{5.2}$$

for the new support struts, where $D = 10$ mm and $t = 1$ mm are the diameter and thickness of the struts.

The bending resistance moduli may be calculated as:

$$W_{z,1} = \frac{bh^2}{6} = 33.33 \text{ mm}^3 \tag{5.3}$$

(a) CAD view

(b) Assembly and placing into the wind tunnel

Figure 5.15: Second turbine protoype

and

$$W_{z,2} = \pi \frac{D^3 - (D - 2t)^3}{32} = 47.9 \text{ mm}^3 \tag{5.4}$$

for the plates and the struts respectively. Finally, the own weight loads may be obtained as:

$$q_1 = \int_0^L A_1 \rho_{Al} \frac{1}{L} dL = 100 \rho_{Al} \left[\frac{\text{kg}}{\text{mm}^3} \right] \text{kg} \tag{5.5}$$

$$q_2 = \int_0^L A_2 \rho_{Al} \frac{1}{L} dL = 28.27 \rho_{Al} \left[\frac{\text{kg}}{\text{mm}^3} \right] \text{kg} \tag{5.6}$$

respectively, where ρ_{Al} is the aluminum density and L is the support length.

From these calculations, it may be observed that the weight of the new support structures is below 30% of the original weight. In addition, the bending resistance modulus has been increased to 140% of its original value.

On the other hand, the centrifugal forces were substantially reduced by changing the turbine solidity and the fixing position of the blades. The cross section areas of the former and new blades are $A_{B1} = 218.81$ mm^2 and $A_{B2} = 516.53$ mm^2 (obtained from the CAD model) Considering the iron core rods, with a cross section $A_{SR} = 25.13$ mm^2, the mass of the blades may be calculated as:

$$m_{blade,1} = m_{B1} + m_{SR} = (\rho_{PLA} A_{B1} + \rho_{Fe} A_{SR}) L_B = 0.282\text{kg} \tag{5.7}$$

and

$$m_{blade,2} = m_{B2} + m_{SR} = (\rho_{PLA} A_{B2} + \rho_{Fe} A_{SR}) L_B = 0.389\text{kg} \tag{5.8}$$

where $\rho_{PLA} = 8.75 \times 10^{-7}$ kg/mm^3 and $\rho_{Fe} = 7.85 \times 10^{-6}$ kg/mm^3 are the PLA (with 70% infill) and iron densities, and L_B is the blade span.

The maximum bending moment of the blades, as a function of the turbine rotational speed ω, may be calculated from the following expressions:

$$M_{b,max1} = \frac{m_{B1} \omega^2 R L_B}{2} = 33840\, \omega^2 \text{ N·mm} \tag{5.9}$$

and

$$M_{b,max2} = \frac{m_{B2}\,\omega^2 R\,0.5 L_B}{2} = 23340\,\omega^2 \text{ N·mm} \tag{5.10}$$

where R is the turbine radius. Note that, due to the change in the fixing position of the blades, the bending distance is half of its original length $0.5L_B$.

Comparing both mass values, the mass of the blades has increased in around 40%. Nevertheless, the new maximum bending moment is below 70% of the original one. Additionally, the bending resistance moduli of the blades were obtained from the CAD models: $W_{z,B1} = 243.45$ mm^3 in the case of the former blades and $W_{z,B2} = 827.71$ mm^3 for the new ones. This represents an increase of 240% in the bending resistance of the blades. Expressing this quantities in terms of the reduction achieved in the maximum bending stress on the blades:

$$\Delta = 1 - \frac{M_{b,max2} W_{z,B1}}{M_{b,max1} W_{z,B2}} = 79.64\% \tag{5.11}$$

Finally, after performing initial tests with the prototype, it was decided to cover the cylindrical struts completely with an airfoil section to reduce the drag on them. The airfoil chosen was an Eppler E862, with a low drag coefficient value for the Reynolds numbers expected during the tests (0.175 at an angle of attack of 0° for an indicative Reynolds number of 50000). This airfoil is symmetrical, as lift generation in the struts, leading to loss of power capture on the blades, is to be avoided. The chord of this covering airfoil is 45 mm.

5.2.5. CFD model of the final experimental prototype

Before proceeding to the experimental setup and results, a numerical simulation of the final experimental prototype was performed in order to obtain a more accurate prediction of the power curve and a more complete description of the turbine flow field. The methodology followed is similar to the one presented in Chapter 4, with the geometrical characteristics collected in Table 5.2. In this case, a newer software, ANSYS ICEM CFD® was used to generate the mesh. This software allows to partition the domain in different blocks that are meshed and subsequently assigned to the domain geometry, making easier to define mesh sizes and future changes in the mesh, if necessary. It also made possible to employ hexahedral elements throughout almost the whole domain, reducing computational time substantially. The simulation domain, mesh and boundary conditions are shown in Figure 5.16. ANSYS FLUENT ® was used to solve the Navier-Stokes equations that describe the fluid dynamics, with the k-ω-SST model for the closure of turbulence. A velocity-inlet condition of 7.5 m/s was imposed at the domain inlet, and a pressure-outlet condition equal to atmospheric pressure was applied at the domain exit. Symmetry conditions were applied to the lateral limits of the domain, and a no-slip wall boundary condition was applied to the blades. An interface zone was defined, separating the rotor moving zone from the rest of the domain. The pressure-velocity coupling is made via the SIMPLE algorithm and the discretization schemes and simulation time step size (0.25°/time step) are the same as the ones used in the CFD model explained in Chapter 4. The use of an hexahedral mesh allowed reducing the number of cells and thus the simulation time to 5 days in a 4-nodes Intel Core i7-52820K at 3.3 GHz and 64 Gb RAM to obtain one point of the power curve.

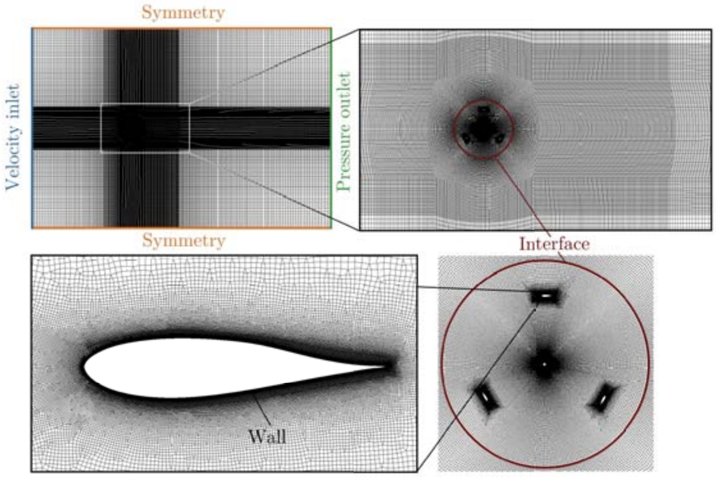

Figure 5.16: Simulation domain, mesh and boundary conditions for the final prototype

5.2.6. Experimental setup and measurement chain

Once the design was improved to withstand the wind tunnel experiment conditions, experiments were performed. Figure 5.17 shows a scheme of the experimental setup and equipment used to characterize both the power of the turbine prototype and the flow velocities in the turbine wake.

The incoming wind conditions were not enough for the turbine to self-start. The nozzle dimensions (115 cm x 100 cm) limited the prototype dimensions to $R = 40$ cm and $H = 60$ cm. With an incoming test velocity of 7.5 m/s, the energy available in the wind is roughly 124 W (around 73.5 W applying Betz's limit). The turbine was only able to reach around 60 rpm by itself ($\lambda = 0.33$). Hence, a 211 W AC motor (Figure 5.18c) was used to enhance turbine rotation. This motor was energized by a DC power source (Figure 5.18b), connected to it via a DC/AC converter with the posibility of regulating the motor speed manually (Figure 5.18d). An uninterruptible power source (UPS) between the equipment and the electrical network prevented losing power during the tests, avoiding unexpected power disruptions that could damage the equipment as well (Figure 5.18a). A flexible coupling was used to connect the motor to the turbine shaft, and an enconder was manufactured in-house using FDM technology (Figure 5.18f). The encoder was connected to an optical tachometer that displayed the rotational speed of the prototype during the tests (Figure 5.18g). In order to characterize the flow in the wake of the turbine using hot wire anemometry, a constant temperature anemometer and a data acquisition system (Figure 5.18e) were employed. A view of the hot-wire probe is shown in Figure 5.18h. These probes are fabricated in-house and calibrated before every measurement campaign in the laboratory of the Fluid Mechanics Area (there is a probe fabrication bench and a probe calibration bench that serve for that purpose [29]). Finally, a laptop was used to register the power consumed by the DC power source, as well as the flow field data provided by the data acquisition system.

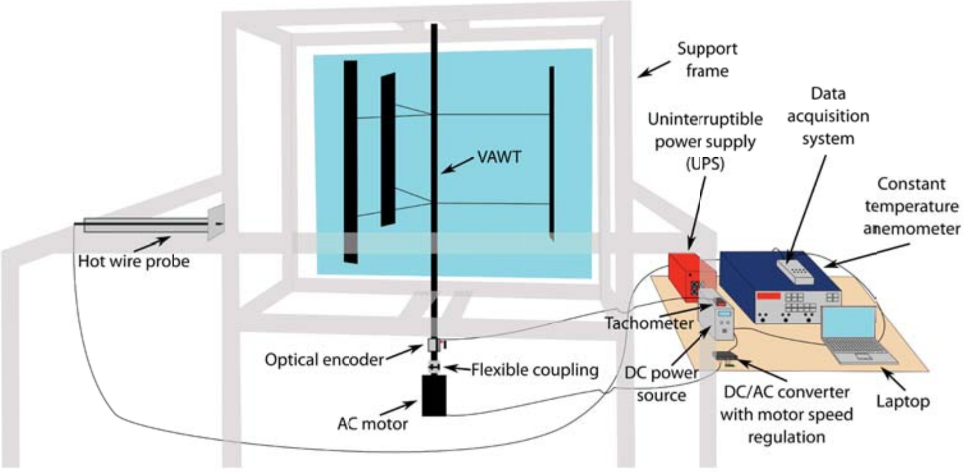

Figure 5.17: Experimental setup and equipment

5.2.7. Estimation of the experimental power curve

The resistive torque at the bearings prevented the turbine from generating a useful power output, so the motor had to work during the whole experimental tests to provide the energy required for the rotation of the prototype. The maximum rotational speed attained during the experiments was 450 rpm, corresponding to $\lambda \approx 2.5$. As this setup made impossible to measure the aerodynamic power produced at the turbine blades, it was necessary to develop a specific methodology, based on the variation of the electrical power consumption of the whole turbine assembly. With a constant incoming wind velocity of 7.5 m/s at the tunnel test section, the turbine was driven manually with the motor up to the desired rotational speed (and the corresponding value of λ). The rotational speed was read from the optical tachometer, whereas the voltage and currrent intensity (and thus the electrical power) provided by the DC power source were registered in a laptop.

Several tests were performed in the wind tunnel, obtaining the power consumption of the turbine assembly at four different conditions:

1. No wind, turbine assembly without blades
2. No wind, turbine assembly with blades
3. Wind=7.5 m/s, turbine assembly without blades
4. Wind=7.5 m/s, turbine assembly with blades

When there is no wind and the blades have not been mounted on the turbine assembly (case 1), the power dissipated by the turbine assembly may be calculated as:

$$W_1 = \eta_{no\,blades} M_{res,1} \omega \tag{5.12}$$

(a) Uninterruptible power source (UPS)

(b) DC power source

(c) AC brushless motor

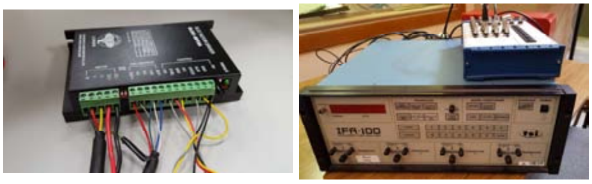

(d) DC/AC converter with motor speed regulation

(e) Constant temperature anemometer and Data acquisition system

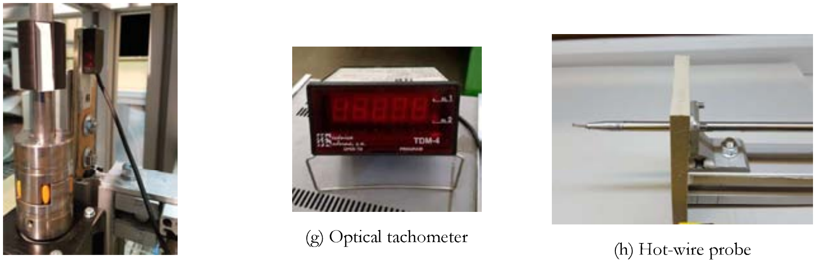

(f) Encoder and flexible coupling

(g) Optical tachometer

(h) Hot-wire probe

Figure 5.18: Experimental equipment

where $\eta_{no\,blades}$ is the total efficiency of the system, including all mechanical and electrical efficiencies from the power source up to the turbine shaft and $M_{res,1}$ is the total resistive torque (mechanical and aerodynamic).

When the wind starts to blow (case 3), the power dissipated by the turbine assembly, assuming the total efficiency of the system remains constant, is

$$W_3 = \eta_{no\,blades} M_{res,3}\omega = \eta_{no\,blades}\left(M_{res,1} + M_{res,struts,3}\right)\omega \tag{5.13}$$

The resistive moment due to the drag on the turbine struts $M_{res,struts}$ may be estimated for cases (1) and (3) as (remember that for case (1) $V_\infty = 0$):

$$M_{res,struts} = \frac{3}{4}\rho C_{D,struts} L R^2 \left(\omega^2 R^2 + V_\infty^2\right) \tag{5.14}$$

where ρ is the air density, $C_{D,struts}$ is the drag coefficient of the struts, L is the characteristic length of the struts, R is the turbine radius, ω is the turbine rotational speed and V_∞^2 is the incoming wind speed.

The power dissipated by the struts is $W_{struts} = M_{res,struts}\omega$. Combining Equations 5.12 and 5.13, the efficiency loss corresponding to the turbine struts may be estimated as:

$$\eta_{struts} = \frac{W_{struts,3} - W_{struts,1}}{W_3 - W_1} \tag{5.15}$$

where $W_{struts,3} - W_{struts,1}$ is the difference in the power dissipation by the struts. With the value of this efficiency, the resistive torque of the turbine assembly without blades may be obtained as:

$$M_{res,1} = \frac{W_1 \eta_{struts}}{\omega} - \frac{3}{4}\rho C_{D,struts} L \omega^2 R^4 + M_{res,struts,1} \tag{5.16}$$

Once the blades are mounted on the turbine assembly, the same procedure may be applied to obtain the decrease in power dissipation (aerodynamic power production) due to the blades. When the blades are mounted on the turbine, the power dissipated by the turbine assembly without wind (case 2) is:

$$W_2 \eta_{with\,blades} = M_{res,2}\omega = \left(M_{res,1} + M_{res,blades}\right)\omega \tag{5.17}$$

where $\eta_{with\,blades}$ is the total efficiency of the system, including all mechanical and electrical efficiencies from the power source up to the turbine shaft and $M_{res,2}$ is the total resistive torque (mechanical and aerodynamic). It has been assumed that adding the blades does not modify the resistive torque $M_{res,1}$ substantially besides the aerodynamic drag on the blades $M_{res,blades}$. This aerodynamic drag may be calculated with the following expression:

$$M_{res,blades} = \frac{3}{2}\rho C_{D,0^\circ} c H \omega^2 R^3 \tag{5.18}$$

as, with no wind impinging on the blades, the angle of attack will be 0° throughout the whole rotation of the machine. $C_{D,0^\circ}$ is the drag coefficient of the blade airfoil at an angle of attack of 0°, c is the blade airfoil chord and H is the blade span.

Once the wind starts to blow (case 4), the power dissipated by the turbine assembly, assuming the total efficiency of the system $\eta_{with\,blades}$ remains constant, is:

$$W_4 = \eta_{with\,blades} M_{res,2}\omega - W_{AERO} \tag{5.19}$$

where W_{AERO} is the decrease in power consumption due to the aerodynamic power generated on the blades, hence, the result that was sought in the experimental tests. Combining Equations 5.17 and 5.19, the aerodynamic power generated on the blades is

$$W_{AERO} = \eta_{with\,blades}\left(W_2 - W_4\right) \tag{5.20}$$

with the total efficiency of the system obtained from

$$\eta_{with\,blades} = \frac{M_{res,1} + \frac{3}{2}\rho C_{D,0^\circ} c H \omega^2 R^3}{W_2}\omega \tag{5.21}$$

with $M_{res,1}$ obtained from Equation 5.16.

5.3. Experimental tests

Once the experimental methodology used for the development of the tests has been introduced, the main experimental results are presented in this section.

5.3.1. Power curve

Figure 5.19 shows a comparison between the results of the DMST model, the CFD simulations and the wind tunnel experiments performed using the methodology described in this chapter. It may be observed that both predictive models follow reasonably well the experimental results, with the DMST model overpredicting slightly the power generation of the turbine. This gap may be ascribed to the assumptions about the flow nature performed by streamtube models, neglecting flow features that may result into the loss of performance. On the other hand, the CFD results seem to underpredict the performance of the turbine. From the mathematical procedure used to estimate the aerodynamic power of the prototype, it may be observed that a significant value of the drag coefficient of the struts might result in an artificial increase in the estimated power values, when calculating the corresponding power differences.

Hence, it can be expected that reducing the drag on the turbine struts may result on a more accurate value of the aerodynamic performance of the turbine blades. When the struts were covered with the Eppler E862 airfoil, the drag coefficient was reduced from 1.2 (cylindrical struts) to 0.175 (profiled section). A comparison between the experimental results from this configuration (the final prototype) and the DMST model and CFD simulations is shown in Figure 5.20. As it may be appreciated, the CFD predictions lie practically on the experimental curve. Although the mesh independence has been already verified in Chapter 4, this results serves as an additional source of validation of the CFD methodology employed throughout this thesis. Despite the great vortex shedding phenomena present at the lowest tip-speed ratio values, the CFD model is able to follow adequately the experimental values. The dynamic stall effects produced by these phenomena have not been considered in the DMST model, leading to the overprediction of the power coefficient values on the left part of the power curve.

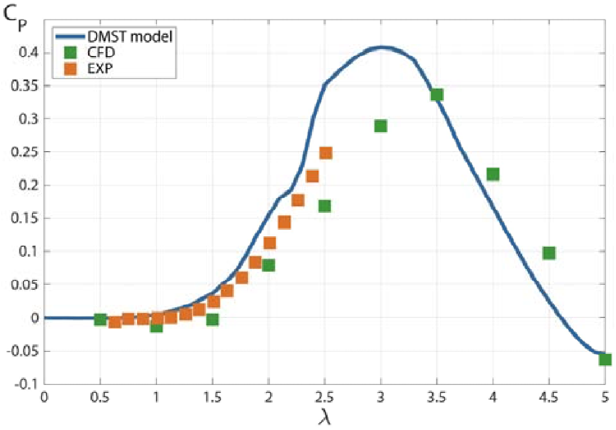

Figure 5.19: Comparison between the results of the DMST model, CFD simulations and wind tunnel experiments with cylindrical struts

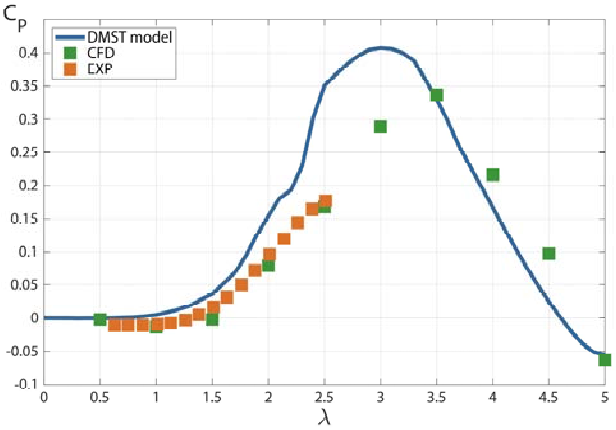

Figure 5.20: Comparison between the results of the DMST model, CFD simulations and wind tunnel experiments with Eppler E862-shaped struts

5.3.2. Wake velocities

The hot-wire measurements in the turbine wake were performed at a $\lambda = 2.5$, corresponding to a low value of the tip-speed ratio simulated with CFD. It was observed that, as the turbine rotational speed increased, a blockage effect started to arise in the wind tunnel and the velocities at the wake started to drop substantially. The hot-wire probes are calibrated for wind velocities higher than 4.5 m/s, so results for lower values should not be trusted. Hence, although the initial measurement campaign comprising a 2D map behind the turbine was performed, only results from the zone where velocities were higher than this threshold value are shown (see zone highlighted in green in Figure 5.21, which depicts a scheme of the turbine inside the wind tunnel, showing the rakes where wake velocities were measured). Additional measurements were made using a Pitot tube to obtain the mean wake velocity profiles, confirming this blockage effect. A higher testing velocity could have been used to obtain trustworthy results at the whole measured positions, but this would have implied higher rotational velocities which would have compromise the mechanical integrity of the prototype. Another option to obtain higher velocities at the turbine wake without increasing the wind tunnel speed (and thus the rotational speed of the turbine) would be enclosing the prototype inside an additional tunnel with the same size of the nozzle exit, so that the flow is forced to pass by the whole turbine. Nevertheless, these conditions would not represent the normal operation of a VAWT in a real open-field situation. Therefore, although a total of 34 measurements were performed in each rake (giving a total of 408 measurement positions), only the measurements performed in the leeward region of the turbine are considered in the remainder of this chapter.

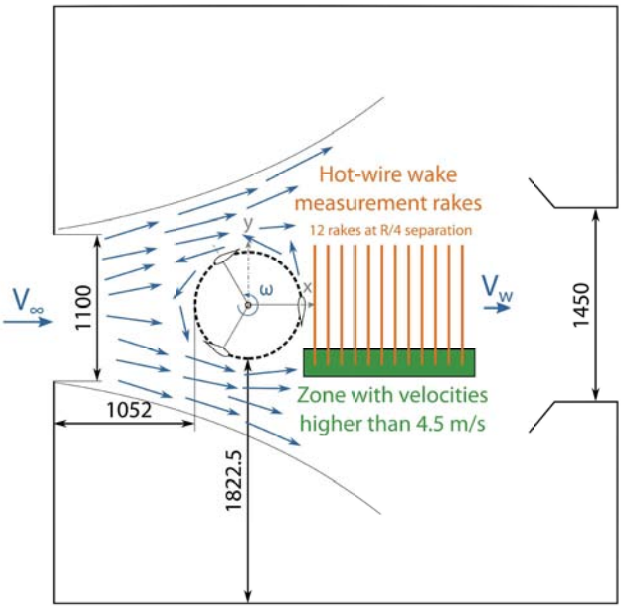

Figure 5.21: Scheme of the turbine inside the wind tunnel and the position of the hot-wire wake measurement rakes

Figure 5.22 shows the evolution of the mean streamwise velocity with the distance to the turbine, inside the turbine wake zone corresponding to the leeward region (shown in green in Figure 5.21). Results from the CFD simulations are plotted alongside the experimental values obtained with the Pitot tube and the hot-wire measurements. It may be appreciated that the CFD is able to follow the tendency of the experimental values quite reasonably. Figure 5.23 depicts the temporal evolution of the streamwise velocity (both CFD and hot-wire results) at the nearest point to the turbine (a distance of R/4) in the line presented in Figure 5.22. Although instability is clearly visible, with a period T_B corresponding to the blade passing period, the magnitude of the velocity fluctuations seems higher in the case of the CFD simulations. This might be ascribed to the faster mixing of the wake in the experimental conditions, which may take longer to develop in the 2D CFD simulation.

Regarding the characterization of turbulent variables, the evolution of the mean turbulent

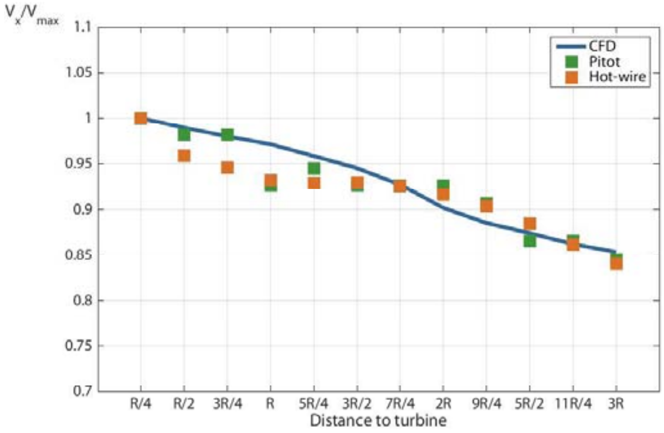

Figure 5.22: Mean normalized velocity in the streamwise direction in the turbine wake: CFD and experiments

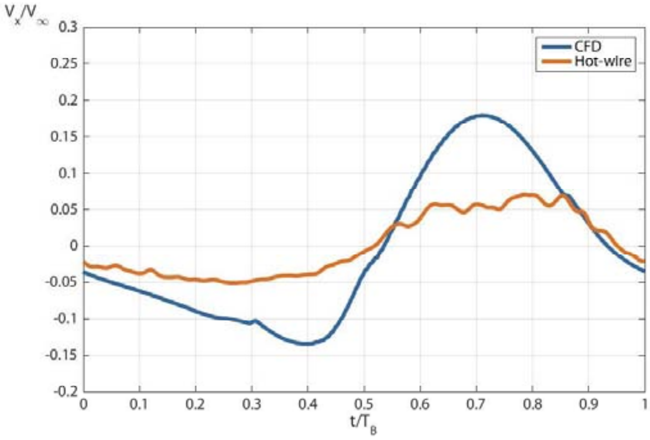

Figure 5.23: Evolution of normalized streamwise velocity with time in the turbine wake: CFD and hot-wire experiments

kinetic energy (TKE) in the turbine wake zone corresponding to the leeward region is shown in Figure 5.24. The value of the TKE is calculated according to the following expression (as the CFD simulations are two-dimensional, only the fluctuations in the longitudinal and transversal directions u' and v' are considered):

$$TKE = \frac{1}{2}\overline{u_i'u_i'} \tag{5.22}$$

Only results from the CFD simulations and hot-wire measurements are presented. It may be appreciated that the CFD simulations are able to follow the experimental values up to a distance of 2R from the turbine. Past this point, the decay in the turbulent kinetic energy is higher in the experiments than in the CFD simulations. This TKE dissipation is related to the transfer of energy from larger to smaller turbulent flow scales, suggesting that the wake is mixing faster under the experiment conditions than in the CFD simulations. This result is in line with the conclusion drawn from the previous analysis of streamwise velocities, as with a 2D simulation it is not possible to account for wake mixing in the vertical direction. The evolution of the TKE at the nearest point to the turbine (a distance of R/4) in the line presented in Figure 5.24 is shown in Figure 5.25. In this case, the magnitude of the TKE is similar for both the CFD and experimental hot-wire results, with a relative increase in turbulence during the blade passing period T_B corresponding to the passing of the blade near the measurement point.

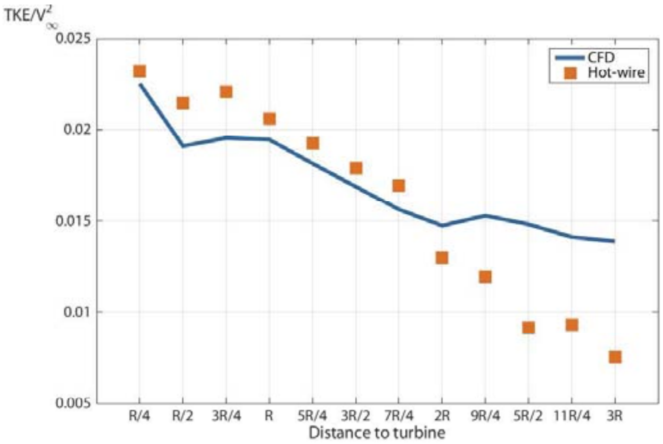

Figure 5.24: Mean normalized turbulent kinetic energy in the turbine wake: CFD and experiments

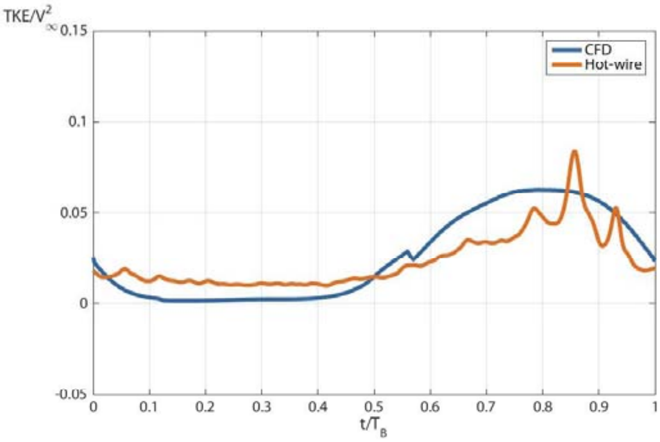

Figure 5.25: Evolution of normalized turbulent kinetic energy with time in the turbine wake: CFD and hot-wire experiments

Finally, Figure 5.26 shows the Power Spectral Density (PSD) of the streamwise velocity fluctuations at the measurement point shown in Figures 5.23 and 5.25. There are two clearly distinguishable peaks, one at 7.467 Hz, corresponding to the turbine rotational speed (448 rpm), and the second one at 22.4 Hz, corresponding to the blade passing frequency (BPF). Harmonics of the turbine rotational frequency and the BPF are also visible at higher frequencies, but with smaller PSD values.

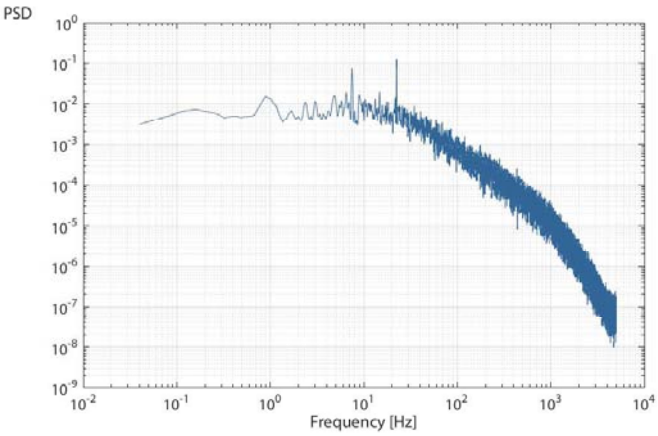

Figure 5.26: Power Spectral Density (PSD) of the streamwise velocity fluctuations at the measuring point

5.4. Conclusions

The methodology explained in the previous chapters of this thesis has been successfully applied to the aerodynamic design of a vertical-axis wind turbine prototype. Considering the constraints imposed by the wind tunnel test section available, a design has been proposed, fabricated and tested in the laboratory of the Fluid Mechanics Area. The wind tunnel turbulence level was reduced in around 40% by assembling a home-made wood honeycomb. Issues when testing the first prototype shifted the research focus towards blade fabrication technologies, acquiring a Fused-Deposition Modeling machine and assembling and adjusting it in the laboratory. A procedure for the in-house fabrication of the blades was developed, finding that the so-called "drop-orientation" of the blade layers resulted in more resistance to bending stresses. Unfortunately, the turbine was not able to self-start at the incoming wind conditions at the test section due to mechanical resistances in the turbine assembly. The final prototype, with a higher solidity and a new design for the support struts, was able to reach a tip-speed ratio of 2.5 when aided by an electrical motor. A procedure for the estimation of the power coefficient of the turbine was developed, finding good correspondence with the results of the predictive models presented in Chapters 3 and 4. Hot-wire measurements were performed in the mid-plane of the turbine wake. However, a blockage effect was detected as the turbine rotational speed increased, with velocities dropping below the hot-wire probe calibration range. Therefore, only results in the wake zone corresponding to the leeward position were trustworthy enough. Nevertheless, the experimental velocity and turbulent kinetic enreg measurements match the predictions of the numerical model. Finally, the computed spectrum of the velocity fluctuations shows a clear peak at the turbine rotational speed, as well as at the blade passing frequency and its harmonics.

From these results, it may be concluded that the design of a small VAWT (diameter less than 1 m) able to self-start and with a value of solidity in the optimal power extraction range is a quite challenging task. The results show that this prototype extracts enough aerodynamic power from the wind to function properly, but all this energy is lost due to mechanical inefficiencies. Future work should comprise the whole characterization of the turbine power curve with the acquisition and assembly of a new motor with higher power. Besides, the open jet at the wind tunnel test section could be enclosed between additional walls, forcing the jet to pass completely across the turbine rotor and increasing the velocities in the wake for the hot-wire measurements. It must not be forgotten that the final aim should be the construction of a real-scale turbine protoype for testing in real field conditions. The small-scale prototype developed in this thesis could be tested as well outside, before proceeding to this final stage.

References

[1] T. Ashwill, *Measured Data for the Sandia 34-Meter Vertical Axis Wind Turbine*, Tech. Rep. (Sandia National Laboratories, Albuquerque, New Mexico, USA, 1992).

[2] B. Kirke and L. Lazauskas, *Experimental verification of a mathematical model for predicting the performance of a self-acting variable pitch vertical axis wind turbine,* Wind Engineering **17**, 58 (1993).

[3] A. Huskey, A. Bowen, and D. Jager, *Wind Turbine Generator System Power Performance Test Report for the Mariah Windspire 1-kW Wind Turbine*, Tech. Rep. (National Renewable Energy Laboratory, Golden, Colorado, USA, 2009).

[4] J. Kjellin, F. Bulow, S. Eriksson, P. Deglaire, M. Leijon, and H. Bernhoff, *Power coefficient measurement on a 12 KW straight bladed vertical axis wind turbine,* Renewable Energy **36**, 3050 (2011).

[5] R. Ramkisson and K. Manohar, *Increasing the power output of the Darrieus vertical axis wind turbine,* British Journal of Applied Science & Technology **3**, 77 (2013).

[6] G. Bergeles, A. Michos, and N. Athanassiadis, *Velocity vector and turbulence in the symmetry plane of a Darrieus wind generator,* Journal of Wind Engineering and Industrial Aerodynamics **37**, 87 (1991).

[7] R. Bravo, S. Tullis, and S. Ziada, *Performance testing of a small vertical-axis wind turbine,* in *Proceedings of the 21st Canadian Congress of Applied Mechanics (CANCAM07)* (Ryerson University, Toronto, Canada, 2007).

[8] A. Fiedler and S. Tullis, *Blade offset and pitch effects on a high solidity vertical axis wind turbine,* Wind Engineering **3**, 237 (2009).

[9] M.Raciti Castelli, A. Englaro, and E. Benini, *The Darrieus wind turbine: Proposal for a new performance prediction model based on CFD,* Energy **36**, 4919 (2011).

[10] Y. Li, F. Feng, W. Tian, and Q. He, *Simulation and wind tunnel test on a straight-bladed vertical axis wind turbine,* Research Journal of Applied Sciences, Engineering and Technology **5**, 2892 (2013).

[11] G. Brochier, P. Fraunié, C. Béguier, and I. Paraschivoiu, *Water channel experiments of dynamic stall on Darrieus wind turbine blades,* Journal of Propulsion **2**, 445 (1986).

[12] N. Fujisawa and M. Takeuchi, *Flow visualization and PIV measurement of flow field around a Darrieus rotor in dynamic stall,* Journal of Visualization **1**, 379 (1999).

[13] N. Fujisawa and S. Shibuya, *Observations of dynamic stall on Darrieus wind turbine blades,* Journal of Wind Engineering and Industrial Aerodynamics **89**, 201 (2001).

[14] P. Bachant and M. Wosnik, *Effects of reynolds number on the energy conversion and near-wake dynamics of a high solidity vertical-axis cross-flow turbine,* Energies **9**, 73 (2016).

[15] H. Dumistrescu, A. Dumitrache, C. Popescu, M. Popescu, F. Fruzulică, and A. Crăcunescu, *Wind Tunnel Experiments on Vertical-Axis Wind Turbines with Straight Blades,* in *Renewable Energy and Power Quailty Journal* (European Association for the Development of Renewable Energy, Environment and Power Quality (EA4EPQ), Córdoba, Spain, 2014).

[16] Y. Li, K. Tagawa, and W. Liu, *Performance effects of attachment on blade on a straight-bladed vertical axis wind turbine,* Current Applied Physics **10**, S335 (2010).

[17] R. Firdaus, T. Kiwata, T. Kono, and K. Nagao, *Numerical and experimental studies of a small vertical-axis wind turbine with variable-pitch straight blades,* Journal of Fluid Science and Technology **10**, 14 (2015).

[18] B. Fortunato, S. Camporeale, M. Torresi, D. De Fazio, and M. Giordani, *Experimental results of a Vertical Axis Wind Turbine,* in *Proceedings of the ASME-ATI-UIT 2010 Conference on Thermal and Environmental Issues in Energy Systems* (ASME, Sorrento, Italy, 2010).

[19] S. Bhuyan and A. Biswas, *Investigations on self-starting and performance characteristics of simple H and hybrid H-Savonius vertical axis wind rotors,* Energy Conversion and Management **87**, 859 (2014).

[20] M. Singh, A. Biswas, and R. Mishra, *Investigation of self-starting and high rotor solidity on the performance of a three S1210 blade H-type Darrieus rotor,* Renewable Energy **76**, 381 (2015).

[21] J. Edwards, L. Danao, and R. Howell, *Novel Experimental Power Curve Determination and Computational Methods for the Performance Analysis of Vertical Axis Wind Turbines,* Journal of Solar Engineering **134**, 031008 (2012).

[22] O. Eboibi, L. Danao, and R. Howell, *Experimental investigation of the influence of solidity on the performance and flow field aerodynamics of vertical axis wind turbines at low Reynolds numbers,* Renewable Energy **92**, 474 (2016).

[23] C. Ferreira, K. Dixon, C. Hofemann, G. van Kuik, and G. van Bussel, *The VAWT in Skew: Stereo-PIV and Vortex Modeling,* in *Proceedings of the 47th AIAA Aerospace Sciences Meeting Including The New Horizons Forum and Aerospace Exposition* (ASME, Orlando, Florida, USA, 2009) pp. 2009–1219.

[24] H. Jeong, S. Lee, and S.-D. Kwon, *Wind tunnel interference effects on power performance of small Darrieus wind turbines,* in *Proceedings of The 2014 World Congress on Advances on Civil, Environmental, and Materials Research (ACEM14)* (International Association of Structural Engineering & Mechanics (IASEM), Busan, Korea, 2009).

[25] C. Parker and M. Leftwich, *The effect of tip speed ratio on a vertical axis wind turbine at high Reynolds numbers,* Experiments in Fluids **57**, 74:1 (2016).

[26] J. Daugherty, *NASA AMES unitary plan wind tunnel blockage recommendations*, Tech. Rep. (National Aeronautics and Space Administration, Washington D.C., USA, 1984).

[27] A. Meana-Fernández, I. Solís-Gallego, J.M. Fernández Oro, K.M. Argüelles Díaz, and S. Velarde-Suárez, *Parametrical evaluation of the aerodynamic performance of vertical axis wind turbines for the proposal of optimized designs,* Energy **147**, 504 (2018).

[28] M. Claessens, *The Design and Testing of Airfoils for Application in Small Vertical Axis Wind Turbines*, Master's thesis (2006).

[29] K.M. Argüelles Díaz, J.M. Fernández Oro, , M. Galdo-Vega, and E. Blanco Marigorta, *Effects of prong-wire interferences in dual hot-wire probes on the measurements of unsteady flows and turbulence in low-speed axial fans,* Measurement **91**, 1 (2016).

6

Conclusion

The ultimate inspiration is the deadline.

Nolan Bushnell, 1943-

Everything will be okay in the end.
If it's not okay, it's not the end.

John Lennon, 1940-1980

IN this last chapter, the most significant conclusions obtained from this work are presented. Firstly, the fulfillment of the research objectives is assessed. Then, the main findings and their implications are discussed. Finally, the last section of this chapter identifies possible future research lines.

6.1. Fulfillment of research objectives

The main aim of this thesis is the development of scientific-technological knowledge applicable to the design of optimized vertical-axis wind turbines, extending the expertise of the Fluid Mechanics research group in this field and helping to consolidate a new research line focused on wind turbines. After performing a thorough review of existing wind power extraction systems and identifying the main analytical, numerical and experimental design and analysis techniques, an analytical model based on momentum theory has been developed. This streamtube model is able to predict the performance of a VAWT design in a computational time of minutes, being suitable for the design of optimized turbines. Additionally, Computational Fluid Dynamics (CFD) models have been developed to obtain a more accurate prediction of the performance of VAWTs and a more precise description of the flow field. Finally, a small-scale VAWT prototype (the first of its kind to be designed and fabricated in the laboratory of the research group) has been built and tested in the wind tunnel available at the laboratory of the Fluid Mechanics Area.

In this sense, it may be claimed that all the research objectives proposed in this thesis have been satisfactorily fulfilled. Analytical, CFD and experimental methodologies for the design and study of VAWTs have been developed and are now available for its use within the research group. The methodology and results obtained from this work will smooth the path for future research performed in the Fluid Mechanics research group regarding VAWTs. Besides, the generated knowledge has and is currently being transferred to small and medium-sized enterprises, which cannot afford complex and high-cost individual studies of this type of machines. Finally, some publications have been realized to share the results of this research with the scientific community.

The following sections collect the main findings and implications of this study, as well as the future research possibilities.

6.2. Main findings and implications

The main available wind power extraction systems have been reviewed, presenting a panoramic view of the performance of typical rotor types. Lift-drive vertical-axis wind turbines represent a feasible solution for in situ generation of clean energy in applications where it is not advisable to employ more conventional technologies. They are able to work with lower wind speeds than horizontal-axis wind turbines and independently of the wind direction. Their noise levels are also lower, and their installation and maintenance operations are substantially easier. Additionally, the blade fabrication process is also much simpler. Nevertheless, the flow field generated by these turbines is so complex that they suffer from difficulties when trying to self-start for low wind velocities.

Analytical models based on streamtube theory have been proven useful for the quick prediction of the performance of vertical-axis wind turbines. The main issue regarding these models is still the lack of available experimental airfoil data. However, this issue may be solved using predictive software to obtain the airfoil lift and drag coefficients until real tests on an airfoil may be performed. The combination of the streamtube models and a database generated for 34 airfoils resulted in a practical tool able to obtain the turbine performance curve in just a few minutes (70 different designs were analyzed in Chapter 3). Although the formulation of the model neglects some flow effects (streamtube expansion, rotor tower and wake effects) and breakdown of the momentum equation may happen at high solidity values, the high ratio between accuracy and computational cost of the model justifies its suitability at turbine design stages, helping designers to propose different designs and predict their performance almost instantaneously.

After validating the developed model with CFD and experimental results, the main parameters influencing the performance of a VAWT were analyzed. An optimal range of solidity of VAWTs was found (0.2–0.5). Using this model to observe the influence of the turbine Reynolds number on its performance, it was possible to provide insight into VAWT self-starting issues. Comparing different airfoil geometries, it was found that thin and nearly symmetrical or low-cambered airfoils were optimal for VAWT applications, allowing for self-starting and the development of a wide high-efficiency band.

Then, focus has been set on CFD models. The applicability of Richardson extrapolation method for the study of the numerical convergence of 2D VAWT simulations has been confirmed, resulting in a straightforward procedure to analyze mesh size and temporal convergence of the simulations. The results of the simulations showed a reasonable agreement with existing benchmarks, confirming the suitability of this methodology to obtain more accurate predictions of the VAWT performance and the developed flow field. The flow field has been analyzed in depth at three characteristic tip-speed ratio values (nominal working point, vortex shedding predominant region and working point beyond nominal). Four different zones may be identified in the turbine (upwind, downwind, windward and leeward), with vortex convection occurring in different ways. Additionally, the loss of performance of the turbine outside the nominal working point has been analyzed and related to the fluid dynamics behavior. Finally, two main unsteadiness generation mechanisms have been identified: blade vortex shedding and the interaction of the turbine rotation with the incoming wind.

Afterwards, different turbulence models have been applied to predict the performance of a typical VAWT airfoil with 3D simulations, finding that the best results were obtained with k-ω-based models. U-RANS models were able to predict the aerodynamic forces accurately with a much lower computational cost than other formulations. On the other hand, SRS (SAS and DES) formulations were able to obtain more information about the smallest flow scales. Hence, it seems meaningful to apply U-RANS or SRS models depending on the desired outcome of the simulations (airfoil aerodynamic forces, airfoil flow field or the simulation of an airfoil as part of a VAWT).

Finally, the methodology developed in this thesis was successfully employed to perform the aerodynamic design of a VAWT experimental demonstrator. A procedure for the in-house fabrication of VAWT blades using Fused Deposition Modeling was developed. It was found that by changing the layer orientation when fabricating the blades to the so-called "drop-orientation", blade resistance to bending stress increased substantially. The wind tunnel constraints reduced the possible size of the experimental prototype below 1 m diameter, and the mechanical resistances found in the turbine assembly consumed all the aerodynamic power generated on the blades. Hence, a motor was used to drive the turbine and a procedure for the estimation of the aerodynamic power of the turbine was developed. The experimental results showed good correspondence with the predictions of both the analytical and CFD models developed in this thesis. Hot-wire measurements in the turbine wake were performed, finding a blockage effect when the rotational speed of the turbine increased. The velocity and turbulence measurements also match the predictions of the CFD model, confirming the validity of the methodology developed in this work for the design and analysis of optimized VAWTs.

6.3. Future research possibilities

There are several research lines that may stem from the results of this work, not only in the field of VAWT modeling and simulation but also in experimentation:

- The streamtube models developed could be improved by adding corrections to consider streamtube expansion, rotor tower and blade wake effects, dynamic stall on the blades, or the influence of the downwind part of the turbine on the upwind part. When performing these modifications, attention should be paid to the increase in computational time, as it might happen than a slight increase in accuracy would not justify a much higher computational cost.

- The similarity found between the wake of the VAWT and the wake shed by a cylinder might justify the development of an analytical model based in the actuator cylinder theory, which accounts for the interaction between the blades at the whole turbine and with the outer flow field. Vortex models could be also studied in future works.

- Regarding CFD simulations, a possible line of research could be extruding the 2D domain used in this thesis and perform 3D simulations, testing the different turbulence models presented in Chapter 4 to obtain a richer description of the flow field. If the computational power available allows for it, it would be interesting to model a whole turbine and study blade tip and aspect ratio effects.

- A User-Defined Function (UDF) to consider mechanical resistances and turbine inertia, as well as to simulate an external load, has been developed and coupled to CFD simulation of a VAWT, with the aim of providing insight into VAWT self-starting.

- The study of multiple VAWTs in a wind farm arrangement is also a topic of interest, seeking to maximize power production as a function of the rotor sizes and spacing between them.

- The experimental characterization of the VAWT prototype of this thesis could be extended to higher tip-speed ratio values. Additionally, enclosing the open jet at the wind tunnel test section to force it to pass completely across the turbine rotor could help identify the effect of blockage on the VAWT performance and increase wake velocities for hot-wire measurements.

- PIV measurements in a small-scale VAWT prototype could be another source of information and validation of predictive models.

- The numerical methodology used for the simulation of VAWT airfoils could be employed for airfoil optimization. Tests using a wind tunnel balance could be performed to verify the optimizations performed.

- Finally, a real scale turbine based on the results of this work could be fabricated and tested in open field.

Some of this future research directions are already underway, such as the development of an actuator cylinder model, the UDF for the study of VAWT self-starting, the experimental characterization of the VAWT prototype at higher tip-speed ratio values and the enclosure of the wind tunel open jet, the proposal and simulation of an optimized VAWT airfoil and the fabrication of a real scale turbine.

EN este último capítulo se presentan las conclusiones más significativas de este trabajo. En primer lugar, se evalúa el cumplimiento de los objetivos de la investigación. Después, se discuten los principales descubrimientos e implicaciones. Finalmente, la última sección de este capítulo identifica posibles líneas de investigación futuras.

6.4. Cumplimiento de los objetivos de la investigación

El principal objetivo de esta tesis es el desarrollo de conocimientos científico-tecnológicos aplicables al diseño de turbinas eólicas de eje vertical optimizadas, extendiendo la experiencia del grupo de investigación de Mecánica de Fluidos en este campo y ayudando a consolidar una nueva línea de investigación centrada en turbinas eólicas. Tras realizar una revisión profunda de los sistemas de extracción de energía eólica e identificar las principales técnicas de análisis y diseño analíticas, numéricas y experimentales, un modelo analítico basado en la conservación del momento. Este modelo de tubos de corriente es capaz de predecir las prestaciones de un diseño de VAWT en tiempos computacionales del orden de minutos, resultado adecuado para el diseño de turbinas optimizadas. Además, se han desarrollado modelos de Dinámica de Fluidos Computacional (CFD) para obtener una predicción más exacta de las prestaciones de VAWTs y una descripción más precisa del campo fluido. Finalmente, se ha diseñado y fabricado un prototipo de VAWT a escala reducida (el primero de este tipo en ser diseñado y fabricado en el laboratorio del grupo de investigación) y se ha ensayado en el túnel de viento disponible en el laboratorio del Área de Mecánica de Fluidos.

En este sentido, puede asegurarse que todos los objetivos de investigación propuestos en esta tesis se han completado satisfactoriamente. Se han desarrollado metodologías analíticas, CFD y experimentales para el diseño y el estudio de VAWTs y ahora están disponibles para su uso por parte del grupo de investigación. La metodología y los resultados obtenidos a partir de este trabajo allanarán el camino para futuras investigaciones que se realicen en el grupo de investigación de Mecánica de Fluidos en relación con VAWTs. Además, el conocimiento generado se ha y se está transfiriendo actualmente a pequeñas y medianas empresas, que no pueden permitirse costosos y complejos estudios individuales para este tipo de máquinas. Finalmente, se han realizado varias publicaciones para compartir los resultados de esta investigación con la comunidad científica.

Las secciones posteriores recogen los principales descubrimientos e implicaciones de este estudio, así como las posibilidades de investigación futuras.

6.5. Principales descubrimientos e implicaciones

Se han revisado los principales sistemas de extracción de energía eólica disponibles, presentando una visión panorámica de las prestaciones de los rotores eólicos más típicos. Las turbinas de eje vertical basadas en sustentación representan una solución factible para la generación in situ de energía limpia en aplicaciones donde no es recomendable utilizar tecnologías más convencionales. Pueden funcionar con velocidades de viento más bajas que las de eje horizontal e independientemente de la dirección del viento. Sus niveles de ruido son menores, y las labores de instalación y mantenimiento son mucho más sencillas. Además, el proceso de fabricación de las palas también es mucho más simple. Sin embargo, el flujo generado por estas turbinas es tan complejo que presentan dificultades de autoarranque a bajas velocidades del viento.

Los modelos analíticos basados en la teoría de tubos de corriente han demostrado ser útiles para la predicción rápida de las prestaciones de turbinas eólicas de eje vertical. El principal problema que presentan es la falta de datos experimentales de perfiles aerodinámicos. No obstante, este problema puede solucionarse utilizando software predictivo para obtener los coeficientes de arrastre y sustentación de los perfiles hasta que se puedan realizar ensayos reales en un perfil. La combinación de los modelos de tubo de corriente y una base de datos generada para 34 perfiles resultó ser una herramienta práctica capaz de obtener la curva de rendimiento de la turbina en un tiempo de tan sólo unos minutos (se analizaron 70 diseños diferentes en el Capítulo 3). Aunque la formulación del modelo no considera algunos efectos del flujo (expansión de los tubos de corriente, efectos del eje de la turbina y de las estelas) y la ecuación del momento puede no ser válida para valores elevados de solidez, la buena relación entre la precisión y el coste computacional del modelo justifica su validez para las etapas de diseño de turbinas, ayudando a los diseñadores a proponer diferentes diseños y predecir sus prestaciones casi al instante.

Tras validar el modelo desarrollado con resultados CFD y experimentales, se analizaron los principales parámetros que influencian el rendimiento de una VAWT. Se encontró un rango óptimo de solidez para VAWTs (0.2–0.5). Utilizando este modelo para observar la influencia del número de Reynolds asociado a la turbina en su rendimiento, fue posible proporcionar una idea acerca de los problemas de autoarranque de las VAWTs. Comparando diferentes geometrías de perfiles, se encontró que perfiles delgados y casi simétricos o con baja curvatura resultan óptimos para aplicaciones relacionadas con VAWTs, permitiendo el autoarranque y una amplia banda de alta eficiencia durante el funcionamiento.

Después, se centró la investigación en modelos CFD. Se confirmó la aplicabilidad del método de extrapolación de Richardson para el estudio de la convergencia numérica de simulaciones 2D de una VAWT, resultando en un procedimiento directo para analizar el tamaño de malla y la convergencia temporal de las simulaciones. Los resultados de las simulaciones muestran un acuerdo razonable con las referencias encontradas en la literatura, confirmando la validez de esta metodología para obtener predicciones más precisas de las prestaciones y el flujo generado por una VAWT. El flujo se ha analizado en profundidad a tres valores característicos de ratio de velocidad de punta (punto de trabajo nominal, región con predominio de desprendimiento de vórtices y punto de trabajo superior al nominal). Se pueden identificar cuatro zonas diferentes en la turbina (cercana al viento, lejana al viento, barlovento y sotavento), con la convección de vórtices ocurriendo de maneras diferentes. Además, se ha analizado la pérdida de rendimiento de la turbina al alejarse del punto de trabajo nominal y se ha relacionado con el comportamiento de la dinámica del fluido. Finalmente, se han identificado dos mecanismos principales de generación de inestabilidades: el desprendimiento de vórtices de las palas y la interacción de la rotación de la turbina con el viento incidente.

Posteriormente, se aplicaron diferentes modelos de turbulencia para predecir las prestaciones de un perfil típico de VAWTs mediante simulaciones 3D, encontrando que los mejores resultados se obtenían utilizando modelos basados en la formulación k-ω. Los modelos U-RANS eran capaces de predecir las fuerzas aerodinámicas con un coste computacional mucho menor al resto de formulaciones. Por otra parte, las formulaciones SRS (SAS y DES) eran capaces de obtener más información sobre las escalas más pequeñas del flujo. Por tanto, parece útil aplicar modelos U-RANS o SRS en función del resultado buscado en las simulaciones (fuerzas aerodinámicas sobre el perfil, campo fluido generado por el perfil, o simulación de un perfil como parte de una VAWT).

Finalmente, la metodología desarrollada en esta tesis se utilizó de manera satisfactoria para realizar el diseño aerodinámico de un demostrador experimental de una VAWT. Se desarrolló un procedimiento para la fabricación propia de palas de VAWT utilizando técnicas de deposición de hilo fundido. Se encontró que, al cambiar la orientación de las capas durante la fabricación a la llamada "orientación tipo gota", la resistencia de las palas a las tensiones de flexión aumentaba de forma sustancial.

Las restricciones del túnel de viento redujeron el tamaño posible del prototipo experimental por debajo de 1 m de diámetro, y las resistencias mecánicas encontradas en el montaje de la turbina consumían toda la potencia aerodinámica generada en las palas. Por tanto, se empleó un motor para mover la turbina y se desarrolló un procedimiento para estimar la potencia aerodinámica generada en las palas. Los resultados experimentales muestran una buena correspondencia con las predicciones tanto del modelo analítico como de los modelos CFD. Se midieron las velocidades de la estela de la turbina con hilo caliente, encontrando un efecto de bloqueo al aumentar la velocidad de rotación de la turbina. Las medidas de velocidad y turbulencia también se corresponden con las predicciones del modelo CFD, confirmando la validez de la metodología desarrollada en este trabajo para el diseño y el análisis de VAWTs optimizadas.

6.6. Posibles líneas de investigación futuras

Hay varias líneas de investigación que pueden abrirse a partir de los resultados de este trabajo, no sólo en el campo del modelado y simulación de VAWTs sino también en el campo de la experimentación:

- El modelo de tubos de corriente desarrollado podría ser mejorado añadiendo correcciones para considerar la expansión de los tubos de corriente y los efectos de las estelas del eje de la turbina y las palas, o la influencia de la parte lejana al viento de la turbina en la cercana. Al realizar estas modificaciones, se debería prestar atención al aumento del tiempo computacional, pues podría suceder que un pequeño incremento en la precisión no justifique un coste computacional mucho mayor.

- La similitud encontrada entre la estela de la VAWT y la estela de un cilindro podría justificar el desarrollo de un modelo analítico basasdo en la teoría del cilindro actuador, que tiene en cuenta la interacción entre las palas en la turbina completa y con el flujo externo. También se podrían estudiar modelos de estela en futuros trabajos.

- Respecto a las simulaciones CFD, una posible línea de investigación podría ser extruir el dominio 2D utilizado en esta tesis y realizar simulaciones 3D, probando los diferentes modelos de turbulencia presentados en el Capítulo 4 para obtener una descripción más completa del campo fluido. Si la potencia computacional disponible lo permitiera, sería interesante modelar una turbina completa y estudiar efectos de punta de pala y de relación de aspecto de la turbina.

- Una función definida por el usuario (UDF) que considera la resistencia mecánica y la intercia de la turbina, se ha desarrollado y acoplado a la simulación CFD de una VAWT para tratar de obtener información sobre el autoarranque de una VAWT.

- El estudio de múltiples VAWTs colocadas en una granja eólica también es un tema de interés, tratando de maximizar la producción de energía en función del tamaño de rotor y el espacio entre turbinas.

- La caracterización experimental del prototipo de VAWT de esta tesis podría extenderse a valores más altos de ratio de velocidad de punta. Además, encerrar el chorro abierto de la sección de ensayo del túnel de viento para forzar su paso al completo a través de la turbina podría ayudar a identificar el efecto del bloqueo en el rendimiento de la VAWT y aumentar las velocidades en la estela para realizar medidas de anemometría térmica.
- Otra fuente de información y validación de los modelos predictivos podría ser la realización de medidas PIV en un prototipo a escala reducida.
- La metodología numérica utilizada para la simulación de perfiles de VAWT podría utilizarse para optimizar perfiles. Podrían realizarse ensayos en túnel de viento con una balanza para verificar las optimizaciones realizadas.
- Finalmente, se podría fabricar y ensayar en campo abierto una turbina a escala real basada en los resultados de este trabajo.

Algunos de estos posibles trabajos futuros ya están en marcha, como el desarrollo de un modelo de cilindro actuador, la función definida por el usuario para el estudio del autoarranque de VAWTs, la caracterización experimental del prototipo de VAWT a mayores valores de ratio de velocidad de punta y el guiado del chorro abierto del túnel de viento, la propuesta y simulación de un perfil optimizado para VAWTs y la fabricación de una turbina a escala real.

Acknowledgements

This thesis has been supported by the **FPU15/00199 predoctoral research scholarship** provided by the Spanish Ministry of Education and Vocational Training. Additional support has been provided by the Projects **Desarrollo de una herramienta de diseño optimizado de perfiles aerodinámicos para su utilización en turbinas eólicas de eje vertical (SV-15-GIJON-1-09)** and **Prototipo experimental para la contrastación de modelos de predicción de prestaciones de turbinas eólicas de eje vertical (VAWT) (SV-18-GIJON-1-05)** from the University Institute of Industrial Technology of Asturias (IUTA), financed by the City Council of Gijón, Spain. This work has been also supported by the Project **Diseño optimizado de una turbina eólica de eje vertical (FUO-EM-165-15)**, from the University of Oviedo Foundation and financed by the company AST Ingeniería. Additionally, a **three-months stay scholarship** at the Technical University of Delft was provided by the Spanish Ministry of Education and Vocational Training, reinforcing the internationalization of the scientific training during this thesis. Finally, the mid-term results of this work, alongside the efforts of the research group, contributed to obtaining more funding with the Project **Desarrollo y construcción de turbinas eólicas de eje vertical para entornos urbanos (ENE2017-89965-P)** from the Spanish Ministry of Economy and Business. This last Project was key to providing enough funds for the construction and testing of the VAWT experimental demonstrator developed in the last year of this thesis.

The author of this thesis is very grateful to the different funding organisms that contributed to the realization of this work.

List of Publications

Peer-reviewed articles in indexed journals

8. **A. Meana-Fernández**, J.M. Fernández Oro, K.M. Argüelles Díaz, M. Galdo-Vega and S. Velarde-Suárez, *Application of Richardson extrapolation method to the CFD simulation of vertical-axis wind turbines and analysis of the flow field*, Engineering Applications of Computational Fluid Mechanics **13**(1), 359-376 (2019).

7. **A. Meana-Fernández**, J.M. Fernández Oro, K.M. Argüelles Díaz and S. Velarde-Suárez, *Turbulence-Model Comparison for Aerodynamic-Performance Prediction of a Typical Vertical-Axis Wind-Turbine Airfoil*, Energies **12**, 488-1-16 (2019).

6. J.M. Fernández Oro, **A. Meana-Fernández**, M. Galdo Vega, B. Pereiras and J. González Pérez, *LES-based simulation of the time-resolved flow for rotor-stator interactions in axial fan stages*, International Journal of Heat and Fluid Flow **29**(2), 657-681 (2019).

5. A. Menéndez Blanco, J.M. Fernández Oro and **A. Meana-Fernández**, *Numerical methodology for the CFD simulation of diaphragm volumetric pumps*, International Journal of Mechanical Sciences **150**, 322-366 (2018).

4. I. Solís-Gallego, **A. Meana-Fernández**, J.M. Fernández Oro, K.M. Argüelles Díaz and S. Velarde-Suárez, *LES-based numerical prediction of the trailing edge noise in a small wind turbine airfoil at different angles of attack*, Renewable Energy **120**, 241-254 (2018).

3. **A. Meana-Fernández**, I. Solís-Gallego, J.M. Fernández Oro, K.M. Argüelles Díaz and S. Velarde-Suárez, *Parametrical evaluation of the aerodynamic performance of vertical axis wind turbines for the proposal of optimized designs*, Energy **147**, 504-517 (2018).

2. I. Solís-Gallego, **A. Meana-Fernández**, J.M. Fernández Oro, K.M. Argüelles Díaz and S. Velarde-Suárez, *Turbulence structure around an asymmetric high-lift airfoil for different incidence angles*, Journal of Applied Fluid Mechanics **10**(4), 1013-1027 (2017).

1. P.E. Blanco Alonso, **A. Meana-Fernández and J.M. Fernández Oro**, *Thermal response and failure mode evaluation of a dry-type transformer*, Applied Thermal Engineering **120**, 763-771 (2017).

Books and book chapters

2. J.M. Fernández Oro, **A. Meana-Fernández** and B. Pereiras García, *Turbulence transport in rotor-stator and stator-rotor stages of axial flow fans*, in Turbulence Modelling Approaches - Current State, Development Prospects, Applications, 123-142. IntechOpen (2017). ISBN 978-953-51-3350-6.

1. **A. Meana-Fernández**, I. Solís-Gallego, J.M. Fernández Oro, K.M. Argüelles Díaz and S. Velarde-Suárez, *Modelos analíticos para la predicción de prestaciones de turbinas eólicas de eje vertical y palas rectas*, in Current Trends in Energy and Sustainability 2015 Edition, 285-295. Real Sociedad Española de Física (20176). ISBN 978-84-608-5438-8.

Conferences

10. **A. Meana-Fernández**, J.M. Fernández Oro, K.M. Argüelles Díaz, M. Galdo-Vega and S. Velarde-Suárez, *Aerodynamic design of a small-scale model of a vertical-axis wind turbine*, in *2nd International Research Conference on Sustainable Energy, Engineering, Materials and Environment* (Mieres, Asturias, Spain, 2018).

9. **A. Meana-Fernández**, L. Díaz-Artos, J.M. Fernández Oro and S. Velarde-Suárez, *Proposal of an airfoil geometry for vertical-axis wind turbine applications*, in *2nd International Research Conference on Sustainable Energy, Engineering, Materials and Environment* (Mieres, Asturias, Spain, 2018).

8. **A. Meana-Fernández**,J .M. Fernández Oro, A. Menéndez-Blanco, M. Galdo-Vega, R. Barrio Perotti and E. Blanco Marigorta, *Tendencias en la innovación docente en enseñanzas técnicas: análisis y propuesta de mejoras para la asignatura Mecánica de Fluidos*, in *XXVI Congreso Universitario de Innovación Educativa en las Enseñanzas Técnicas (26 CUIEET)* (Gijón, Asturias, Spain, 2018).

7. J.M. Fernández Oro, **A. Meana-Fernández**, R. Barrio Perotti, J. González Pérez and E. Blanco Marigorta, *Evaluación significativa de prácticas de laboratorio: portfolios versus prueba final objetiva*, in *XXVI Congreso Universitario de Innovación Educativa en las Enseñanzas Técnicas (26 CUIEET)* (Gijón, Asturias, Spain, 2018).

6. L. García, A. Fernández, N. Rodríguez, E. Álvarez, **A. Meana**, J. Fernández, *Caracterización de microturbina hidrocinética mediante modelo numérico de dinámica de fluidos computacional*, in *V Jornadas de Ingeniería del Agua* (A Coruña, Galicia, Spain, 2017).

5. **A. Meana-Fernández**, J.M. Fernández Oro, K.M. Argüelles Díaz, M. Galdo-Vega, S. Velarde-Suárez, L. García, A. Fernández, N. Rodríguez and E. Álvarez, *Selección de perfil hidrodinámico para la construcción de un modelo a escala de una microturbina hidrocinética*, in *V Jornadas de Ingeniería del Agua* (A Coruña, Galicia, Spain, 2017).

4. J.M. Fernández Oro, **A. Meana-Fernández**, B. Pereiras García and E. Fernández-González, *Modelo de evaluación docente del profesorado en procesos de seguimiento y mejora de Títulos de Grado y Máster*, in *XXV Congreso Universitario de Innovación Educativa en las Enseñanzas Técnicas (25 CUIEET)* (Badajoz, Extremadura, Spain, 2017).

3. I. Solís-Gallego, **A. Meana-Fernández**, J.M. Fernández Oro, K.M. Argüelles Díaz and S. Velarde-Suárez, *Optimization of Wind Turbine Airfoils using Geometries based on Humpback Whale Flippers*, in *6th International Congress on Energy and Environmental Engineering and Management* (Paris, France, 2015).

2. **A. Meana-Fernández**, I. Solís-Gallego, J.M. Fernández Oro, K.M. Argüelles Díaz and S. Velarde-Suárez, *Modelos analíticos para la predicción de prestaciones de turbinas eólicas de eje vertical y palas rectas*, in *XXXV Reunión Bienal de la Real Sociedad Española de Física* (Gijón, Asturias, Spain, 2015).

1. **A. Meana-Fernández**, I. Solís-Gallego, J.M. Fernández Oro, K.M. Argüelles Díaz and S. Velarde-Suárez, *Prediction of the performance of Straight-Bladed Vertical Axis Wind Turbines using analytical models*, in *Spain Minergy Congress* (Gijón, Asturias, Spain, 2015).